Kinetics of Electrochemical Oxidation on Platinum Single-Crystal Surfaces

by

Chentian Yuan
B.Sc., St. Francis Xavier University

A Thesis Submitted in Partial Fulfillment of the
Requirements for the Degree of

Master of Science

in the Department of Chemistry

Kinetics of Electrochemical Oxidation on Platinum Single-Crystal Surfaces

by

Chentian Yuan

B.Sc., St. Francis Xavier University

Supervisory Committee

Dr. D. A. Harrington, Supervisor (Department of Chemistry)

Dr. A. G. Brolo, Departmental Member (Department of Chemistry)

Abstract

Understanding the structure and kinetics of electrochemical oxidation of platinum single-crystal surfaces at the atomic level is important to understanding and improving the electrocatalysis of platinum in fuel cells. This thesis concerns the analysis of data from combined electrochemical and surface X-ray diffraction (SXRD) experiments on Pt(111) and Pt(100). In the early stages of oxidation, Pt atoms are extracted from their metal lattice sites and become part of a metal oxide. Their locations have been measured by collaborators using SXRD. The corresponding charges measured electrochemically are determined by integration of cyclic voltammetry, potential step and potential sweep-hold experiments, and used to propose reactions that are occurring in the oxidation.

The measured charge consists of the wanted charge that passes in the electrochemical reactions and a capacitive charge associated with charging the electrical double-layer. Different ways of subtracting the double-layer charge were investigated. Reactions were proposed for optimally corrected charges, and for the worst case where no correction is made, in order to determine the reliability of the proposed reactions.

From cyclic voltammetry experiments on Pt(111) surfaces, during oxidation 0.5 ML adsorbed oxygen and a few extracted PtO (less than 0.1 ML) are formed. Without baseline correction the data are consistent with 0.5 ML O_{ads} and a few extracted PtO_2. After fast scans, the Pt(111) surface is restructured as shown by the X-ray signal, but the oxide peaks in CV are nearly unchanged, which suggests that the electron transfer and Pt extraction do not need to be tightly coupled.

From CV experiments on Pt(100) surfaces, during oxidation many more extracted Pt are formed than on Pt(111). These form long chains with PtO_2 units (0.25 to 0.39

ML) together with O_{ads} and a total coverage of 0.5 ML. If CV isn't baseline corrected, the data is not consistent with long chains with PtO_2 units, but short Pt_3O_8 chains with equal numbers of independent PtO_2 groups. From potential step experiments on Pt(100), there is an expectation from the literature that the charge will grow linearly with log t. However, this relationship was only found during the first second of each step, and then is unchanged after $\sim$1 s. The slopes of the logarithmic plots are linearly related to potential. From sweep hold experiments on Pt(100), both charges and coverage of extracted Pt atoms are not very linear vs log t, and their slopes are also not linearly related to potential but change sharply during the potential range of Pt extraction.

Table of Contents

List of Tables

List of Figures

Nomenclature

Symbol	Meaning	Unit
θ	Surface Coverage	ML
θ	angle for the rotation of Pt sample	$^\circ$
κ	solution conductivity	cm^2 S mol^{-1}
λ	wavelength of X-ray beam	Å
μ	angle of X-ray beam with Pt surface	$^\circ$
ν	wave frequency of X-ray beam	Hz
ρ	resistivity	Ω cm
σ	Surface charge density	μC cm^{-2}
τ	Time constant	s
$(\mathbf{a}, \mathbf{b}, \mathbf{c})$	Three axes of 3-D unit cell	Å
$(\mathbf{a}^*, \mathbf{b}^*, \mathbf{c}^*)$	Axes of 3-D cell reciprocal space	Å^{-1}
$(\mathbf{a_{2D}}, \mathbf{b_{2D}})$	Two axes of 2-D unit cell	Å
$(\mathbf{a^*_{2D}}, \mathbf{b^*_{2D}})$	Axes of 2-D cell reciprocal space	Å^{-1}
A	Surface area	cm^2
c	Light speed	m s^{-1}
C	Capacitance	μF cm^{-2}
d	spacing of the 3-D Pt planes	Å
E	Potential	V
E	Energy of X-ray beam	eV
F	Structure factor	
F	Reciprocal lattice vector, Crystal momentum	
h	Planck constant	eV Hz^{-1}
(h,k,l)	Miller indices	

Symbol	Meaning	Unit
I	Current	A
I	X-ray intensity	c/s
j	Current density	A cm^{-2}
k	Reciprocal vector of X-ray beam	
p	Momentum of a photon in X-ray beam	kg m s^{-1}
Q	Charge	C
R_s	Solution resistance	Ω cm^2

Abbreviation	Meaning
2-D	Two-dimension(al)
3-D	Three-dimension(al)
ads	Adsorption
CE	Counter electrode
CV	cyclic voltammetry
dl	Double layer
DFT	Density functional theory
e^-	Electron
ex	Platinum extraction
fcc	Face centered cubic (crystal)
H UPD	Underpotential deposited hydrogen
ML	Monolayer
Pt	Platinum
RE	Reference electrode
RHE	Reversible hydrogen electrode
WE	Working electrode

Acknowledgements

I would firstly like to thank the University of Victoria for giving me the chance to continue my studies on this interesting field of chemistry. Also I thank the staff at the ESRF and DESY beamlines for technical support for the experiments. I thank our collaborators, Dr. Jakub Drnec and his group from ESRF and Dr. Olaf M. Magnussen's and his group from Kiel University for the opportunity and for assistance throughout this project, and especially Timo Fuchs for help with the X-ray parts of the data analysis.

This work is part of an ongoing project with synchrotron beamtime funded by the ESRF and DESY, and other financial support from Deutsche Forschungsgemeinschaft and the Natural Sciences and Engineering Research Council of Canada.

I also thank the teachers and students in the Chemistry Departments and other parts of UVic for help and memorable experiences during my study life at UVic. I especially thank my parents for giving me physical and mental supports to study in a foreign land far away from home. Finally, I thank my supervisor Dr. David Harrington for giving me continuous support and guidance during my study at UVic.

To my parents and the world.

Chapter 1

Introduction

Platinum (Pt) is a hot topic in electrochemistry in the recent years, especially in electrocatalytic reactions [1–5]. It is widely used in energy conversion and storage, especially in the polymer electrolyte membrane fuel cell (PEMFC) [2, 3, 6–9]. The hydrogen fuel cell is a typical PEMFC using platinum as catalyst [10–13]. The hydrogen fuel cell had a vehicle market of $3.85 billion in 2021 with a growth rate of 38.8% compared with 2020, including cars [14], trucks [15], buses [16], or even trains in the future [17]. In a hydrogen fuel cell supplied with enough hydrogen and oxygen gases, hydrogen gas is oxidized to H^+ ions on its anode with reaction in Eq. 1.1 at a standard electrode potential of 0 V, and oxygen gas is reduced to water on its cathode with reaction in Eq. 1.2 at a standard electrode potential of 1.231 V.

$$H_2 \rightarrow 2H^+ + 2e^- \tag{1.1}$$

$$O_2 + 4H^+ + 4e^- \rightarrow 2H_2O \tag{1.2}$$

The open circuit potential of Pt electrode without oxygen is 0.8 V. The experimental open circuit potential of Pt with oxygen in real hydrogen fuel cell is around 1.0 V [18, 19], and the practical operating range is around 0.5 to 0.8 V [18, 20]. Pt oxide exists on the surface for potentials above about 0.8 V. So when fuel cell is turned off, the potential of Pt electrode increases from <0.8 V to 1.0 V and is oxidized on the surface, then no matter the cell is turned on again, or left there with oxygen gas gone, its potential will drop to <0.8 V and Pt oxide will be reduced back to Pt atoms. This repeated oxidation and reduction of oxide restructures the Pt surface, which leads to lower platinum's ability to catalyse the above reactions and limit the lifetime of the Pt catalyst [4, 21]. In order to understand how to minimize these negative effects, it is important to understand the mechanism of electrochemical oxidation of Pt at the atomic level. This research is focused on understanding some of the details of the kinetics of platinum oxidation.

The main topic of this research is the oxidation kinetics of the low index platinum surfaces, Pt(100) and Pt(111). During oxidation, some of the platinum surface atoms are oxidized and leave their original sites under a specific potential range, then during reduction they will go back to their original place or another place on the platinum surface [22–24]. To research this topic, we use the electrochemical techniques, like cyclic voltammetry, potential steps, and sweep holds. These methods control the potential of the platinum surface to make the reaction happen, and the resulting currents are measured. The current-time information is converted to charge densities on the platinum surface, and then converted to electrons transferred per platinum atom [25]. Also surface X-ray diffraction (SXRD) is used to detect the changes to the platinum surface caused by platinum oxidation [26–30]. The SXRD is measured at the same time as the electrochemical techniques, so the X-ray data on the number of

oxidized Pt atoms can be directly compared with the charges from electrochemistry. Therefore we can get the stoichiometry of the reactions and the oxidation states of the species.

This research is part of a large collaboration involving groups from France, Germany, Spain, and Canada. The experiments were carried out at the European Synchrotron Radiation Facility (ESRF) in Grenoble, France or at the Deutsches Elektronen-Synchrotron (DESY) in Hamburg, Germany. In some cases the equipment was controlled remotely online through the servers of ESRF or DESY. The determination of the numbers of the atoms and their locations from the X-ray data were the primary responsibility of the groups of Dr. Jakub Drnec from ESRF, France and Dr. Olaf M. Magnussen from Kiel University, Germany. Dr. Serhiy Cherevko's group from Friedrich–Alexander University Erlangen–Nürnberg has carried out parallel experiments on dissolution on Pt surfaces using mass spectrometric methods. For the case of the Pt(111) and Pt(100) surfaces, Dr. Federico Calle-Vallejo from Spain carried out Density Functional Theory (DFT) calculations to determine the atom locations, which helped to interpret the X-ray data. Our group from University of Victoria, Canada focuses on electrochemical (EC) aspects of the data collected during beamtimes IHCH925, IHCH10377, CH4977, CH5523, CH5700, and CH5918. All the groups from Germany and Canada have contributed to the running the experiments, and the present author joined beamtime CH5700 in November 2020 and DESY beamtime in April 2021, and was involved in remote operation of the EC control during beamtime CH5700.

To clearly describe the background and results of this research, this thesis is divided in 5 chapters. This chapter 1 is the introduction to this thesis. Chapter 2 gives background about the electrochemistry theory and techniques, and informa-

tion about platinum. It also describes the methods of electrochemical and X-ray techniques used in this research. Chapter 3 is presents the results and discusses their interpretation. Chapter 4 is the conclusions and suggestions for the future direction of this research.

Chapter 2

Background and Literature Review

In this chapter, some knowledge of electrochemistry will be introduced, such as the solution resistance, the electrical double layer, the reference electrode, and different types of electrochemical experiments. Also, platinum related electrochemistry will be covered, like the different types of platinum surface, the definition of coverage and monolayer, and the performance and reactions of the peaks of platinum in cyclic voltammogram. Last the X-ray diffraction will be introduced.

2.1 Introduction to Electrochemistry

2.1.1 Electrochemical Cell

The electrochemical cell is a device to make chemical reactions with electrical energy gained or imported. It works as left part of Fig. 2.1 shows, there is a potentiostat to provide electricity between the working electrode (WE), the counter electrode (CE), and the reference electrode (RE). The current flow goes from the working electrode

(WE) mostly to the counter electrode (CE), very little part to the reference electrode (RE). The potential between WE and RE can be controlled and measured by potentiostat, and the current between WE and CE is measured during experiments. The reference electrode (RE) is a kind of electrode with stable and well-known potential. It measures the potential of a point in the solution between WE and CE. The process happening on WE surface is what we study in this research.

To study the WE surface with X-ray techniques, the hanging meniscus cell shown as right part of Fig. 2.1 is used to replace the traditional fully encased electrochemical cell and let the X-ray beam pass through. There is a glass tube on the top, with the reference electrode, the counter electrode and electrolyte inside suspended above the round Pt surface with 7 mm diameter connected by the working electrode, and the electrolyte goes down from the glass tube and wet the Pt surface to make the meniscus that the X-rays pass through.

2.1.2 Solution Resistance

The solution resistance (R_s) is the ability of electrolyte to impede the current flow. In an electrochemical cell like Fig. 2.1, the solution has resistance to oppose this current flow between working electrode (WE) with counting electrode (CE) and reference electrode (RE), and this resistance can lower the potential between electrodes. Since the measured potential is between the WE and RE, the R_s really measured in experiments is the resistance between WE and RE, and the solution resistance between WE and CE is unknown.

In this research, for most platinum electrochemical experiments, the distance between WE and RE is 4 mm, and 0.1 M (1×10^{-4} mol cm^{-3}) $HClO_4$ solution is used

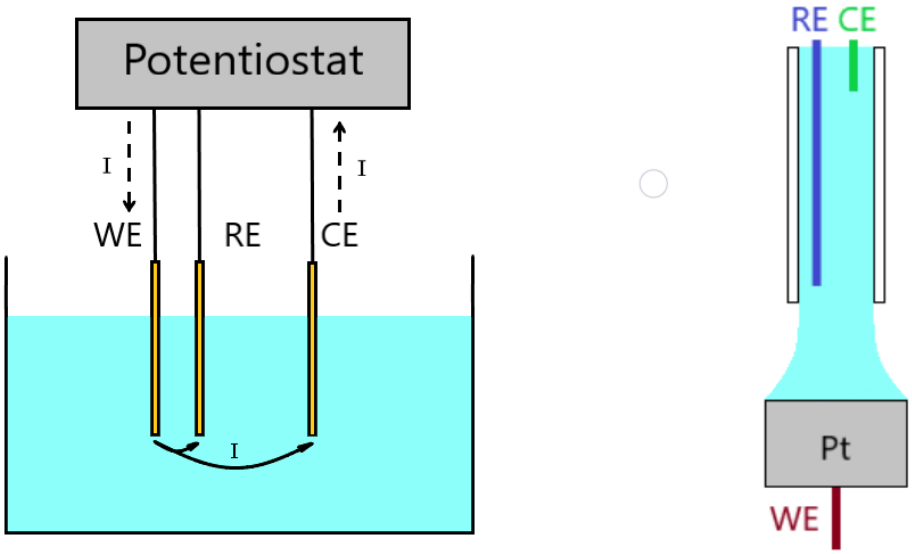

Figure 2.1: Schematic of the electrochemical cell with anodic reaction (left), a potential is given by potentiostat to make the current flow from the working electrode (WE) through solution to the counter electrode (CE), also a little part to the reference electrode (RE), and then back to potentiostat. Also schematic of the hanging meniscus cell used in this research (right), both CE and RE are in a glass tube suspended above the platinum surface connected by WE. The electrolyte goes down from the glass tube, just wets the Pt surface, to form an electrochemical cell.

in most experiments. To get the solution resistance, solution conductivity (κ) can be found from the molar conductivities of ions at infinite dilution, 349.65 cm^2 S mol^{-1} for H^+ and 6.73 cm^2 S mol^{-1} for ClO_4^- [31] as $\kappa = (349.65+6.73)\times1\times10^{-4} = 3.56\times10^{-2}$ S cm^{-1}. Then the resistivity (ρ), reciprocal of conductivity, is $\rho = \frac{1}{\kappa} = \frac{1}{3.56\times10^{-2}} = 28.1$ Ω cm. Now, if we assume the electric field is uniform and normal to WE surface, the electrical resistance (R_s) has relation with resistivity (ρ) as $\rho = R\frac{A}{l}$, in which A is the area of WE surface, and l is the distance between WE and RE, so the solution resistance (R_s) with WE surface area included, is $R_s = \rho \times l = 28.1 \times 0.4 = 11.2$ Ω cm^2.

$$R_s = \frac{0.4}{(349.65 + 6.73) \times 1 \times 10^{-4}} = 11.2 \quad \Omega \text{ cm}^2 \tag{2.1}$$

And for a round Pt working electrode with diameter of 0.7 cm, R_s is 29.1 Ω.

However, in the real experiments, the electric field can't be uniform and normal to WE surface. As right part of Fig. 2.1 shows, the WE is a surface at the bottom, but the CE is a wire on the top, so the electric field is more like a circular cone with the end of CE as top point and WE surface as bottom surface, and the end of RE is off-centre and about 4 mm from the bottom of this circular cone. Because of this, it's hard to describe the location of RE in this electric field and to calculate the R_s. Therefore, the ideal R_s from the calculation may be not suitable for the real experiments, and the measurement of R_s is needed. From beamtime CH5918, the measured R_s varied in the range 35-50 Ω, larger than 29.1 Ω from calculation.

2.1.3 Reference Electrode

As Fig. 2.1 shows, the reference electrode is used in electrochemistry experiments, so the potentials are always versus reference electrode and can be translated to versus reversible hydrogen electrode (RHE), which is a kind of standard electrode with potential only related to the pH value of electrolyte, $E(RHE) = E(SHE) - 0.059V \times pH$. For example, in the cyclic voltammetry experiment at the CH5700 beamtime shown as Fig. 2.2, 3.5 M Ag/AgCl reference electrode is used, and all raw potential data shown in the left vertical coordinate of Fig. 2.2 need additional 0.274 V to be converted to RHE, which is shown in the right vertical coordinate of Fig. 2.2.

2.1.4 Electrical Double Layer and X-ray Beam Damage

The electrical double layer is a structure made by one layer of charges on the electrode surface, and ions with opposite charge on the solution near the electrode, and Fig. 2.3 shows a simple model of the double layer, the Helmholtz double layer model. It's an early simple model for electrical double layer. The part on the solution near the electrode has the change located at fixed locations in planes. It is a few Ångstroms thick and has two layers, inner Helmholtz plane with one layer of solvent molecules as water here, and outer Helmholtz plane with solvated cations or anions covered by solvent with counter charges of electrode. For example in Fig. 2.3 with $HClO_4$ solution, it is a charged positive electrode, so there is one layer of positive charges on the electrode surface, then one layer of water dipoles on the electrode surface as inner Helmholtz layer, and then there is one layer of ClO_4^- anions as the outer Helmholtz plane. These charges are called the double-layer charges [32–35]. The

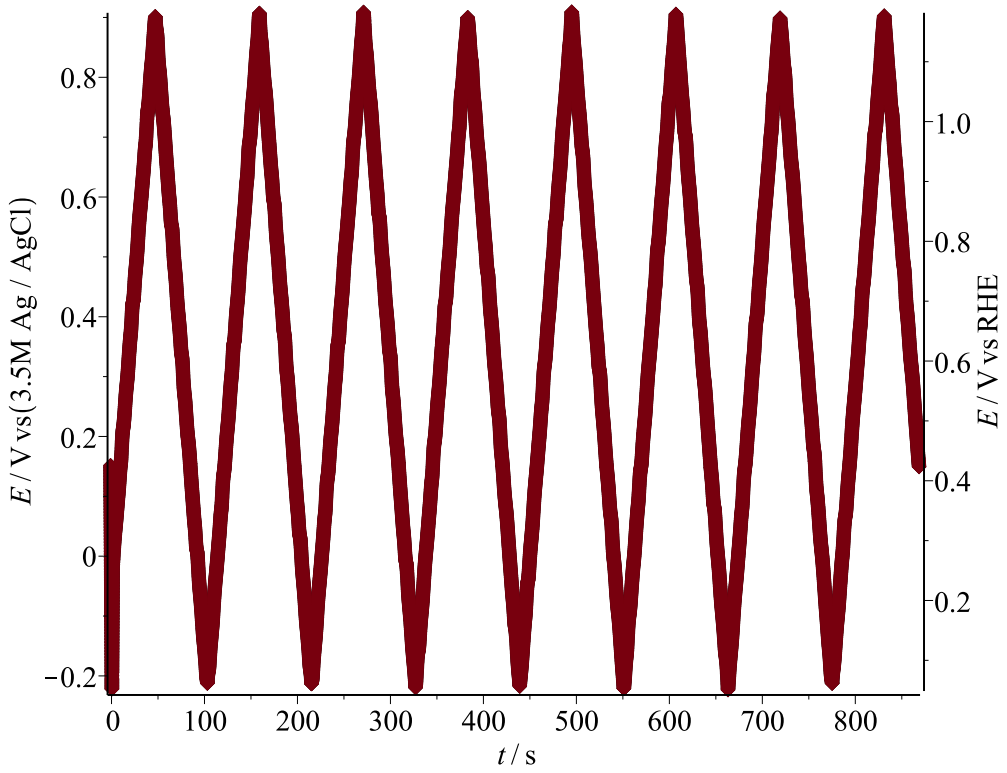

Figure 2.2: Potential vs time for Pt(111) cyclic voltammetry. There are ∼5 data points each 5 mV. The left vertical coordinate is potential vs 3.5 M Ag/AgCl electrode, the right left vertical coordinate is potential vs RHE. The start potential of each cycle is 0.424 V vs RHE, the minimum potential is 0.054 V vs RHE, and the maximum potential is 1.174 V vs RHE. Sweep rate as 20 mV/s. Data from Cycle 136 to 143 of EC file 25 at the CH5700 beamtime at ID31 at the ESRF in November 2020.

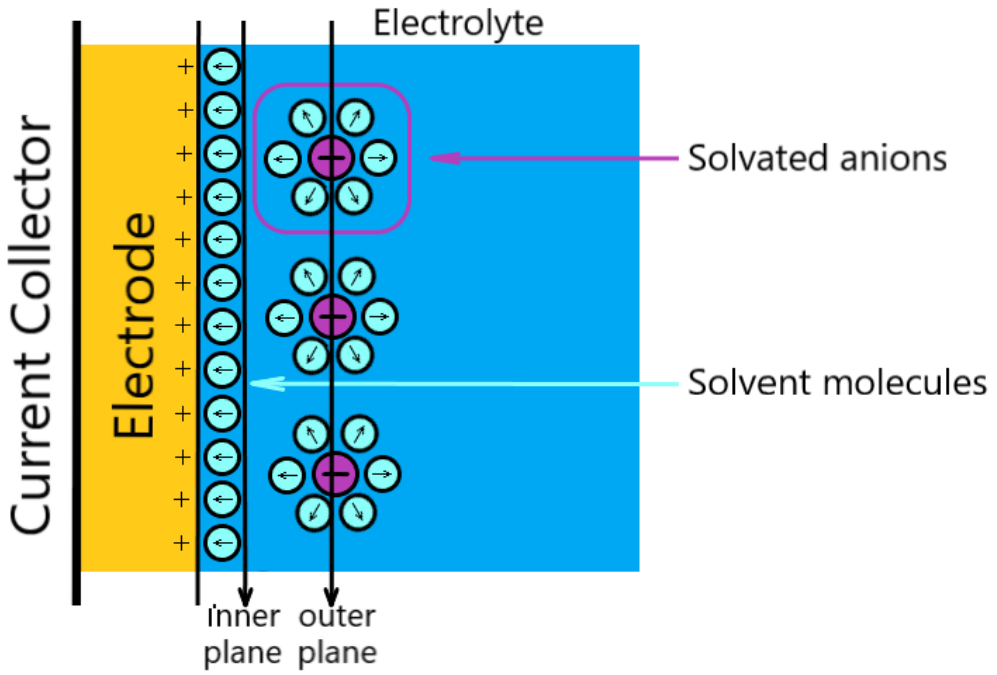

Figure 2.3: Schematic of electrical double layer near the surface of a positive electrode.

double layer capacitance, the ratio of charges to potential, is largely independent of potential [36, 37]. This agrees with the simple Helmholtz double layer model well, and therefore a more complicated double-layer model is not needed in this work. The double layer capacitance of Pt(111) is ~20 μF cm^{-2} under any potentials [36, 38], and that of Pt(100) is 20 - 30 μF cm^{-2} under most potentials, except ~50 μF cm^{-2} around -0.1 V vs SCE [39].

The total current between the electrode and solution includes Faradaic current associated with charge transfer between the electrode surface and solution associated with an electrochemical reaction, and a non-Faradaic process like charging of the electrical double layer. So non-Faradaic current should be removed from total current

if Faradaic current is needed to describe the electrochemical reactions.

Also, X-ray beam damage can form H_2O_2 in the solution near the Pt surface. H_2O_2 is typically oxidized above about 0.8 V in acidic solvent as below [40]:

$$H_2O_2 \rightarrow O_2 + 2H^+ + 2e^- \tag{2.2}$$

and reduced below 0.8 V in acidic solvent as below [40]:

$$H_2O_2 + 2H^+ + 2e^- \rightarrow 2H_2O \tag{2.3}$$

This makes current higher when potential is higher than 0.8 V, and makes current lower when potential is lower than 0.8 V. However, when OH groups are adsorbed on the Pt surface, OH film blocks Pt surface tightly, and so H_2O_2 reduction is suppressed.

2.1.5 Cyclic Voltammetry

Cyclic voltammetry (CV) is an electrochemical technique extensively used in this research. In this technique, a specific potential program is applied between the working electrode and the reference electrode, and the corresponding current is recorded. The potential program always decreases from a start potential to a minimum potential with a constant sweep rate, then increases to a maximum potential, decreases to the start potential, and repeats as the next cycles. For example, for the chosen cycles in the CV experiment at the CH5700 beamtime shown as Fig. 2.2, the sweep rate is 20 mV/s, the start potential is 0.424 V vs RHE, the minimum potential is 0.054 V vs RHE, and the maximum potential is 1.174 V vs RHE. For the spectrum of one of

the cycle, it is shown as Fig. 2.4.

For further CV data treatment in this research, currents are translated to current density (j) by dividing by the area of the working electrode, which is a circle with diameter as 7 mm, also double layer currents need to be removed by baseline correction as stated in section 2.1.4, to get charges transferred in reaction, which will be converted to coverage of electrons transferred, θ_e. This will be further discussed in section 2.2.2, where it will be compared with coverage of extracted Platinum, θ_{ex} from X-ray data, which will be introduced later.

2.1.6 Potential Step

Potential step is another kind of electrochemical technique which can provide different information about electrode surface compared with cyclic voltammetry. In potential step, the potential jumps between different potentials and is held at the final potential without sweeping between them as cyclic voltammetry. In the specific experiment here, it will drop to and stay at a lower hold potential between steps, e.g., 0.15 V in Fig. 2.5. For each step as in Fig. 2.6, which is the first 2 s of a 60-second step, the potential keeps at a potential of 0.95 V with no change. The current increases sharply, then slowly decreases to a positive current very close to 0 inside 1 s, then fluctuates around it due to beam damage. More details and data treatment will be further discussed in section 3.2.4

2.1.7 Double Layer charging for Potential Step

As Section 2.1.4 introduced, double layer current appears whenever potential changes and the electrode starts charging, and this is true also for the potential step experi-

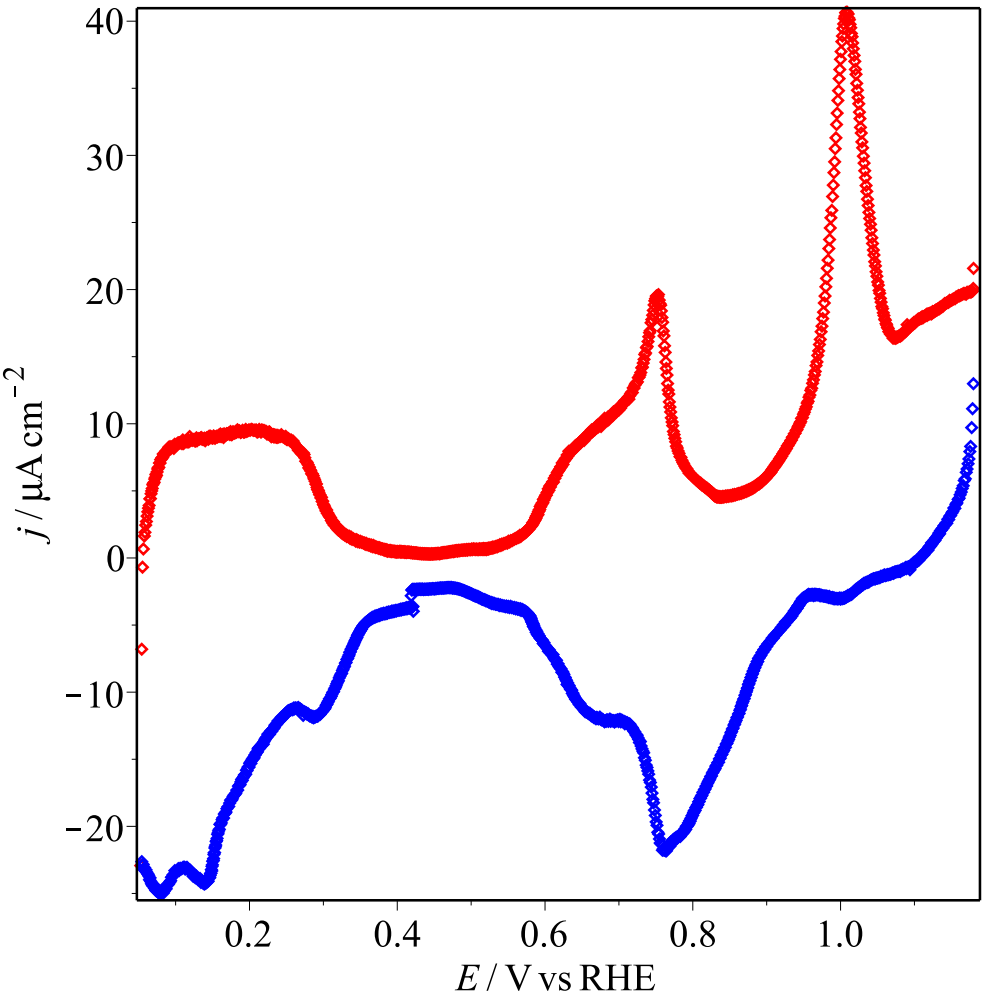

Figure 2.4: Pt(111) cyclic voltammogram spectrum. The red points are forward sweep and the blue points are reverse sweep. Sweep rate as 20 mV/s. Data from Cycle 140 of EC file 25 at the CH5700 beamtime at ID31 at the ESRF in November 2020.

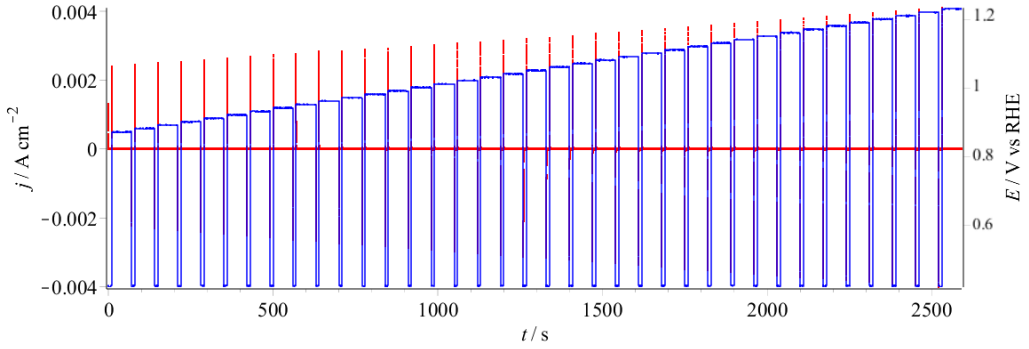

Figure 2.5: Pt(100) Potential steps in 0.1 M $HClO_4$ from the double layer. The red curve is current density and the blue curve is potential. Data from EC file 57 at the CH4977 beamtime at ID31 at the ESRF in July 2017.

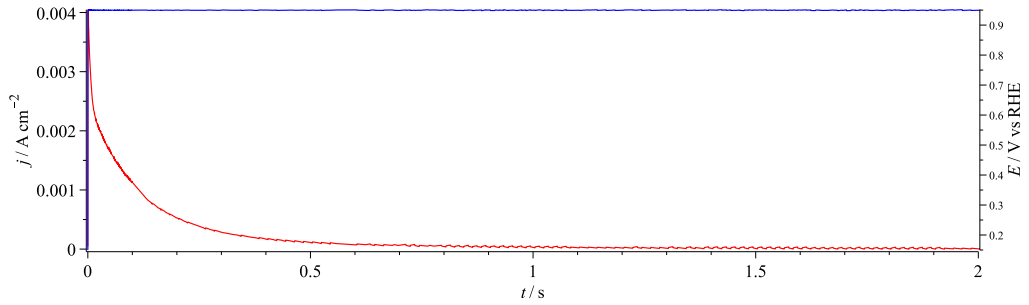

Figure 2.6: First 2 s of the oxidation portion of potential step to 1.20 V on Pt(100) in 0.1 M $HClO_4$ from the double layer. The red curve is current density and the blue curve is potential. Data from EC file 57 at the CH4977 beamtime at ID31 at the ESRF in July 2017.

ments. Unlike in the cyclic voltammetry where the potential slowly scans from one voltage to another, in the potential steps, the potential suddenly increases from a low initial potential to a high one, like the step in Fig. 2.6, which increases from 0.15 V to 0.95 V in the beginning, so the double-layer charging current exists and is very obvious when the step begins.

The double layer charging depends on two quantities, the solution resistance (R_s) and the double layer capacitance (C_{dl}) as Fig. 2.7 shows. The relation of potential (E) and current density (j) of two parts are:

$$E_s = R_s j_s \tag{2.4}$$

$$j_{dl} = C_{dl} \frac{\mathrm{d}E_{dl}}{\mathrm{d}t} \tag{2.5}$$

Then as Kirchoff's laws, the current density of the solution resistance and the double layer capacitance are the same, and the step-in potential (E_f) is the sum of the potentials of the solution resistance and the double layer capacitance:

$$j_s = j_{dl} \tag{2.6}$$

$$E_f = E_s + E_{dl} \tag{2.7}$$

The charges on the electrode can't change instantaneously when the step begins, so we assume the initial potential (E_i) as the voltage across the capacitor before step:

$$E_{dl}(0) = E_i \tag{2.8}$$

So if we combine these three equations together, we can get:

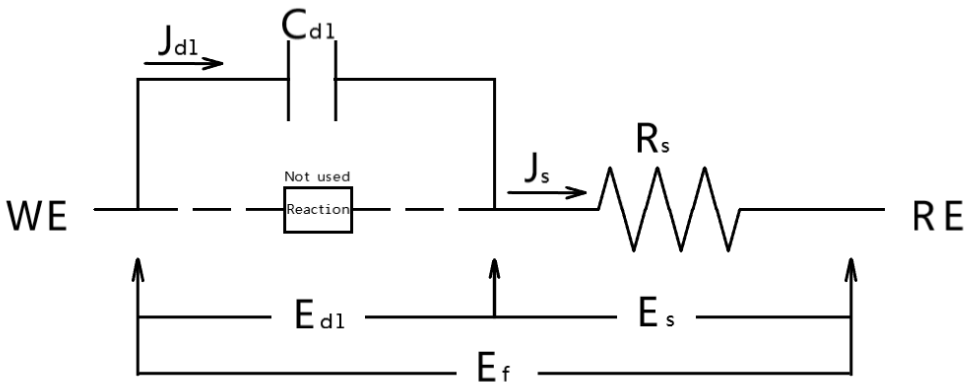

Figure 2.7: [Schematic of solution resistance (R_s) and double layer capacitance (C_{dl}) in electrochemical cell, J is the current density, and E is the potential.

$$j = j_0 exp(-\frac{t}{\tau_{dl}}) \tag{2.9}$$

where the time constant $\tau_{dl} = R_s C_{dl}$, and $j_0 = \frac{E_f - E_i}{R_s}$, also we assume j_0 as the current density at 0 second in potential step experiments, for the Faradaic current from reactions appears 10^{-2} s, much slower than the non-Faradaic double layer current, faster than 10^{-3} s.

In this research, as the expected solution resistance (R_s) of 0.1 M $HClO_4$ is 11.2 Ω cm^2 from Section 2.1.2, and the double layer capacitance (C_{dl}) of Pt(111), Pt(100) is 20 μF cm^{-2} from Section 2.1.4, so the expected time constant from the function is:

$$\tau_{dl} = R_s C_{dl} = 11.2 \quad \Omega \text{ cm}^2 \times 20 \quad \mu\text{F cm}^{-2} = 0.224 \quad \text{mS} \tag{2.10}$$

However, in the real experiments, the electric field isn't uniform and normal to working electrode surface as Section 2.1.2 expected, the solution resistance is different

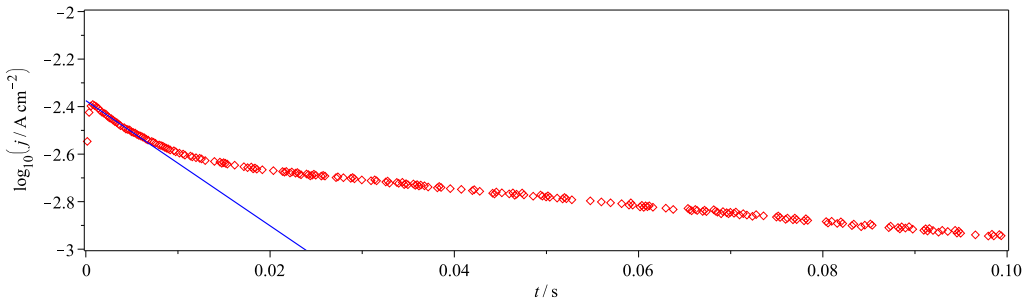

Figure 2.8: $\log_{10}$(current density) of potential step to 1.20 V on Pt(100) in 0.1 M $HClO_4$ from the double layer. The red curve is the $\log_{10}$(current density). The blue line is fitted line of very first part from 0 to 0.002 s to remove double layer capacitance. Data from EC file 57 at the CH4977 beamtime at ID31 at the ESRF in July 2017.

from expected. τ_{dl} and j_0 can be calculated by fitting the very beginning part of the $\log_{10}(j)$ vs t plot of each step, with the intercept of fitted line as $\log_{10}(j_0)$, and τ_{dl} as $\frac{-1}{slope}$. The baseline can be used to remove double layer currents in potential steps, and an example is shown as Fig. 2.8, and the corresponding corrected current density plot is shown as Fig. 2.9.

2.2 Introduction to Platinum Electrochemistry

This section is to introduce the platinum electrochemistry, like what does the platinum surface look like, different types of platinum surface, the definition of coverage and monolayer, the performance and reactions of the peaks of platinum in cyclic voltammogram, also platinum extraction and dissolution.

2.2.1 Platinum Surfaces

What does the platinum surface look like, different types of platinum surface is covered in this subsection. Different crystalline materials have different structures, which can be simplified as a repeatable unit cell. Platinum (Pt) has a face centered cubic (fcc) crystal, and its unit cell is shown as Fig. 2.10.a. If we set the edges in three dimensions of a Pt unit cell cube, also three axis vectors as $(\mathbf{a}, \mathbf{b}, \mathbf{c})$, their length are equal, so $a = b = c$, and for platinum it's 3.9242 Å. There are eight $\frac{1}{8}$ atoms in each corner of the unit cell, and six $\frac{1}{2}$ atoms on each face centre of the unit cell, so there are 4 Pt atoms in all in each unit cell.

If the crystal unit cell is cut in different ways, it can show different surfaces, such as Pt(100), Pt(111), and Pt(110) in Fig. 2.10. To describe the surface orientation and planes parallel to the surface, we use a set of numbers (h, k, l) known as Miller indices. Miller indices is based on $(\mathbf{a}, \mathbf{b}, \mathbf{c})$ with the unit of lattice parameters. If the cut surface passes the endpoint of the axes, like all three axes $(\mathbf{a}, \mathbf{b}, \mathbf{c})$ for Pt(111) in Fig. 2.10.c, then we mark the intercepts of (a, b, c) as $(1, 1, 1)$. As the cut surface has the distance as one lattice parameter in the directions **a**, **b** and **c**, the Miller indices are the reciprocals of these numbers, $(h, k, l) = (\frac{1}{1}, \frac{1}{1}, \frac{1}{1}) = (1, 1, 1)$. If the cut surface is parallel to one or two axes, like for Pt(100) in Fig. 2.10.b, the surface has the distance as one lattice parameter in the direction **a**, and is parallel to axes **b** and **c**, then we mark $(a, b, c) = (1, \infty, \infty)$, so Miller indices as $(h, k, l) = (\frac{1}{1}, \frac{1}{\infty}, \frac{1}{\infty}) = (1, 0, 0)$; also for Pt(110) in 2.10.d, the surface passes the endpoint of axes a, b and is parallel to axis c, so $(a, b, c) = (1, 1, \infty)$, and Miller indices $(h, k, l) = (\frac{1}{1}, \frac{1}{1}, \frac{1}{\infty}) = (1, 1, 0)$. If the cut surface passes $\frac{1}{2}$ of an axis like a, then we mark $a = \frac{1}{2}$, and Miller index $h = \frac{1}{1/2} = 2$.

In bottom pictures of Pt(100), Pt(111), and Pt(110) in Fig. 2.10, there are three

black parallelogram frames, which are the 2-D unit cells of each platinum surface, and in Fig. 2.11, the blue rhombus frame is 2-D unit cell of Pt(111), with its two deep blue axes as $(\mathbf{a_{2D}}, \mathbf{b_{2D}})$ and $a_{2D} = b_{2D}$, is the reference unit cell described as (1×1). For another cell in Fig. 2.11 with red parallelogram frame, the length of its axes, which are marked as $(\mathbf{a'_{2D}}, \mathbf{b'_{2D}})$ to differ from blue 2-D unit cell, isn't the same as unit cell, $a'_{2D} = b'_{2D} = \sqrt{3}a_{2D}$, so we describe it as $(\sqrt{3} \times \sqrt{3})$. Also the direction of axes $\mathbf{a'_{2D}}, \mathbf{b'_{2D}}$ rotate 30° from the axes $\mathbf{a_{2D}}, \mathbf{b_{2D}}$, so we describe it as $(\sqrt{3} \times \sqrt{3})R30°$. Then this red cell is to show the ratio of adsorbed H atoms to Pt surface atoms with coverage of $\frac{2}{3}$ ML, so we finally describe it as $(\sqrt{3} \times \sqrt{3})R30°$-$\frac{2}{3}$H.

2.2.2 Coverage

The ratio of the number of total adsorbed groups, or total transferred e^-s to the number of Platinum surface atoms can be described as coverage, θ. The unit to describe coverage is monolayer (ML), for example, the red parallelogram frame in Fig. 2.11 is a Pt(111) $(\sqrt{3} \times \sqrt{3})$ R30° - H unit cell with two adsorbed H atoms as black circles and 3 Pt surface atoms as white circles, so its coverage is $\frac{2}{3}$ ML.

In cyclic voltammetry, coverage of electrons, θ_e, is used as the ratio of transferred e^-s to platinum surface atoms. The coverage θ_e of a specific CV peak, such as the coloured ones in Fig. 2.12, is used to figure out how many groups or atoms are adsorbed to Platinum surface through reaction. 1 ML θ_e of different Pt surface is determined by the charge density of one-atom 2-D unit cell with 1 e^- each Pt atom, which are three black parallelogram frames on Pt(100), Pt(111), and Pt(110) surface in Fig. 2.10, and the coverage θ_e of specific peak is got from dividing the charge density passed by the charge density corresponding to 1 ML θ_e of coverage shown above.

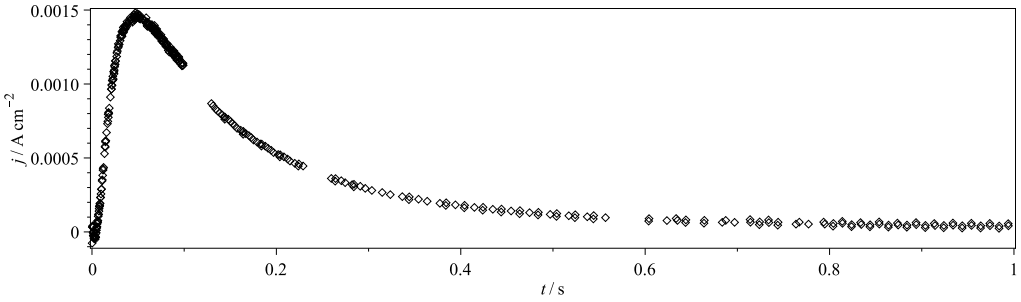

Figure 2.9: Double layer corrected current of the oxidation portion of potential step to 1.20 V on Pt(100) in 0.1 M $HClO_4$ from the double layer. Data from EC file 57 at the CH4799 beamtime at ID31 at the ESRF in July 2017.

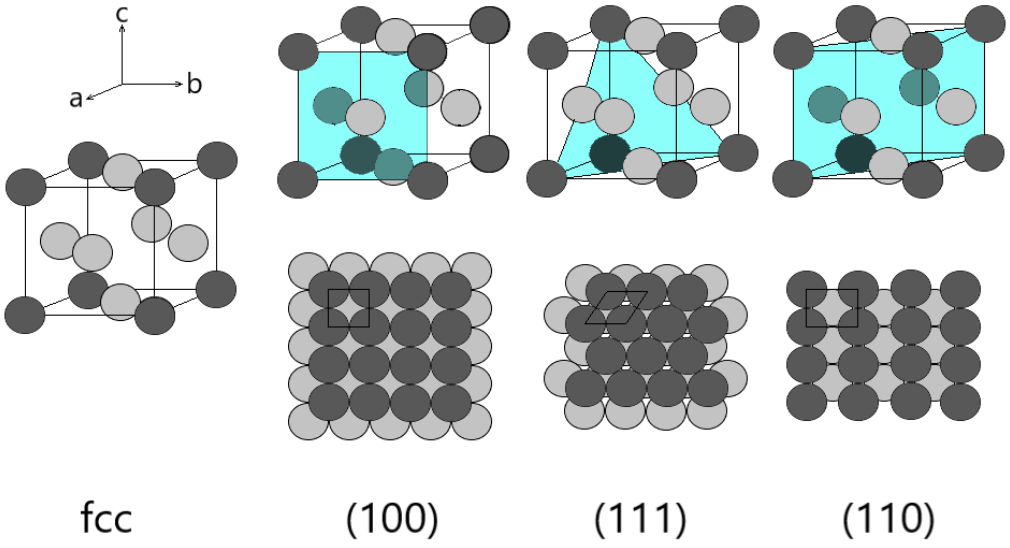

Figure 2.10: Schematic of (a) Face Centered Cubic (fcc) crystal unit cell, (b) Pt(100) surface, (c) Pt(111) surface, (d) Pt(110) surface.

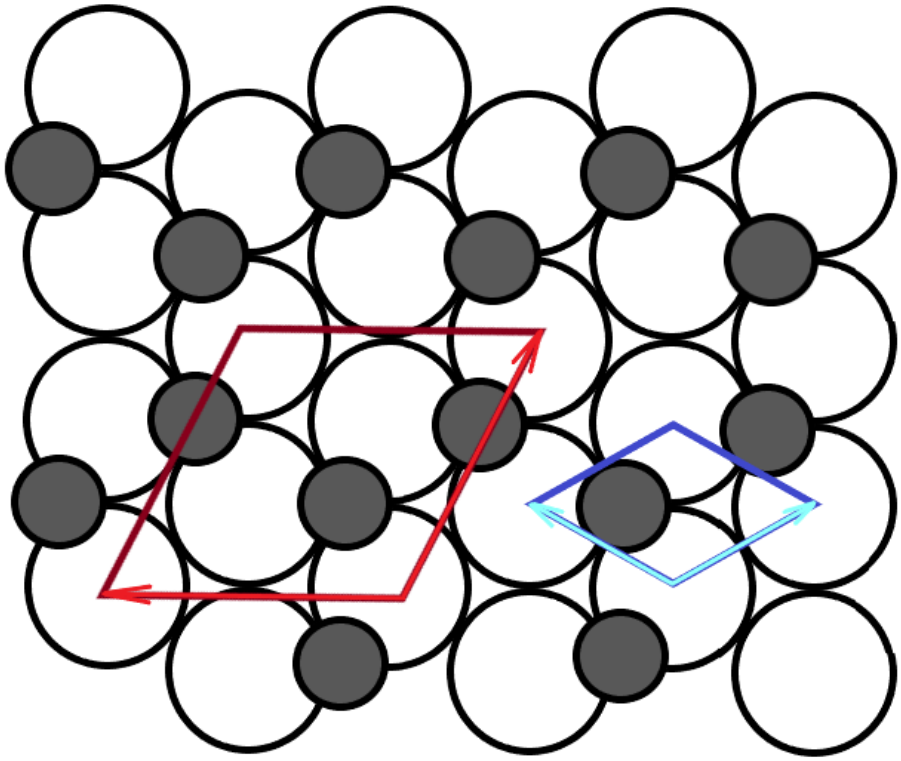

Figure 2.11: Schematic of H UPD adatams in 3-fold hollow site on fcc(111) surface. The blue rhombus frame is a (1×1) unit cell for clear surface. The red parallelogram frame is a $(\sqrt{3} \times \sqrt{3})R30^{\circ}$-H unit cell with θ of H UPD adatoms as 2/3 ML.

For example, the unit cell cube of Platinum crystal shows in Fig. 2.10, for Pt(100), the length of the edge of Pt(100) one-atom 2-D unit cell is $a_{2D} = \frac{a}{\sqrt{2}}$, in which a is the edge of 3-D unit cell, its area is $A = \left(\frac{a}{\sqrt{2}}\right)^2$. If we divide charge of 1 e^- by this area A, then 1 ML θ_e corresponds to a charge density of 208.08 $\mu C/cm^2$. For Pt(111) with 2-D one-atom unit cell as a rhombus, its edge is $a_{2D} = \frac{a}{\sqrt{2}}$, its area is $A = \frac{\sqrt{3}}{2} \times \left(\frac{a}{\sqrt{2}}\right)^2$, and 1 ML θ_e corresponds to a charge density of 240.27 $\mu C/cm^2$. For Pt(110) with 2-D one-atom unit cell as a rectangle, its edge is $a_{2D} = \frac{a}{\sqrt{2}}$ of one side, and $b_{2D} = a$ for another, its area is $A = \frac{a^2}{\sqrt{2}}$, so the charge density of 1 ML θ_e is 147.13 $\mu C/cm^2$.

2.2.3 Peaks of Platinum in CVs

There are three anodic peaks for Platinum on cyclic voltammograms: the reverse of H underpotential deposition (H UPD) peak [41–43], the OH adsorption (OH_{ads}) peak [41, 44–46], and the Pt oxide peak [47, 48], at which the platinum oxidation only takes place. Cyclic voltammograms with different parts marked in different colors for Pt(111) and Pt(100) are shown in Fig. 2.12 and Fig. 2.13. Sometimes peaks are merged with each other, like H UPD peak and OH_{ads} peak of Pt(100). Between the range of peaks are the flat low-potential area with only double layer charging and no reactions with solution, which are marked as brown in Fig. 2.12 and Fig. 2.13, like 0.4 to 0.6 V for Pt(111) and 0.7 to 0.9 V for anodic process of Pt(100).

Peaks of Pt(111) in $HClO_4$

The H UPD peak for Pt(111), shown as green in Fig. 2.12, is before 0.4 V [49–51]. The H UPD means underpotential deposited hydrogen, and they are adsorbed and

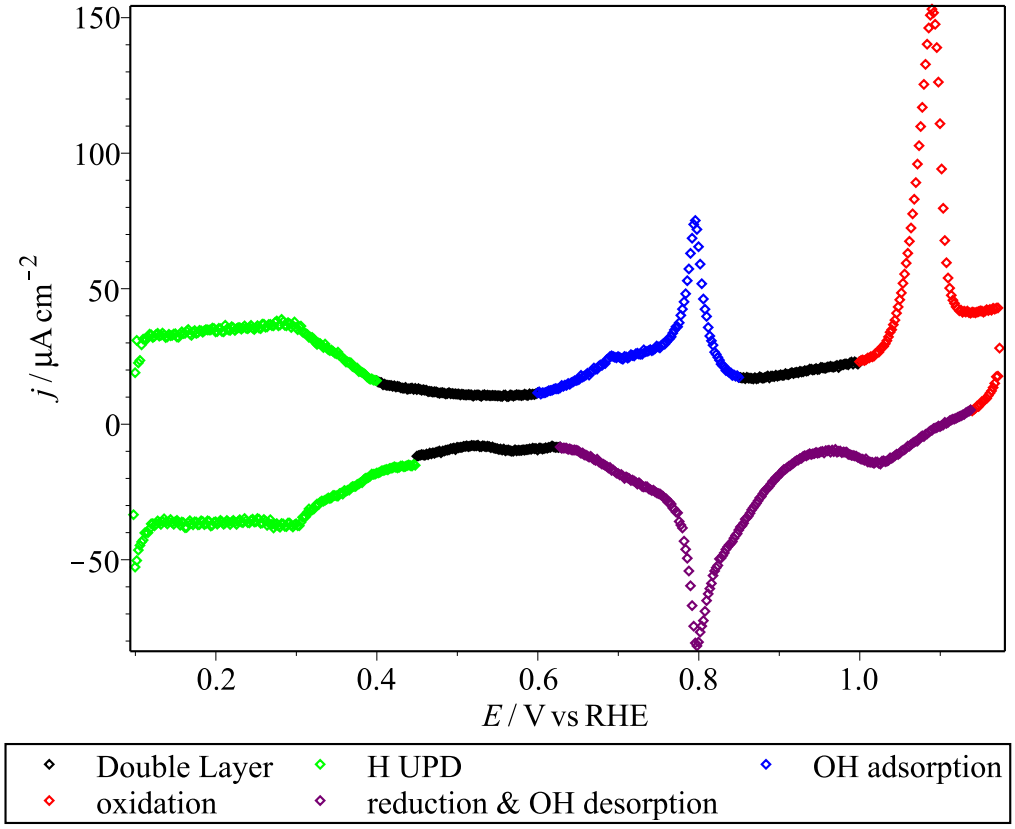

Figure 2.12: Pt(111) CV with different parts in different colors in 0.1 M $HClO_4$. Sweep rate as 50 mV/s. Data from the prep time at the CH5523 beamtime in September 2018.

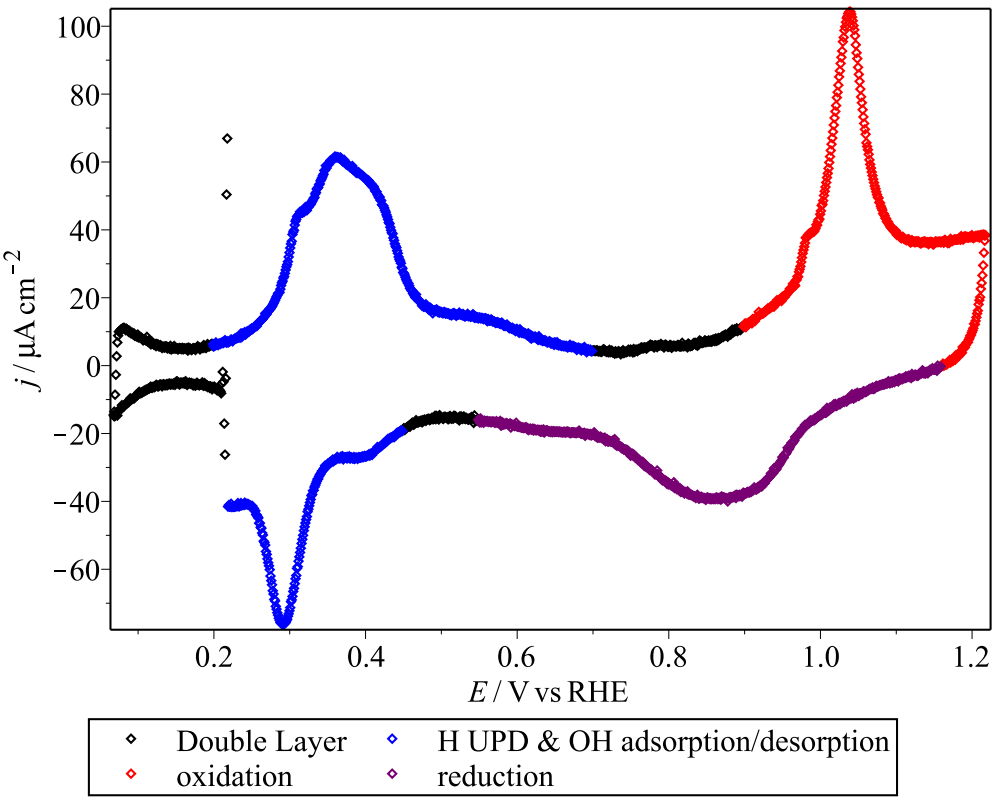

Figure 2.13: First cycle Pt(100) CV with different parts in different colors in 0.1 M $HClO_4$. Sweep rate as 50 mV/s. Data from the prep time at the CH5523 beamtime in September 2018.

dissociated as shown in Eq. (2.11), where $*$ means a free adsorption site on Pt surface [50, 52, 53], with coverage as 2/3 ML from experiments [52–55], for the strongly repulsion between H UPD adatoms, and shown as schematic in Fig. 2.11 with blue parallelogram frame as unit cell and explained in Section 2.2.2 [56]. Also, there are some density functional theory (DFT) studies but with coverage from models far away from 2/3 ML [55, 57]. The adsorption site is found as 3-fold hollow sites on the fcc(111) surface as thermodynamic result from chemisorbed sulphur poisoning which was used to block the sites [56, 58]. As X-ray research shows, the first two outermost Pt layers remain expanded with a little decrease after the H UPD adatoms are removed [49].

$$H_3O^+ + * + e^- \rightarrow H(ads) + H_2O \tag{2.11}$$

The OH_{ads} peak, shown as blue in Fig. 2.12, is from 0.6 to 0.85 V [59], with a broad part from 0.6 to 0.75 V and sharp peak centred at 0.8 V, which gives it the name as "butterfly peak". The cathodic OH_{ads} peak is mixed with oxide peak and shown as purple in Fig. 2.12. The OH_{ads} is produced from solvent water, and the reaction is shown in Eq. (2.12) in acidic $HClO_4$ solvent [59, 60]. The coverage, shown in Table (2.1), is around 110 μC cm^{-2}(0.46 ML) from experiments and 1/2 ML theoretically from research of Feliu and other groups [46, 52, 53, 61, 62]. For another voice, the coverage is 1/3 ML from DFT research without high electrode potential, ca. 1.30 V [50, 63–65], with 2/3 ML water covered on Pt(111) surface as X-ray research shows [66], connected with very strong OH-H_2O hydrogen bond and no more empty holes for additional OH_{ads} groups on Pt surface [64, 67].

$$H_2O + * \rightarrow OH(ads) + H^+ + e^- \tag{2.12}$$

OH_{ads}	water	total
1/2 ML	1/2 ML	1 ML [52, 53, 68]
1/2 ML	1/4 ML	3/4 ML [62]
1/3 ML	2/3 ML	1 ML [50, 64, 65]
1/3 ML	Existing	Unknown [63, 69]

Table 2.1: Water/OH_{ads} coverage for OH_{ads} peak of Pt(111) from different DFT studies

The Pt oxide peak, shown as red in Fig. 2.12, is also very sharp and centred at 1.05 V. O_{ads} is formed from OH_{ads} as the Eq. (2.13), with extra OH_{ads} formed from O_{ads} and water as Eq. (2.14) [50]. The water/OH_{ads}/O_{ads} layer is formed with potential over 1 V, which is more stable than the water/OH_{ads} layer for the OH_{ads} peak [53]. Coverage from DFT studies are shown in Table (2.2). Coverage of O_{ads} for Feliu's research is 0.5 ML, which is the coverage of whole oxide peak in the CV experiments, and place exchange isn't taken care of [52, 53]. Work from Fuchs et al supports 0.67 ML O_{ads} from the DFT research of further reactions for place exchange [70], also the running integral from Feliu's research have O_{ads} peaks with charges as 170 μC cm^{-2} (0.7 ML) under different sweep rate [52, 53]. Hawkins's research makes DFT studies on several coverages of O_{ads} on the sites of both surface and subsurface platinum, and favors the coverage $>$ 0.5 ML [71–73]. Gu's and Karp's research on energy of fcc Pt surface supports the coverage of adsorbed atomic oxygen is 0.25 ML [65, 74, 75]. There are no more than 1/2 ML OH_{ads} from butterfly peak to be converted to O_{ads} [49, 50, 52, 53, 63, 64, 69], and therefore for coverage of O_{ads} higher than 0.5 ML, with additional O_{ads} directed formed from water as Eq. (2.14). For the further introduction on platinum extraction, it will be introduced in Section 2.2.4.

$$\mathrm{OH(ads)} \rightarrow \mathrm{O(ads)} + \mathrm{H^+} + \mathrm{e^-} \tag{2.13}$$

$$H_2O(ads) \rightarrow O(ads) + 2H^+ + 2e^- \tag{2.14}$$

O_{ads}	OH_{ads}	water
0.5 ML	Existing	Existing [52, 53, 63]
0.67 ML	Slightly	Existing [70]
>0.5 ML (0.5625 ML)	Unknown	Existing [71–73]
0.25 ML	Unknown	Unknown [65, 74, 75]

Table 2.2: Water/OH_{ads}/O_{ads} coverage for oxide peak of Pt(111) from different DFT studies

Peaks of Pt(100) in $HClO_4$

The H UPD peak, shown as blue in Fig. 2.13, is mixed with the OH_{ads} peak from 0.2 to 0.7 V and is mainly the sharp part before 0.45 V [76]. In Fig. 2.13, the cycle starts at 0.22 V, drops to minimum 0.07 V, then rises up to 1.17 V, last drops back to 0.22 V. Pt(100) surface also adsorbs H as Eq. (2.11) but in 4-fold hollow sites [56]. Unlike Pt(111), the coverage of H UPD peak for Pt(100) is hard to get from DFT research because the significant charge from OH_{ads} especially after 0.4 V [77]. Some DFT research shows the coverage of UPD H can be up to 1 ML [78].

The OH_{ads} peak, shown as blue in Fig. 2.13, is the right half small broad part of mixed H/OH peak from 0.2 to 0.7 V, mainly after 0.4 V [77]. OH_{ads} also forms as in Eq. (2.12), but the coverage is also hard to get for the same reason as H UPD peak [77]. The bonding between OH_{ads} and following O_{ads} to step sites is much stronger than that in Pt(111) as ultrahigh vacuum experiment shows, and coverage might also be higher [50, 79]. Some DFT research shows the coverage is most possible at 1/3 ML OH_{ads} with 1/3 ML H_2O_{ads}, or 1/2 ML OH_{ads} with 1/2 ML H_2O_{ads} [80].

The Pt oxide peaks, shown as red and purple in Fig. 2.13, is also very sharp and centred around 1.05 V, similar to Pt(111).From some DFT studies, the coverage of O_{ads} is possible from 0.25 to 1 ML [81], or most stable at 0.5 ML [82, 83]. Similar to Pt(111), the O_{ads} is also formed as in Eq. (2.13), and platinum oxidation starts from 1.0 V, as the complete Pt oxide peak and later flat part, also discussed later in Section 2.2.4.

For the blue H/OH mixed peak in Fig. 2.13, the anodic peak is much larger than the cathodic peak, and the cathodic peak has a discontinuity 0.22 V. This is because the cycle starts and ends at 0.22 V, and a part of the cathodic peak isn't fully reacted and recorded in the next cycle. This also shows that second and subsequent cycles are different.

Peaks of Pt(111) in H_2SO_4

For Pt(111) reacted in H_2SO_4, there is still a pair of broad flat peaks from 0 to 0.3 V as H UPD peak [84], and forms H_{ads} groups same as Pt(111) in $HClO_4$ reacted as Eq. 2.11.

For the butterfly peak, it is lowered to 0.3 to 0.55 V [84], with peak centred around 0.5 V. Without the OH_{ads}/water system in $HClO_4$ [49], SO_4^{2-} (HSO_4^-) and water(H_3O^+) will take its place with reactions as in Eq.s (2.15, 2.16 and 2.17) [85].

$$HSO_4^- + * \rightarrow HSO_4(\text{ads}) + e^- \tag{2.15}$$

$$HSO_4^- + * \rightarrow SO_4(\text{ads}) + H^+ + e^- \tag{2.16}$$

$$HSO_4^- + H_2O + * \rightarrow H_3O - SO_4(ads) + e^- \quad (2.17)$$

The oxide peak shifts to 1.4 V as a very sharp peak, much higher than 1.05 V in $HClO_4$, with much wider range of flat part with only double layer current from 0.6 to 1.4 V, because the strongly-adsorbed sulfate inhibits the Pt oxidation [86]. In the peak, there is no O_{ads} formed, but Pt place exchange gives a PtO layer as in Eq. (2.18). The corresponding cathodic peak at 0.7 V is broader.

$$Pt + H_2O + * \rightarrow PtO + 2H^+ + 2e^- \quad (2.18)$$

2.2.4 Platinum Extraction

Platinum extraction is the process of Pt atoms moving during platinum oxidation. The O-containing absorbed species react with the Pt surface, and the Pt atoms leave their original lattice sites to become part of a developing oxide [87–89]. Some of these oxidized Pt atoms don't go back to their original sites during reduction, and so the Pt surface is restructured [23]. On Pt(111), O and Pt atoms can exchange their places during oxidation, this is called platinum place exchange [22, 27, 74, 90]. The place exchange on Pt(111) starts from higher than 1.1 V, in the second half of the Pt oxide peak and then in the flat part after it shown in Fig. 2.12. The different structures of extracted Pt(111) and Pt(100) from Fuchs et al [70, 91] are shown in Fig. 2.14. For Pt(111), atoms are oxidized independently as shown in Fig. 2.14.c. The extracted Pt(111) atom is 2.41 Å above the Pt surface from X-ray data [51], which agrees with >2.23 Å from DFT study [70].

However, for Pt(100), the O atoms aren't underneath oxidized Pt for other sur-

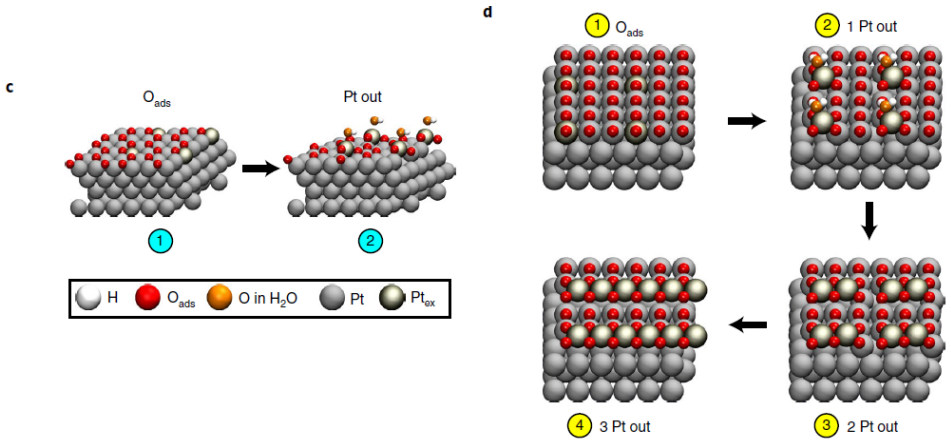

Figure 2.14: Pt oxidized models of **c.**Pt(111) and **d.**Pt(100). Reprinted by permission from Springer Nature: Nature Catalysis, Structure dependency of the atomic-scale mechanisms of platinum electro-oxidation and dissolution, Timo Fuchs et al, Copyright 2020 [70].

faces as shown in Fig. 2.14, so Pt(100) extraction can't be called place exchange [70, 91]. The extraction of Pt(100) starts from 1.0 V [92], and occurs throughout the complete Pt oxide peak and later in the flat part as shown in Fig. 2.13. The oxide peak of Pt(100) occurs at lower potentials than on Pt(111), mainly because of the difference in the crystal structure for surface Pt atoms between (100) and (111). Different from Pt(111), Pt(100) atoms are oxidized one by one. One oxidized Pt(100) atom makes it easier for the next Pt(100) to be oxidized as in Fig. 2.14.d, and this model leads to much higher coverage of extracted Pt for Pt(100). The extracted Pt(100) atoms are in a stripe structure 1.40 Å above the Pt surface atoms from X-ray data, which agrees with <1.42 Å from DFT study [70].

For Pt(111), the platinum oxide is said to be PtO in most research in $HClO_4$ solutions [70–72], formed by the reaction in Eq. (2.19) [23] with 1 e^- transferred for each extracted Pt atom, or 2 e^- transferred for each extracted Pt atom as in Eq. (2.18). However, for oxidation in H_2SO_4 solutions, the expected reaction has

2 e^-s transferred for each extracted Pt atom as in Eq. (2.18). However, there are some extra reactions to remove sulfate from the Pt surface before Eq. (2.18) that complicate the situation in this case. There are also some DFT studies based on experiments that show PtO_2 rather than PtO as the product of the platinum extraction when the coverage is under 0.5 ML [93, 94]. The coverage of extracted PtO from some DFT studies is around 0.2 to 0.25 ML at 1.17 V [95–97], but much lower for experimental analyse as 0.06 ML at 1.15 V [97].

$$Pt - OH(ads) \rightarrow PtO(ex) + H^+ + e^- \tag{2.19}$$

2.2.5 Platinum Dissolution

During the reduction of extracted Pt, most platinum oxides are turned back to Pt atoms at the same site or other places on Pt surface, however a part of Pt oxides are dissolved into the solution and can never be turned back to Pt atoms. This is called Pt dissolution. It happens together with normal Pt extraction, but it is only at the mML level (approximately ng cm^{-2}). This is just 1/100 of Pt extraction [98–101], however it still causes a significant mass loss over time, and is a main reason that lowers the lifetime of Pt catalysts in PEMFC after thousands of cycles of use [21]. For different Pt surfaces, as some DFT and experimental studies show, soluble Pt on Pt(100) surface is much lower than Pt(111) at high potential (1.15 V) [73, 102].

2.2.6 Oxide Film Growth Law

During the oxidation of the Pt surface, under a given potential and temperature, the Pt 2-D oxide film will grow logarithmically with time with the same original film

structure [25, 103–105], and the film growth is linearly related to the potential under given temperature [103, 104], and linearly related to the temperature under given potential [106, 107]. As shown in Fig. 2.15, the charge of Pt oxidation increases linearly related to the logarithm of time under a given potential, and the slopes of these lines linearly increases vs holding potential. In some early research of Conway and other groups with H_2SO_4 as electrolyte, the charge linearly increases to over 1000 μC cm^{-2} (more than 4 ML for both Pt(100) and Pt(111) surface) as log(time) increases [104], but in Jerkiewicz's research on Pt surface in aqueous CF_3SO_3H, the upper limit of oxide film is 2 ML when θ_O is 1 ML, and in Minguzzi's research on Pt surface in $HClO_4$ solvent with X-ray, the upper limit of θ_{ex} is 1 ML, and the charge is steady at 1 ML after θ_{ex} arrives 1 ML [108].

For some early research of Conway and other groups, the oxide film grows in logarithmic law because of the place exchange between oxide film and metal surface (or Pt extraction because place exchange is only for Pt(111) surface as described in Section 2.2.4), and the reaction rate is related to its inter-molecular bonding energy of Pt extraction. This model is called as place-exchange model [103, 104, 109]. When a surface Pt atom is extracted, it has 9 neighbouring atoms for Pt(111) (6 in the same plane and 3 in the plane underneath), and 8 neighbouring atoms for Pt(100) (4 in the same plane and 4 in the plane underneath), and these neighbouring atoms are just between oxide film and metal surface, so they are easy to be oxidized and become a part of the film afterwards, then after these 8 or 9 atoms are extracted, their neighbouring atoms are also easy to be oxidized [47, 103, 104].

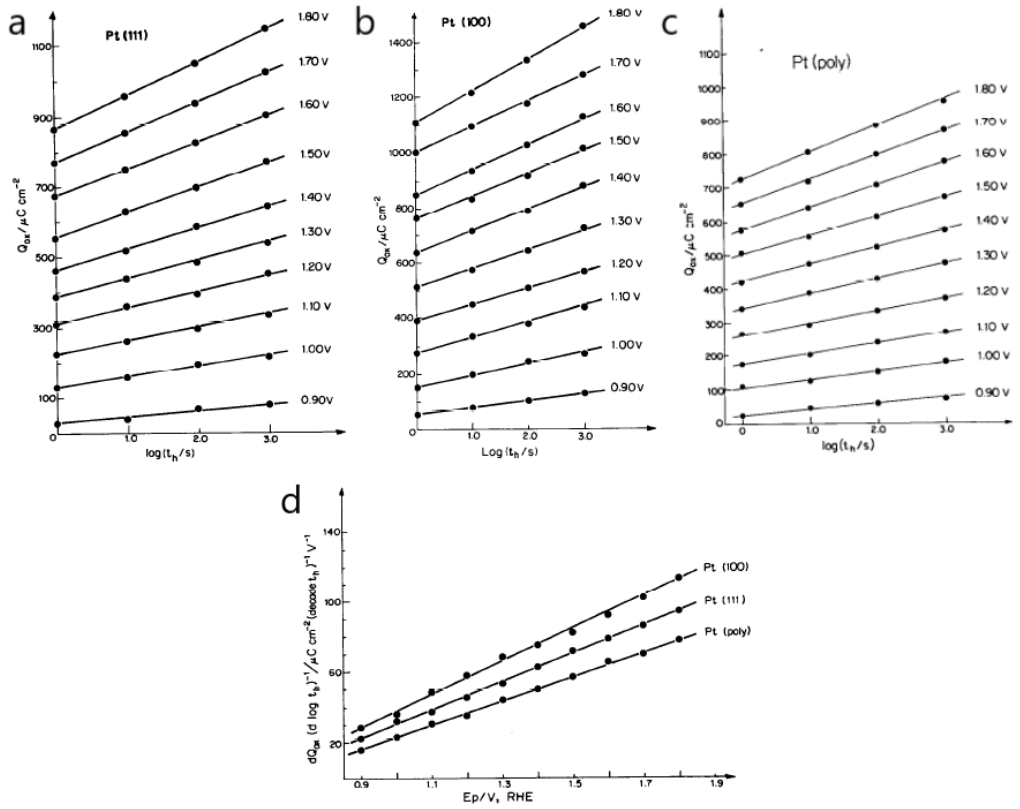

Figure 2.15: (a) Pt(111), (b) Pt(100), and (c) Pt(poly) oxide film direct logarithmic law growth plots in H_2SO_4, and relation of their slopes vs holding potential. Reprinted from Journal of Electroanalytical Chemistry, 339(1-2), Brian E. Conway, Gregory Jerkiewicz, Surface orientation dependence of oxide film growth at platinum single crystals, Pages 123-146, Copyright 1992, with permission from Elsevier [104].

2.3 Introduction to X-ray Diffraction

This section is to introduce the surface X-ray diffraction techniques, including the experimental techniques and processes, reciprocal space, Bragg reflections, and crystal truncation rods.

2.3.1 Surface X-ray Diffraction Experimental Processes

In this research, surface X-ray diffraction (SXRD) is used to study the oxide on the platinum surface, as its wavelength is comparable to lattice spacings [28, 110–112]. It's the most common technique in the form of X-ray crystallography, and can get very deep into crystal as very many unit cells to measure the bulk periodicity, but here it is limited in a small angle to only learn the few layers on the surface. It is a non-destructive technique to learn the surface structure and need very high energy particles. The SXRD operates simultaneously with the electrochemical techniques as shown in Fig. 2.16. At potentials where the Pt oxide and extraction of Pt occurs, the oxide is detected at the same time by illuminating the surface by X-ray beam at a small angle (μ) [113, 114], and detecting the scattering X-ray by a 2-D detector. Also, the electrochemical cell is mounted on a goniometer to move the Pt sample in six directions, so it can accurately align the X-ray beam to the crystal and detector.

The experiments in this research were done at the European Synchrotron Radiation Facility (ESRF) in Grenoble, France and at the Deutsches Elektronen-Synchrotron (DESY) in Hamburg, Germany. For the ID31 beamtime in ESRF, a typical X-ray beam energy is 70 keV, so the wave frequency (ν) is shown as below, with h as Planck constant:

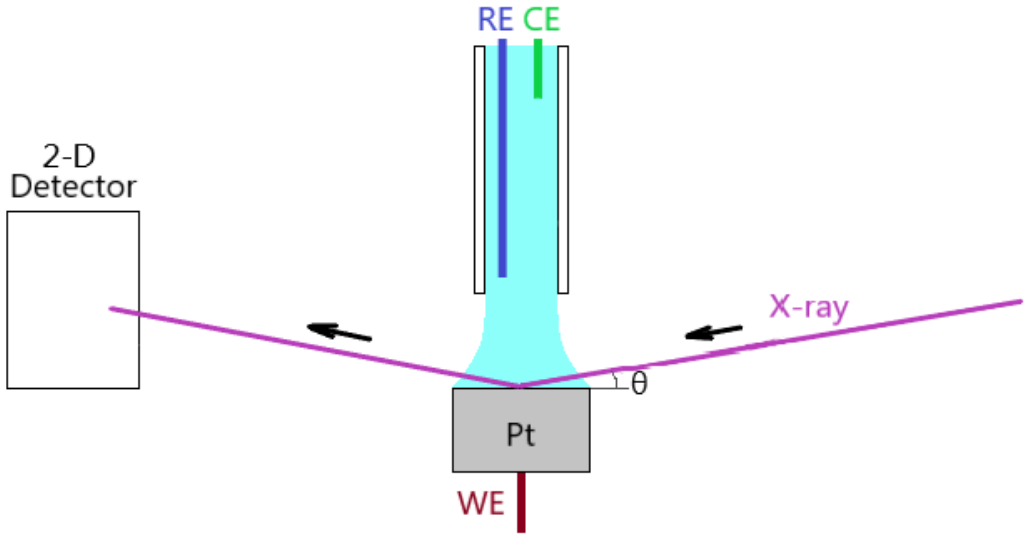

Figure 2.16: Schematic of the hanging meniscus cell with X-ray. The reference electrode (blue) and the counter electrode (green) are in a glass tube suspended above the Pt surface (grey) connected by the working electrode (red). The electrolyte goes down from the glass tube, just wets the Pt surface, to form an electrochemical cell. The Pt surface can rotate to find a good angle (θ) for the X-ray beam (purple) to pass through the cell with a small angle (μ) with the Pt surface, scatter on the Pt surface, and then be collected by the 2D detector.

$$\nu = \frac{E}{h} = \frac{70 \times 10^3 \text{ eV}}{4.135 \times 10^{-15} \text{ eV Hz}^{-1}} = 1.69 \times 10^{19} \text{ Hz} \tag{2.20}$$

And the wavelength (λ) of X-ray beam can be calculated from frequency and light speed (c) as:

$$\lambda = \frac{c}{\nu} = \frac{3.00 \times 10^8 \text{ m s}^{-1}}{1.69 \times 10^{19} \text{ Hz}} = 0.177 \text{ Å} \tag{2.21}$$

Also as de Broglie hypothesis, the momentum (p) of a photon of the X-ray beam is related to its wavelength (λ), and also linearly related to its energy (E) through two previous equations as:

$$p = \frac{h}{\lambda} = \frac{E}{c} = \frac{70 \times 10^3 \text{ eV}}{3.00 \times 10^8 \text{ m S}^{-1}} \frac{1.602 \times 10^{-19} \text{ J}}{1 \text{ eV}} = 3.74 \times 10^{-23} \text{ kg m s}^{-1} \tag{2.22}$$

The relation between energy (E) and momentum (p) can be performed in another way as below, with $\hbar = \frac{h}{2\pi}$ and $k = \frac{2\pi}{\lambda}$:

$$E = \frac{hc}{\lambda} = \frac{h}{2\pi} \frac{2\pi}{\lambda} c = \hbar k c = pc \tag{2.23}$$

The momentum $p = \hbar k$ here can be used to perform other things as electrons, and k here is linearly related to momentum (p), so also linearly related to energy (E).

2.3.2 Reciprocal Space

To determine the surface atomic arrangement of the crystal, the reciprocal space is used in the X-ray diffraction. It is a Fourier transform of the real space, which is introduced in the Section 2.2.1. The reciprocal axis vectors, $(\mathbf{a}^*, \mathbf{b}^*, \mathbf{c}^*)$, have relations with real space vectors, $(\mathbf{a}, \mathbf{b}, \mathbf{c})$, as: $\mathbf{a}^* \cdot \mathbf{a} = 2\pi$, $\mathbf{b}^* \cdot \mathbf{b} = 2\pi$, $\mathbf{c}^* \cdot \mathbf{c} = 2\pi$, $\mathbf{a}^* \cdot \mathbf{b} = \mathbf{a}^* \cdot \mathbf{c} = \mathbf{b}^* \cdot \mathbf{a} = \mathbf{b}^* \cdot \mathbf{c} = \mathbf{c}^* \cdot \mathbf{a} = \mathbf{c}^* \cdot \mathbf{b} = 0$. So as Fig. 2.17 shows, for a cubic unit cell the three vectors of reciprocal space are parallel to their corresponding vectors in the real space, with length as 2π over the reciprocal of their corresponding real vectors, and perpendicular to other two, like $\mathbf{a}^*$ is parallel to $\mathbf{a}$, and perpendicular to $\mathbf{b}$ and $\mathbf{c}$. The length of reciprocal vector $\mathbf{a}^*$ is $\frac{2\pi}{a}$; for the Pt crystal unit cell a is 3.9242 Å, so its $a^* = \frac{2\pi}{3.9242\ \text{Å}} = 1.6021\ \text{Å}^{-1}$. This relation also can be performed as $k = \frac{2\pi}{\lambda}$, in which k is the reciprocal vector and λ is the real vector, so the reciprocal vector length of 70 keV beam in ID31 of ESRF is $\frac{2\pi}{0.177\ \text{Å}} = 35.5\ \text{Å}^{-1}$. Also the relation between reciprocal axis vectors and real space vectors can be performed by matrix as:

$$\begin{bmatrix} (\mathbf{a}^*)^T \\ (\mathbf{b}^*)^T \\ (\mathbf{c}^*)^T \end{bmatrix} = 2\pi \begin{bmatrix} \mathbf{a} & \mathbf{b} & \mathbf{c} \end{bmatrix}^{-1}$$

The lattice point (h, k, l) in reciprocal space corresponds to the (hkl) plane in real space. The reciprocal lattice vector $\mathbf{G} = h\mathbf{a}^* + k\mathbf{b}^* + l\mathbf{c}^*$, e.g., for Pt(100) $G_{100} = 1 \cdot \mathbf{a}^* + 0 \cdot \mathbf{b}^* + 0 \cdot \mathbf{c}^*$, is normal to the (hkl) plane in real space, with length as $|G| = \frac{2\pi}{d}$, in which d is the spacing of the (hkl) plane.

Similar to the end of previous Section 2.3.1, the crystal planes also have an effective momentum (p), and it is linearly related to reciprocal lattice vector (G), with relation similar to Eq. 2.23 as $p = \hbar G$.

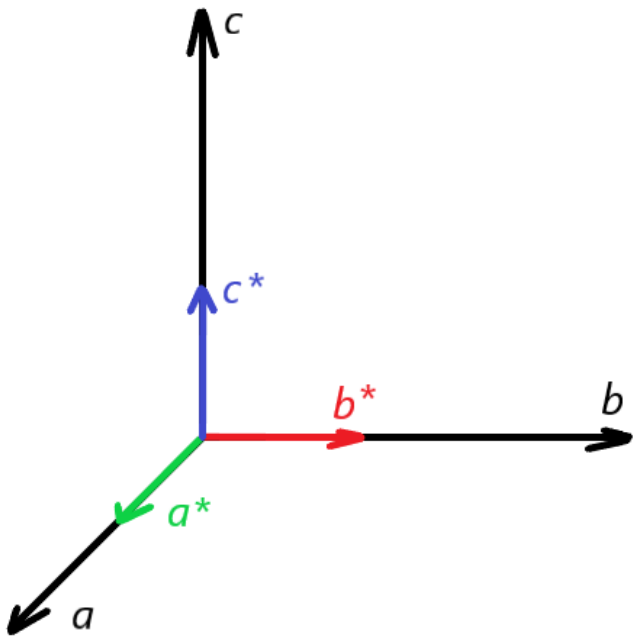

Figure 2.17: Schematic of the reciprocal space $(\mathbf{a}^*, \mathbf{b}^*, \mathbf{c}^*)$ and real space $(\mathbf{a}, \mathbf{b}, \mathbf{c})$ of cubic 3-D unit cell with all angles 90°.

For the reciprocal space of 2-D platinum surface, the reciprocal vectors can be transferred in the same way as previous 3-D unit cell for the rectangle unit cell of Pt(100) and Pt(110), as $\mathbf{a^*_{2D}} = \frac{2\pi}{\mathbf{a_{2D}}}$ and $\mathbf{b^*_{2D}} = \frac{2\pi}{\mathbf{b_{2D}}}$. However, for the Pt(111), its $\mathbf{a_{2D}}$ and $\mathbf{b_{2D}}$ has an angle of 120°, this is called the hexagonal unit cell, and can't be directly treated in the previous way. So as Fig. 2.18 shows, we can get Pt(111)'s reciprocal vectors through matrix if we put its real vectors in the rectangular coordinate system, as $\mathbf{a_{2D}} = \begin{bmatrix} a \\ 0 \end{bmatrix}$, and $\mathbf{b_{2D}} = \begin{bmatrix} -\frac{1}{2}a \\ \frac{\sqrt{3}}{2}a \end{bmatrix}$, then we can get the reciprocal vectors as below.

$$\begin{bmatrix} (\mathbf{a^*_{2D}})^T \\ (\mathbf{b^*_{2D}})^T \end{bmatrix} = 2\pi \begin{bmatrix} \mathbf{a_{2D}} & \mathbf{b_{2D}} \end{bmatrix}^{-1} = 2\pi \begin{bmatrix} a & -\frac{1}{2}a \\ 0 & \frac{\sqrt{3}}{2}a \end{bmatrix}^{-1} = \frac{2\pi}{a} \begin{bmatrix} 1 & \frac{\sqrt{3}}{3} \\ 0 & \frac{2\sqrt{3}}{3} \end{bmatrix}$$

So, reciprocal axis vectors are: $\mathbf{a^*_{2D}} = \frac{2\pi}{a} \begin{bmatrix} 1 \\ \frac{\sqrt{3}}{3} \end{bmatrix}$, $\mathbf{b^*_{2D}} = \frac{2\pi}{a} \begin{bmatrix} 0 \\ \frac{2\sqrt{3}}{3} \end{bmatrix}$

2.3.3 Bragg Reflection

As the X-ray beam can go through into the platinum crystal for very many monolayers to learn its structure, it can be explained by a schematic of reflection interference due to Bragg. In an ideal infinite crystal, if the energy and momentum are conserved, as left part of Fig. 2.19 shows, in which X-ray beam incidents on Pt crystal with angle μ. In left part of Fig. 2.19, two parallel rays inside X-ray beam reflect on two adjacent Pt (hkl) planes, and there are difference of light path length shown as two little red lines on both incident and reflected X-ray beam, with length as $d \sin \mu$ each. Also for interference this difference of light path length is an integral number of the wavelength, so $n\lambda = 2d \sin \mu$, in which n is an integer, and this is the Bragg's law.

Also, for the reciprocal space, as right part of Fig. 2.19 shows, the reciprocal

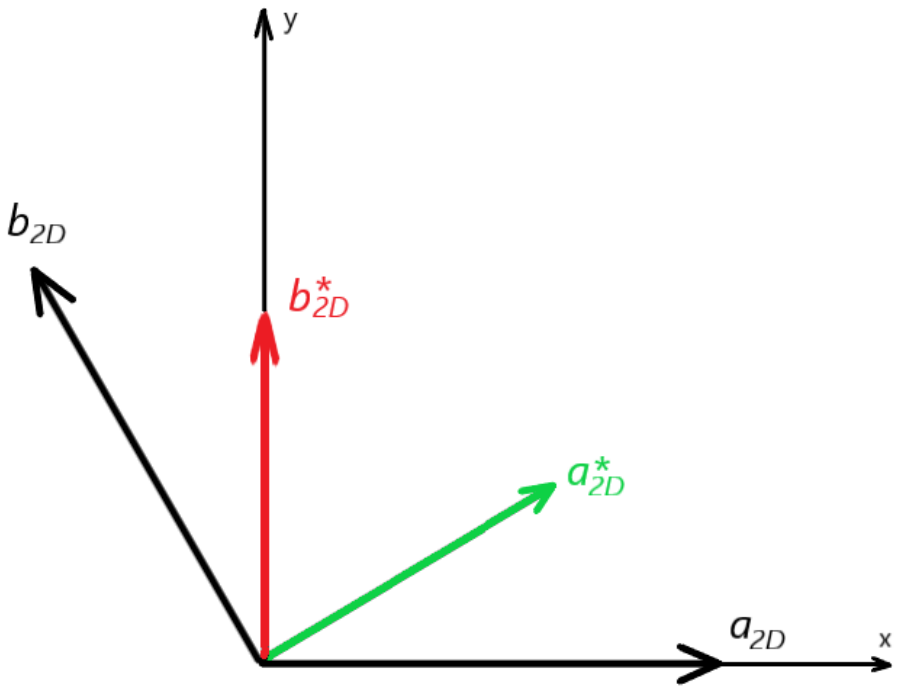

Figure 2.18: Schematic of the reciprocal space ($\mathbf{a^*_{2D}}, \mathbf{b^*_{2D}}$) and real space ($\mathbf{a_{2D}}, \mathbf{b_{2D}}$) of 2-D unit cell of Pt(111) surface.

vector of incident X-ray beam is $\mathbf{k_0}$, the reciprocal vector of the diffracted X-ray beam is $\mathbf{k}$, the momentum of crystal is $\mathbf{G}$, and $|k| = |k_0|$ for conservation of energy and $\mathbf{k} = \mathbf{k_0} + \mathbf{G}$ for the conservation of momentum. The angle of reflection μ can be performed as $\sin\mu = \frac{\frac{1}{2}|G|}{|k_0|}$, if we transfer $\mathbf{G}$ and $\mathbf{k_0}$ from reciprocal the space to the real space, then it is shown as below. This geometric construction is called Ewald's sphere, and we can get the same result as previous Bragg's law with $n = 1$.

$$\sin\mu = \frac{\frac{1}{2}|G|}{|k_0|} = \frac{\frac{1}{2}|\frac{2\pi}{d}|}{|\frac{2\pi}{\lambda}|} = \frac{\lambda}{2d} \tag{2.24}$$

For the platinum surface X-ray diffraction we did with 70 keV X-ray beam in ID31 beamtime at ESRF, the wavelength (λ) of X-ray beam is 0.177 Å from Section 2.3.1, and the spacings of the (hkl) planes (d) for Pt(100), Pt(110), Pt(111) are $|a|$, $\sqrt{2}|a|$, $\sqrt{3}|a|$, as Fig. 2.10 shows in Section 2.2.1, and Pt crystal unit cell side length $|a|$ is 3.9242 Å, then we can get the angles of reflection as below.

$$\theta_{\mathrm{Pt(100)}} = \arcsin\frac{\lambda}{2|a|} = \arcsin\frac{0.177\ \text{Å}}{2\times 3.9242\ \text{Å}} = 1.292^\circ \tag{2.25}$$

$$\theta_{\mathrm{Pt(110)}} = \arcsin\frac{\lambda}{2\sqrt{2}|a|} = \arcsin\frac{0.177\ \text{Å}}{2\times 3.9242\ \text{Å}} = 0.914^\circ \tag{2.26}$$

$$\theta_{\mathrm{Pt(111)}} = \arcsin\frac{\lambda}{2\sqrt{3}|a|} = \arcsin\frac{0.177\ \text{Å}}{2\times 3.9242\ \text{Å}} = 0.746^\circ \tag{2.27}$$

2.3.4 Crystal Truncation Rod

As previous sections described, the reciprocal space lattice points correspond to real space planes, and will have no intensity between them for the case of an ideal infinite crystal. But the real experiments, diffractions are taken place on the mix of 2-D

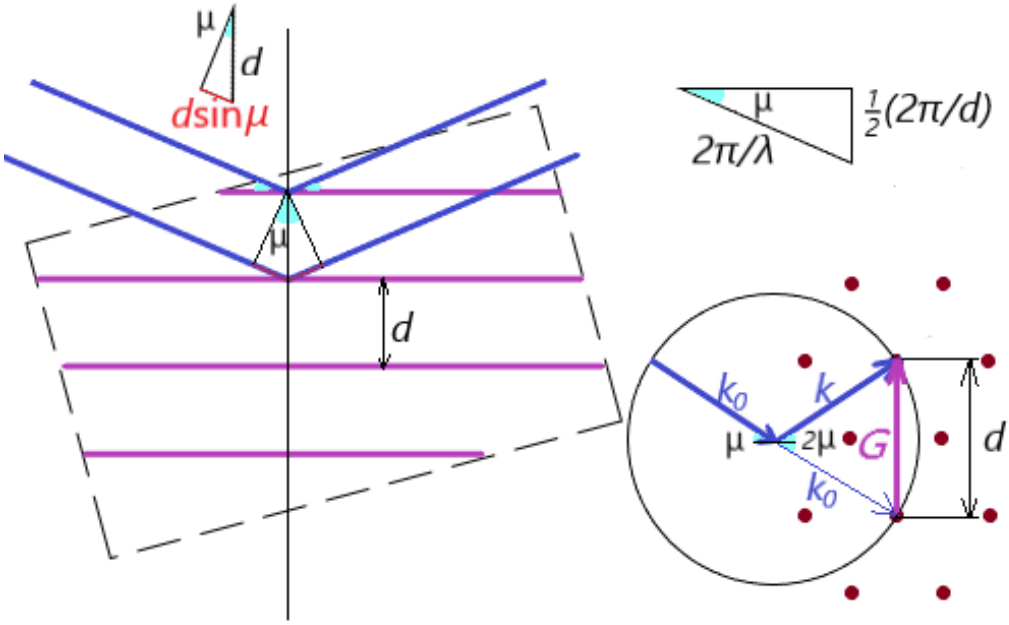

Figure 2.19: Schematic of the Bragg reflection (left) and Ewald's sphere (right). The red points are Pt atoms, the purple lines are different (hkl) planes with spacing d and crystal momentum $\mathbf{G}$, the blue lines are X-ray beam with frequency as λ and Bragg angle as μ (light blue triangle), and the red lines are the path length difference of X-ray beams reflected on two adjacent (hkl) planes. $\mathbf{k_0}$ is the reciprocal vector of incident X-ray beam, and $\mathbf{k}$ is the reciprocal vector of the diffracted X-ray beam.

surface and 3-D crystal with limited size, so there will be lines of sharply changing intensity between Bragg peaks, and this is called the crystal truncation rod (CTR) [27, 28, 112, 115]. The changes on the intensity of X-ray beam along the CTRs is sensitive to the surface structure of the crystal. In the experiments, only the intersections of CTRs and Ewald's sphere as right part of Fig. 2.19 can be detected, so the crystal sample must be rotated to make the Ewald's sphere intersect different points.

The intensity (I) of the detected X-ray beam can be converted to the structure factor (F). For $I \propto |F|^2$, we get the magnitude of the structure factor as $|F| = \sqrt{\frac{I}{I_0}}$, in which I is the intensity of different data points, and I_0 is the intensity at 0.9 V. In the anodic process for both Pt(111) and Pt(100), at 0.9 V, the Pt atoms are at their bulk locations, and it is the flat part between the OH_{ads} peak and Pt oxide peak in CVs as Fig. 2.12 and Fig. 2.13 show. Fig. 2.20 from Fuchs et al [70] is an example of CTRs under different potentials converted to the structure factor for the structure of extracted Pt atoms, with some fits to an atomic model. The intensity is very large when (h, k, l) in the left bottom corner of Fig. 2.20 are all odd as l = 1, 3, 5, 7 for $(11l)$ on left side, or all even as l = 0, 2, 4, 6 for $(20l)$ on the right side. These are the Bragg reflections. When (h, k, l) are not all odd or even, there is intensity in Fig. 2.20, because the crystal isn't infinite but has a cut surface, and the Pt surface structure can be learned from these signals. We can build a Pt surface model and predict these intensity changes, which is the grey fitted curves in Fig. 2.20. These fitted curves can check whether the experimental data fit the model of Pt surface. Once the correct structure is found, a simplified function relating the F to coverage of extracted platinum atoms (θ_{ex}) at a particular point in reciprocal space can be found. For example the linear functions, Eq. 2.28 for Pt(111) at (1, 1, 1.5) is used in

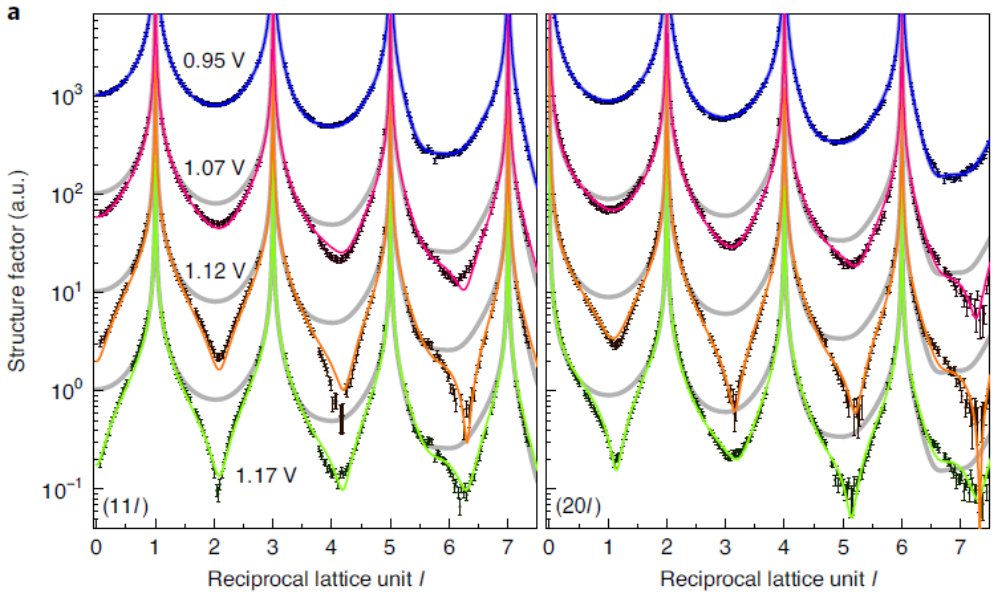

Figure 2.20: Pt(100) CTR spectra example under different potentials with model fits, with data points as black points, the best fits as colorful curves, and the CTR fits as grey curves. The intensity is very high when (h, k, l) are all odd as $(11l)$ on the left side, or all even as $(20L)$ on the right side. Between these Bragg peaks, the intensity is sensitive to the surface structure. Reprinted by permission from Springer Nature: Nature Catalysis, Structure dependency of the atomic-scale mechanisms of platinum electro-oxidation and dissolution, Timo Fuchs et al, Copyright 2020 [70].

the Section 3.1.2 and Eq. 2.29 for Pt(100) at (1, 1, 2.1) is used in the Section 3.2.2.

$$\theta_{ex} = 0.198 - 0.201|F| \tag{2.28}$$

$$\theta_{ex} = 0.5007(1 - |F|) \tag{2.29}$$

Also there is another type of experiments to follow the intensity with time for kinetic experiments, like the X-ray voltammetry or potential step. The X-ray diffrac-

tion is carried out at the same time as cyclic voltammetry or potential steps. An X-ray voltammogram is shown in Fig. 2.21. The coverage of extracted platinum atoms (θ_{ex}) from intensity can be from Eq. 2.28 for Pt(111) or Eq. 2.29 for Pt(100), and then compared with the coverage of transferred electrons (θ_e) from cyclic voltammetry or potential steps to get the electrons transferred per extracted platinum.

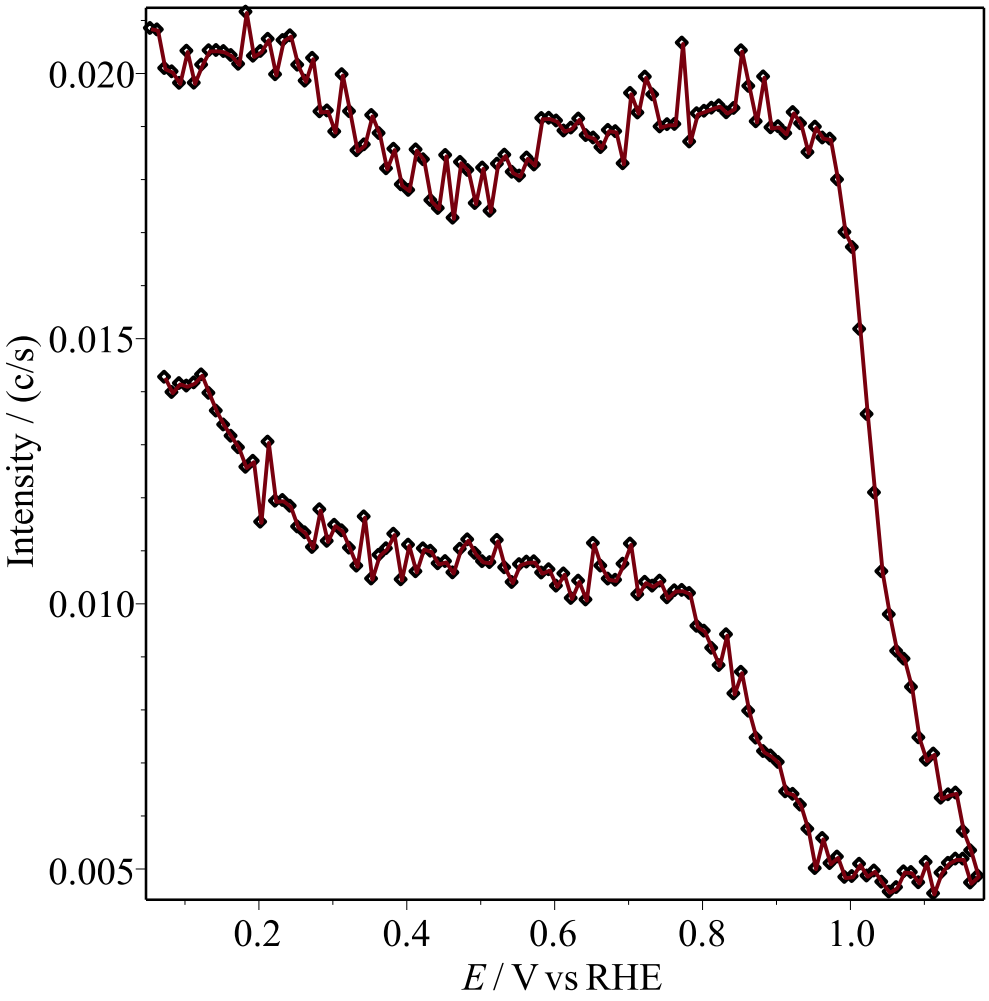

Figure 2.21: Pt(100) X-ray voltammogram example. Sweep rate as 20 mV/s. Source Data from run 664 at the IHCH925 beamtime in February 2015.

Chapter 3

Results and Discussion

In this chapter, the results of this research is discussed, as the integrations of CVs, and the compare of it with X-ray data for Pt(111) and Pt(100), also the results from the potential step experiments.

3.1 Pt(111) Cyclic Voltammetry and X-ray

In this section, the data treatment of Pt(111) cyclic voltammetry and X-ray is discussed, as the integrations of CVs, the θ_e vs θ_{ex} plot from CVs and X-ray, and its performance after fast scans.

3.1.1 Pt(111) Integrations of Cyclic Voltammetry

In this subsection, Pt(111) cyclic voltammogram is baseline corrected and integrated to get the coverage of electrons, θ_e, of different peaks introduced by section 2.2.3.

Voltammogram from CH5523 prep

The voltammogram in Fig. 3.1 is from the prep time at the CH5523 beamtime in September 2018.

There are three anodic peaks for the oxidation process, the H UPD peak before 0.4 V, the butterfly peak from 0.6 to 0.85 V, and oxide peak after 1.0 V centred at 1.09 V, also the "roll back" part from 1.175 V to 1.15 V with potential decreasing but current still positive, so oxide is still being formed. In these peaks, the H UPD peak is a broad peak with flat part from 0.11 to 0.3 V, but it has a little positive slope for the peroxide reduction from X-ray beam damage. The butterfly peak is a combination of a short broad peak with lower potential and a high sharp peak with higher potential. The oxide peak is a tall sharp peak.

There are also two flat parts between peaks with potential from 0.4 to 0.6 V and 0.85 to 1.0 V. As the literature from Feliu's group [52, 53] shows, the CV curve here should be flat with very low constant double-layer charging component. In this CV figure, the valley from 0.4 to 0.6 V is very flat, but another one from 0.85 to 1.0 V has a positive slope for the platinum surface samples.

There are only two group of peaks for the reduction process. The cathodic H UPD peak is similar to its corresponding anodic one, and has potential range before 0.45 V, the start point. But the cathodic butterfly and oxide peaks are mixed together and it's difficult to calculate their charge densities separately.

Baseline Correction of Voltammogram

As section 2.1.4 said, there are double layer currents in the electrochemical experiments like CVs, and it always appears as a constant current under any potentials.

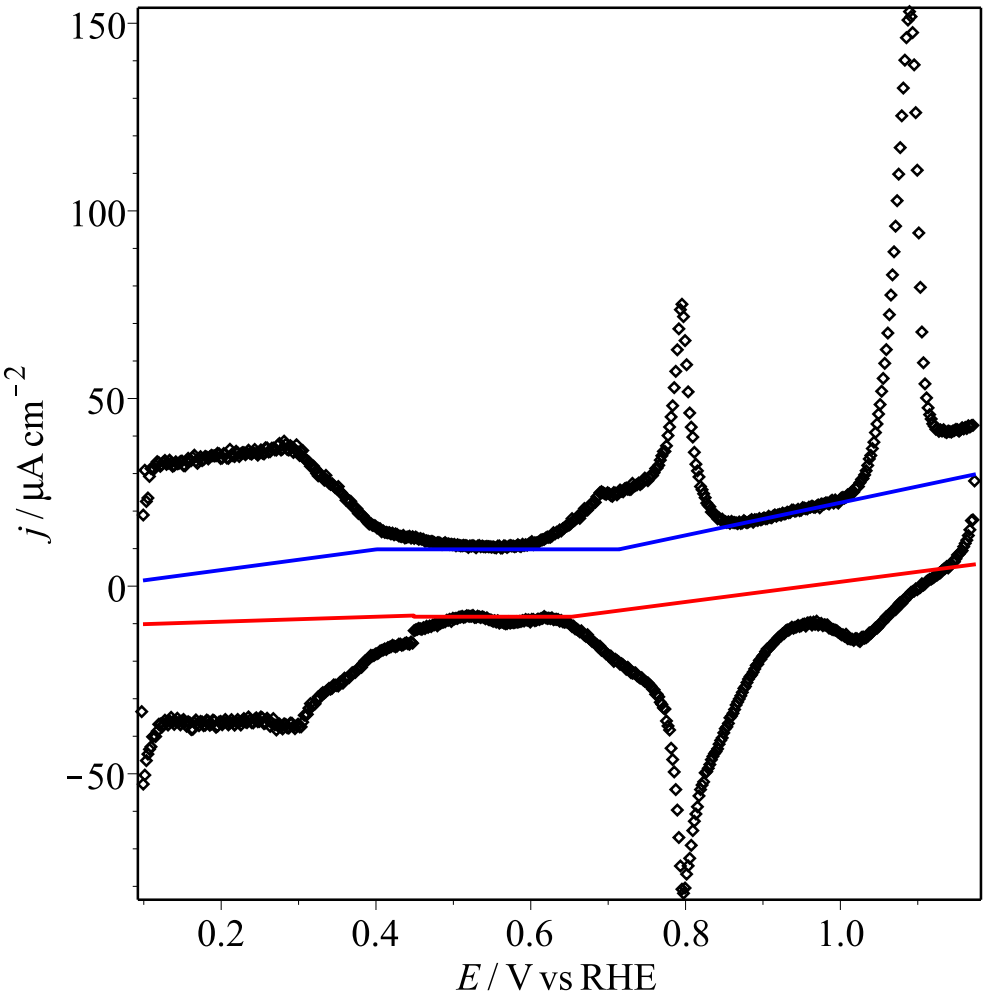

Figure 3.1: Pt(111) cyclic voltammogram in 0.1 M $HClO_4$. Sweep rate as 50 mV/s. Data from the prep time at the CH5523 beamtime in September 2018.

Also, CV goes down on left side and goes up on right side as Fig. 3.1 shows, so we need baseline to correct these two parts from integration of peaks.

To get the baselines, for the anodic parts, first to make sure the flat part from 0.4 to 0.6 V, which were both flat in this figure and the literature, close to zero current by making a horizontal line pass its lowest point. Then for another linear part from 0.85 to 1.0 V, line is fitted by least squares regression for the whole part, to make sure the curve of this part also horizontal with current close to zero after corrected, and these two baselines will meet somewhere inside the butterfly peak close to 0.6 V. Next for the H UPD part, though it should have broad peak with a horizontal top as the compared literature is shown as Fig. 3.2, it also has a small positive slope in this figure, which makes its anodic raw charge density (0.77 ML) a little lower than cathodic one (0.92 ML), so a baseline with the same slope as top part from 0.11 to 0.3 V is used for the H UPD anodic peak, and this baseline will pass the endpoint of the baseline for first flat part's at 0.4 V.

For the baselines of cathodic parts, they are treated in the same three ways as the anodic ones but with different ranges, for the anodic and cathodic peak separation from the irreversibility of the reaction. For the horizontal part, the baseline is formed in the same way. The horizontal baseline passes the highest point of this part, but with potential range from 0.45 V to 0.63 V, from the end potential of this CV scan to the left endpoint of mixed cathodic peaks. For the baseline of the mixed peaks, it has similar slope as the anodic baseline, and passes the 0.63 V left endpoint and 1.15 V right endpoint. For the H UPD part, the baseline also has slope same as the 0.11 to 0.3 V top of the peak and touches the 0.45 V left endpoint of horizontal baseline.

The CV diagram corrected by baselines shows as the Fig. 3.2. The literature CV figure is from Gómez-Marín's research in Feliu's group [52, 53]. The corrected

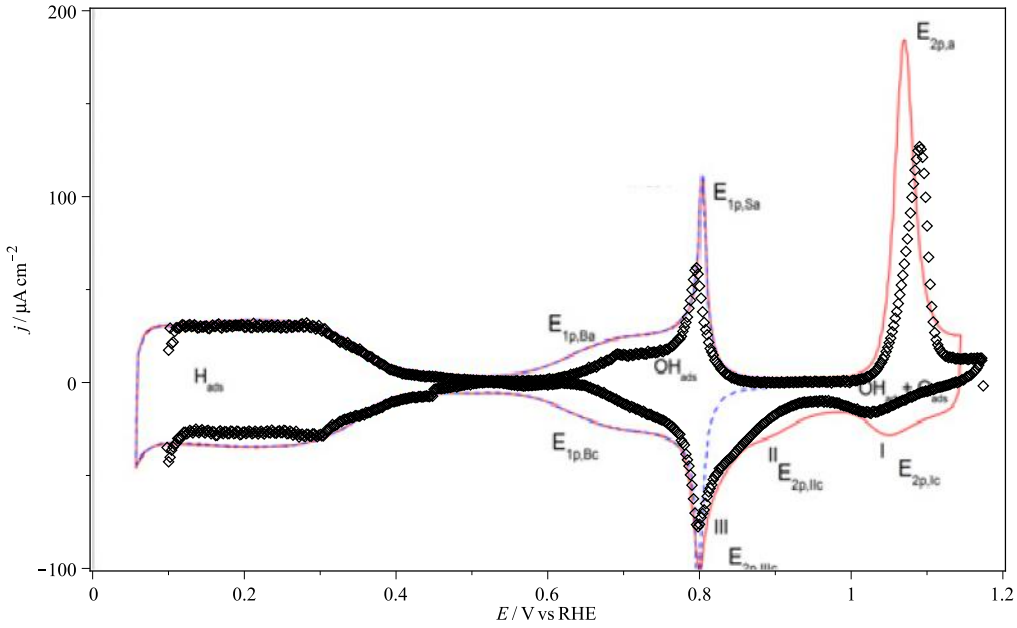

Figure 3.2: Baseline corrected Pt(111) cyclic voltammogram in 0.1 M $HClO_4$ compared with literature, H UPD peaks are similar, OH_{ads} peak is lower than literature (0.31 ML vs 0.5 ML), and Oxide peak is also lower (0.46 ML vs 0.5 ML). Sweep rate as 50 mV/s. Data from the preparation for the CH5523 beam time in September 2018. Literature reprinted from Journal of Electroanalytical Chemistry, 688, Ana M. Gómez-Marín, Jean Clavilier, Juan M. Feliu, Sequential Pt(111) oxide formation in perchloric acid: An electrochemical study of surface species inter-conversion, Pages 360-370, Copyright 2013, with permission from Elsevier [53].

CV diagram is very similar to the literature, also the anodic part near the maximum potential has a slope close to zero and not that close to x-axis.

Anodic and cathodic charges

This run of CV scan begins and ends at about 0.45 V in the cathodic processes, and like the Fig. 3.1 shows, this voltammogram closes, so this means in this case the Pt oxide production is reversible, and it is expected that anodic and cathodic charges

are equal.

The area and coverage of different peaks of this Pt(111) cyclic voltammogram are compared with data from other beamtimes in Table. 3.1.

Beamtime	CH5523		IHCH925		CH5918		CH5700	
EC File name	prep time		run 664		Pt111_10		run 25	
Sweep rate / mV/s	50		20		20		20	
Corrected?	No	Yes	No	Yes	No	Yes	No	Yes
Range / V	0.099—1.175		0.099—1.175		0.084—1.184		0.054—1.181	
Total Anodic / ML	2.62	1.44	2.79	1.35	1.97	1.55	2.14	1.39
Total Cathodic / ML	1.94	1.47	2.57	1.36	1.89	1.48	2.16	1.50
H UPD / V	0.099—0.4		0.099—0.4		0.084—0.4		0.054—0.34	
H UPD / ML	0.77	0.63	0.71	0.53	0.58	0.64	0.42	0.50
OH_{ads} / V	0.6—0.85		0.6—0.87		0.6—0.85		0.57—0.84	
OH_{ads} / ML	0.55	0.31	0.62	0.33	0.40	0.30	0.49	0.45
Oxide / V	1.0—1.175		1.0—1.175		1.0—1.184		0.93—1.181	
Oxide / ML	0.84	0.46	0.98	0.46	0.82	0.75	1.07	0.42
Roll-back / V	1.15—1.175		1.16—1.175		1.15—1.184		1.17—1.181	
Roll-back / ML	0.03	0.01	0.03	0.003	0.00	0.008	0.02	0.005
H_{ads} / V	0.099—0.45		0.099—0.45		0.084—0.4		0.054—0.42	
H_{ads} / ML	0.92	0.66	1.10	0.55	0.82	0.70	1.09	0.63
Reduce & OH_{des} / V	0.6—0.85		0.6—0.87		0.6—0.85		0.57—0.84	
Reduce & OH_{des} / ML	0.87	0.79	1.47	0.81	1.07	0.78	1.07	0.87

Table 3.1: Coverages of peaks from Pt(111) cyclic voltammograms in 0.1 M $HClO_4$

Comparison with literature values:

The expected H UPD charge density from literature[52–54] is 2/3 ML. The baseline-corrected data is 0.63 ML, very close to it.

The expected OH_{ads} peak is 1/3 ML in the literature [50, 63, 64], and other literature gives 1/2 ML [52, 53], which is also shown in Fig. 3.2. The baseline-corrected coverage is 0.31 ML, very close to 1/3 ML but much lower than 1/2 ML.

The expected oxide peak from literature[52, 53] is 0.5 ML as Fig. 3.2 shows. The baseline-corrected coverage is 0.46 ML, a little lower than 1/2 ML.

Relevant references are from Feliu's group [52, 53].

3.1.2 Pt(111) θ_e vs θ_{ex} Plot

In this subsection, Pt(111) cyclic voltammogram is baseline corrected then integrated as in section 3.1.1, and then it is compared with the corresponding X-ray data to get e^-s transferred per place-exchanged Pt surface atoms.

Cyclic Voltammetry Data Treatment

The X-ray voltammogram in Fig. 3.3 is from the run 664 at the IHCH925 beamtime in February 2015; the same data as Figure 1b in ref. [70].

The voltammogram in Fig. 3.4 is baseline corrected in the same way as section 3.1.1, and θ_e is found by dividing the charge density of Pt(111) of a specific part on baseline treated CV diagram in Fig. 3.5 by the theoretical charge density of Pt(111) surface, 240.3 μC cm^{-2}. The coverages of all peaks are shown in Table. 3.1, very close to the results in Section 3.1.1.

X-ray Data Treatment

The X-ray voltammogram in Fig. 3.6 is from the same experiment as Fig. 3.3. The curve goes down very slowly from lowest potential to 1.03 V with some noise, due to the surface relaxation as the UPD H is removed. But it sharply goes down from 1.03 V until the highest potential, 1.16 V. Also for the cathodic processes, the curve

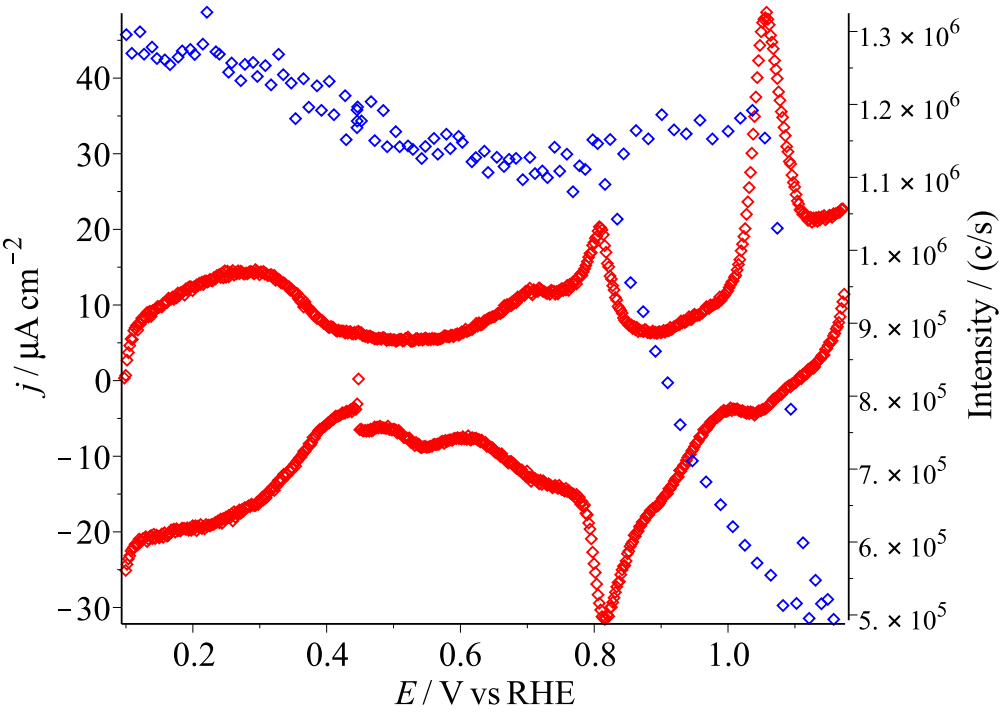

Figure 3.3: Pt(111) X-ray voltammogram. Sweep rate 20 mV/s. Data from run 664 at the IHCH925 beamtime in February 2015.

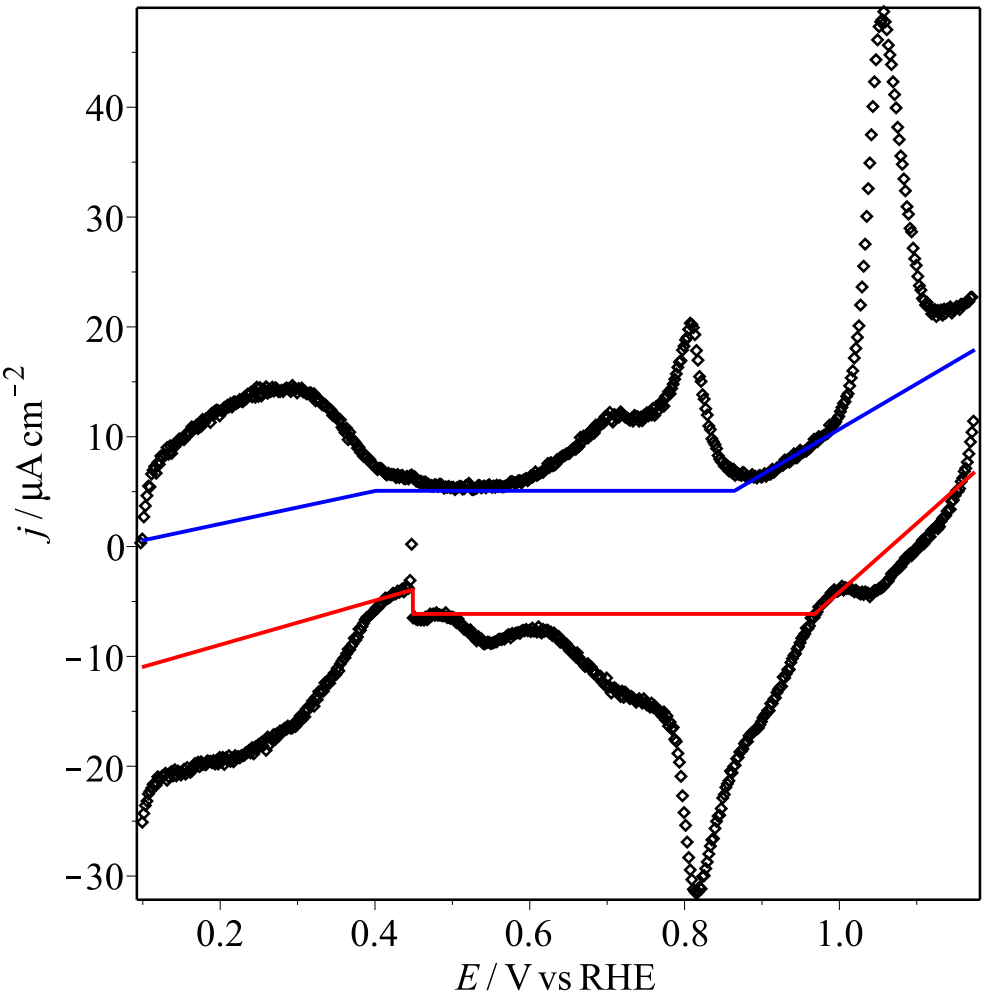

Figure 3.4: Pt(111) cyclic voltammogram. Sweep rate as 20 mV/s. Data from run 664 at the IHCH925 beamtime in February 2015.

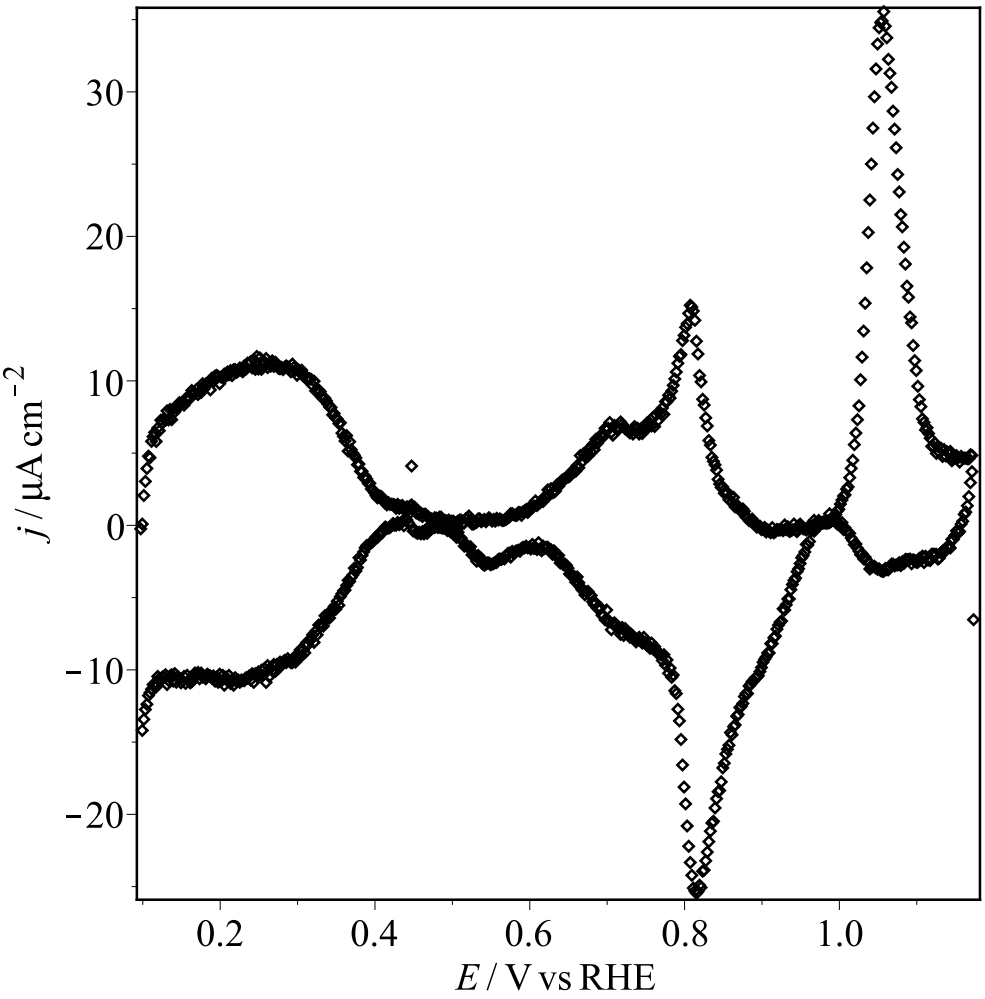

Figure 3.5: Baseline corrected Pt(111) cyclic voltammogram. Sweep rate as 20 mV/s. Data from run 664 at the IHCH925 beamtime in February 2015.

goes up sharply after briefly staying flat unit 1.1 V. It then has similar intensity to the anodic process from 0.8 V to lowest potential.

To turn the X-ray data into θ_{ex}, it is normalized by the data of point at 0.9 V in the anodic process, because 0.9 V is in the flat part of cyclic voltammogram between the anodic butterfly peak and oxide peak with current density as zero after the baseline correction in Fig. 3.5. The normalization equation is $\theta_{ex} = 0.198 - 0.201 \times \sqrt{\frac{I}{I_{0.9V}}}$ from section 2.3.4, and the normalized diagram shows as in the Fig. 3.7.

Coverages θ_e and θ_{ex} from CV and X-ray

This section describes the analysis of θ_e vs θ_{ex} for the oxidation of Pt(111) from cyclic voltammetry and X-ray data.

The θ_e vs θ_{ex} diagram of the anodic process is shown in Fig. 3.8. The 8 points on the diagram are from the sharp part in Fig. 3.6 from 1.03 to 1.16 V.

Although the CV and X-ray are measured at the same time, they are measured on different instruments with different data acquisition times. Therefore, the potentials of their data points don't match each other point by point, and the points in cyclic voltammetry spectrum, Fig. 3.4 are much more dense than that in the X-ray, Fig. 3.6. So to solve this problem, we use the potentials from the X-ray data to match θ_e. If the potential from X-ray data doesn't have a matching point in the cyclic voltammetry data, the θ_e vs potential point we used is found from a straight line between two neighbouring points in the cyclic voltammetry data.

The θ_e vs θ_{ex} data were then analysed by fitting least squares lines. In Fig. 3.8, the blue line is from the least squares fitting of the 3rd point to the end, compared with green and red lines with one more or less point. The slope of the blue line is

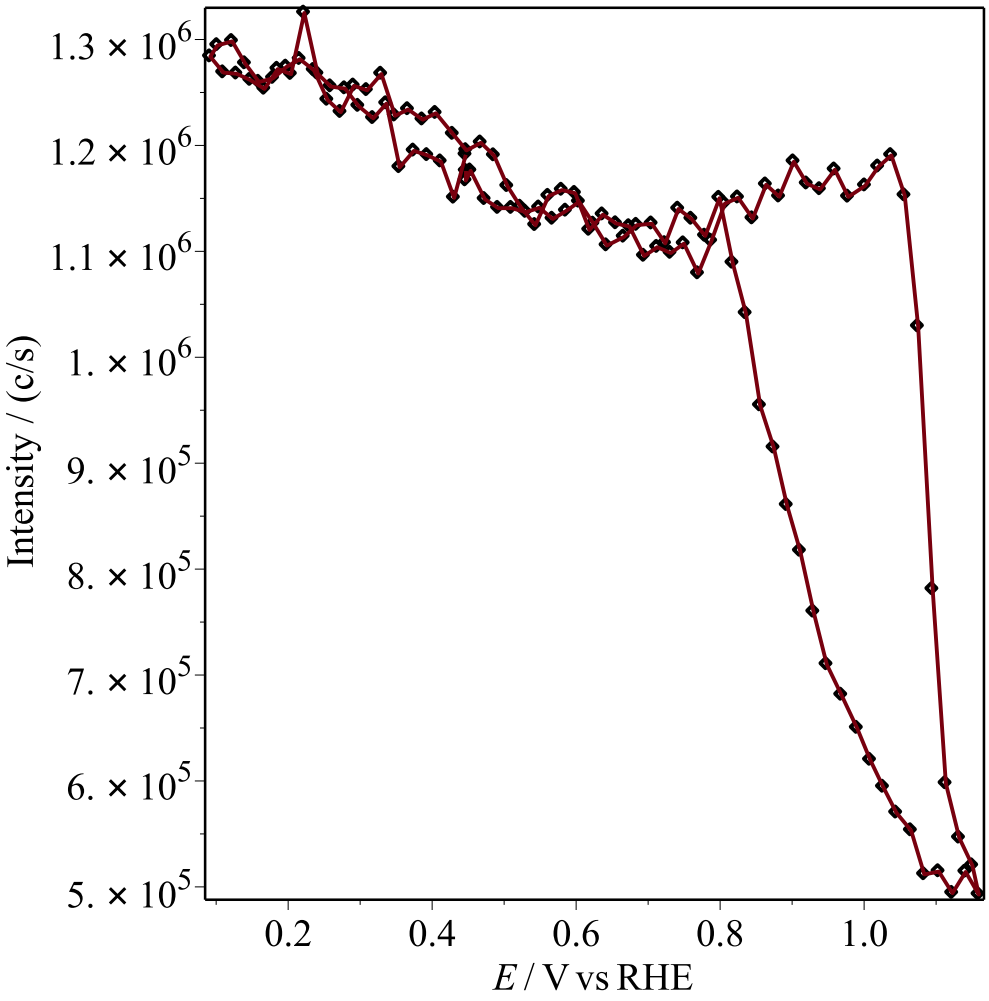

Figure 3.6: (1 1 1.5) Pt(111) X-ray intensity. Sweep rate as 20 mV/s. Data from run 664 at the IHCH925 beamtime in February 2015.

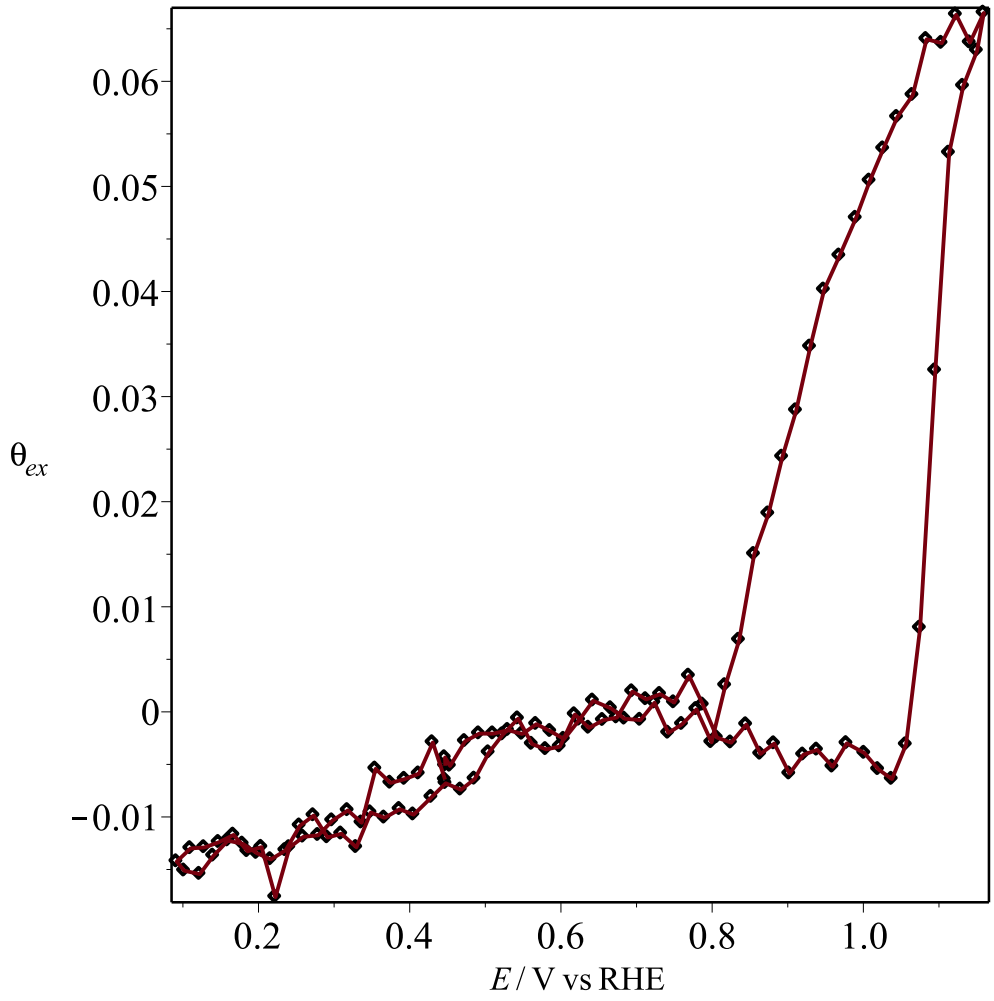

Figure 3.7: Normalized (1 1 1.5) Pt(111) X-ray intensity. Sweep rate as 20 mV/s. Data from run 664 at the IHCH925 beamtime in February 2015.

2.70, and the standard error is 0.16. If one more point is included (green line), the slope is 3.57 and the standard error increases to 0.44. If there is one less point, and the fit starts from the 4th point (red line), the slope is 2.46 with standard error as 0.31, also much larger than 0.16. Therefore, the region from the 3rd point on is taken as the appropriate linear section of the data.

A similar analysis of θ_e vs θ_{ex} for the reduction process of Pt(111) from cyclic voltammetry and X-ray data was carried out, and shown in Fig. 3.9. There are 16 points inside the the sharp cathodic part from 1.1 to 0.8 V in Fig. 3.6. The same interpolation and fitting process was carried out as for the anodic data.

The fitted line for θ_e vs θ_{ex} is shown as the blue line in Fig. 3.9, and was obtained from the lowest squares fit of the last 10 points, the slope of the line is 2.17 with standard error as 0.24. This line has the least standard error compared with other two lines, the green line with last 11 points with slope as 2.68 and error as 0.32, the red line with last 9 points with slope as 1.82 and error as 0.24.

Also anodic θ_e vs θ_{ex} without baseline correction is analysed and shown in Fig. 3.10, the θ_es are much larger than baseline corrected ones, and the curve of θ_e vs θ_{ex} is different from Fig. 3.8, it rises up sharply first, then becomes flat, and lastly increases sharply, and the slope of medium flat part is 5.16. The largest θ_e is 0.77 ML, so the overall slope from the first point to the last point is 11.6. Also, the corresponding cathodic θ_e vs θ_{ex} plot without baseline correction is shown in Fig. 3.11, and the slope is 6.49, a little larger than the anodic slope.

Discussion on Extraction of Pt(111)

In brief, the spectra of θ_e vs θ_{ex} for oxidation and reduction processes of Pt(111) from previous sections are shown in Fig. 3.8 and 3.9. The slopes show the number of

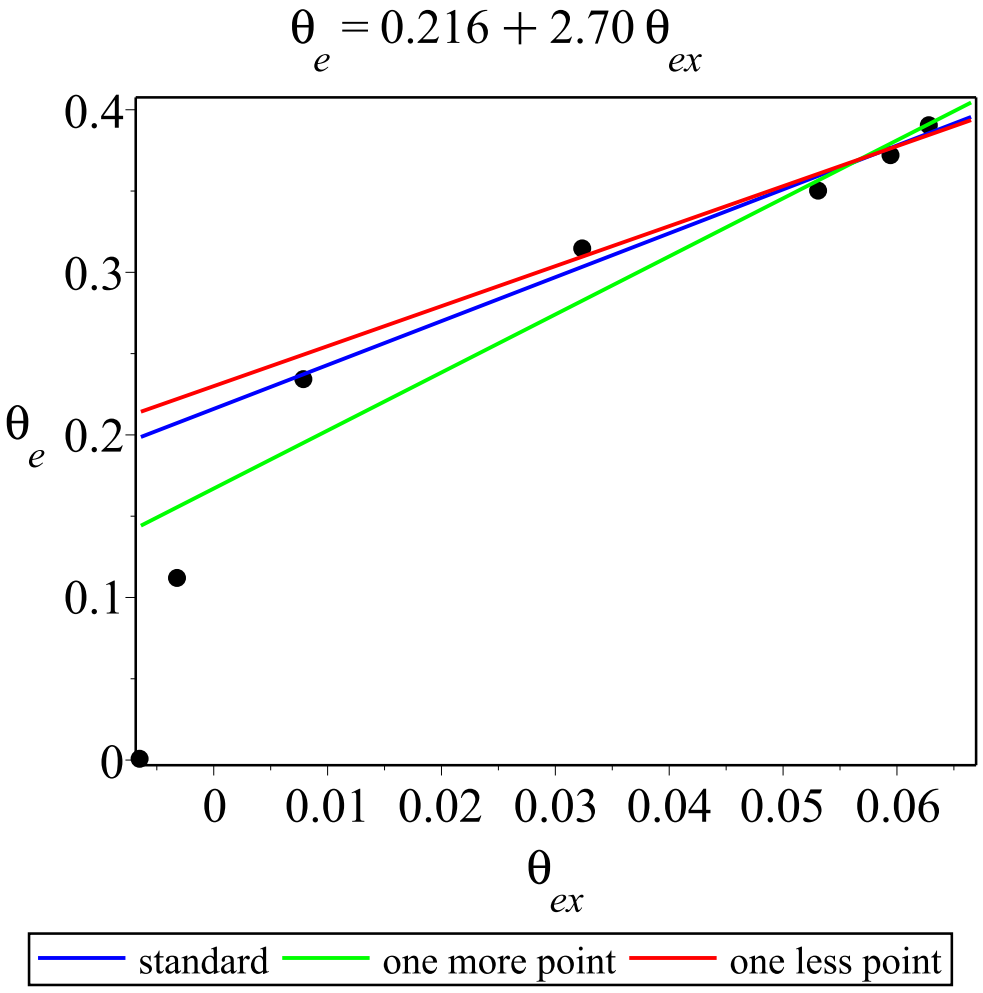

Figure 3.8: Anodic θ_e vs θ_{ex} for Pt(111) with segmented baseline correction. Data from run 664 at the IHCH925 beamtime in February 2015.

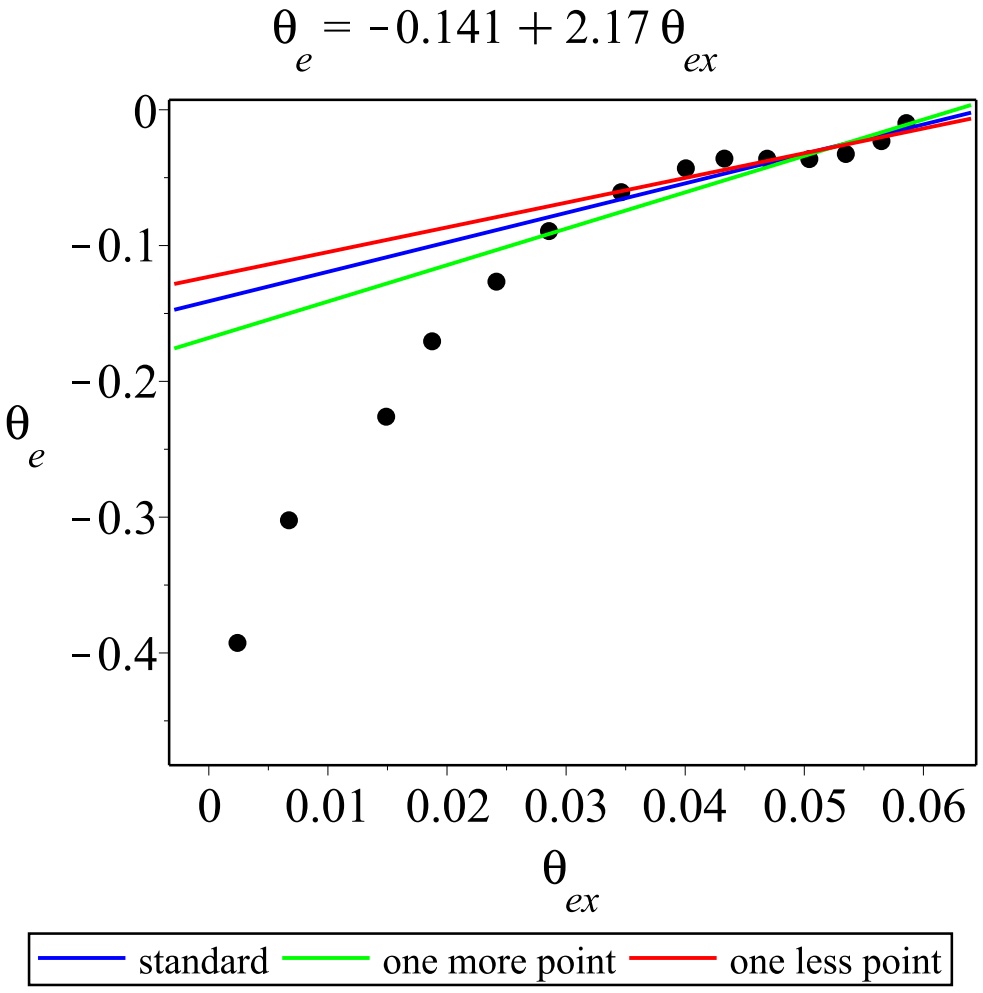

Figure 3.9: Cathodic θ_e vs θ_{ex} for Pt(111) with segmented baseline correction. Data from run 664 at the IHCH925 beamtime in February 2015.

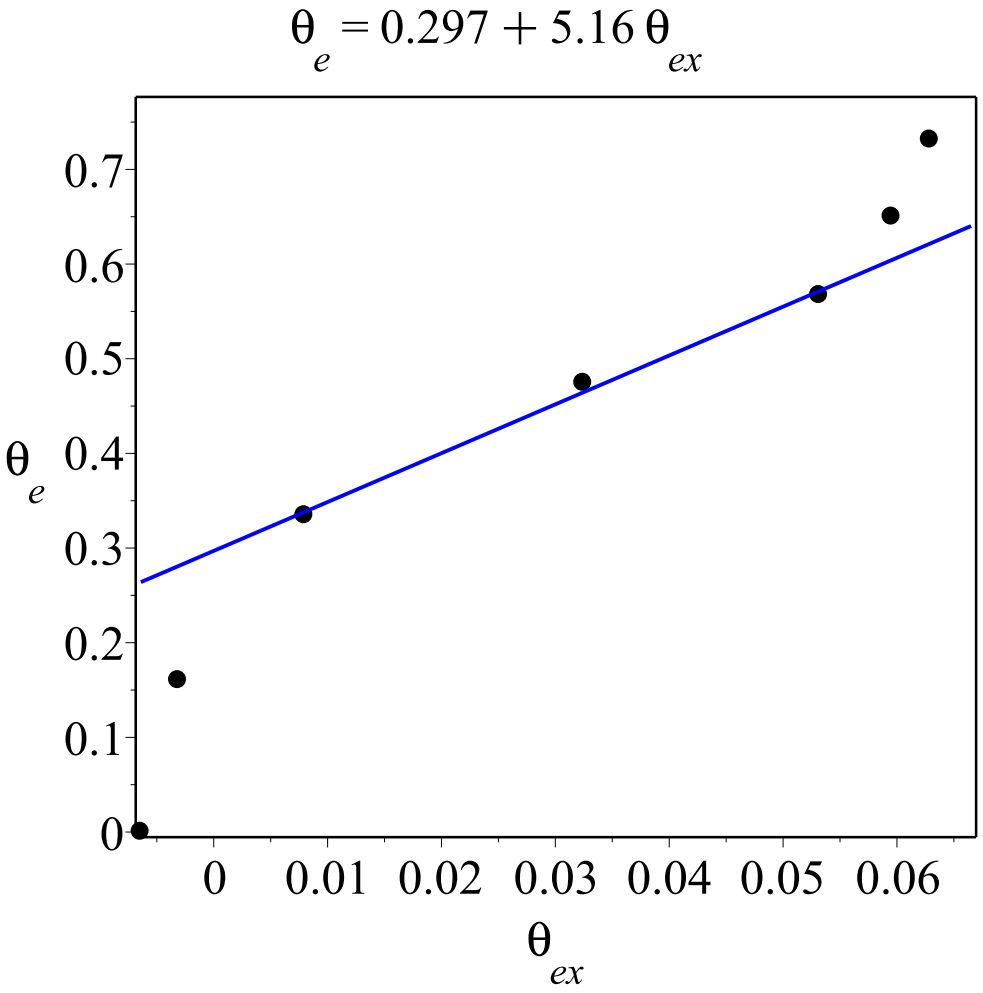

Figure 3.10: Anodic θ_e vs θ_{ex} for Pt(111) without baseline correction. Data from run 664 at the IHCH925 beamtime in February 2015.

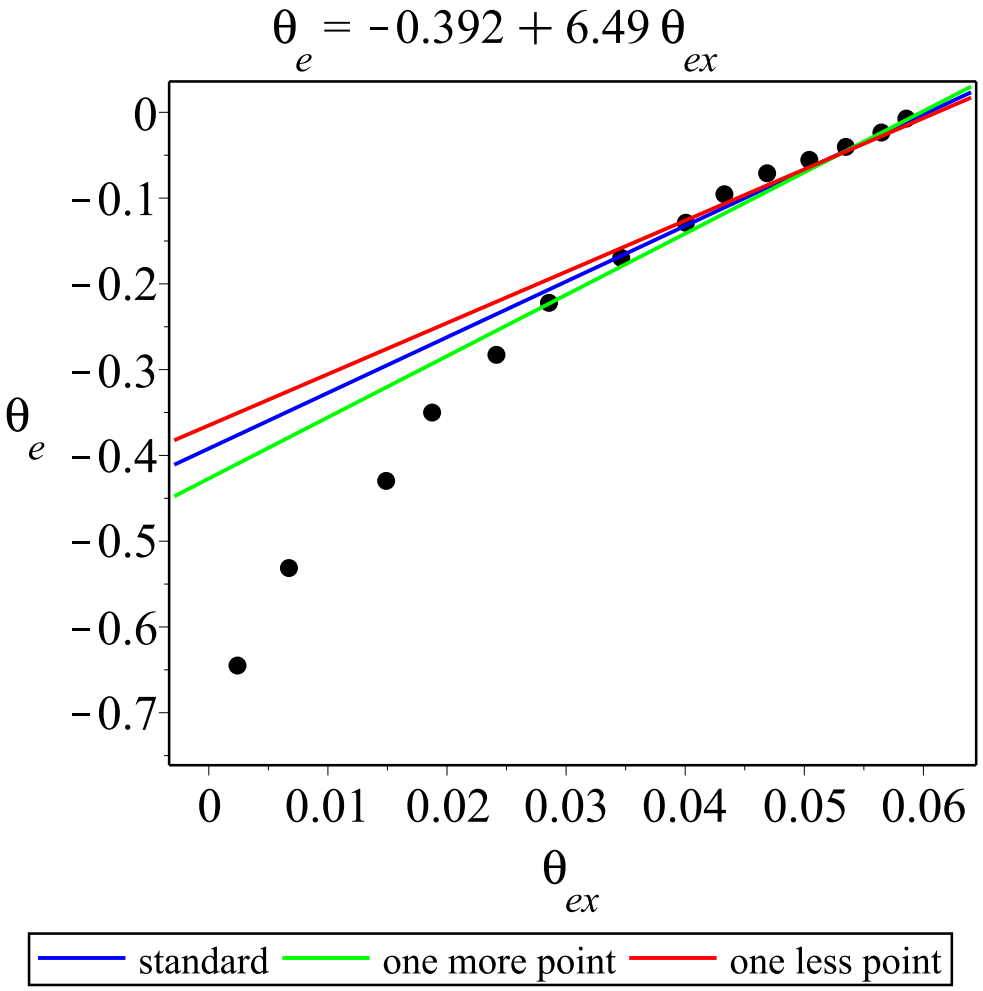

Figure 3.11: Cathodic θ_e vs θ_{ex} for Pt(111) without baseline correction. Data from run 664 at the IHCH925 beamtime in February 2015.

electrons transferred per Pt by θ_e for coverage of electrons from cyclic voltammetry and θ_{ex} for coverage of extracted Pt atoms from x-ray. Here baseline-corrected θ_e at 1.17 V is 0.46 ML and θ_{ex} at 1.17 V is 0.066 ML, close to 0.07 ML at 1.1 V and much lower than 0.18 ML at 1.2 V from Koper's place-exchange model without mass-conservation, but very close to 0.06 ML at 1.15 V from Koper's experimental data of the sweep hold experiment to 1.35 V [97]. The θ_e vs θ_{ex} curve for Pt(111) oxidation rises up sharply from 0 to 0.02 ML θ_{ex}, than linearly increases more gently from 0.02 to 0.066 ML with slope 2.70, which means 2.70 e^-s are transferred per extracted platinum. Its shape is very different from the straight line in Koper's research, with slope as 4 e^-s per extracted platinum before 1.15 V [97]. Also our overall $\frac{\theta_e}{\theta_{ex}}$ is 6.9, much higher than 4 from reference [97].

From the slope of the θ_e vs θ_{ex} curve, 2.70 e^-s are transferred per extracted platinum. It's much higher than 2 e^-s of oxidation from Pt(0) to Pt(II). This is because the O_{ads} groups keep forming as the Pt extraction happens. When θ_e increases from 0 to 0.2 ML in Fig. 3.8, there is no Pt extraction but O_{ads} formation as Eq. 3.1, and the reaction process works as Step 2 to Step 3 in Fig. 3.12. When θ_e increases from 0.2 to 0.4 ML, there is a part of O_{ads} formation, and mainly Pt extraction as Eq. 3.2, in which extracted PtO is the most possible product for place-exchanged Pt with O underneath from references [70–72]. Here θ_e is totally 0.46 ML from CV, so 0.5 ML OH_{ads} from butterfly peak is enough for O_{ads} formation and Pt extraction through Eq. 3.1 and 3.2, and Pt is extracted from OH_{ads} groups like left side of Step 3 to Step 4 in Fig. 3.12. Here there is 0.46 ML θ_e and 0.066 ML θ_{ex}, so possible reactions of the oxide peak are, for each 14 surface Pt atoms:

$$6 \times (\mathrm{OH(ads)} \rightarrow \mathrm{O(ads)} + \mathrm{H^+} + \mathrm{e^-}) \tag{3.1}$$

$$1 \times (\mathrm{Pt} + (\mathrm{OH(ads)} \rightarrow \mathrm{PtO(ex)} + \mathrm{H^+} + \mathrm{e^-}) \tag{3.2}$$

If the reaction continues, and there were not enough OH_{ads} for reaction, Pt surface atoms are directly extracted by water as Eq. 3.3, and the reaction process happens as the right side of Step 3 to Step 4 in Fig. 3.12.

$$\mathrm{Pt} + \mathrm{H_2O} \rightarrow \mathrm{PtO(ex)} + 2\mathrm{H^+} + 2\mathrm{e^-} \tag{3.3}$$

There is also another possibility for extracted PtO_2 from Eq. 3.5 as product of place exchange, for some research and experiments show that PtO_2 is also a possible product of Pt extraction when the coverage is less than 0.5 ML [93]. If the CV isn't corrected by baseline, and the product is PtO_2 [97], θ_{ex} is 0.066 ML, close to $\frac{1}{15}$ ML, θ_e is 0.77 ML, close to $\frac{23}{30}$ ML, so the reaction happens as below, for each 14 surface Pt atoms:

$$7 \times (\mathrm{OH(ads)} \rightarrow \mathrm{O(ads)} + \mathrm{H^+} + \mathrm{e^-}) \tag{3.4}$$

$$1 \times (\mathrm{Pt} + 2\mathrm{H_2O} \rightarrow \mathrm{PtO_2(ex)} + 4\mathrm{H^+} + 4\mathrm{e^-}) \tag{3.5}$$

4 e^- per Pt_{ex} is close to Jacobse's model [97], and just a little lower than 5.16, slope of θ_e vs θ_{ex} with uncorrected CV in Fig. 3.10.

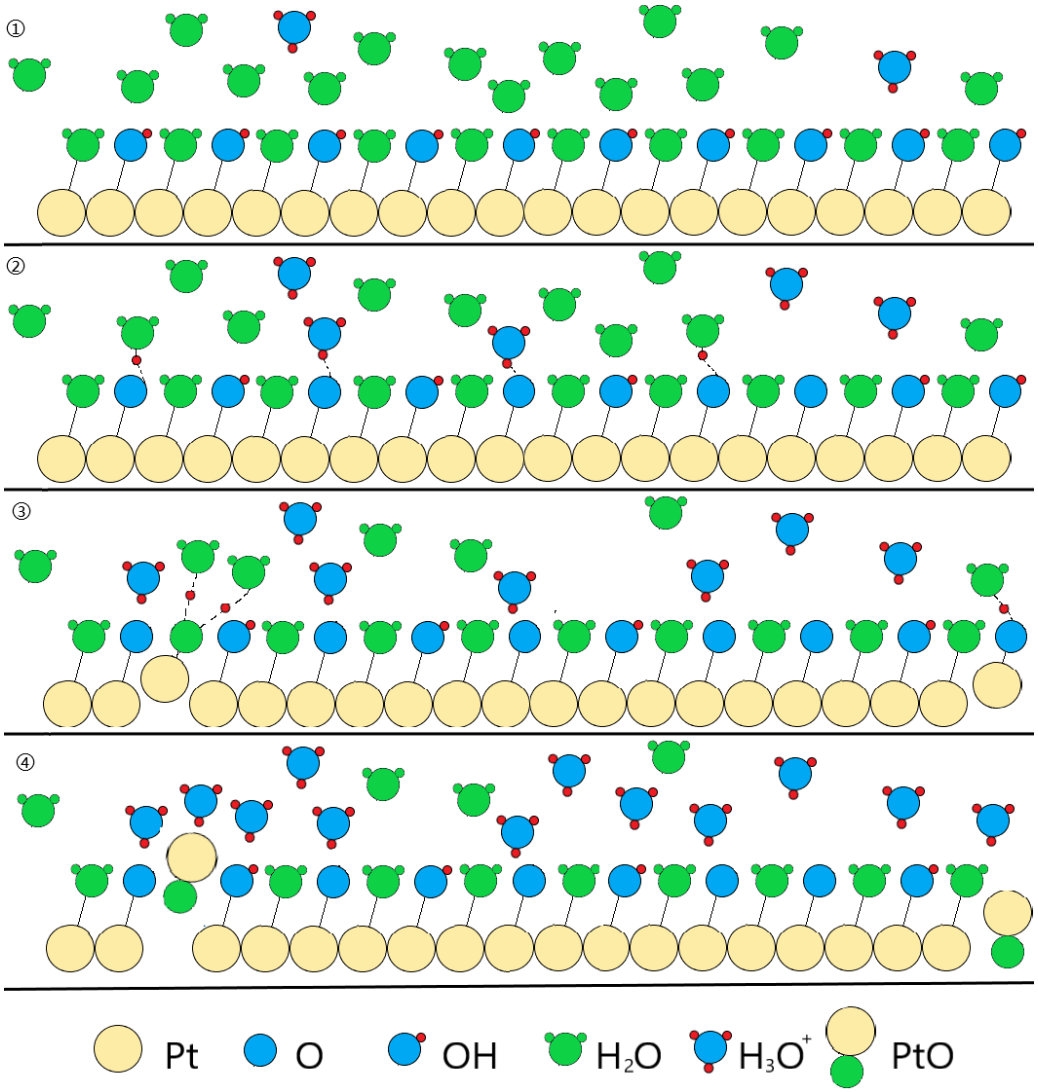

Figure 3.12: Reaction processes for the formation of O_{ads} and place exchange on Pt(111) surface. 1. Pt surface with 1/2 ML OH_{ads} and 1/2 ML water before the oxide peak. 2. OH_{ads} are turned to O_{ads}. 3.OH_{ads} and H_2O are Pt extracted to PtO. 4. Place extraction has happened and PtO has formed.

3.1.3 Pt(111) θ_e vs θ_{ex} under Different Sweep Rates

In this subsection, Pt(111) cyclic voltammetry data are baseline corrected then integrated to charges, then compared with X-ray data to get e^-s transferred per place-exchanged Pt surface atom, as described in Section 3.1.2.

Data from EC file Pt111_09 of CH5918

Cyclic voltammetry data is from EC file Pt111_09 and corresponding X-ray file Pt111_3 at the CH5918 beamtime at ID31 at the ESRF in July 2021. All raw potentials are turned to RHE as section 2.1.3 introduced, all currents (I) are turned to current density (j) by dividing the area of Pt working electrode, and all X-ray intensity has been corrected by removing the background intensity. The CVs run several cycles to 1.174 V vs RHE with different sweep rates and some cycles to 0.894 V vs RHE to separate them. The sweep rate for cycles to 1.174 V decreases as cycle number increases, with 1 V/s for cycle 1 to 4, 250 mV/s for cycle 9 to 10, 100 mV/s for cycle 15, 50 mV/s for cycle 19, 20 mV/s for cycle 23, and 5 mV/s for cycle 27. The cyclic voltammograms for different cycles are shown as Fig. 3.13, and the corresponding X-ray voltammograms are shown as Fig. 3.14.

CV & X-ray Data Treatment

The cyclic voltammogram is shown as Fig. 3.15, in which the current density (j) is turned to pseudocapacitance (C) by dividing by the scan rate of each cycle for easy comparison. When cycle number increases and scan rate decreases, the H UPD peak and butterfly peak slowly increases, the potential of oxide peak top decreases

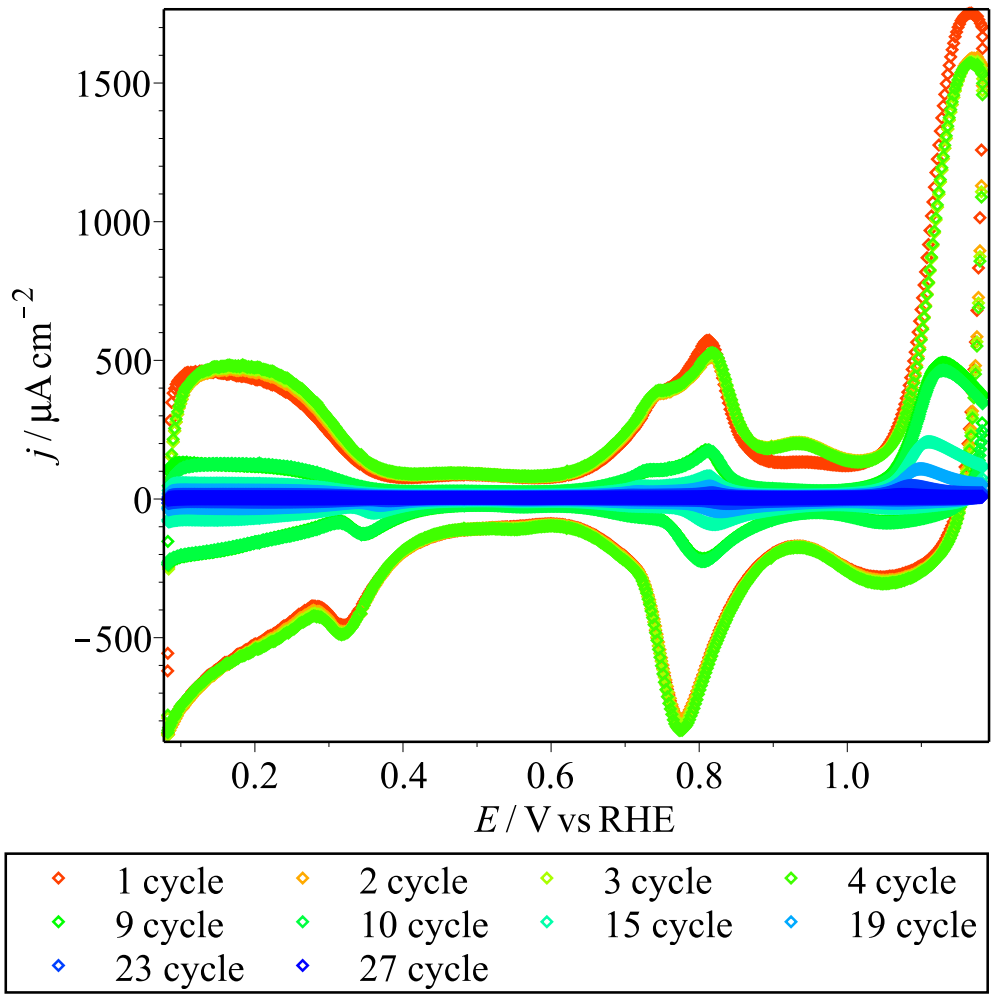

Figure 3.13: Pt(111) cyclic voltammogram under different sweep rates. 1 V/s for cycle 1 to 4, 250 mV/s for cycle 9 to 10, 100 mV/s for cycle 15, 50 mV/s for cycle 19, 20 mV/s for cycle 23, and 5 mV/s for cycle 27. Data from EC file Pt111_09 at the CH5918 beamtime at ID31 at the ESRF in July 2021.

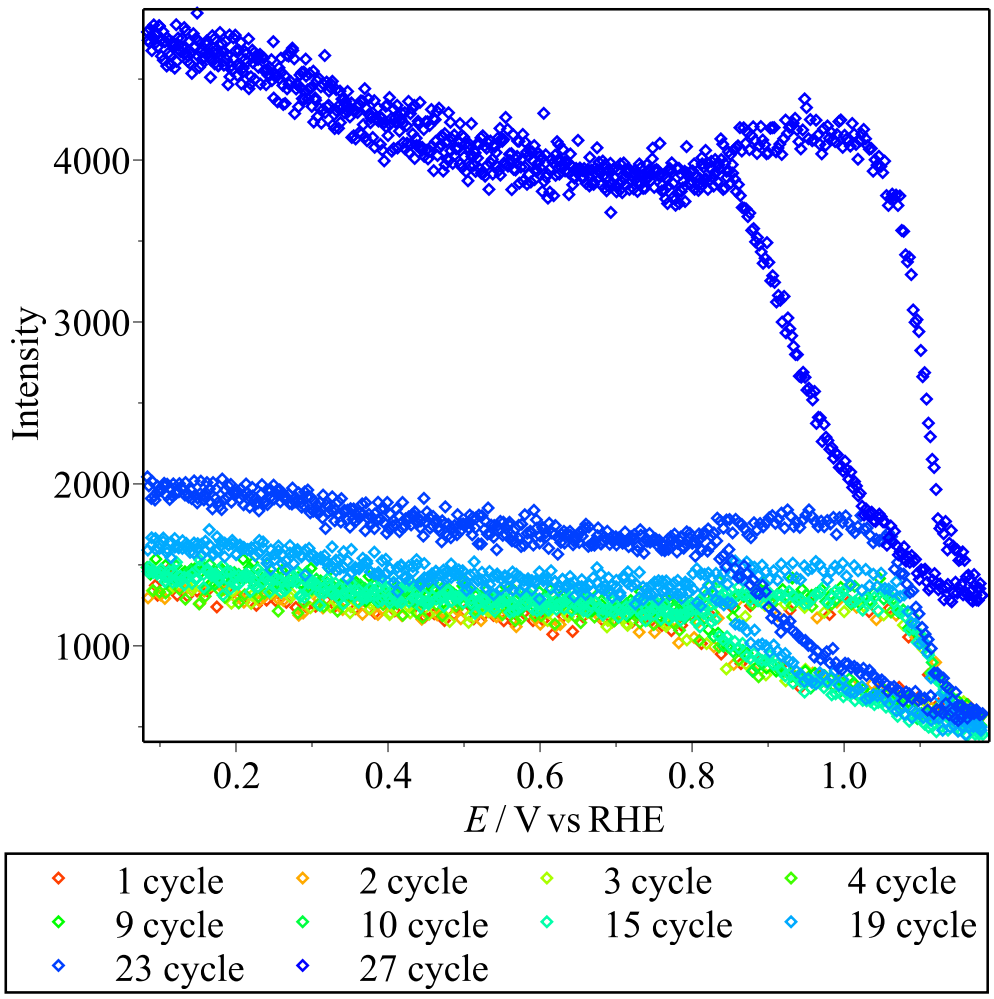

Figure 3.14: Pt(111) X-ray intensities under different sweep rates. 1 V/s for cycle 1 to 4, 250 mV/s for cycle 9 to 10, 100 mV/s for cycle 15, 50 mV/s for cycle 19, 20 mV/s for cycle 23, and 5 mV/s for cycle 27. Data from X-ray file Pt111_3 at the CH5918 beamtime at ID31 at the ESRF in July 2021.

from 1.17 V to 1.07 V, and the potential of cathodic OH/O mixed peak maximum increases from 0.77 V to 0.87 V.

Then, for the anodic flat part of CV from 0.85 to 1.0 V is very flat with slope close to zero, so H_2O_2 from X-ray beam damage can be neglected and only horizontal baseline to remove double layer is used here, as cycle 1 in Fig 3.16 for example. Then the integration of current density vs potential divided by scan rate is made to get the charge density vs potential shown as Fig. 3.17 for cycles under different scan rates. When cycle number increases and scan rate decreases, the charge density of the butterfly peak increases from 55 to 85 μC cm^{-2}, and the charge density of the oxide peak is 150 μC cm^{-2} for 1 V/s and 170 μC cm^{-2} for the rest.

Next the charges of different peaks are divided by 240.27 μC cm^{-2} to turn to coverage of electrons, θ_e, in monolayer (ML) as in Section. 2.2.2, and the result is shown as Fig. 3.18. When cycle number increases and sweep rate decreases, the H UPD peak increases from 0.52 ML to 0.68 ML, the butterfly peak increases from 0.22 ML to 0.30 ML, and the oxide peak keeps $\sim$0.55 ML when 1 V/s and keeps $\sim$0.7 ML for the rest cycles with scan rate lower than 1 V/s. Also, peak coverages under 20 mV/s is compared with data from other beamtimes in Table. 3.1, and its X-ray voltammogram is shown in Fig. 3.19.

The X-ray intensities are transferred to structure factors (F) as $|F| = \sqrt{\frac{I}{I_{0.9V}}}$ with standard as intensity of 0.9 V for each cycle. As Fig. 3.20 shows, the potential when the structure factors start dropping, and the dropping speed is independent of sweep rate. The cathodic processes are a little different for different scan rates. Then the structure factors are turned to θ_{ex} using $0.198 - 0.201|F|$ as described in Section 2.3.4.

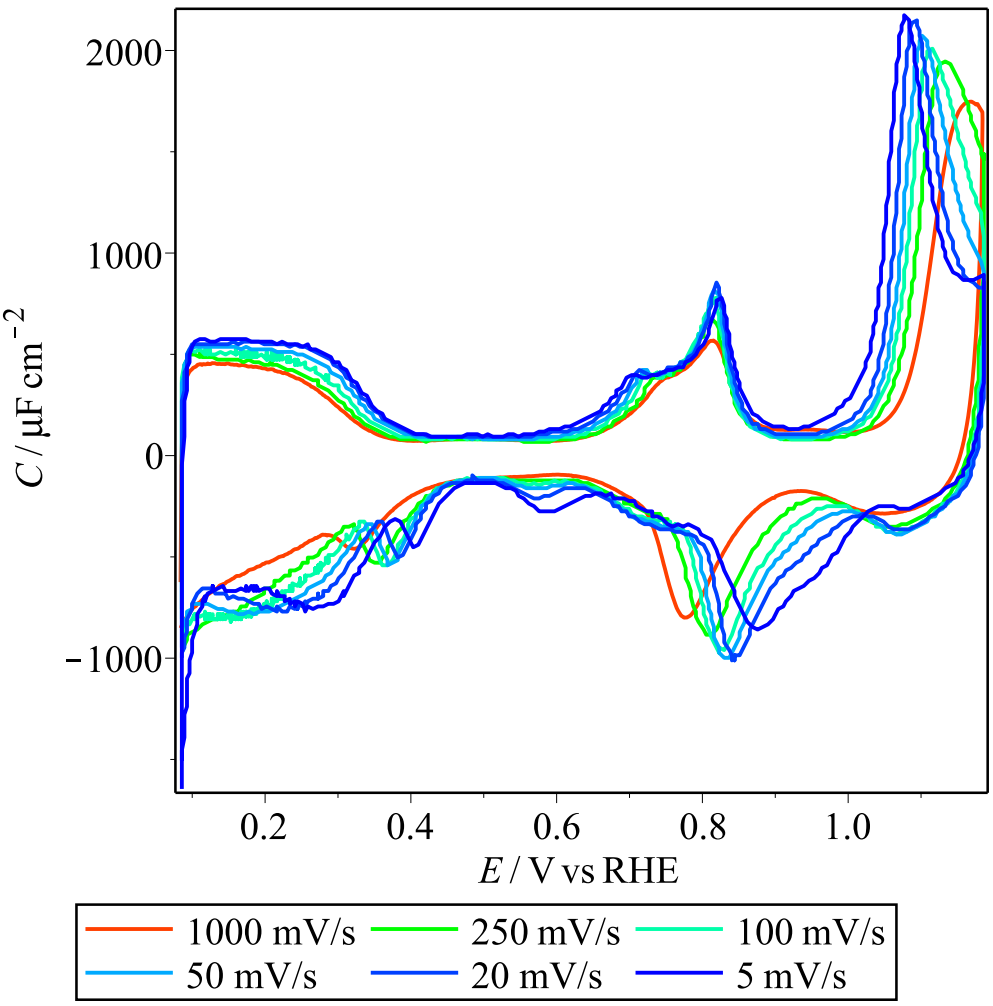

Figure 3.15: Pt(111) cyclic voltammogram under different sweep rates. 1 V/s, 250 mV/s, 100 mV/s, 50 mV/s, 20 mV/s, and 5 mV/s. Data from EC file Pt111_09 at the CH5918 beamtime at ID31 at the ESRF in July 2021.

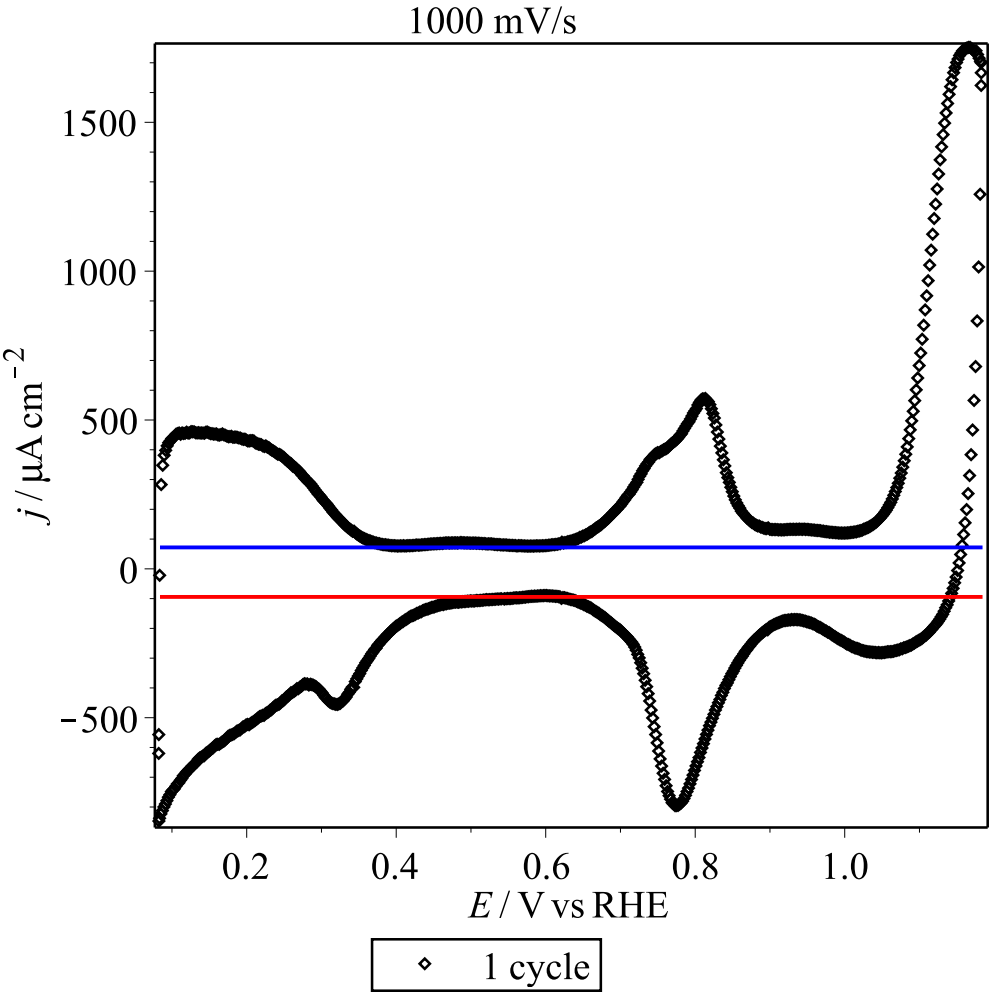

Figure 3.16: Pt(111) cyclic voltammogram with sweep rate, as 1 V/s. The blue line is anodic baseline. The red line is cathodic baseline. Data from cycle 1 of EC file Pt111_09 at the CH5918 beamtime at ID31 at the ESRF in July 2021.

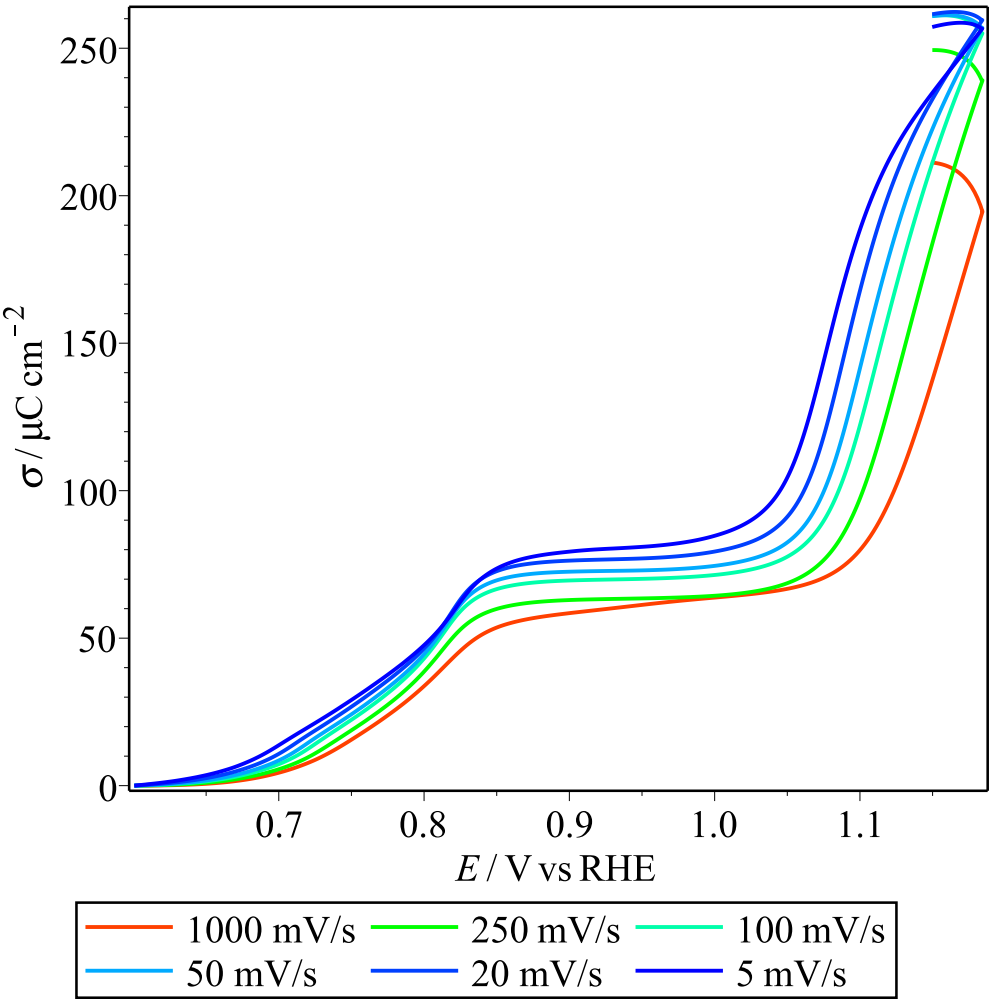

Figure 3.17: Pt(111) anodic charge plots under different sweep rates. 1 V/s, 250 mV/s, 100 mV/s, 50 mV/s, 20 mV/s, and 5 mV/s. Data from EC file Pt111_09 at the CH5918 beamtime at ID31 at the ESRF in July 2021.

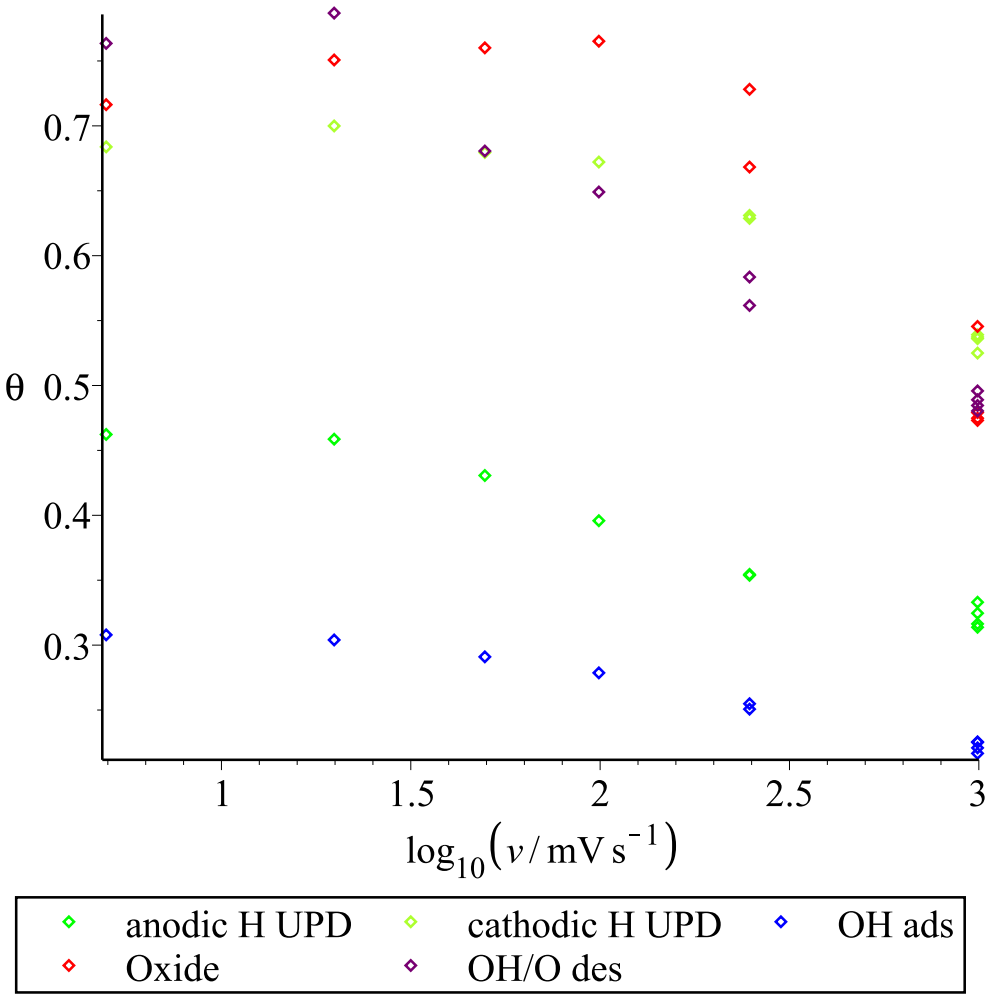

Figure 3.18: Pt(111) coverage of electrons for peaks in cyclic voltammetry spectra under different sweep rates. 1 V/s, 250 mV/s, 100 mV/s, 50 mV/s, 20 mV/s, and 5 mV/s. Data from EC file Pt111_09 at the CH5918 beamtime at ID31 at the ESRF in July 2021.

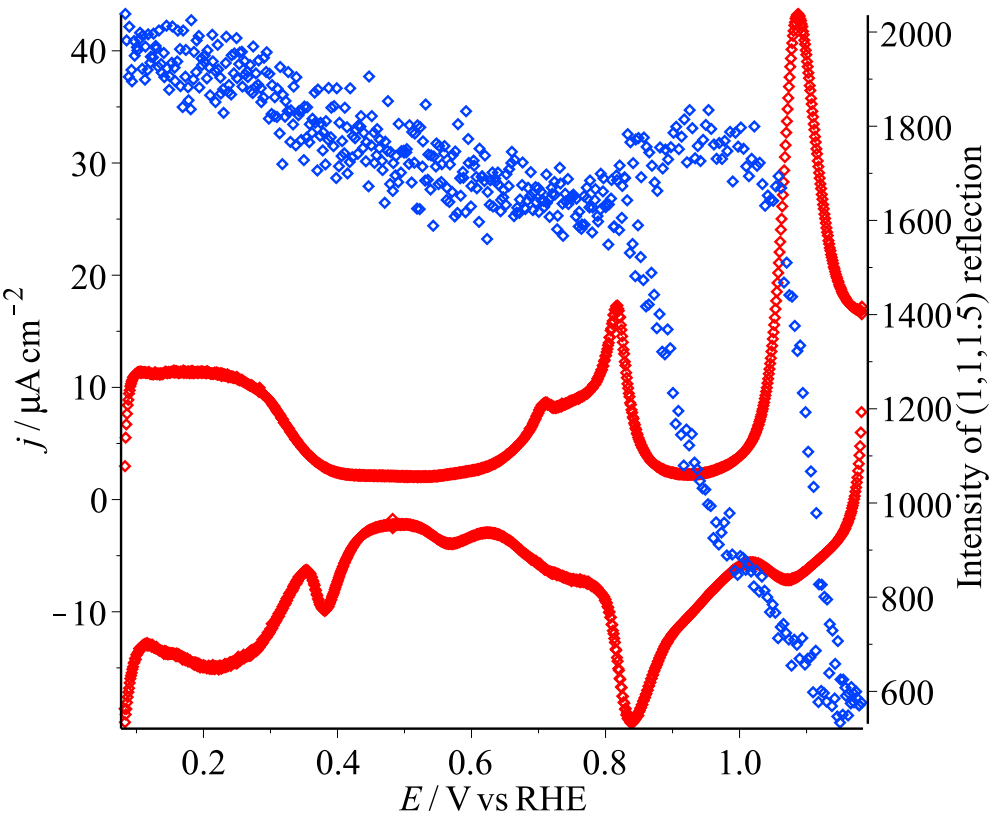

Figure 3.19: Pt(111) X-ray intensities under 20 mV/s. Data from EC file Pt111_09 and X-ray file Pt111_3 at the CH5918 beamtime at ID31 at the ESRF in July 2021.

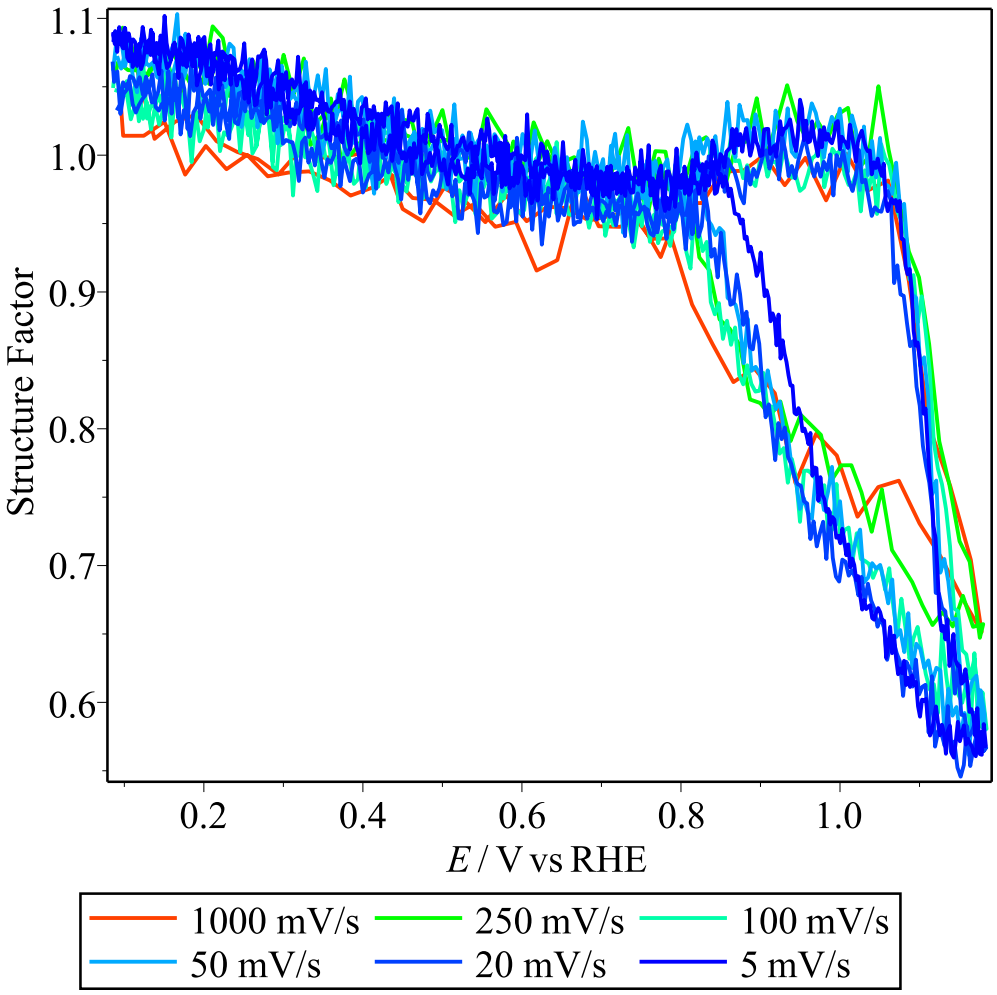

Figure 3.20: Pt(111) X-ray voltammograms with structure factors under different sweep rates. 1 V/s, 250 mV/s, 100 mV/s, 50 mV/s, 20 mV/s, and 5 mV/s. Data from X-ray file Pt111_3 at the CH5918 beamtime at ID31 at the ESRF in July 2021.

Coverages θ_e vs θ_{ex} from CV and X-ray

θ_e and θ_{ex} for the sweep rate dependent CV and X-ray data are compared in Fig. 3.21. Fig. 3.21 shows the θ_e and θ_{ex} at the end of anodic processes. Both θ_e and θ_{ex} are much lower than others when the sweep rate is 1 V/s, at which θ_e is 0.5 ML and θ_{ex} is 0.065 ML. For the lower sweep rates between 250 mV/s and 5 mV/s with higher cycle number, θ_e is 0.7 ML and θ_{ex} is 0.08 ML.

Then θ_e vs θ_{ex} in the potential range of the anodic intensity decreasing part and cathodic intensity increasing part are plotted, with linear fits similarly to Section. 3.1.4, and the summary of slopes for both plots is shown in Fig. 3.25. The anodic θ_e vs θ_{ex} is shown as Fig. 3.22, and the plot under 20 mV/s, which is compared with data from other beamtimes in Table. 3.1, is shown in Fig. 3.24. The slope of fitted line for all cycles is around 7.50. The points of θ_e vs θ_{ex} for different cycles are different when $\theta_{ex} < 0.05$ ML for different sweep rates, but the plots are almost linear and the same when $\theta_{ex} > 0.05$ ML, which can show the reaction of Pt oxide and e^-s transferred per extracted Pt are independent from the sweep rate. The cathodic θ_e vs θ_{ex} is shown as Fig. 3.23, and the slope of the fitted line is approximately constant at 5.02.

Also, anodic θ_e vs θ_{ex} plots under different sweep rates without CV baseline correction are shown in Fig. 3.26. The anodic slope of fitted line is 5.02, very close to 5.16 in Section 3.1.2. The overall slope from first to last point in 9.12, a little higher than the baseline corrected slope 7.50, but much lower than 11.6 as uncorrected slope in Section 3.1.2, mostly from lower double layer charges. The corresponding cathodic θ_e vs θ_{ex} plots are shown in Fig. 3.27. The cathodic slope of the fitted line is 6.89, very close to 6.49 in Section 3.1.2.

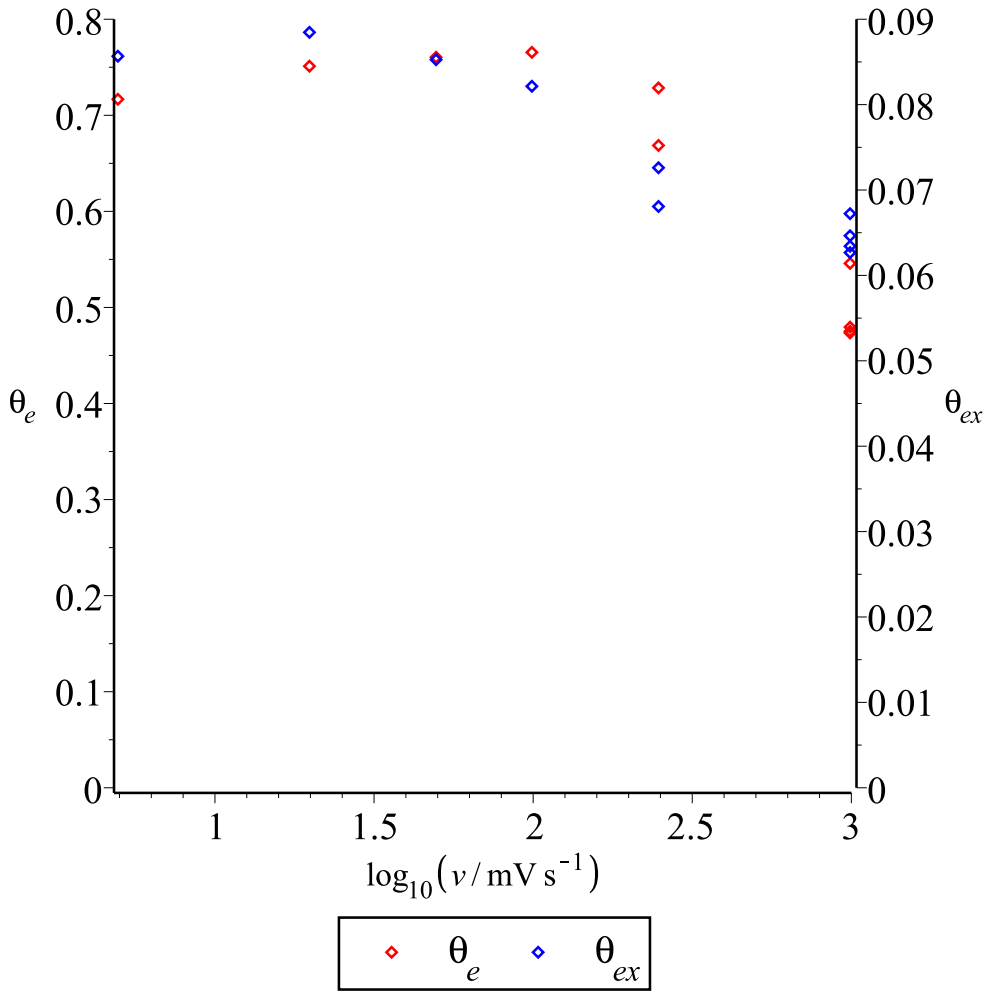

Figure 3.21: Pt(111) θ_e and θ_{ex} plots under different sweep rates. 1 V/s, 250 mV/s, 100 mV/s, 50 mV/s, 20 mV/s, and 5 mV/. Data from EC file Pt111_09 and corresponding X-ray file Pt111_3 at the CH5918 beamtime at ID31 at the ESRF in July 2021.

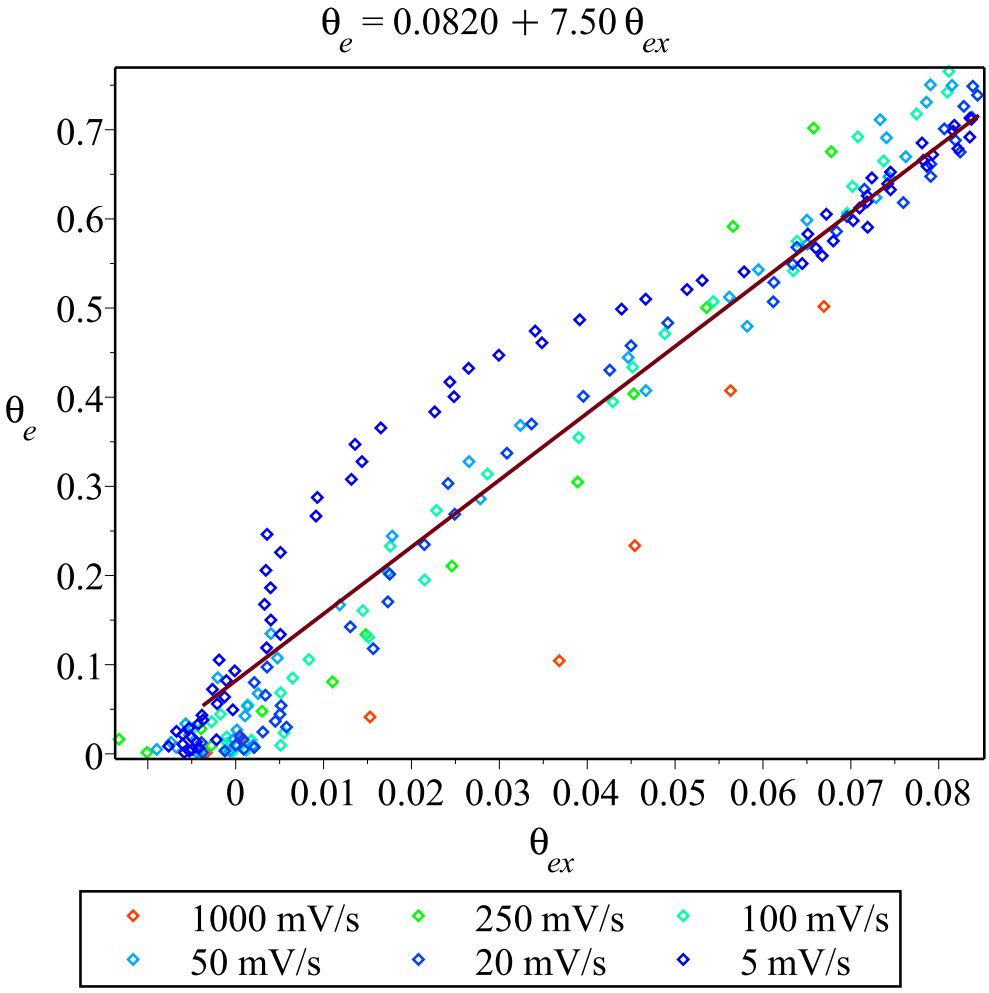

Figure 3.22: Pt(111) anodic θ_e vs θ_{ex} plots of all cycles with segmented baseline correction with different sweep rate, as 1 V/s, 250 mV/s, 100 mV/s, 50 mV/s, 20 mV/s, and 5 mV/s. Data from EC file Pt111_09 and corresponding X-ray file Pt111_3 at the CH5918 beamtime at ID31 at the ESRF in July 2021.

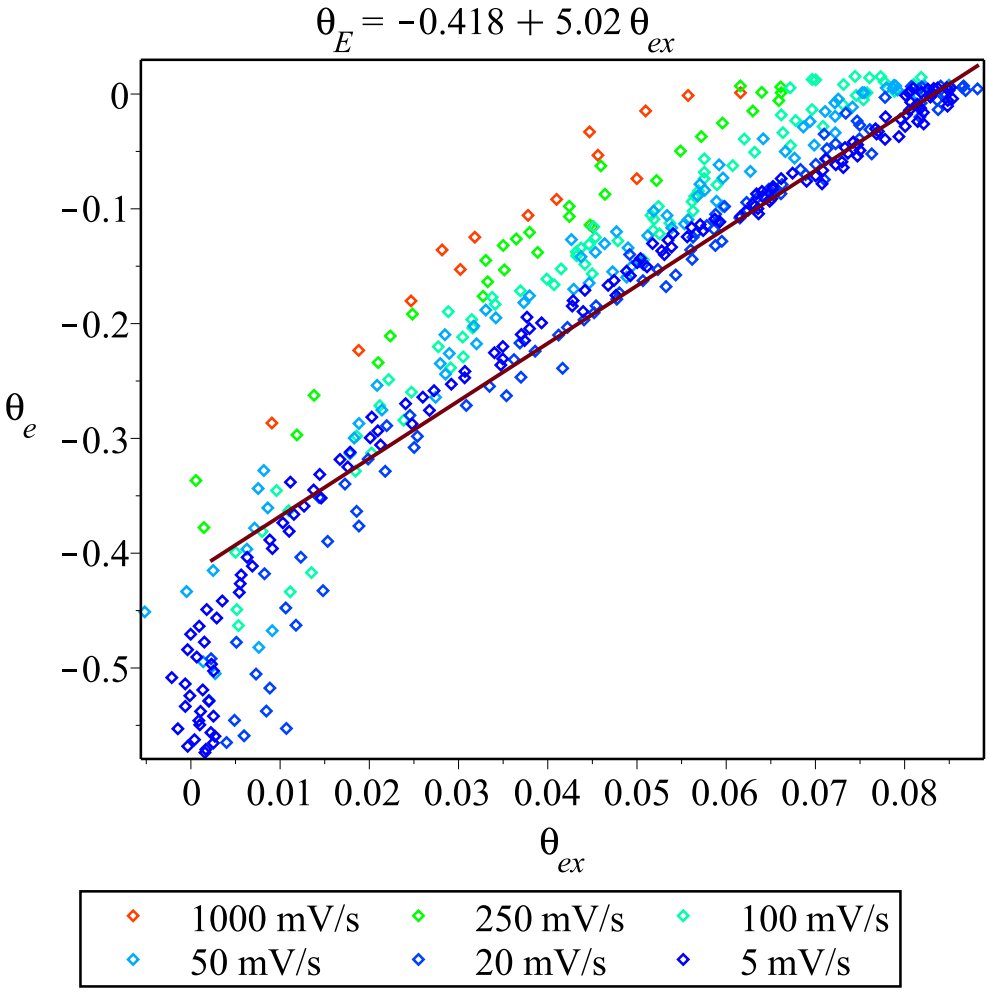

Figure 3.23: Pt(111) cathodic θ_e vs θ_{ex} plots with segmented baseline correction under different sweep rate, as 1 V/s, 250 mV/s, 100 mV/s, 50 mV/s, 20 mV/s, and 5 mV/s. Data from EC file Pt111_09 and corresponding X-ray file Pt111_3 at the CH5918 beamtime at ID31 at the ESRF in July 2021.

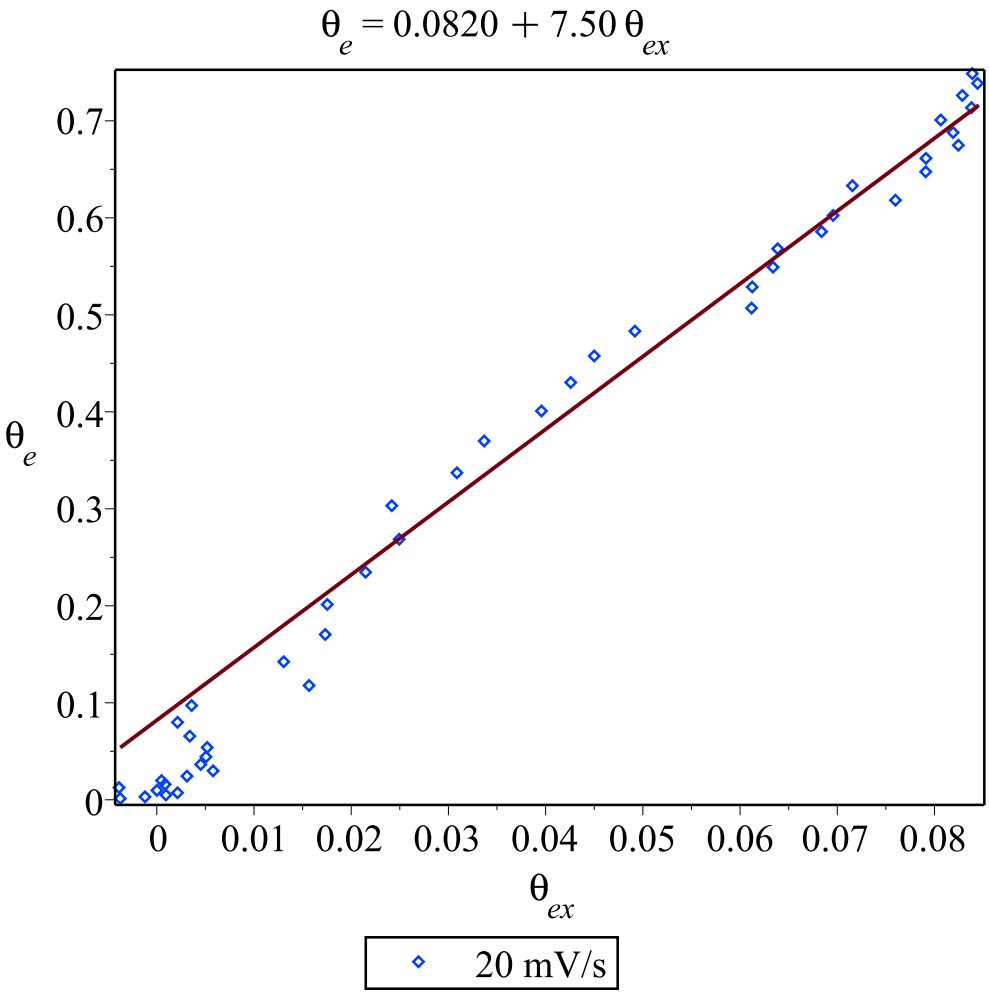

Figure 3.24: Pt(111) anodic θ_e vs θ_{ex} plots of all cycles with segmented baseline correction under 20 mV/s. Data from EC file Pt111_09 and corresponding X-ray file Pt111_3 at the CH5918 beamtime at ID31 at the ESRF in July 2021.

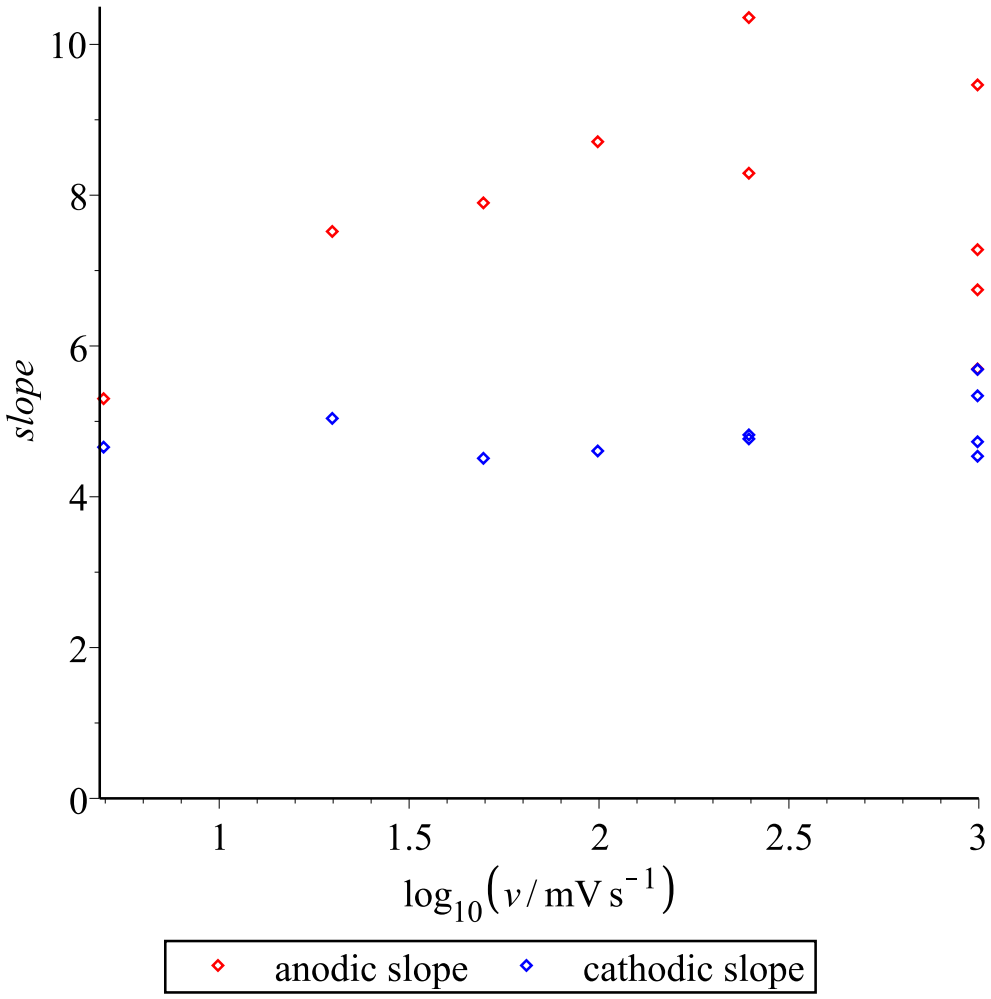

Figure 3.25: Pt(111) slopes of fitted line of θ_e vs θ_{ex} with segmented baseline correction under different sweep rate, as 1 V/s, 250 mV/s, 100 mV/s, 50 mV/s, 20 mV/s, and 5 mV/s. Data from EC file Pt111_09 and corresponding X-ray file Pt111_3 at the CH5918 beamtime at ID31 at the ESRF in July 2021.

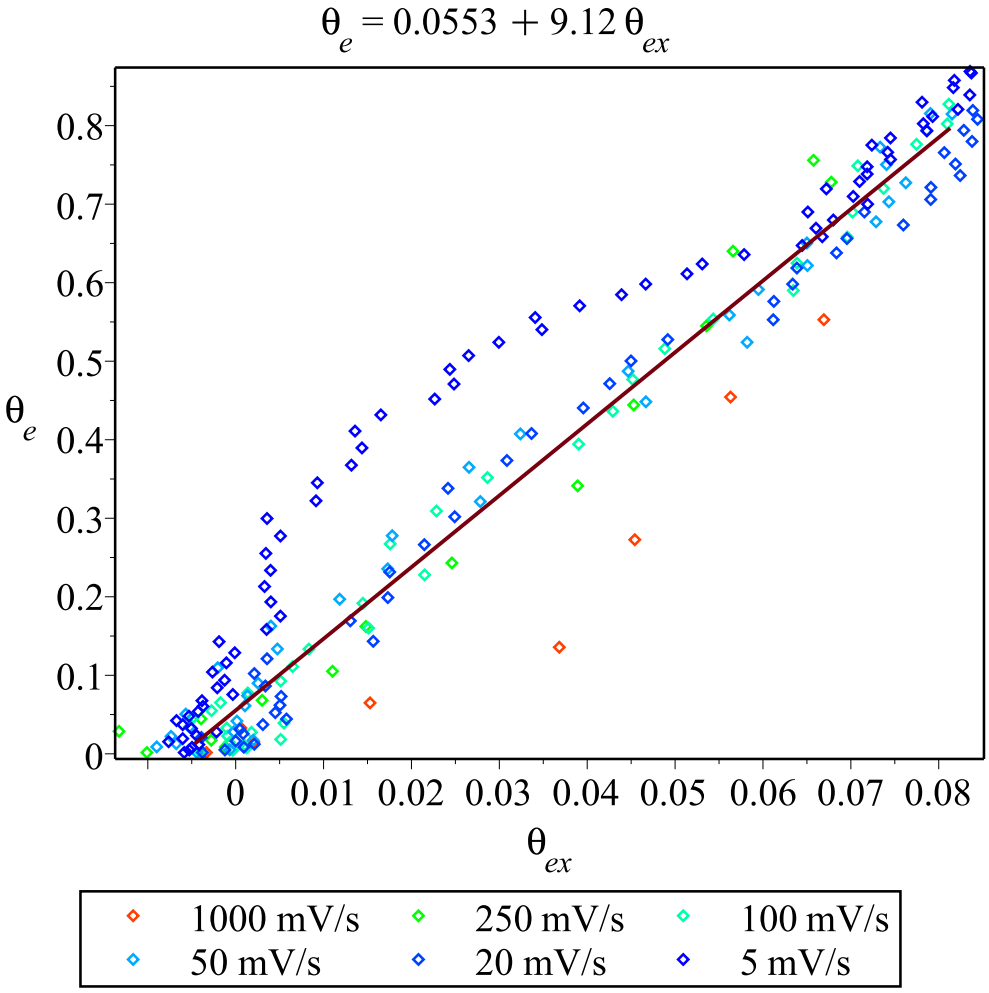

Figure 3.26: Pt(111) anodic θ_e vs θ_{ex} plots of all cycles without baseline correction with different sweep rate, as 1 V/s, 250 mV/s, 100 mV/s, 50 mV/s, 20 mV/s, and 5 mV/s. Data from EC file Pt111_09 and corresponding X-ray file Pt111_3 at the CH5918 beamtime at ID31 at the ESRF in July 2021.

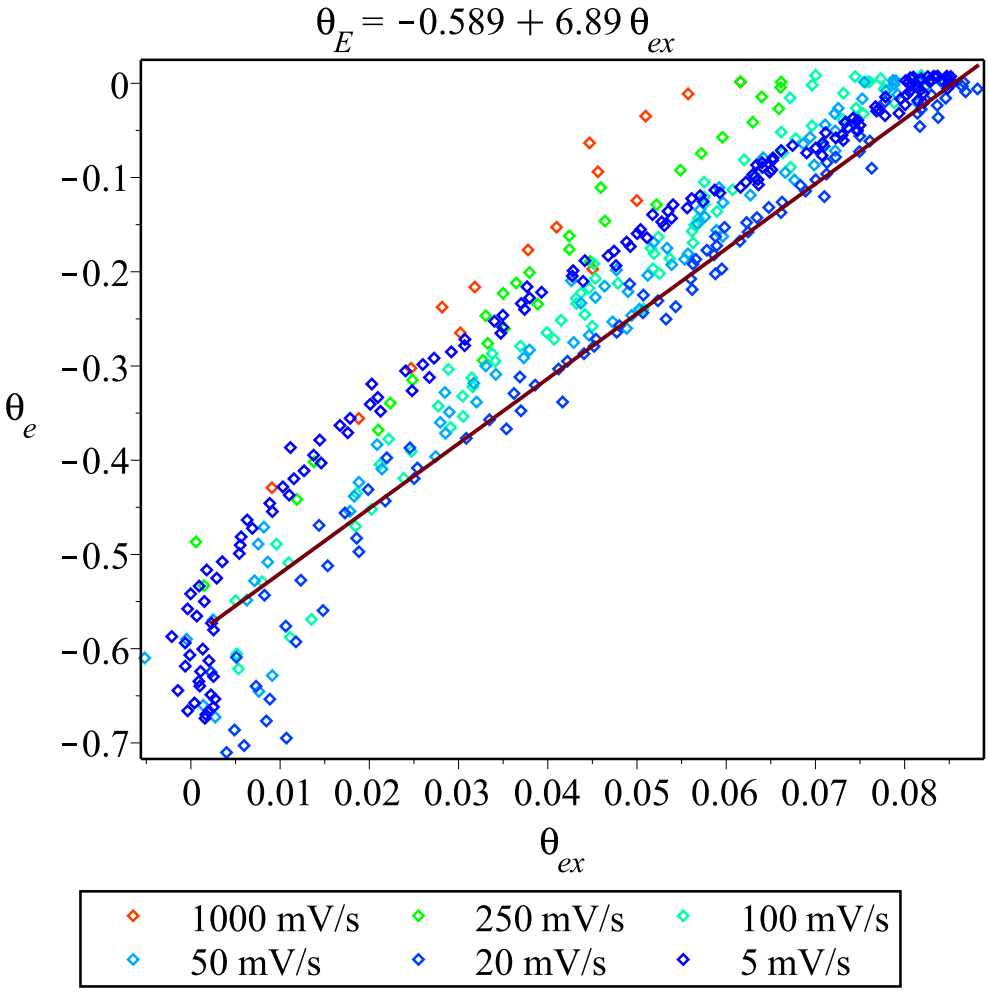

Figure 3.27: Pt(111) cathodic θ_e vs θ_{ex} plots of all cycles without baseline correction with different sweep rate, as 1 V/s, 250 mV/s, 100 mV/s, 50 mV/s, 20 mV/s, and 5 mV/s. Data from EC file Pt111_09 and corresponding X-ray file Pt111_3 at the CH5918 beamtime at ID31 at the ESRF in July 2021.

Discussion on Extraction of Pt(111) under Different Sweep Rates

For the treated cyclic voltammetry data, it is compared with reference from Feliu's work [53] shown as Fig. 3.28. The butterfly peak here increases from 55 to 85 μC cm^{-2} ($\sim$1/4 to 1/3 ML) when sweep rate decreases from this test, but it is constant at 120 μC cm^{-2} (1/2 ML) and independent from the sweep rate in Ref [53]. For the oxide peak, the potential of its top is from 1.17 V to 1.07 V when sweep rate is from 1 V/s to 5 mV/s, but that from Feliu's work [53] decreases from 1.11 V to 1.03 V for the same sweep rates. Also the oxide peaks in this research have lower peak height than reference [53]. The coverage of oxide peaks are $\sim$0.75 ML, a little higher than 0.5 ML from Feliu's research [53], expect for the cycles under 1 V/s (red curve on left side) which don't have enough time for reaction. The oxide peaks here have higher coverage then the reference, and the peak is sharper and appears later in potential. These differences are likely due to some small differences in the initial surface condition.

Then, the anodic structure factors from X-ray intensity drop from 1.05 V under any sweep rates in Fig. 3.20. No matter how the sweep rate and oxide peak in CV spectra changes, the Pt extraction, shown by change of X-ray intensity, stays the same and isn't affected by these conditions.

Next for the θ_e vs θ_{ex}, the intercept of anodic fitted line increases as sweep rate decreases in Fig. 3.22, which shows the Pt extraction starts from the very early part of the e$^-$ transfer in the Pt oxide peak under high sweep rates (1 V/s, 250 mV/s), also it happens at the same time of e$^-$ transfer in the Pt oxide peak under middle sweep rates (100 mV/s, 50 mV/s, 20 mV/s), and happens after e$^-$ transfer of Pt oxide peak under very low sweep rate (5 mV/s). The maximum θ_{ex} is 0.085 ML, a little higher than 0.066 ML in Section 3.1.2, but still much lower than 0.18 ML at

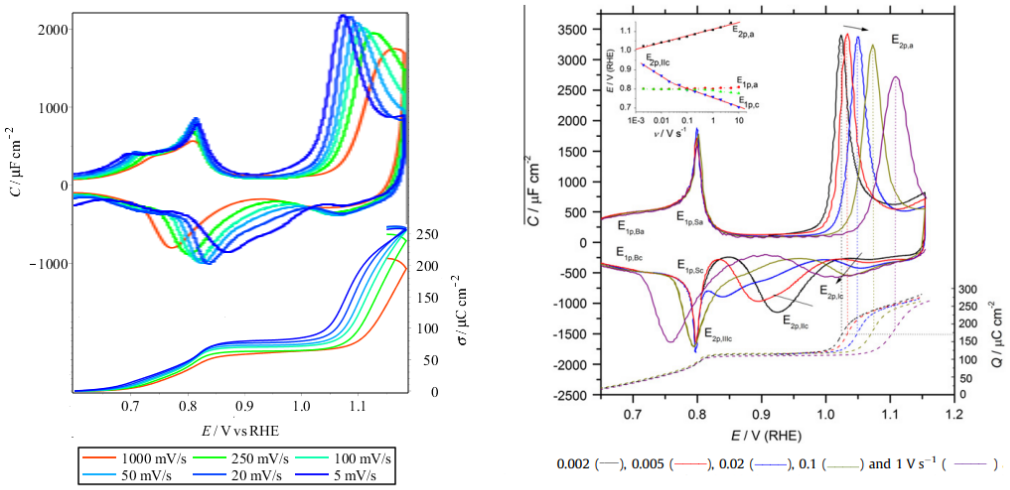

Figure 3.28: Pt(111) cyclic voltammetry spectra and charge densities under different sweep rate on the left side compared with reference on the right side. Data on the left side from EC file Pt111_09 at the CH5918 beamtime at ID31 at the ESRF in July 2021. Fig on the right side reprinted from Journal of Electroanalytical Chemistry, 688, Ana M. Gómez-Marín, Jean Clavilier, Juan M. Feliu, Sequential Pt(111) oxide formation in perchloric acid: An electrochemical study of surface species interconversion, Pages 360-370, Copyright 2013, with permission from Elsevier [53].

1.2 V from Koper's place-exchange model [97]. The θ_e vs θ_{ex} curve is generally linear in Fig. 3.22, same as Koper's experimental data, but our slope 7.50, nearly twice of the value of 4 in reference [97].

Lastly for the reactions of oxide peak, except the cycles under 1 V/s which the oxide peak isn't complete, θ_e is ∼0.7 ML, close to 2/3 ML, and θ_{ex} is ∼0.085 ML, close to 1/12 ML. The following equation is a possible reaction for Pt oxide peak per 12 surface Pt atoms with OH_{ads} from butterfly peak as 1/2 ML, at which PtO(ex) means extracted Pt, formed as Eq. 3.3, coverage of extracted Pt is 1/12 ML, and coverage of O_{ads} peak is 1/2 ML:

$$6 \times (\mathrm{OH(ads)} \rightarrow \mathrm{O(ads)} + \mathrm{H^+} + \mathrm{e^-}) \tag{3.6}$$

$$1 \times \mathrm{Pt} + \mathrm{H_2O} \rightarrow \mathrm{PtO(ex)} + 2\mathrm{H^+} + 2\mathrm{e^-} \tag{3.7}$$

Like Section 3.1.2, if the extracted Pt forms PtO_2 and the CV isn't baseline corrected, θ_e is 0.85 ML, close to $\frac{10}{12}$ ML, the reaction is shown as below:

$$6 \times (\mathrm{OH(ads)} \rightarrow \mathrm{O(ads)} + \mathrm{H^+} + \mathrm{e^-}) \tag{3.8}$$

$$1 \times (\mathrm{Pt} + 2\mathrm{H_2O} \rightarrow \mathrm{PtO_2(ex)} + 4\mathrm{H^+} + 4\mathrm{e^-}) \tag{3.9}$$

Same as Section 3.1.2, the equation is also made by $\frac{1}{2}$ ML O_{ads} formed from OH_{ads}, but just higher coverage of Pt extraction, as $\frac{1}{12}$ ML PtO_2 formed from surface Pt and water. In all, this equation is in agreement with Eq. 3.5 in Section 3.1.2.

3.1.4 Pt(111) Performance after Fast Scans

In this subsection, performance of Pt(111) CV and X-ray data after fast scans is compared with after a normal slow scan as in section 3.1.2, with the data treated in the same way.

Data from EC file 25 of CH5700

Cyclic voltammetry data is from EC file 25 at the CH5700 beamtime at ID31 at the ESRF in November 2020, and all raw potentials are converted to RHE with additional 0.274 V as section 2.1.3 introduced. Cyclic voltammetry spectra of 8 different steps are shown in Fig. 3.29. From cycle 1 to 4 as (a) in Fig. 3.29, it has potential range up to 0.574 V vs RHE and scan rate as 50 mV/s, with only a pair of H UPD peaks from 0 to 0.3 V. Then there are 8 cycles of voltammetry up to 0.874 V as (b) in Fig. 3.29, with an extra pair of butterfly-like OH_{ads} peaks from 0.6 to 0.9 V with tops centred as 0.75 V. From cycle 13 to 100 as (c) in Fig. 3.29, the scan rate is increased to 2000 mV/s with potential range unchanged, and OH_{ads} peaks are turned to single peaks, with anodic tops centred as 0.78 V and cathodic one centred as 0.68 V. For the next 27 cycles as (d) in Fig. 3.29, the scan rate is back to 50 mV/s with potential range unchanged and spectra are same as Fig. (b) of cycle 5 to 12. Next, for cycle 128 to 135 as (e) in Fig. 3.29, the potential range is increased to 1.174 V, the scan rate is changed to 250 mV/s, so they are also called as fast cycles, and the spectra look similar to previous ones, but with an extra huge anodic oxide single peak from 1.0 V to maximum centred at 1.10 to 1.06 V, with mixed cathodic O/OH peak centred at 0.75 V. Then, for cycle 136 to 143 as (f) in Fig. 3.29, or slow cycles compared with (e), the scan rate is lowered to 20 mV/s, nearly 1/10 of 250 mV/s in (e), so the current for top of oxide peak is dropped to 1/10 of (e), and

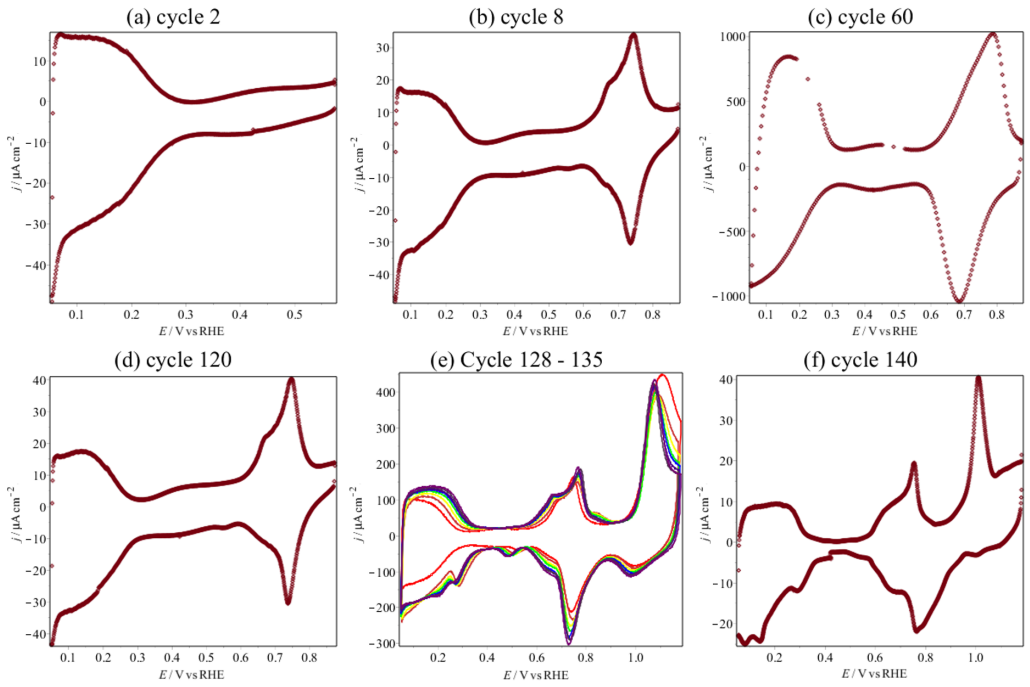

Figure 3.29: Pt(111) cyclic voltammetry spectra for Cycle 2, 8, 60, 120, 128 - 135, 140. Cycle 128 - 135 is the fast cycle with scan rate 250 mV/s, with corresponding colors as red, orange, yellow, green, blue, indigo, violet, then purple. Cycle 140 is the slow cycle with scan rate 20 mV/s. Data from EC file 25 at the CH5700 beamtime at ID31 at the ESRF in November 2020.

anodic oxide peak is dropped to 0.93 to 1.08 V centred at 1.01 V, much lower than (e) and Fig. 3.1.

Cyclic Voltammetry After Fast Scans

Cycle 140 in EC file 25 at CH5700 beamtime is selected for CV data treatment, as X-ray voltammogram in Fig. 3.30. All data treatment in this section is similar to section 3.1.1.

For the voltammogram in Fig. 3.31, the double layer is less and the surface of

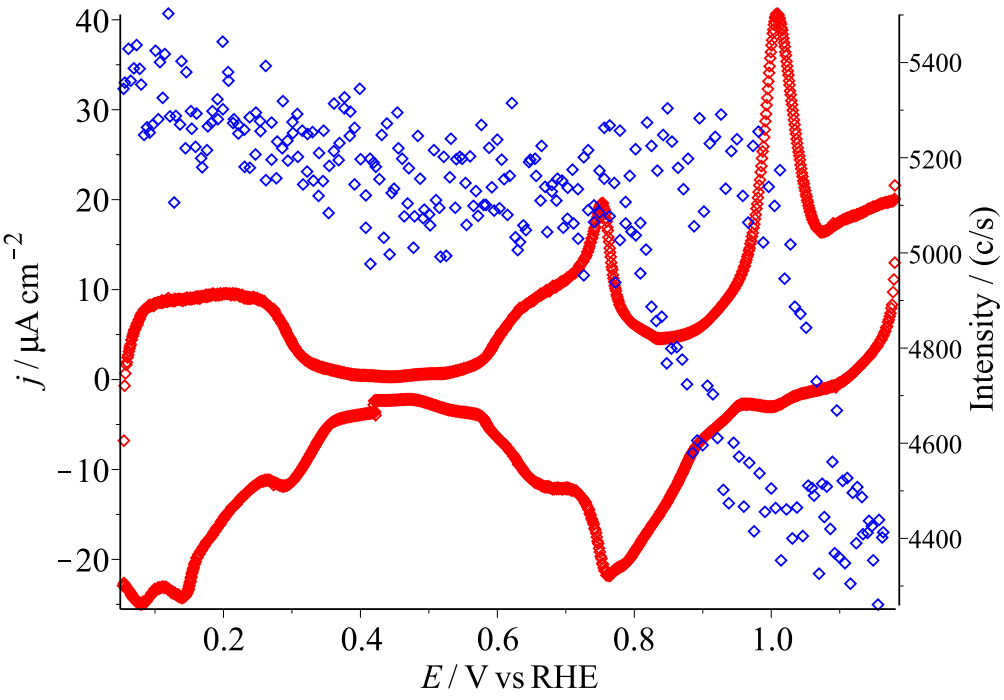

Figure 3.30: Pt(111) X-ray voltammogram after fast scans. Sweep rate as 20 mV/s. Data from cycle 140 of EC file 25 at the CH5700 beamtime at ID31 at the ESRF in November 2020.

Pt electrode is changed by several runs of CV with high scan rate of 250 mV/s, which is much larger than normally 20 mV/s or 50 mV/s. The spectrum corrected by segmented baseline for double layer charges and H_2O_2 from X-ray beam damage is shown as Fig. 3.32. Then charge densities are obtained from integration of current density vs potential over sweep rate, and then converted to θ_e by dividing 240.3 μC cm^{-2} as in Section 2.2.2.

The peak coverages are compared with data from other beamtimes in Table. 3.1. Different from normal Pt(111) CV in Section 3.1.1 and 3.1.2, the baseline-corrected anodic oxide peak in Fig. 3.31 starts from 0.93 V vs RHE, and is 0.07 V less than normal Pt(111) anodic oxide peak, which starts from 1.0 V, also it is centred at 1.01 V, and is 0.05 V lower than normal centre 1.06 V. For the coverages, the anodic H UPD peak is 0.49 ML, the Pt oxide peak is 0.42 ML, and the "roll-back" part is 0.005 ML; they are similar to earlier data from Section 3.1.1. However, the coverage of the anodic butterfly peak is 0.45 ML, close to 1/2 ML [52, 53], and much higher than $\sim$1/3 ML in Section 3.1.1 [50, 63, 64].

If the CV isn't baseline corrected, the anodic H UPD peak is 0.42 ML and the cathodic one is 1.09 ML, much less than the anodic value 0.42 ML. The butterfly peak is 0.49 ML, the oxide peak is 1.07 ML, the roll-back part is 0.02 ML, and the addition of these 3 parts are 1.69 ML. The cathodic mixed peak is 1.07 ML, much less than the anodic value 1.69 ML.

X-ray Data Treatment

The X-ray data is from scan 14 of X-ray file Pt110_24 at CH5700 beamtime, which is corresponding to cycle 140 in EC file 25 and starts and ends at 0.424 V vs RHE in reduction process, is selected and has only half second's differences to times in CV

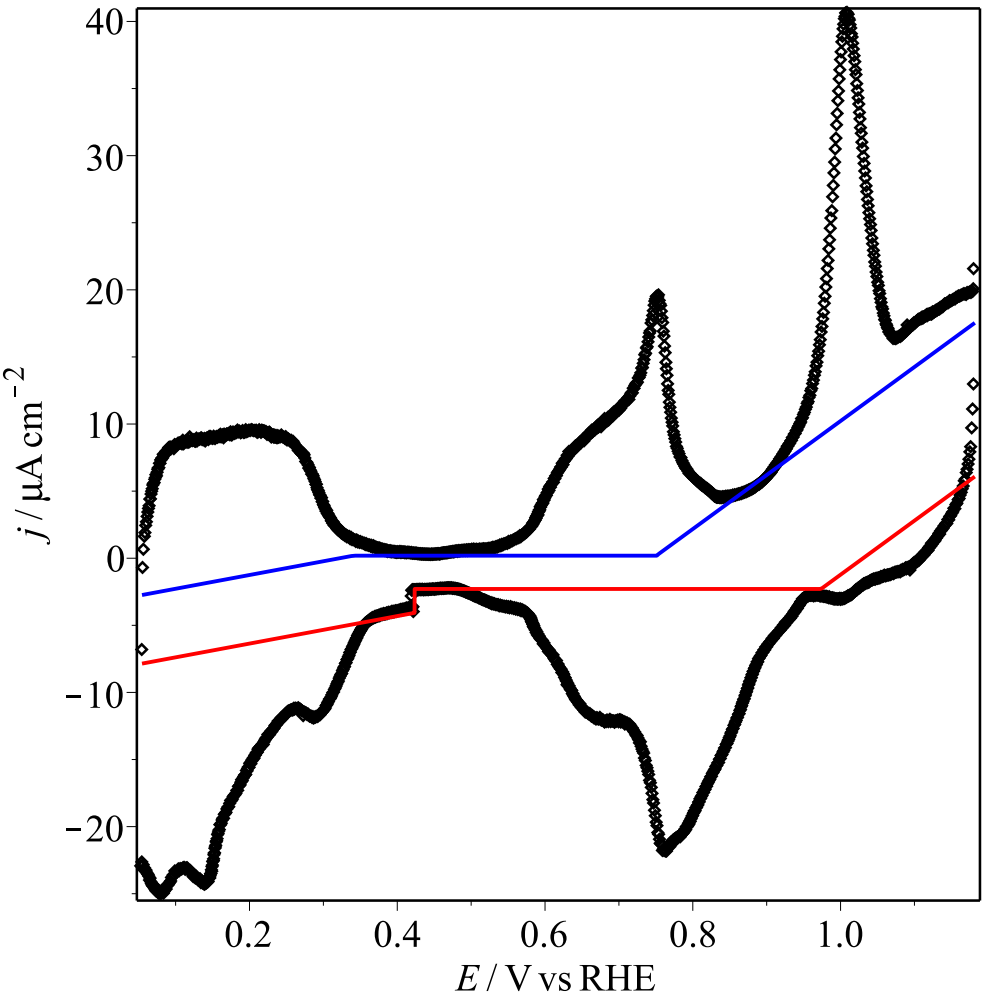

Figure 3.31: Pt(111) cyclic voltammogram after fast scans. Sweep rate as 20 mV/s. Data from Cycle 140 of EC file 25 at the CH5700 beamtime at ID31 at the ESRF in November 2020.

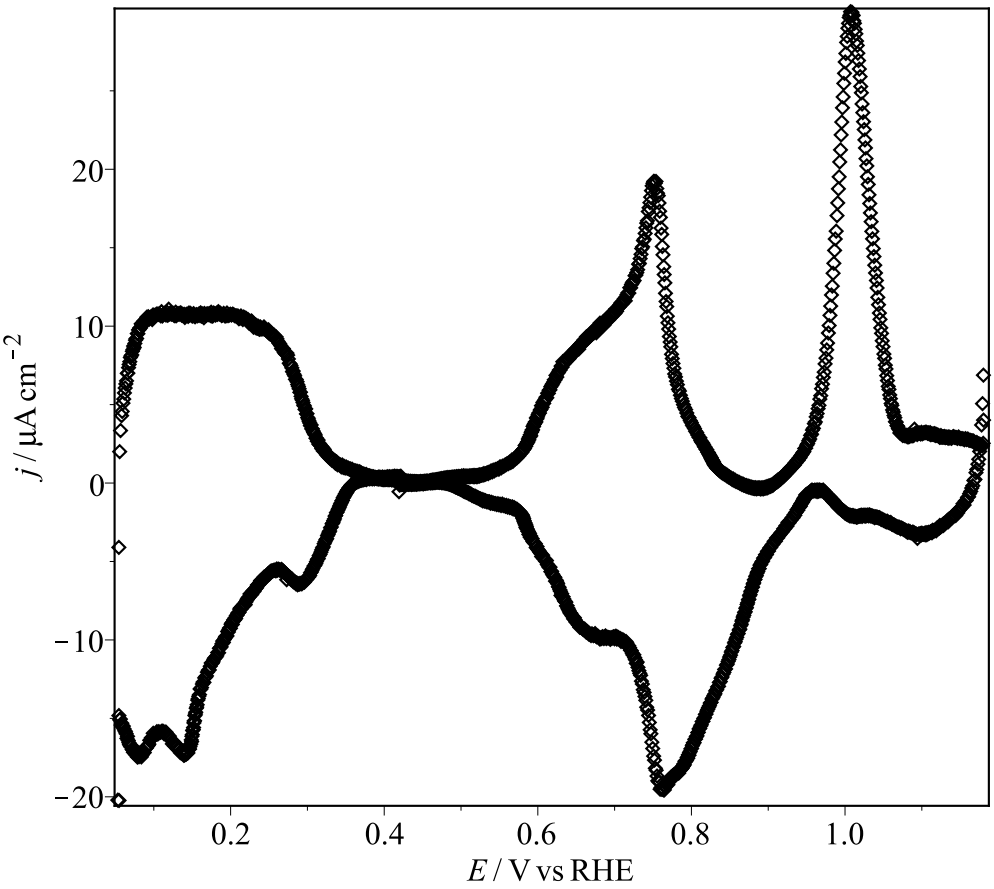

Figure 3.32: Baseline corrected Pt(111) cyclic voltammogram after fast scans. Sweep rate as 20 mV/s. Data from EC file 25 at the CH5700 beamtime at ID31 at the ESRF in November 2020.

data. The X-ray spectrum is shown in Fig. 3.33. It is normalized to θ_{ex} same as Section 3.2.2 to the point of 0.9 V vs RHE in oxidation process, and shown in Fig. 3.34. Also, the difference between the two X-ray diagrams is shown in Fig. 3.35, and all X-ray intensities have been converted to the structure factor as Equation $|F| = \sqrt{\frac{I}{I_{0.9V}}}$ from Section 2.3.4. The blue curve from CH5700 drops much less compared with brown curve from IHCH925 in Section 3.1.2. This is probably caused by the influence of the previous 250 mV/s cycles before analysis.

Discussion on Extraction of Pt(111) after fast scans

θ_e from CV is 0.42 ML, close to 0.46 ML on flat untreated surface in section 3.1.2, and the oxide peak in Fig. 3.31 in section 3.1.2. So probably, the reactions of oxide peak still occur as on the untreated surface: OH_{ads} groups still form O_{ads} and Pt is extracted. However, the largest apparent anodic θ_{ex} is 0.014 ML, nearly $\frac{1}{5}$ of 0.066 ML in section 3.1.2, which is also shown by the difference in X-ray intensity drops in Fig. 3.35, because the Pt surface has been degraded before analysis, and there has been some θ_{ex} at 0.9 V, the standard potential of X-ray intensity, from Pt surface degradation, but it is calculated as zero here. So to get a better θ_{ex} here, the standard X-ray intensity $I_{0.9V}$ before fast scans on untreated Pt surface need to be analyzed, for analysis of X-ray data after surface degradation from fast scans.

However, there are also several cycles with fast sweep rates of 1 V/s before the cycle with 20 mV/s in Section 3.1.3, but its θ_{ex} is 0.085 ML similar section 3.1.2, which shows the surface seems isn't degraded, and its mechanism need to be researched.

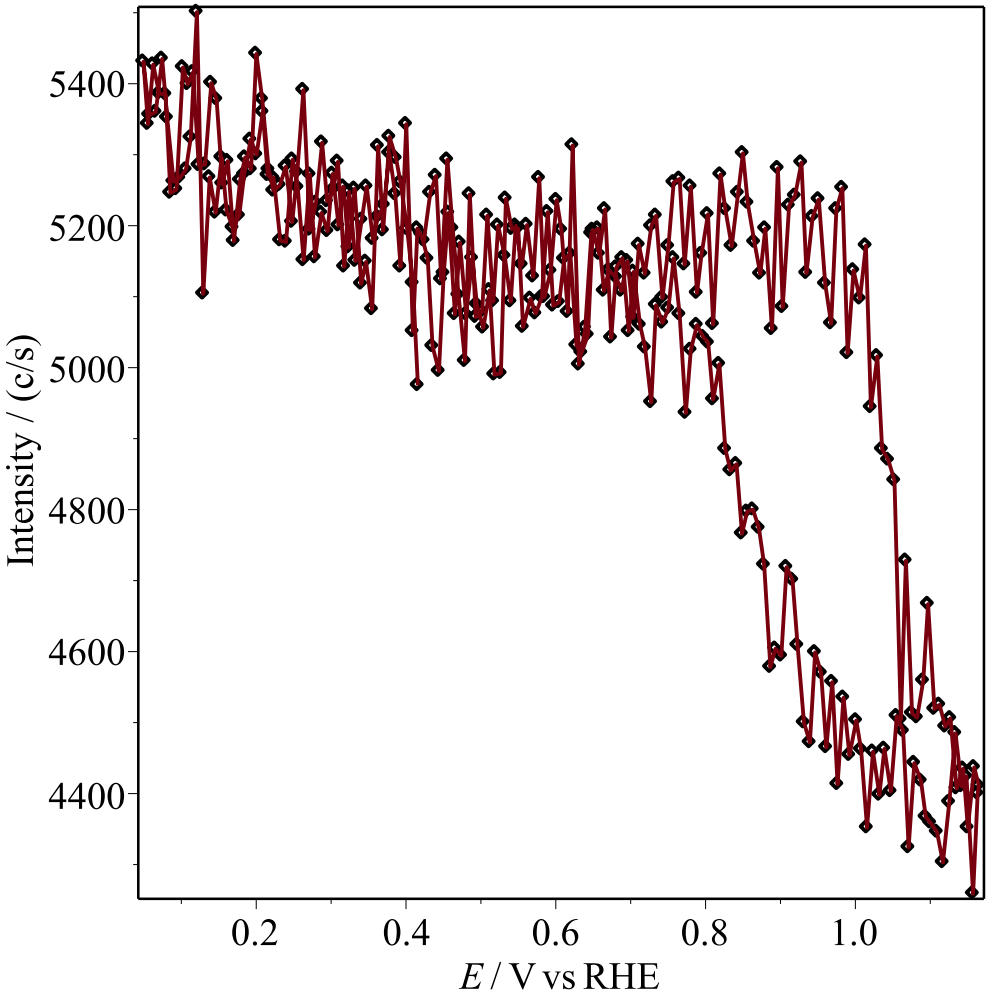

Figure 3.33: Pt(111) X-ray intensity after fast scans. Sweep rate as 20 mV/s. Data from EC file 25 at the CH5700 beamtime at ID31 at the ESRF in November 2020.

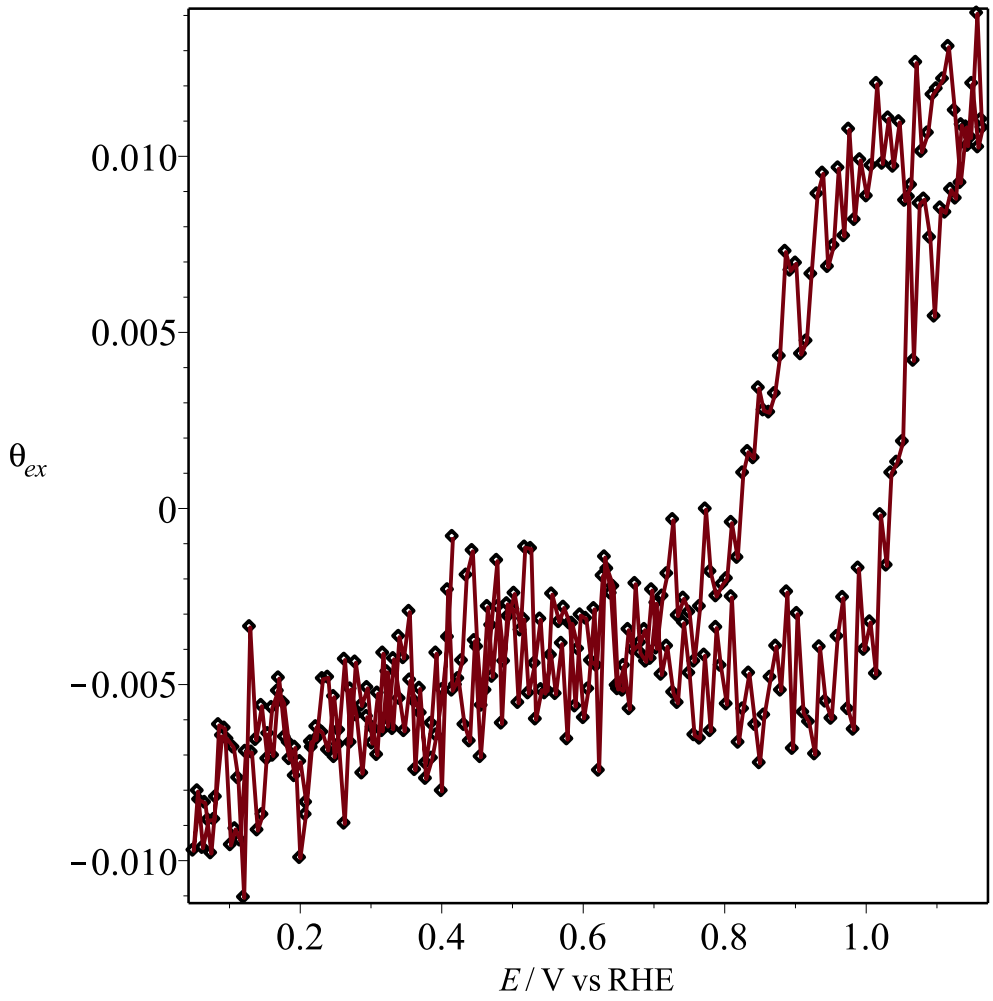

Figure 3.34: Normalized Pt(111) X-ray intensity after fast scans. Sweep rate as 20 mV/s. Data from EC file 25 at the CH5700 beamtime at ID31 at the ESRF in November 2020.

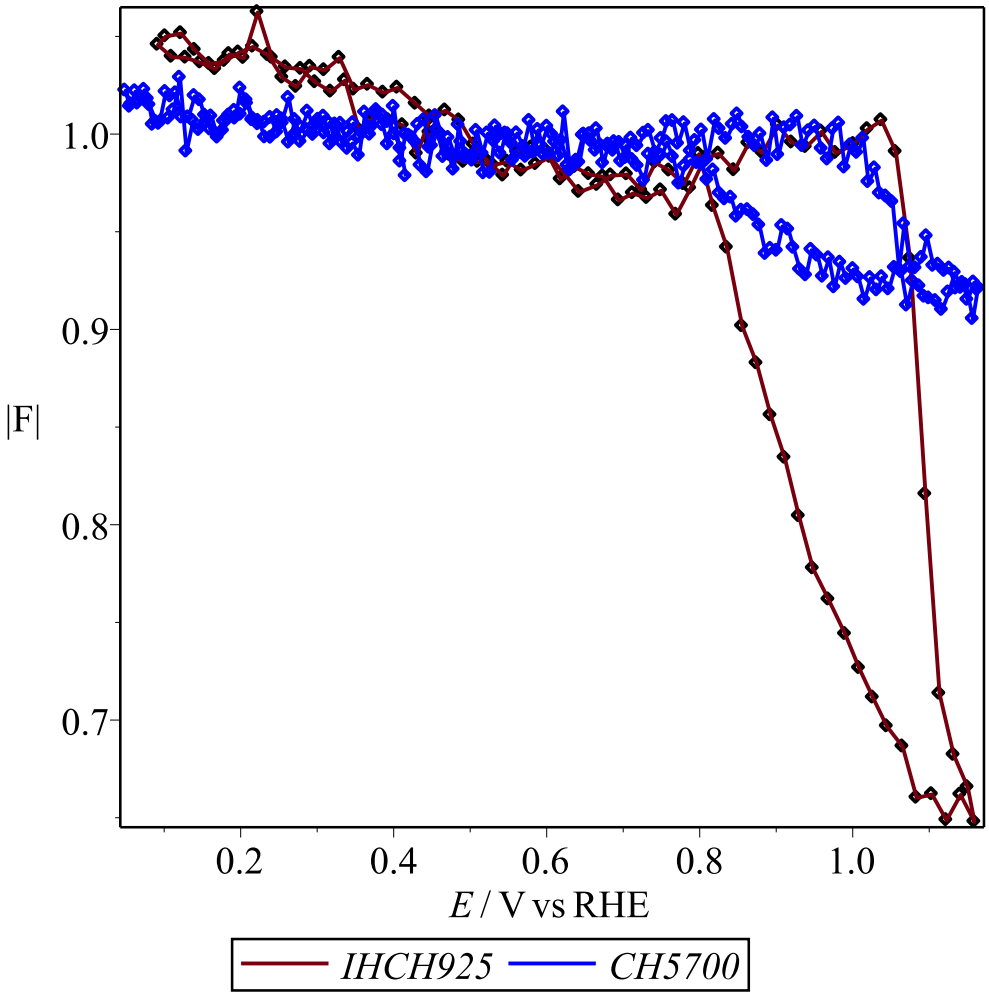

Figure 3.35: Pt(111) X-ray voltammogram after fast scans(blue) vs under normal conditions(brown). Sweep rate as 20 mV/s. Blue data from EC file 25 at the CH5700 beamtime at ID31 at the ESRF in November 2020. Brown data from run 664 at the IHCH925 beamtime in February 2015.

3.2 Pt(100) Cyclic Voltammetry and X-ray

In this section, the data treatment of Pt(100) cyclic voltammetry and X-ray is discussed, as the integrations of CVs, the θ_e vs θ_{ex} plot from CVs and X-ray, and potential step experiments.

3.2.1 Pt(100) Integrations of Cyclic Voltammetry

In this subsection, Pt(100) cyclic voltammogram is baseline corrected and integrated to get the coverage of electrons, θ_e, of different peaks introduced by section 2.2.3.

Voltammogram from CH5523 prep

The voltammogram in Fig. 3.36 is from the prep time at the CH5523 beamtime.

There are two large peaks on the top in the anodic process, and two corresponding peaks on the bottom in the cathodic process. The anodic peak from 0.2 to 0.7 V is the H/OH mixed anodic peak for the adsorption of OH and the desorption of H. It is the combination of one large sharp peak from 0.2 to 0.5 V and another small broad peak from 0.5 to 0.7 V. The cathodic peak from 0.22 to 0.45 V is the corresponding H/OH mixed cathodic peak for the adsorption of H and the dissociation of OH.

The sharp peak from 0.9 to 1.1 V and the flat high stage from 1.1 to 1.219 V is the Pt oxide peak and the start of further oxidation. From 1.219 V to 1.16 V is the "roll-back" part, in which the potential decreases but oxidation still happens. The corresponding cathodic Pt reduction peak is from 0.55 to 1.16 V.

Before 0.2 V, there are flat parts on both anodic and cathodic sides. Between the H/OH mixed peak and Pt oxide peak, there are also flat parts on both anodic and

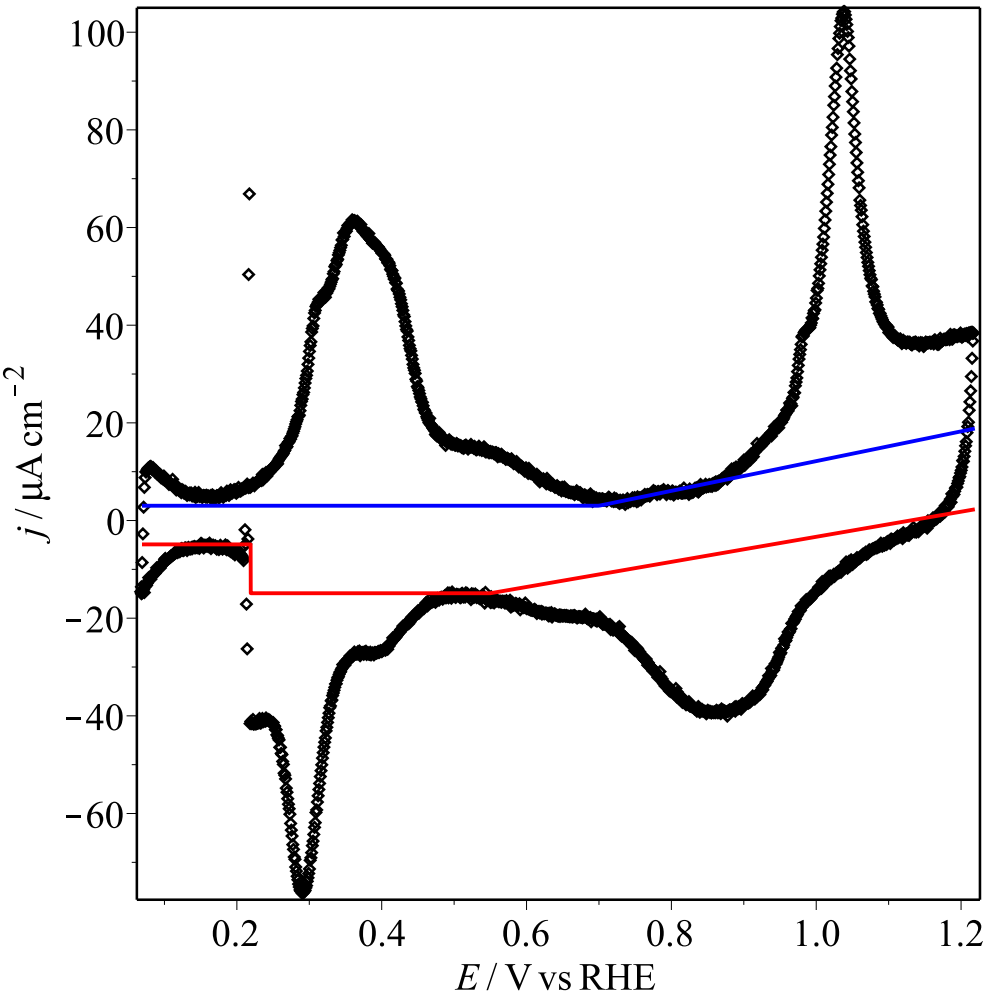

Figure 3.36: Pt(100) cyclic voltammogram in 0.1 M $HClO_4$. Sweep rate as 50 mV/s. Data from the prep time at the CH5523 beamtime in September 2018.

cathodic sides, which ate not affected by reactions for both the H/OH mixed peak and the Pt oxide peak. The anodic flat part is from 0.7 to 0.9 V, and the cathodic flat part is from 0.45 to 0.55 V.

Baseline Correction of Voltammogram

The baselines are shown in Fig. 3.36. They are made by horizontal lines on the left side to remove the large double layer charges, and lines with small positive slope on the right side to remove the effect of H_2O_2 from X-ray beam damage. After the baseline correction, the voltammogram can more accurately give the charge density of the H/OH mixed peaks and oxide peaks.

For the anodic baseline before 0.7 V, to remove the double layer charging, a horizontal line to cross the lowest point of the flat parts is made.

For the anodic baseline after 0.7 V, fit the flat part from 0.7 to 0.9 V to make a straight line with a small positive slope; this linear part isn't affected by reactions of oxide peak and H/OH mixed peak but only double layer charges and X-ray beam damage.

Then comes the baselines of the corresponding cathodic peaks. For the cathodic baseline on the left side before 0.55 V, the cycle starts and ends at 0.22 V. Because the cycle doesn't close on itself at 0.22 V, the cathodic horizontal baselines of 0.069 V to 0.22 V and 0.22 to 0.55 V are made separately to cross the highest points of both parts.

For the cathodic baseline after 0.55 V, draw a line with similar slope to the corresponding anodic one, and connected to the left endpoint as 0.55 V, and right side as 1.16 V, which is the cut-off point between the Pt reduction peak and the

"roll-back" part.

After the data points are baseline corrected, the voltammogram shows as Fig. 3.37. Then the charge density is calculated from the integration of current density (j) vs potential (E) over the sweep rate, also the coverages is from it by dividing 208.08 μC/cm^{-2} as in Section 2.2.2.

Also, voltammogram with only horizontal baselines is shown as Fig. 3.38 to compare with previous baseline correction. The horizontal baselines are same as left half part of previous baseline correction in Fig. 3.36.

Peak charges

The voltammogram doesn't close on itself, showing that the Pt oxide production is irreversible, and therefore we don't expect the overall anodic and cathodic charges to be equal. But given that the dissolution charge expected to be a small percentage of the oxide charge, comparison of the anodic and cathodic charges tells about the irreversibility of the oxide.

The following is the area and coverage of different anodic peaks in Pt(100) cyclic voltammogram, also the coverages are compared with data from other beamtimes in Table. 3.2.

If CV data are corrected by only horizontal baselines in Fig. 3.38, the baseline corrected Pt oxide peak has charge density as 247.5 μC cm^{-2} = 1.19 ML, and the "roll-back" part has charge density as 27.3 μC cm^{-2} = 0.13 ML. However, the corresponding raw cathodic peak for Pt oxide peak has baseline corrected density as 81.5 μC cm^{-2} = 0.39 ML, much lower than 1.31 ML = 1.19 ML + 0.13 ML from anodic oxide peak and "roll back" part, so baselines with small slopes seems to be

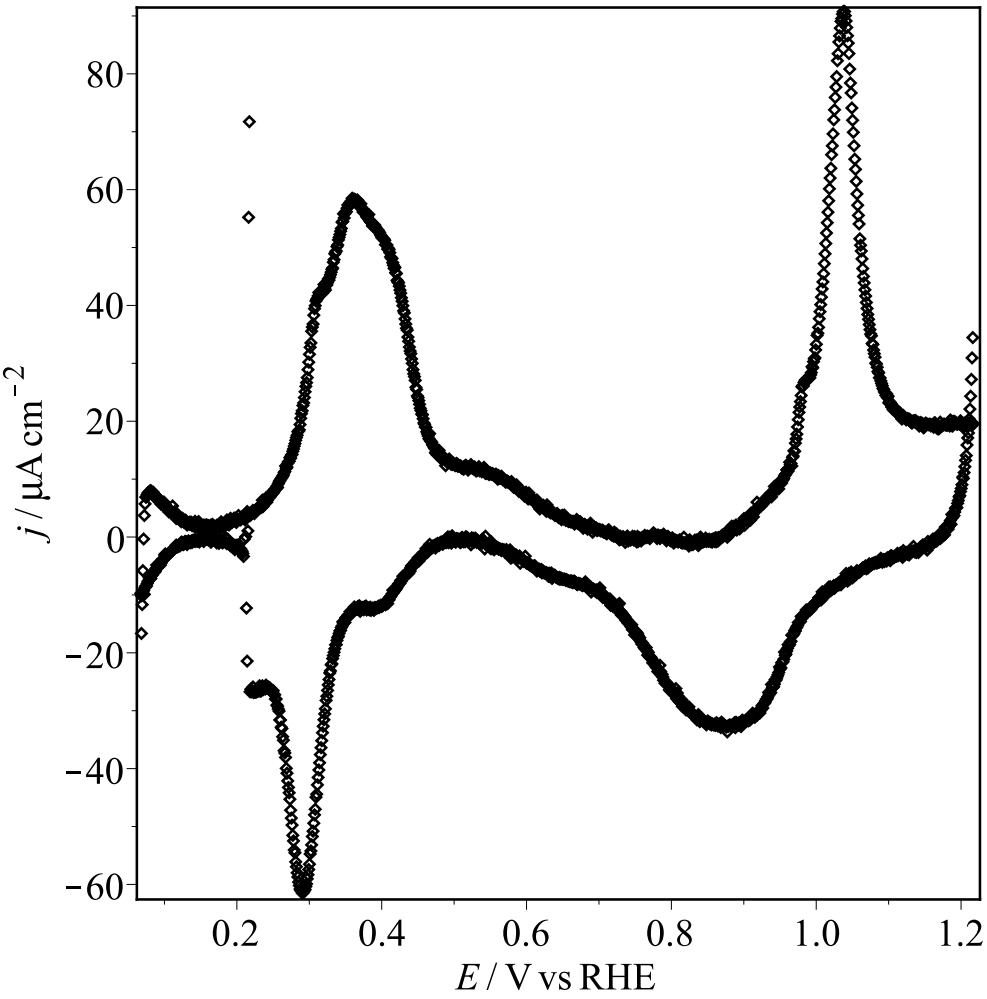

Figure 3.37: Baseline Corrected Pt(100) cyclic voltammogram in 0.1 M $HClO_4$. Sweep rate as 50 mV/s. Data from the prep time at the CH5523 beamtime in September 2018.

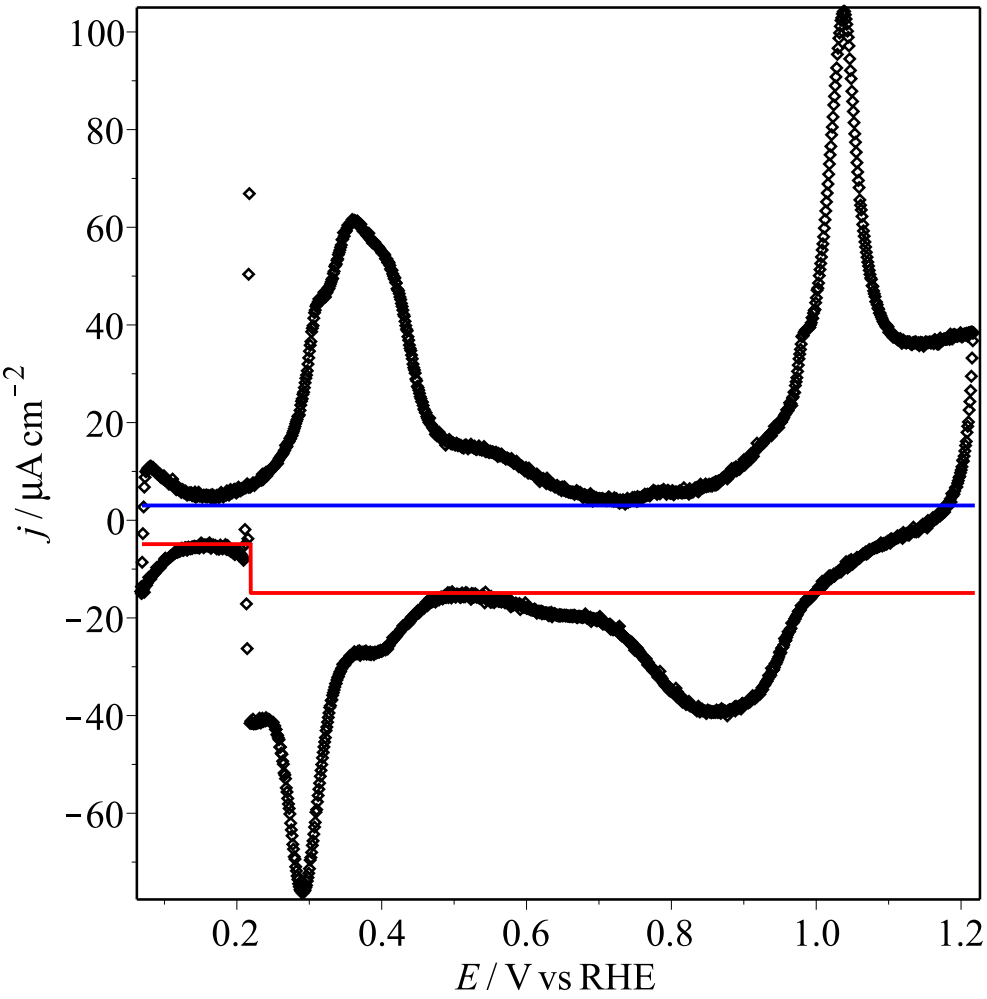

Figure 3.38: Pt(100) cyclic voltammogram in 0.1 M $HClO_4$ with horizontal baseline. Sweep rate as 50 mV/s. Data from the prep time at the CH5523 beamtime in September 2018.

more suitable for Pt oxide peak of Pt(100).

Beamtime	CH5523		IHCH925		CH5918	
EC File name	prep time		run 664		Pt100_07	
Corrected?	No	Yes	No	Yes	No	Yes
Range / V	0.069—1.219		0.054—1.174		0.054—1.174	
Total Anodic / ML	2.55	1.91	3.23	1.99	3.03	2.10
Total Cathodic / ML	2.40	1.45	2.61	1.86	2.81	1.97
H UPD & OH_{ads} / V	0.17—0.7		0.2—0.7		0.2—0.7	
H UPD & OH_{ads} / ML	1.13	0.98	1.34	0.96	1.15	0.87
Oxide / V	0.7—1.219		0.9—1.174		0.9—1.174	
Oxide / ML	1.28	0.85	1.44	0.95	1.66	1.19
Roll-back / V	1.16—1.219		1.15—1.174		1.15—1.174	
Roll-back / ML	0.04	0.04	0.09	0.04	0.08	0.05
H_{ads} & OH_{des} / V	0.069—0.5		0.054—0.45		0.054—0.45	
H_{ads} & OH_{des} / ML	0.88	0.55	1.13	0.82	1.33	0.84
Reduce / V	0.5—1.16		0.6—1.15		0.6—1.15	
Reduce / ML	1.26	0.85	1.21	1.00	1.25	1.09

Table 3.2: Coverages of peaks from Pt(100) cyclic voltammograms in 0.1 M $HClO_4$

3.2.2 Pt(100) θ_e vs θ_{ex} Plot

In this subsection, Pt(100) cyclic voltammogram is baseline corrected then integrated following Section 3.2.1, then it is compared with corresponding X-ray data to get e^-s transferred by place-exchanged Pt surface atoms.

Cyclic Voltammetry Data Treatment

The X-ray voltammogram in Fig. 3.39 is from run 664 at the IHCH925 beamtime in February 2015; the same data as in Figure 1c in Ref [70]. During this cycle, the potential starts at the minimum potential 0.054 V, then increases to the maximum

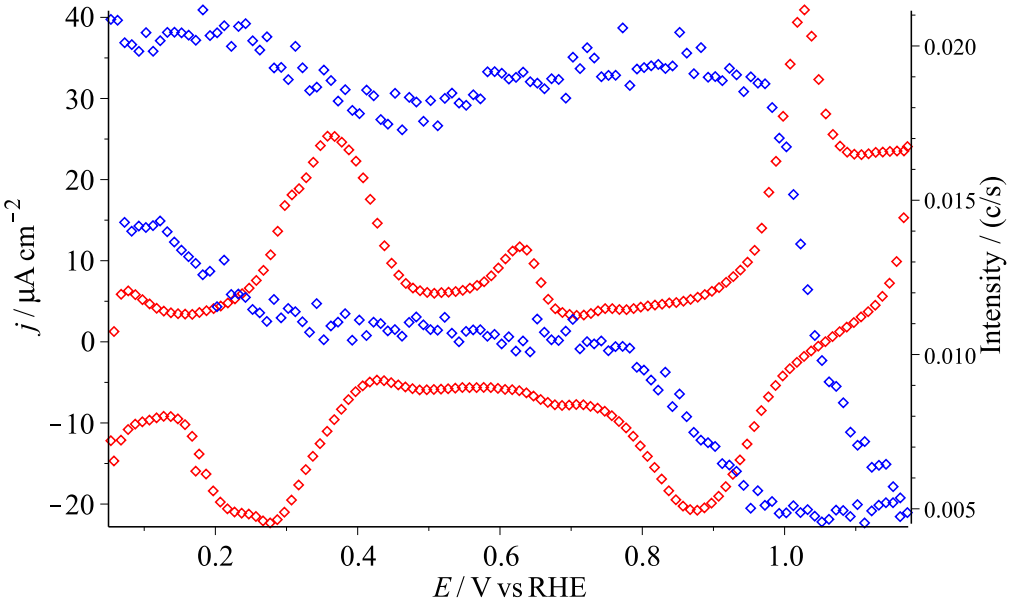

Figure 3.39: Pt(100) X-ray voltammogram. Sweep rate as 20 mV/s. Source Data from run 664 at the IHCH925 beamtime in February 2015.

potential 1.174 V, last drops back to the minimum potential 0.054 V. There are large and small anodic peaks from 0.2 to 0.7 V as H UPD peaks, and a large peak from 0.9 to 1.1 V as the oxide peak. There are flat parts between 0.1 and 0.2 V, also between 0.7 and 0.9 V. The cathodic peaks corresponding to the anodic peaks are from the lower limit potential 0.054 V to 0.4 V, and from 0.6 to 1.0 V. The flat cathodic part is from 0.4 to 0.6 V.

For the voltammogram in Fig. 3.40, the baseline is obtained in the same way as in the previous Section 3.2.1. The voltammogram after the baseline correction is shown in Fig. 3.41.

The coverages of peaks are shown and compared with data from other beamtimes in Table. 3.2. Because the cycle starts and ends at the minimum potential 0.054 V, it looks like to close on itself, so the overall anodic and cathodic charge density can

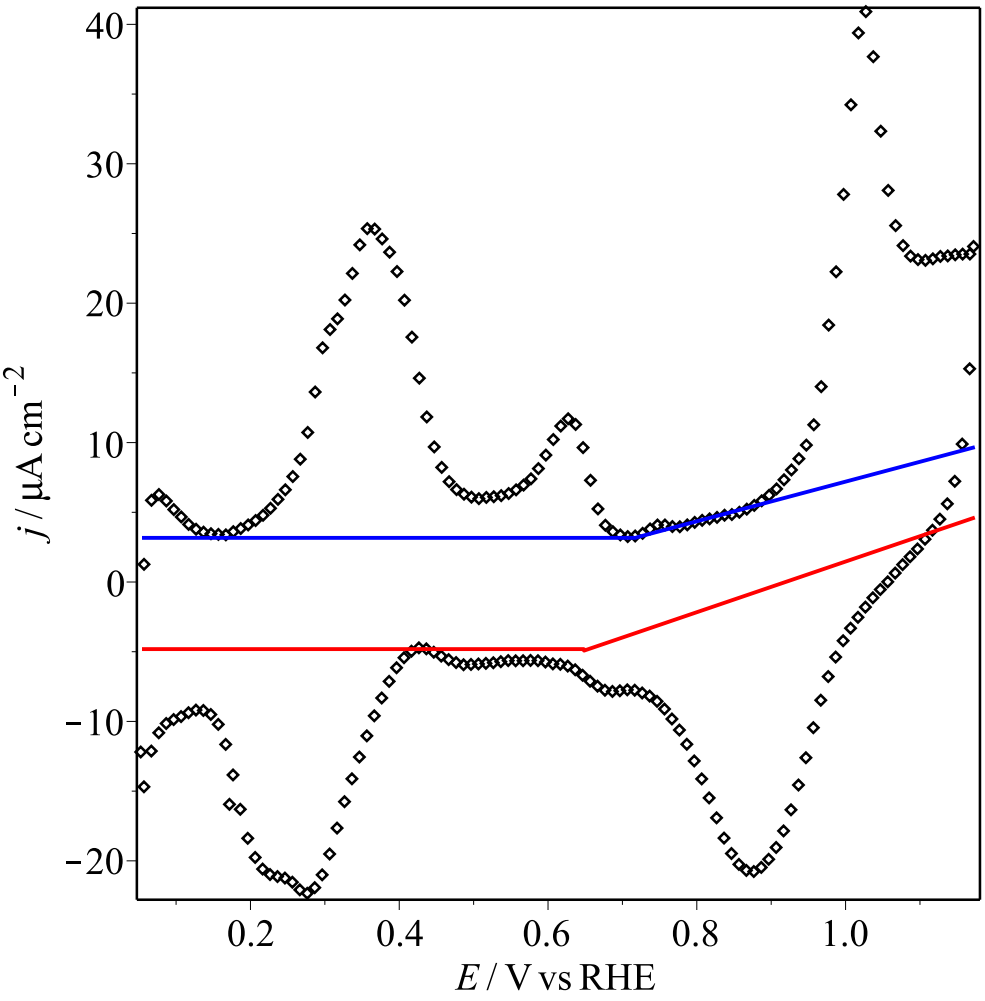

Figure 3.40: Pt(100) cyclic voltammogram. Sweep rate as 20 mV/s. Source Data from run 664 at the IHCH925 beamtime in February 2015.

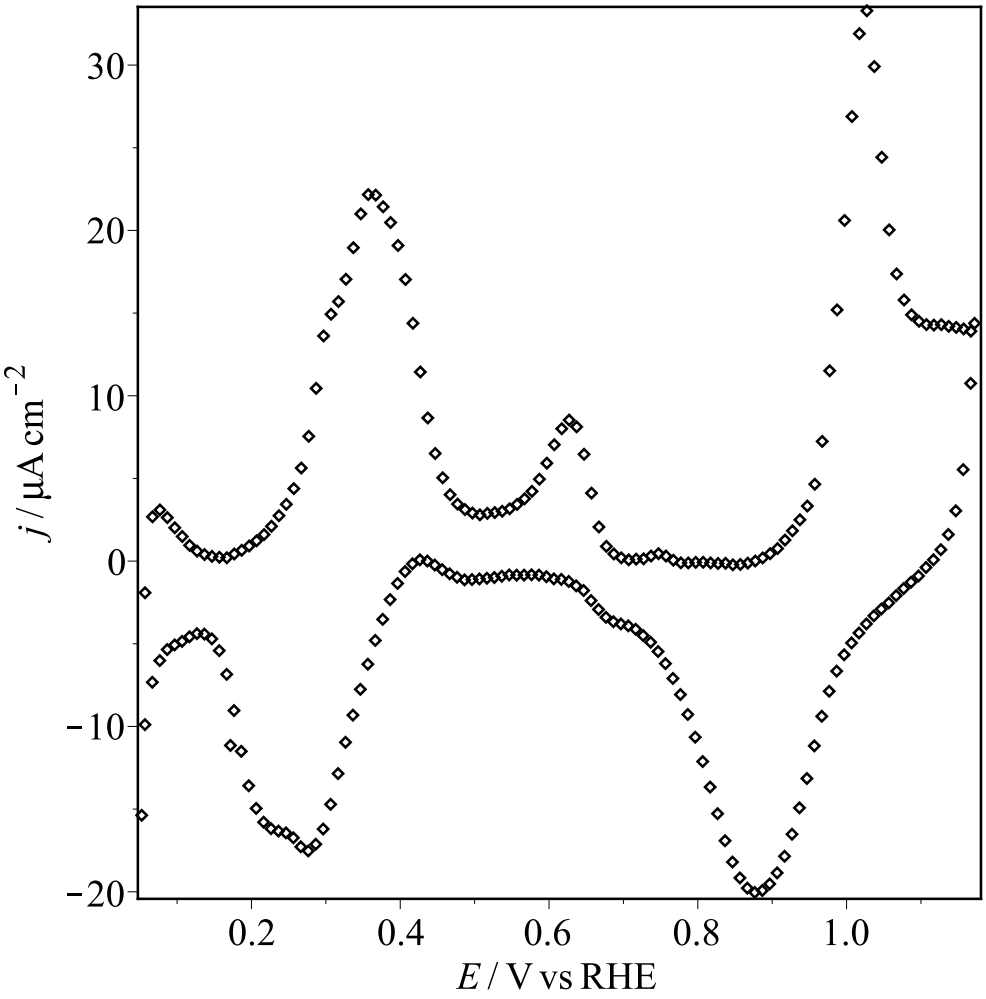

Figure 3.41: Baseline corrected Pt(100) cyclic voltammogram. Sweep rate as 20 mV/s. Source Data from run 664 at the IHCH925 beamtime in February 2015.

be compared.

Also, if the voltammogram is corrected by just horizontal baselines as Fig. 3.42, similar to Section 3.2.1, the baseline corrected charge density of Pt reduction, 0.53 ML is much lower than 1.39 ML = 1.24 ML + 0.15 ML of Pt oxide peak and "roll-back" part. Also the overall cathodic charge density, 1.39 ML is much lower than 2.46 ML of the anodic one.

X-ray Data Treatment

The X-ray voltammogram in Fig. 3.43 is from the same experiment as Fig. 3.39. The curve slowly drops from lowest potential to 0.97 V with some noise. Then it sharply goes down from 0.97 V till the highest potential, 1.17 V. Also for the cathodic processes, the curve goes up sharply after briefly staying flat until 0.95 V, and then goes flat under 0.7 V, but with much lower than original intensity.

To turn the X-ray data into θ_{ex}, the intensities are normalized by equation $\theta_{ex} = 0.5007(1 - \sqrt{\frac{I}{I_{0.9V}}})$ from Section 2.3.4, with the reference point the intensity at 0.9 V in anodic sweep, which is the flat part in Fig. 3.41. The normalized spectrum is shown in Fig. 3.44.

Coverages θ_e vs θ_{ex} from CV and X-ray

The following is θ_e vs θ_{ex} for the oxidation of Pt(100) from EC and X-ray data.

The figure of θ_e vs θ_{ex} for the anodic process is shown in Fig. 3.45, and there are 21 points in the diagram, which were in the peak between 0.97 and 1.17 V in X-ray figure as in Fig. 3.43.

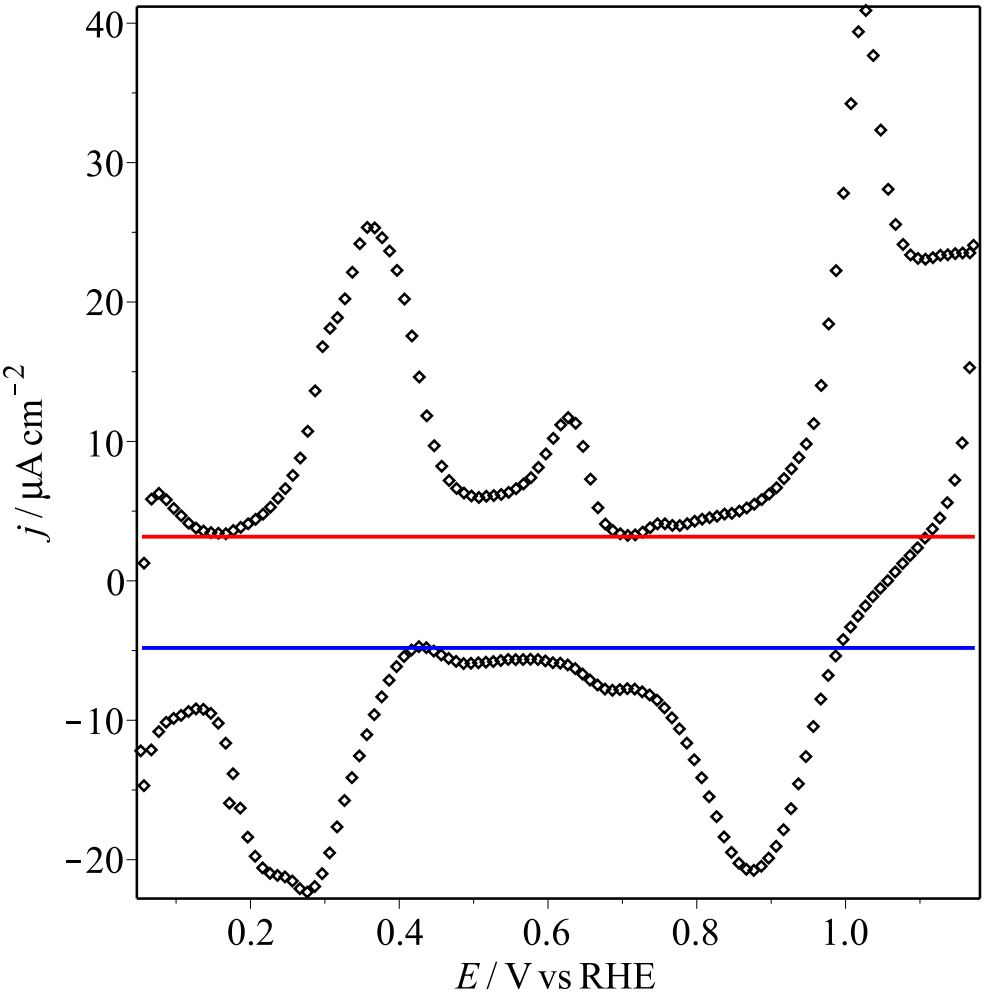

Figure 3.42: Pt(100) cyclic voltammogram with only horizontal baselines. Sweep rate as 20 mV/s. Source Data from run 664 at the IHCH925 beamtime in February 2015.

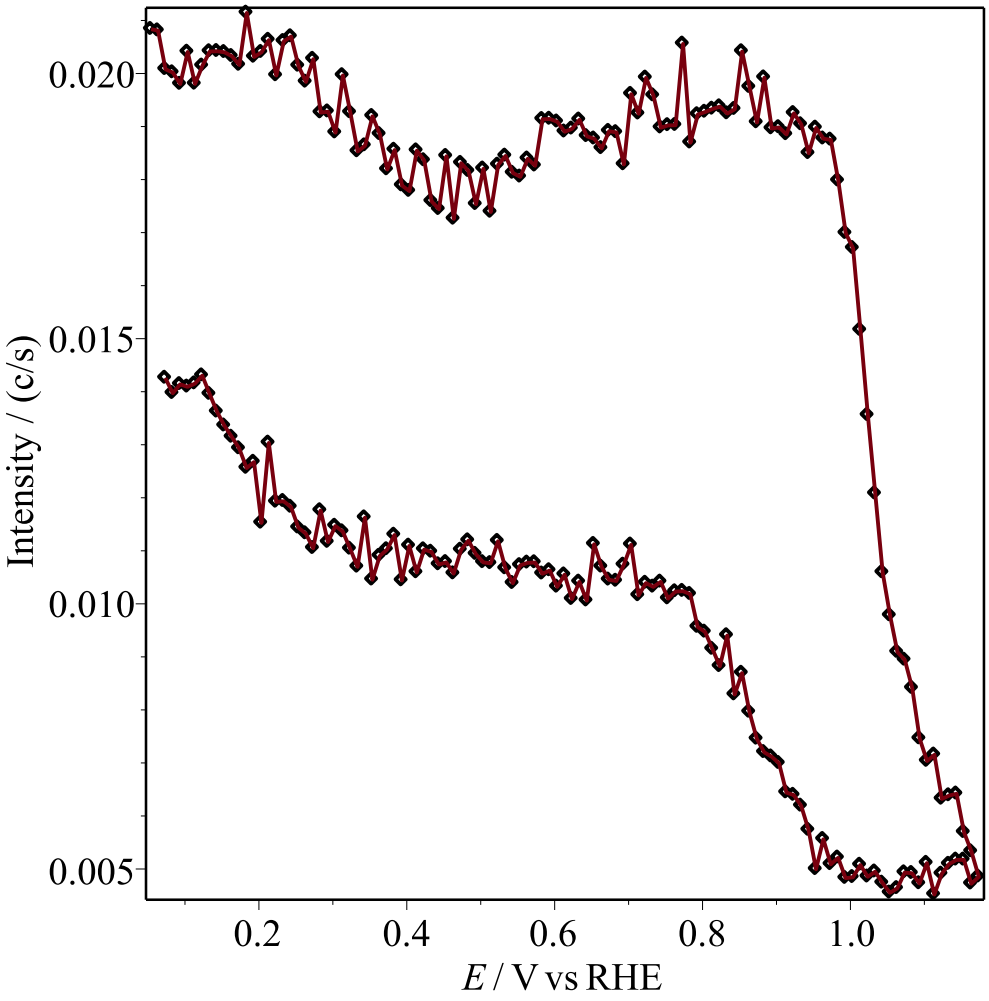

Figure 3.43: (1 1 2.1) Pt(100) X-ray intensity. Sweep rate as 20 mV/s. Data from run 664 at the IHCH925 beamtime in February 2015.

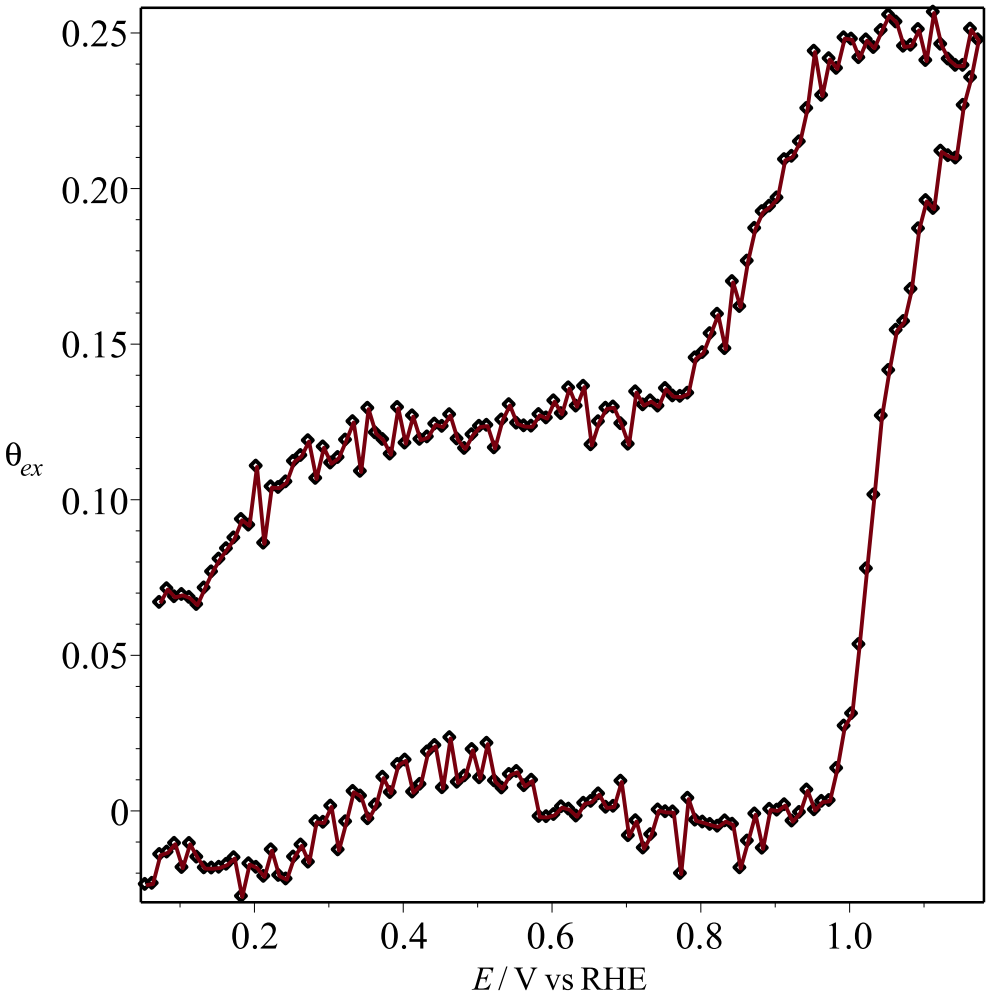

Figure 3.44: Normalized (1 1 2.1) Pt(100) X-ray density. Sweep rate as 20 mV/s. Data from run 664 at the IHCH925 beamtime in February 2015.

Using the same treatment of data as for Pt(111), θ_e for θ_{ex} points are found by matching potentials from X-ray data to θ_e vs potential plot.

The curve in Fig. 3.45 looks similar to a straight line, so linear least squares was used to fit the data, and the slope of the line was 3.69.

The following is θ_e vs θ_{ex} for reduction process of Pt(100) from cyclic voltammetry and X-ray data.

The figure of θ_e vs θ_{ex} of the cathodic process is shown in Fig. 3.46, and there are 26 points in the diagram, which were inside the cathodic sharp part between 0.95 and 0.7 V in X-ray figure as the Fig. 3.43. It was treated in the same way as the anodic one.

The curve in Fig. 3.46 looks similar to a straight line, and linear least squares fit gave the slope as 8.00. This cathodic slope was very different to the anodic one, which was 3.69. In Fig. 3.43, the intensity of the cathodic flat part before 0.7 V is very different from the anodic flat part before 0.97 V. This is very different from the X-ray diagram for Pt(111) in Fig. 3.6, where the two intensities are very close.

Also, the θ_e vs θ_{ex} of anodic process without baseline correction of CV data is analyzed and shown in Fig. 3.47. The curve is similar to Fig. 3.45 with baseline correction but with much higher slope as 5.20.

Discussion on Extraction of Pt(100)

The graph of θ_e vs θ_{ex} with segmented baseline correction for oxidation and reduction processes of Pt(100) from previous sections are shown in Fig. 3.45 and 3.46. The slopes of Pt(100) are 3.69 and 8.00, which are much larger than 2.70 of Pt(111). This is mainly because of the different way of extraction as Fig. 2.14 shows in Section

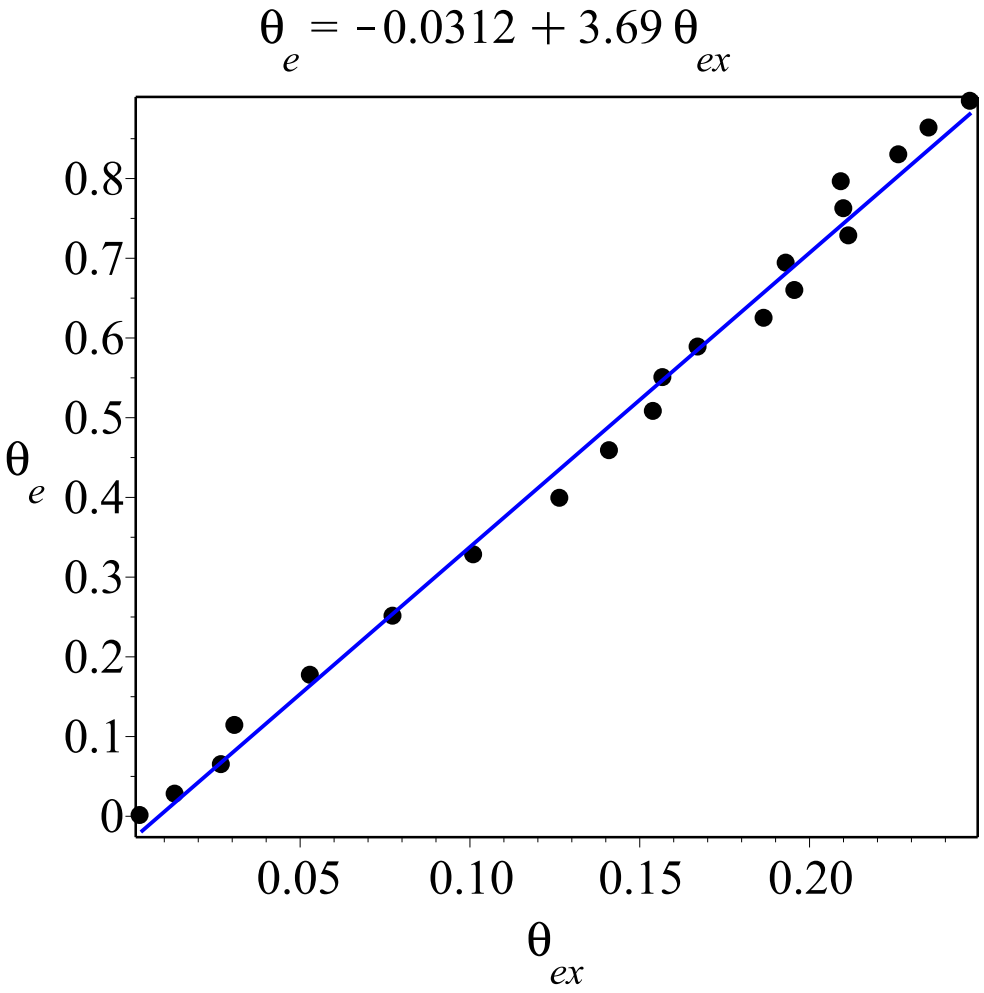

Figure 3.45: Anodic θ_e vs θ_{ex} for Pt(100) with segmented baseline correction. Data from run 664 at the IHCH925 beamtime in February 2015.

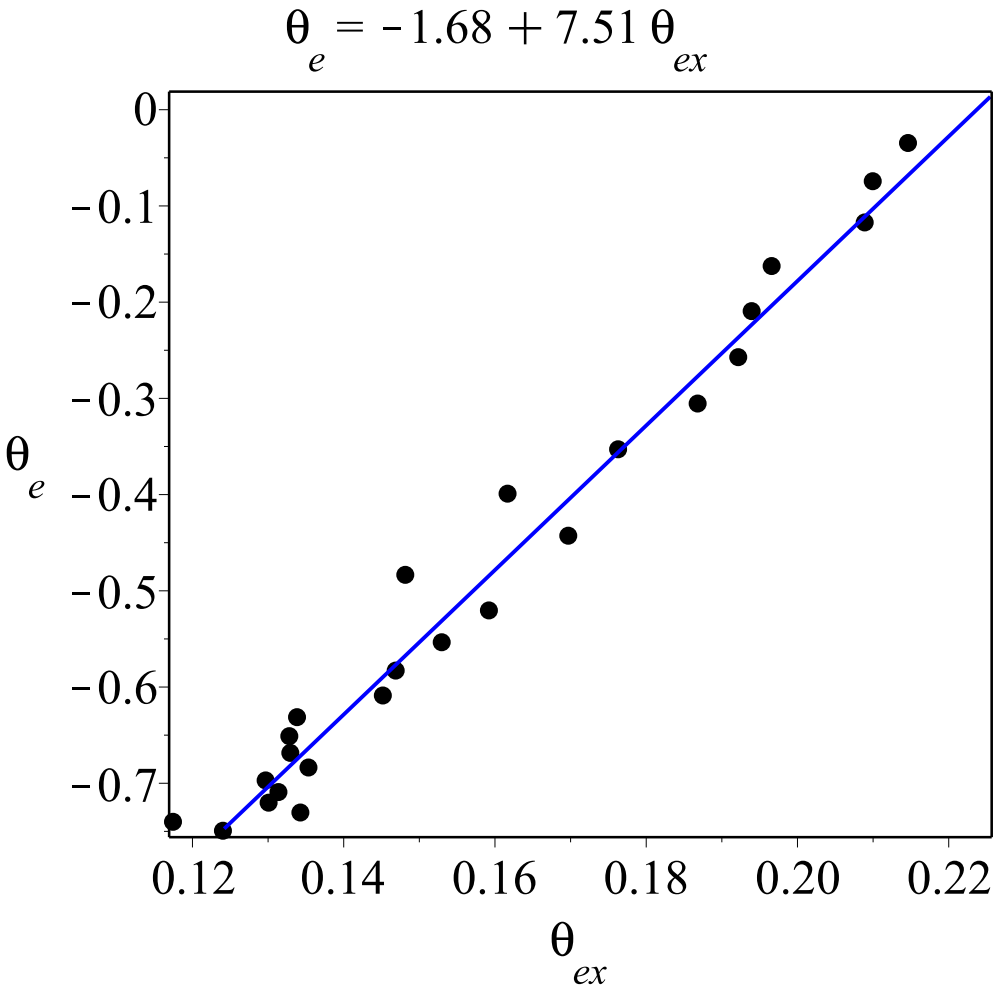

Figure 3.46: Cathodic θ_e vs θ_{ex} for Pt(100) with segmented baseline correction. Data from run 664 at the IHCH925 beamtime in February 2015.

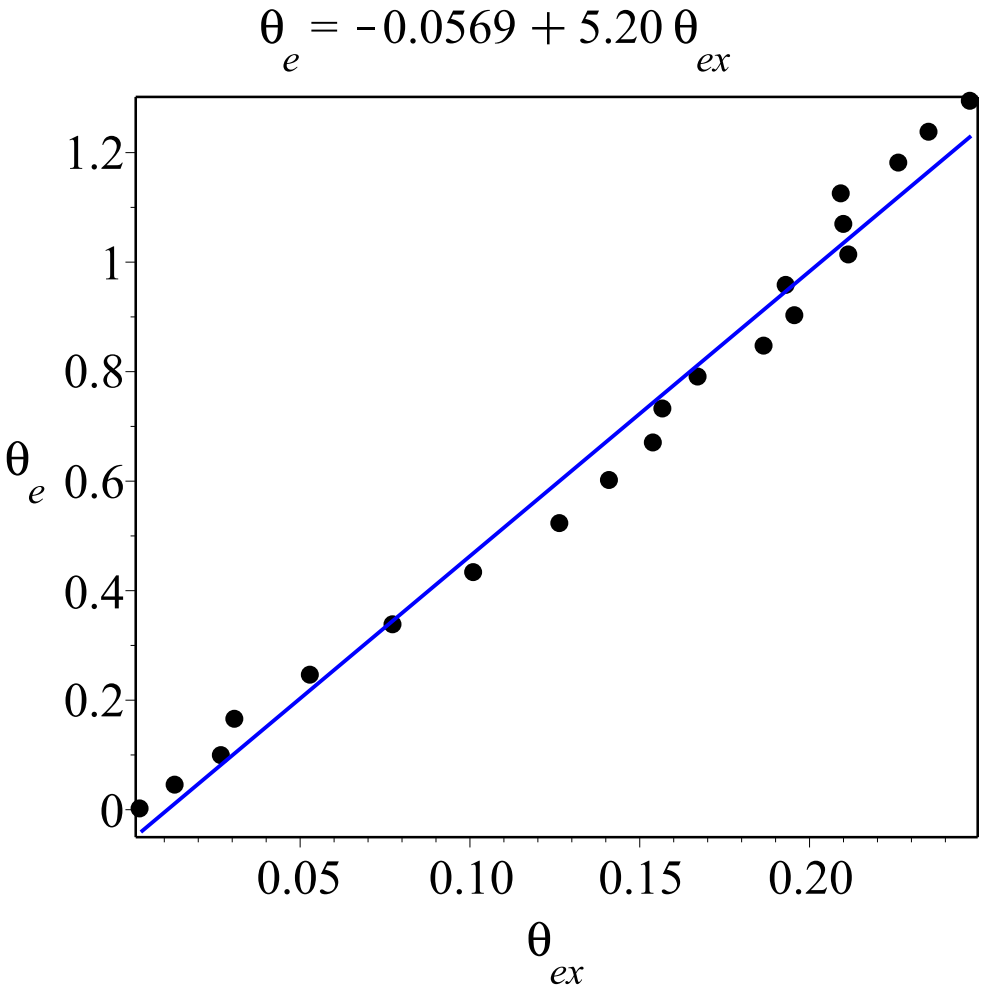

Figure 3.47: Anodic θ_e vs θ_{ex} for Pt(100) without baseline correction. Data from run 664 at the IHCH925 beamtime in February 2015.

2.2.4. Also, the Pt extraction of Pt(100) starts at 1.0 V, same as O_{ads} formation, much earlier than Pt(111).

For the final θ_e, it's 0.95 ML from CV and 0.90 ML from θ_e vs θ_{ex}, a little different because the potential range of the first one starts from 0.9 V, the start point of oxide peak; but the potential range of the later one starts from ∼0.97 V, the first point before θ_{ex} rises up. For the coverage of extracted Pt, or θ_{ex}, it's 0.25 ML for Pt(100) in Fig. 3.45, much higher than 0.066 ML for Pt(111) in Fig. 3.8, and this is explained by the stripe model for the oxide shown in Section 2.2.4 from Fuchs's research [70]. To explain θ_{ex} 0.25 ML, θ_e 0.95 ML, and the anodic slope is 3.7, the possible reaction below is suggested, for each 12 surface Pt atoms:

$$3 \times (\mathrm{OH(ads)} \rightarrow \mathrm{O(ads)} + \mathrm{H^+} + \mathrm{e^-}) \tag{3.10}$$

$$3 \times (\mathrm{Pt} + \mathrm{OH(ads)} + \mathrm{H_2O} \rightarrow \mathrm{PtO_2(ex)} + \mathrm{Pt} + 3\mathrm{H^+} + 3\mathrm{e^-}) \tag{3.11}$$

If there are higher θ_{ex} and lower anodic slope, there are more extracted PtO_2 formed and fewer adsorbed O formed.

The reaction of Pt(100) oxide peak forms O_{ads} atoms and long chains with PtO_2 units as shown in Fig. 3.48. It is based on research of Fuchs et al in Fig. 2.14, and has 1/4 ML θ_{ex}. In Fig. 3.48, for each 12 Pt(100) surface atoms, 3 Pt atoms are extracted to Pt_nO_{2n} long chains, 3 adsorbed oxygen is formed, and 12 e^-s are transferred, so θ_e is 1 ML, close to 0.95 ML, and θ_{ex} is 1/4 ML, close to 0.25 ML.

If the CV isn't baseline corrected, θ_e is 1.44 ML from CV, and 1.24 ML from θ_e vs θ_{ex}. Unlike the segmented baseline corrected one, the difference is very large as 0.20

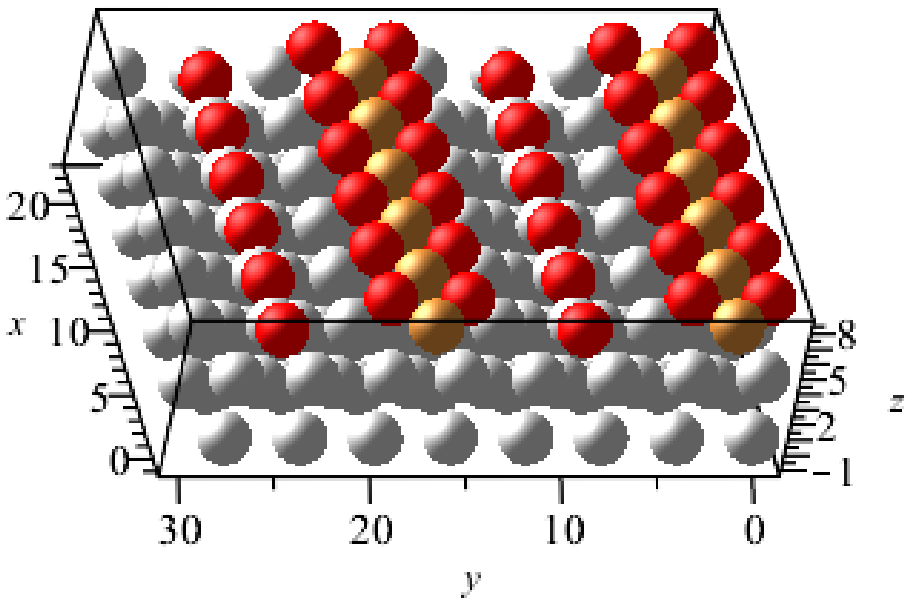

Figure 3.48: Model of Extracted Pt(100) from DFT calculations [70]. The orange balls are extracted Pt atoms, the red balls are O atoms, and the grey balls are Pt surface atoms.

ML. The coverage of Pt reduction peak is 1.13 ML, much lower than the anodic θ_e. θ_e 1.24 ML is close to 5/4 ML, and θ_{ex} is 0.25 ML, close to 1/4 ML, so the reaction is shown as below, for each 16 surface Pt atoms:

$$4 \times (\mathrm{OH(ads)} \rightarrow \mathrm{O(ads)} + \mathrm{H^+} + \mathrm{e^-}) \tag{3.12}$$

$$1 \times (4\mathrm{Pt} + 4\mathrm{OH(ads)} + 6\mathrm{H_2O} \rightarrow \mathrm{Pt_4O_{10}(ex)} + 16\mathrm{H^+} + 16\mathrm{e^-}) \tag{3.13}$$

Here the products are 1/4 ML O_{ads}, and 1/16 ML short extracted Pt chain with 4 Pt_{ex} atoms, like shown in Fig. 3.49.a. The O atoms in Fig. 3.49 are lower than extracted Pt atoms because they are connected with other Pt atoms on the surface as Fuchs's model in Section 2.2.4. The Pt extraction may happen in another way, for each 16 surface Pt atoms:

$$4 \times (\mathrm{OH(ads)} \rightarrow \mathrm{O(ads)} + \mathrm{H^+} + \mathrm{e^-}) \tag{3.14}$$

$$1 \times (4\mathrm{Pt} + 4\mathrm{OH(ads)} + 6\mathrm{H_2O} \rightarrow \mathrm{Pt_3O_8(ex)} + \mathrm{PtO_2(ex)} + 16\mathrm{H^+} + 16\mathrm{e^-}) \tag{3.15}$$

Here the products are 1/4 ML O_{ads}, 1/16 ML short extracted Pt chain with 3 Pt_{ex} atoms, and 1/16 ML independent extracted PtO_2, like shown in Fig. 3.49.b.

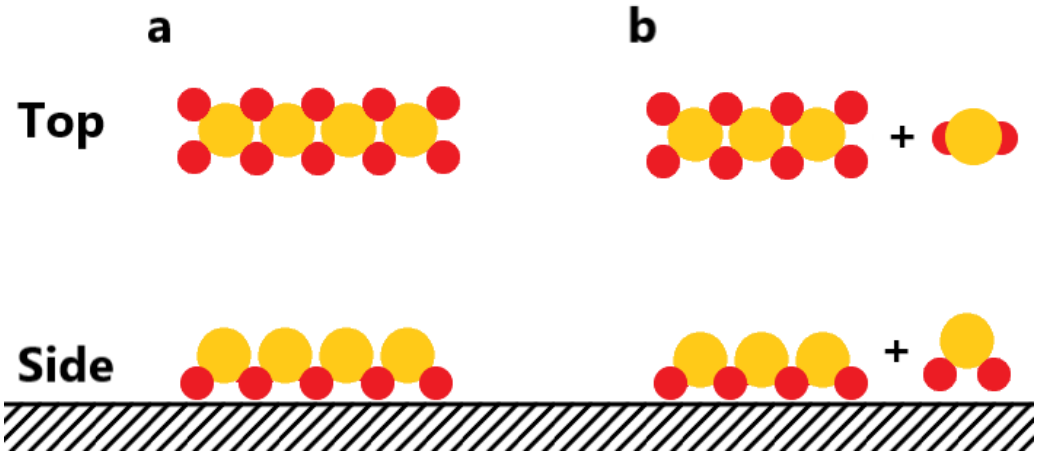

Figure 3.49: Models of Extracted Pt(100). The orange balls are Pt atoms, and the red balls are O atoms. In (a) the product is short chain with 4 extracted Pt atoms. In (b) the products are short chain with 3 extracted Pt atoms and equal quantity of independent extracted PtO_2.

3.2.3 Pt(100) θ_e vs θ_{ex} Plot with 11 cycles

In this subsection, Pt(100) cyclic voltammetry is continued for multiple cycles as the surfaces degrades. After baseline correction, integrated and comparison with corresponding X-ray data, the e^-s transferred per extracted Pt surface atoms are calculated as in section 3.2.2.

Cyclic Voltammetry Data Treatment

Cyclic voltammetry data is from EC file Pt100_07 at the CH5918 beamtime at ID31 at the ESRF in July 2021. The CVs run 19 cycles to 0.824 V, then 11 cycles to 1.174 V vs RHE at 20 mV/s. The cyclic voltammograms for different cycles are shown in Fig. 3.50.

In Fig. 3.50, as cycle number increases, the top of the H/OH mixed peak before

0.7 V slowly shifts from 0.31 V to 0.36 V, the Pt oxide peak at 1.01 V sharply decreases, and an extra peak at 0.83 V appears and increases.

All cyclic voltammetry data are baseline corrected by the method in Section 3.2.1 shown as the first cycle in Fig. 3.51. For the H/OH peak before 0.7 V, it is corrected by horizontal baseline to remove double layer charges. For the part after 0.7 V, including the linear section before oxide peak, the Pt oxide peak and the high flat stage after oxide peak, baseline linear fitted from the linear section with small positive slope is needed to remove both double layer charges and H_2O_2 from X-ray beam damage. Then the data of current density vs potential is integrated and divided by sweep rate 20 mV/s to get charge densities (σ), which can be converted to θ_e by dividing by the charge density for 1 ML Pt(100) surface atoms, 208.1 μC cm^{-2}. The θ_e of the whole Pt oxide peak after 0.9 V for each cycle with segmented baseline correction is shown as red points in Fig. 3.52; it linearly decreases from 1.24 ML to 0.88 ML. θ_e without baseline correction is shown as the purple points in Fig. 3.52; it linearly decreases from 1.74 ML to 1.27 ML. The coverages of peaks for first cycle are compared with data from other beamtimes in Table. 3.2.

X-ray Data Treatment

X-ray data is from X-ray file Pt100_03 at the CH5918 beamtime at ID31 at the ESRF in July 2021. All raw potentials are turned to RHE as section 2.1.3 introduced, and all X-ray intensity was corrected by removing the background intensity. It runs 11 cycles to 1.174 V vs RHE at 20 mV/s. The X-ray intensities for different cycles are shown as Fig. 3.53, which is corresponding to the cyclic voltammogram in Fig. 3.50.

The X-ray intensities in Fig. 3.53 are translated to θ_{ex} by equation $\theta_{ex} = 0.5007 \times (1 - \sqrt{I/I_{0.9V}})$ from section 2.3.4, in which $I_{0.9V}$ is the intensity of anodic 0.9 V in

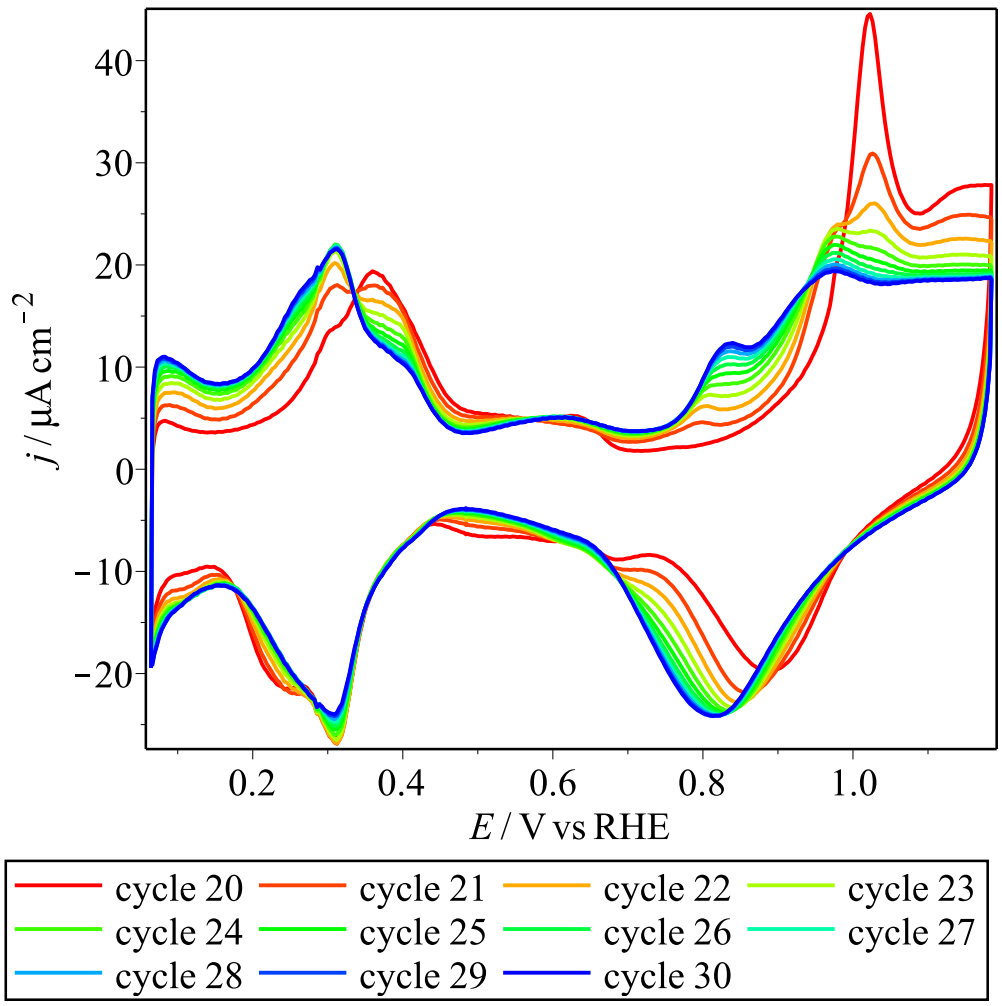

Figure 3.50: Pt(100) cyclic voltammetry spectra with 11 cycles at sweep rate 20 mV/s. Data from EC file Pt100_07 at the CH5918 beamtime at ID31 at the ESRF in July 2021.

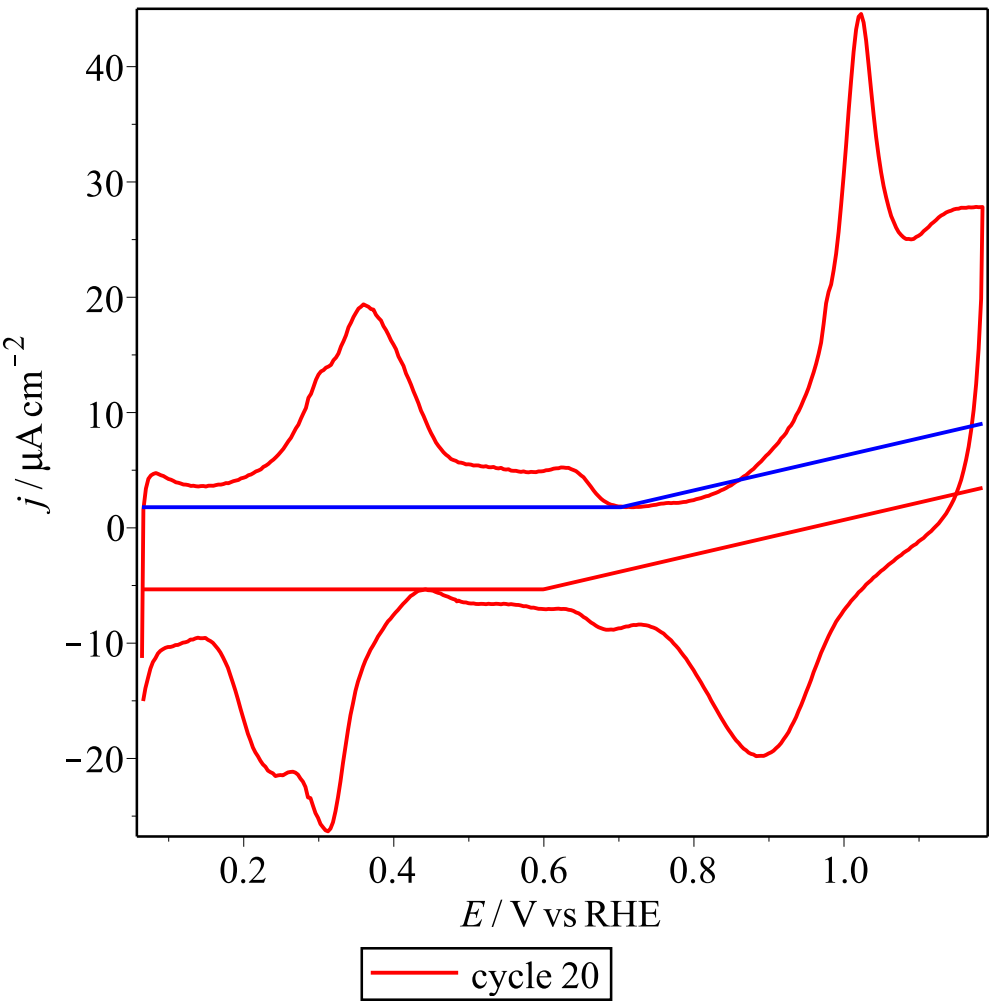

Figure 3.51: Pt(100) cyclic voltammetry spectra of first cycle with baseline correction (blue for anodic process and red for cathodic process). Data from EC file Pt100_07 at the CH5918 beamtime at ID31 at the ESRF in July 2021.

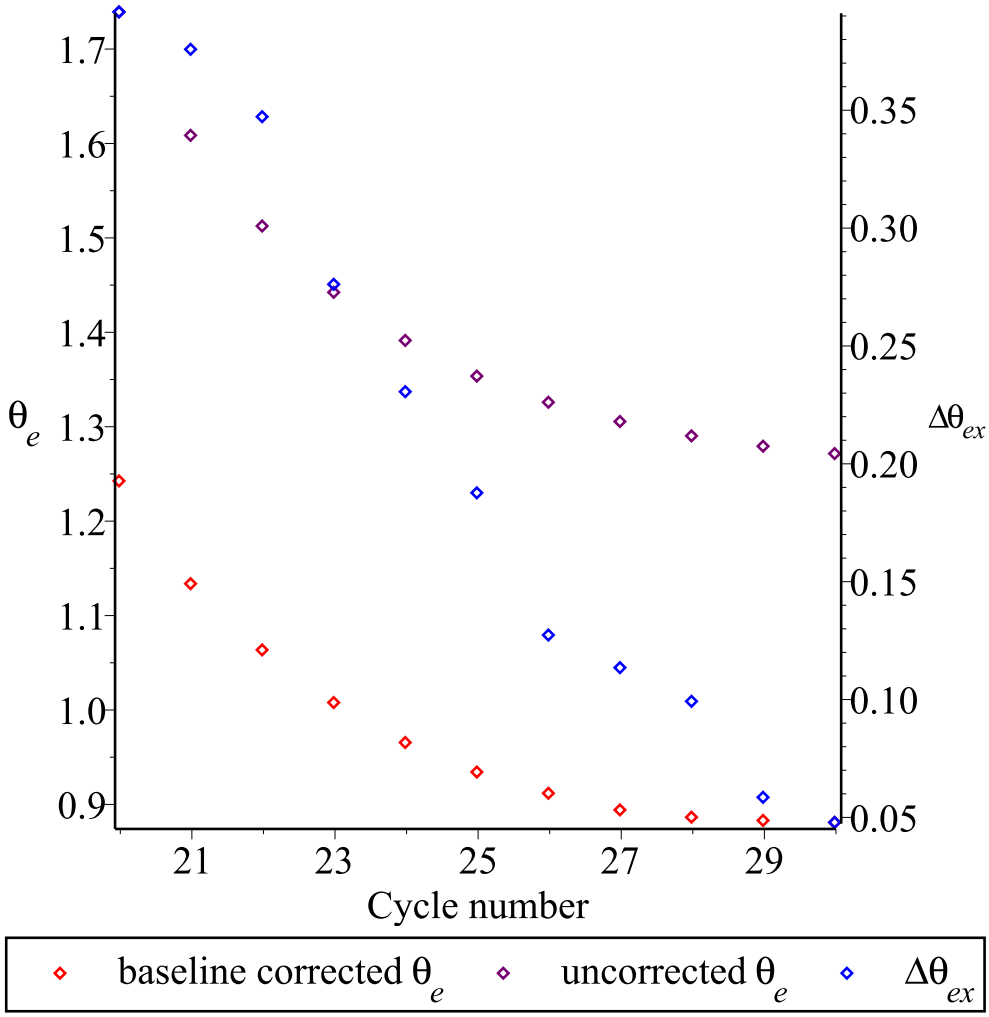

Figure 3.52: Pt(100) θ_e and θ_{ex} Plot for 11 cycles at sweep rate 20 mV/s. The red points are segmented baseline corrected θ_e, the purple points are θ_e without baseline correction, and the blue points are the increase inθ_{ex} in each cycle. Data from EC file Pt100_07 and X-ray file Pt100_03 at the CH5918 beamtime at ID31 at the ESRF in July 2021.

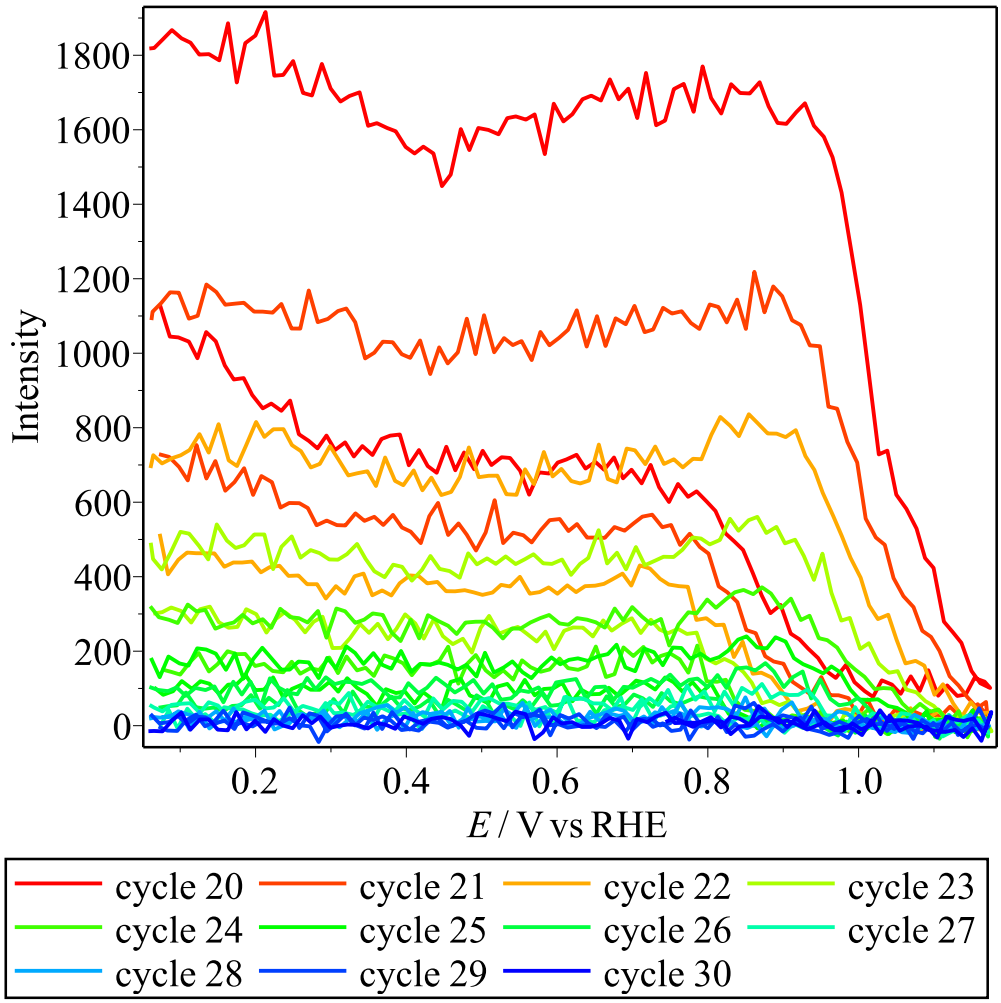

Figure 3.53: Pt(100) X-ray intensities for 11 cycles with sweep rates as 20 mV/s. Data from X-ray file Pt100_03 at the CH5918 beamtime at ID31 at the ESRF in July 2021.

X-ray voltammogram of first cycle for all 11 cycles' data. The θ_{ex} of all 11 cycles is shown as Fig. 3.54, also blue points in Fig. 3.52. The initial θ_{ex} at 0.9 v, the max θ_{ex} with lowest intensity at 1.0 V, and the final θ_{ex} at 0.072 V for first cycle of X-ray spectrum is shown in Fig. 3.55. The total θ_{ex} increases to 0.5 ML. The change in θ_{ex} per cycle decreases towards zero as the cycle number increases.

Coverages θ_e vs θ_{ex} from CV and X-ray

After getting θ_e and θ_{ex} from CV in Fig. 3.50 and X-ray in Fig. 3.53, they are compared via potential, and then a linear fit is used to get the slope, which means e^- transferred per extracted Pt. The anodic and cathodic linear fits of θ_e vs θ_{ex} for the first cycle are shown in Fig. 3.56 and Fig. 3.57. The anodic and cathodic slopes are shown as Fig. 3.58; the anodic slope slowly increases from 3 to 6 as the cycle number increases.

Also, there are θ_e and θ_{ex} plots without baseline correction of CV data analyzed and the slopes are shown in Fig. 3.59. Both anodic and cathodic slopes are a little larger than the ones with baseline correction in Fig. 3.58. The anodic θ_e and θ_{ex} plot for first cycle with uncorrected CV is shown in Fig. 3.60, and the corresponding cathodic θ_e and θ_{ex} plot is shown in Fig. 3.61.

Discussion on Extraction of Pt(100)

For Pt(100) surface, different from Pt(111), permanent changes caused by platinum extraction take place on the platinum surface in each cycle. The flat part in the X-ray intensity in Fig. 3.53 decreases with cycle number, and the beginning θ_{ex} in Fig. 3.54 increases for each cycle. So we mainly focus on the first cycle without

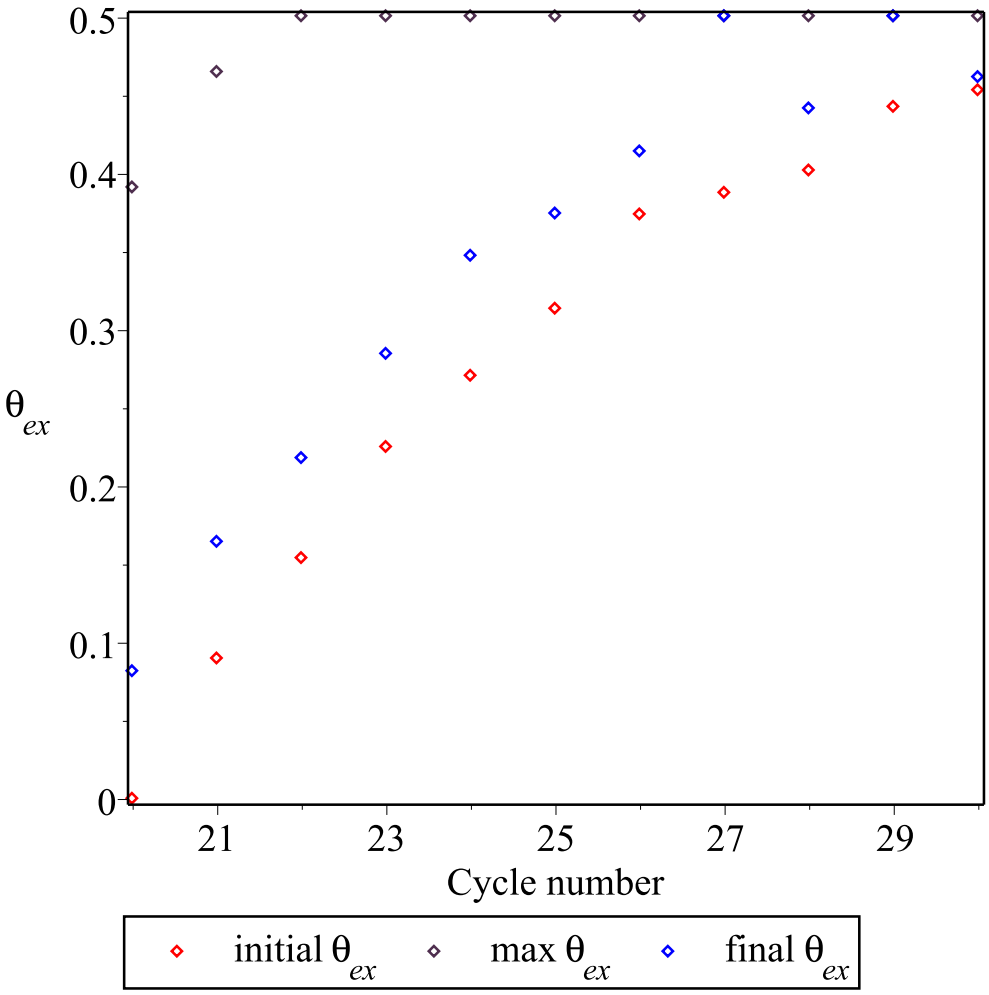

Figure 3.54: Pt(100) θ_{ex} plot for 11 cycles at sweep rates 20 mV/s. The red points are θ_{ex} at anodic 0.9 V of each cycle, the violet points are θ_{ex} at the end of anodic process, the blue points are θ_{ex} at the end of each cycle. Data from X-ray file Pt100_03 at the CH5918 beamtime at ID31 at the ESRF in July 2021.

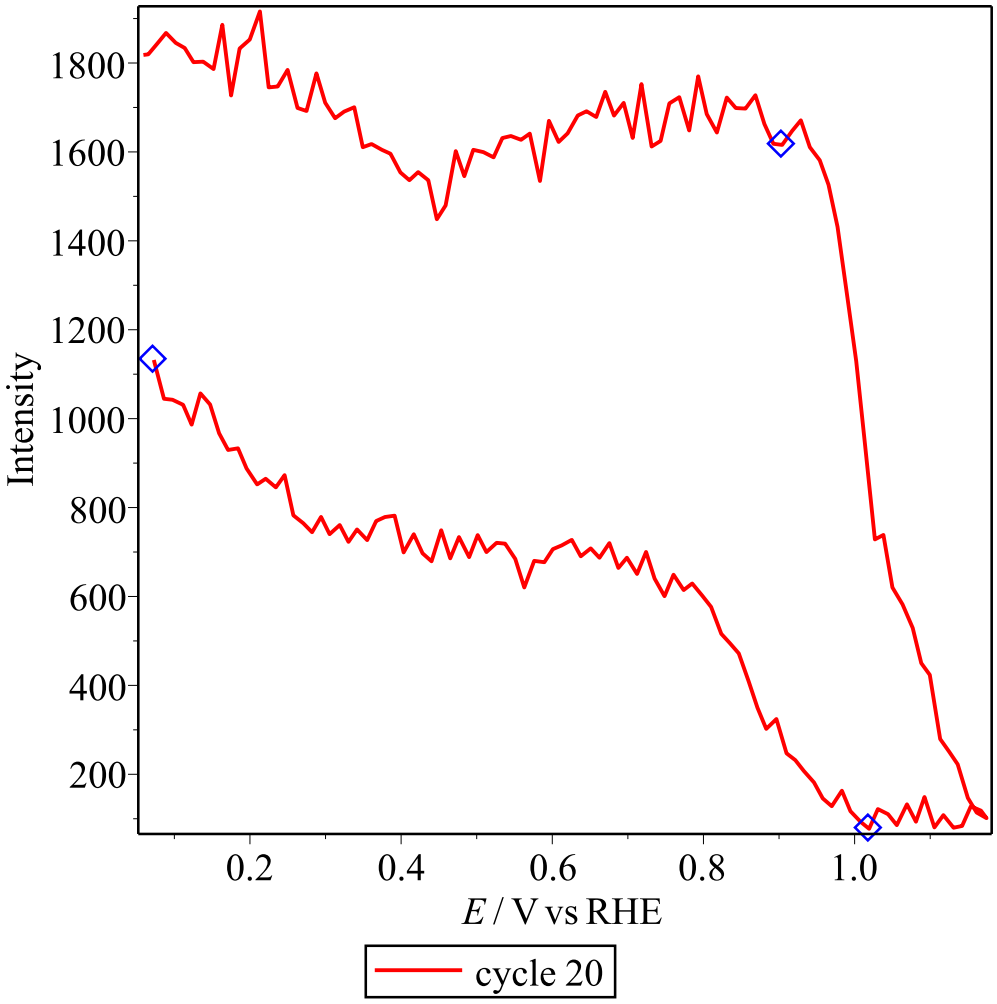

Figure 3.55: Pt(100) X-ray intensities for first cycle with sweep rates as 20 mV/s. The blue point at anodic 0.9 V is for initial θ_{ex} in Fig. 3.54, the blue point at 1.0 V with lowest intensity is for max θ_{ex} in Fig. 3.54, and the blue point at cathodic 0.072 V is for final θ_{ex} in Fig. 3.54. Data from X-ray file Pt100_03 at the CH5918 beamtime at ID31 at the ESRF in July 2021.

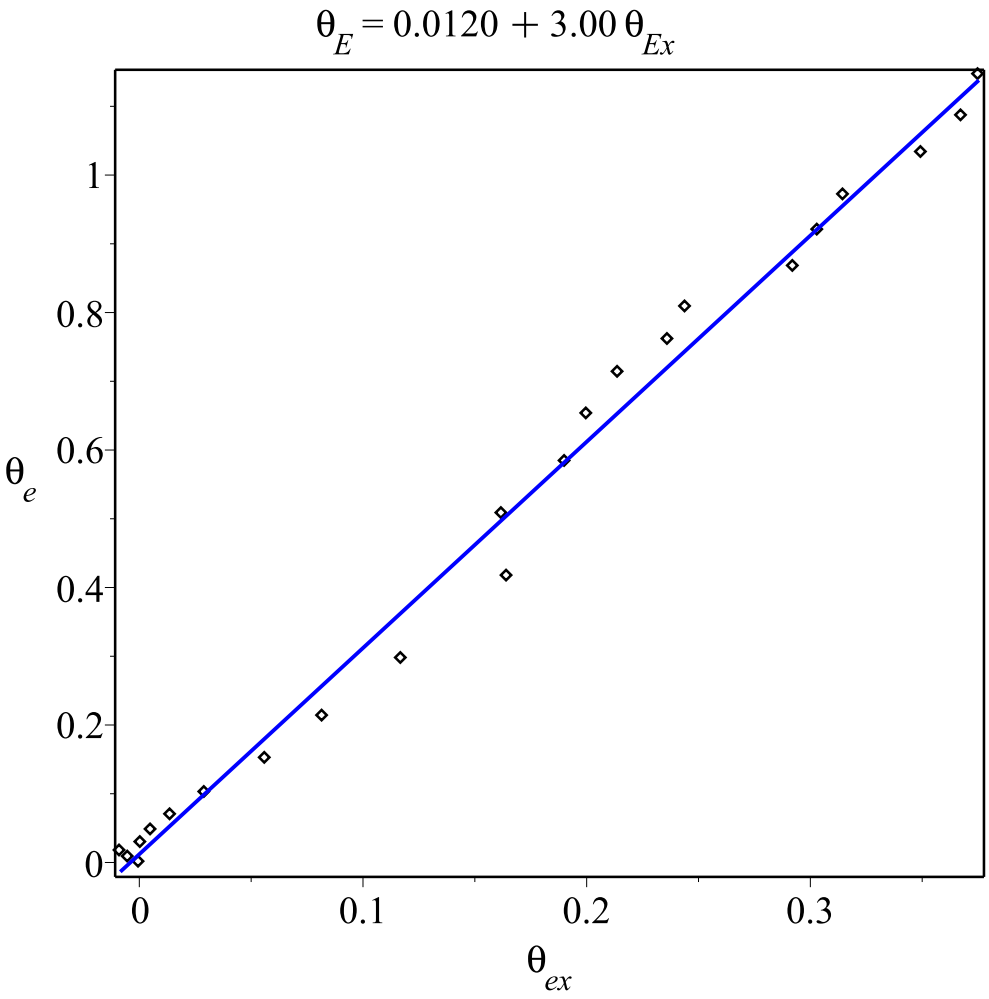

Figure 3.56: Pt(100) anodic θ_e vs θ_{ex} Plot with segmented baseline correction for first cycle with sweep rate 20 mV/s. Data from EC file Pt100_07 and X-ray file Pt100_03 at the CH5918 beamtime at ID31 at the ESRF in July 2021.

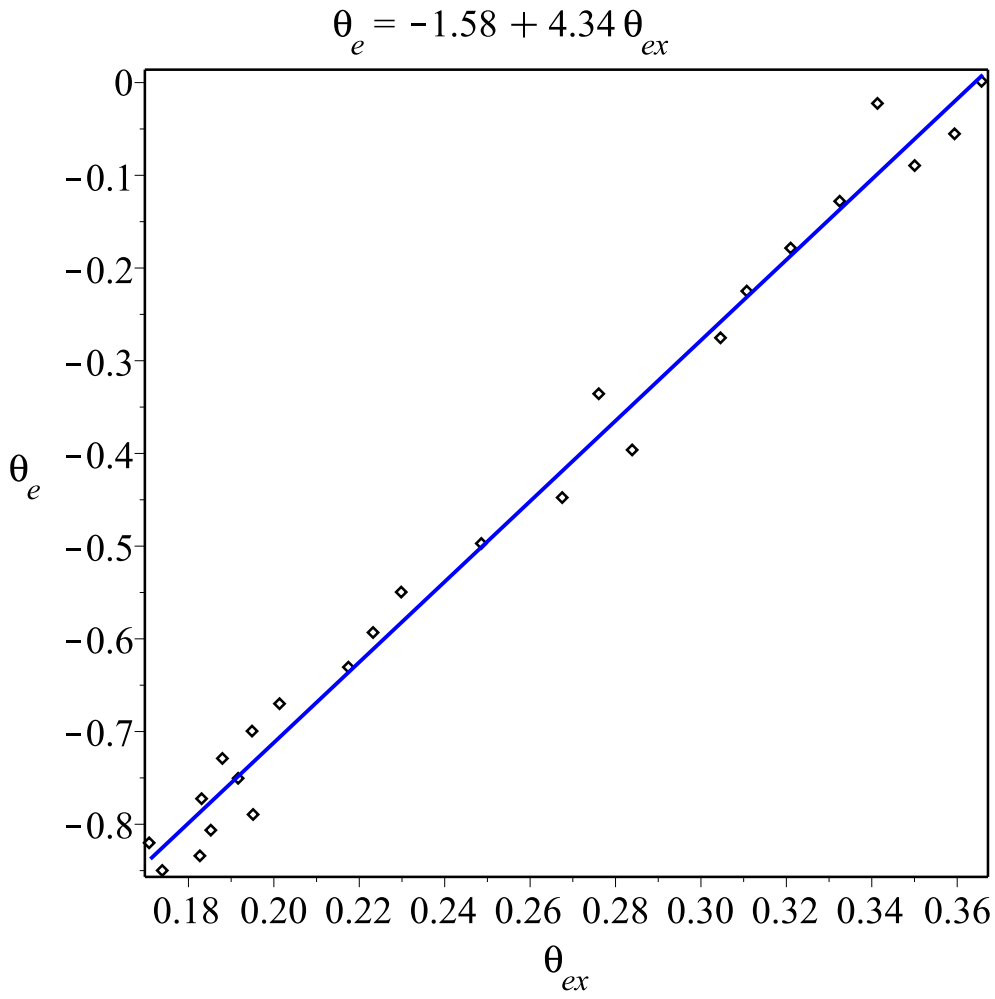

Figure 3.57: Pt(100) cathodic θ_e vs θ_{ex} Plot with segmented baseline correction for first cycle with sweep rate 20 mV/s. Data from EC file Pt100_07 and X-ray file Pt100_03 at the CH5918 beamtime at ID31 at the ESRF in July 2021.

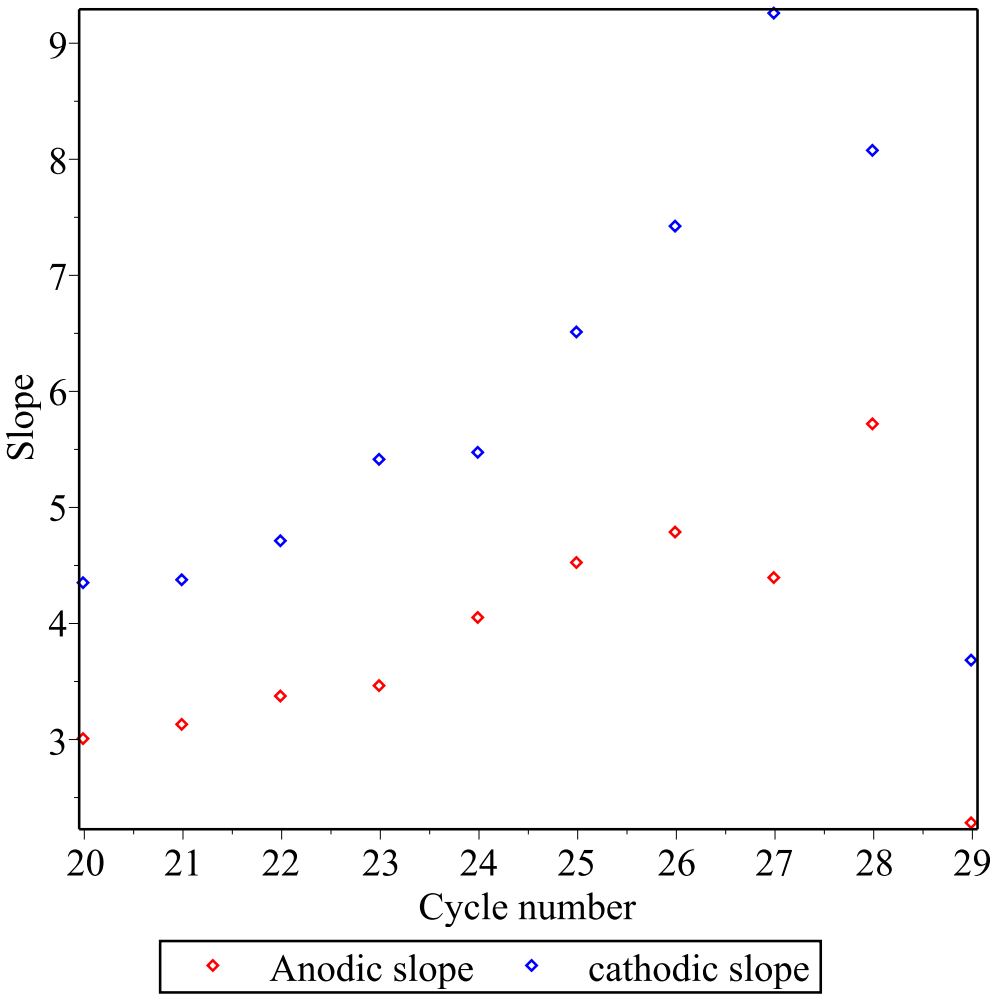

Figure 3.58: Pt(100) slopes of fitted line for θ_e and θ_{ex} plot for 11 cycles with segmented baseline correction with sweep rate as 20 mV/s. The red points are anodic slope, and the blue points are cathodic slope. Data from EC file Pt100_07 and X-ray file Pt100_03 at the CH5918 beamtime at ID31 at the ESRF in July 2021.

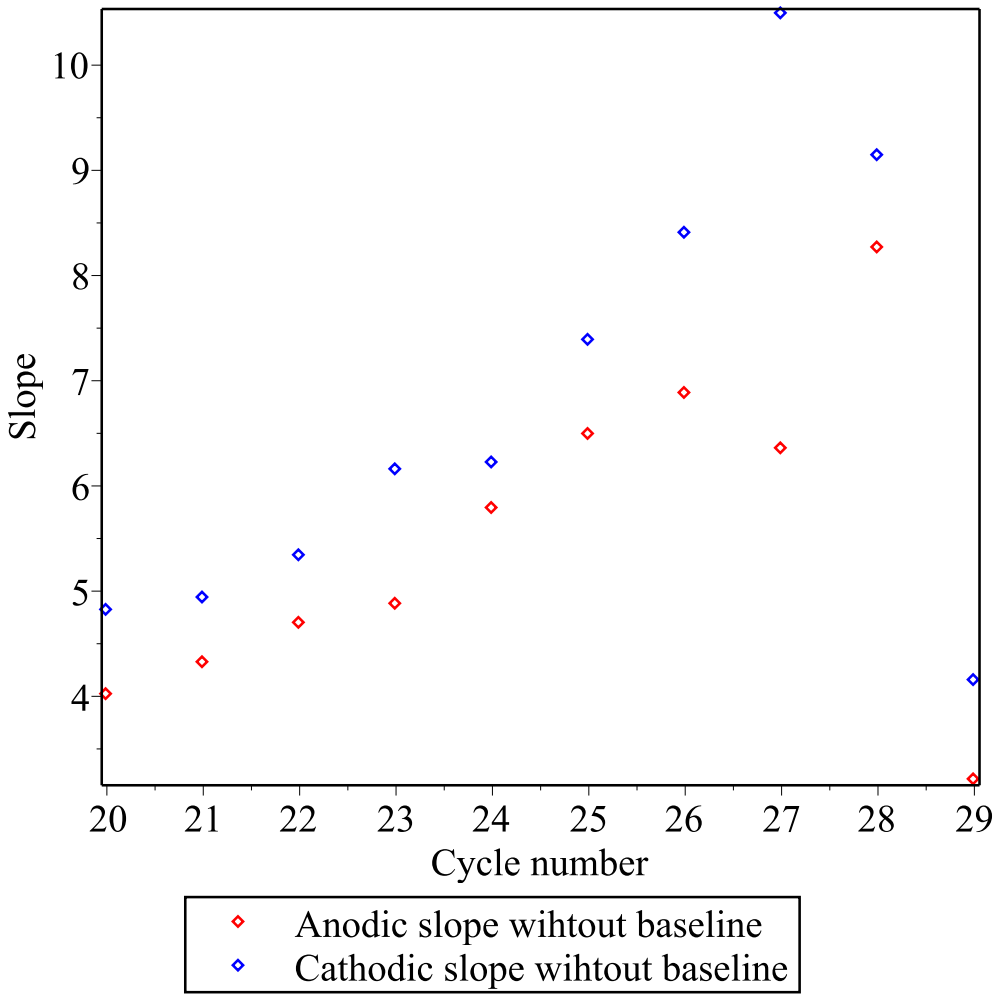

Figure 3.59: Pt(100) slopes of fitted line for θ_e and θ_{ex} plot without baseline corrections for 11 cycles with sweep rate as 20 mV/s. The red points are anodic slope without baseline correction, and the blue points are cathodic slope without baseline correction. Data from EC file Pt100_07 and X-ray file Pt100_03 at the CH5918 beamtime at ID31 at the ESRF in July 2021.

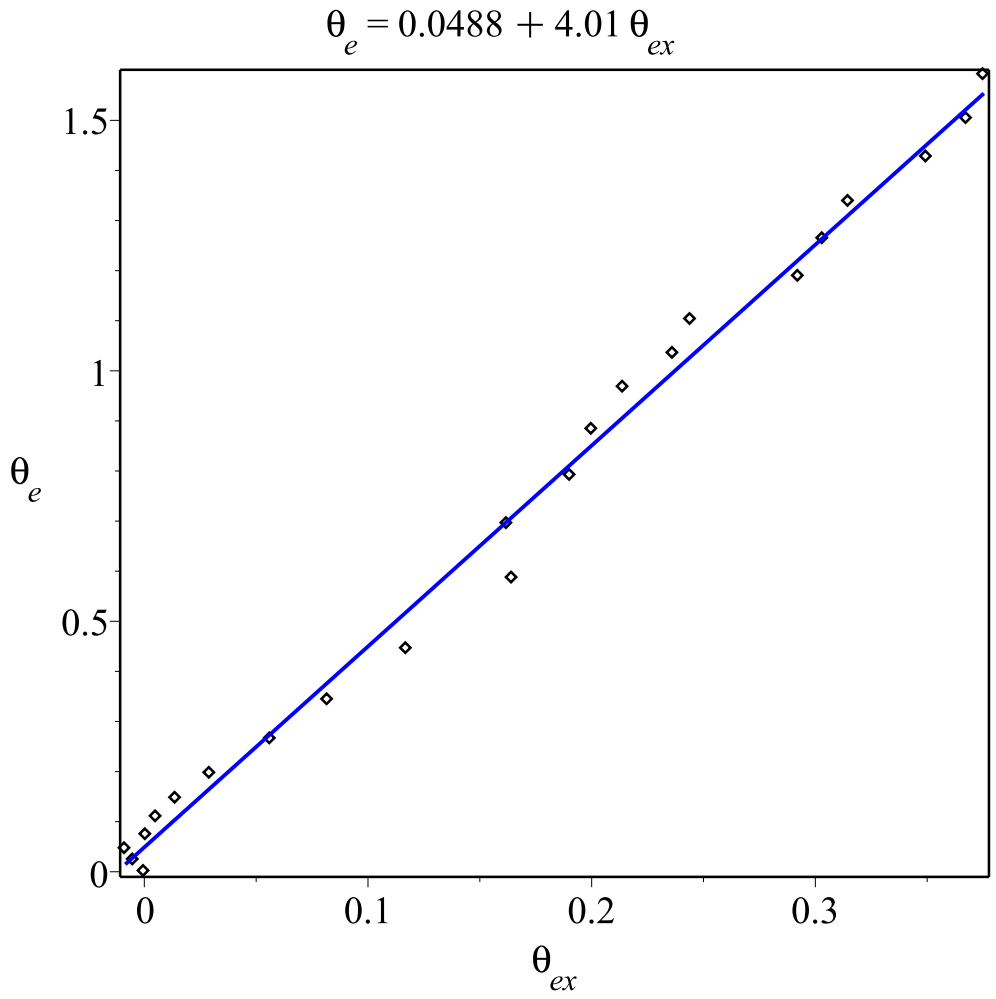

Figure 3.60: Pt(100) anodic θ_e vs θ_{ex} Plot with uncorrected CV with fitted line for first cycle with sweep rate 20 mV/s. Data from EC file Pt100_07 and X-ray file Pt100_03 at the CH5918 beamtime at ID31 at the ESRF in July 2021.

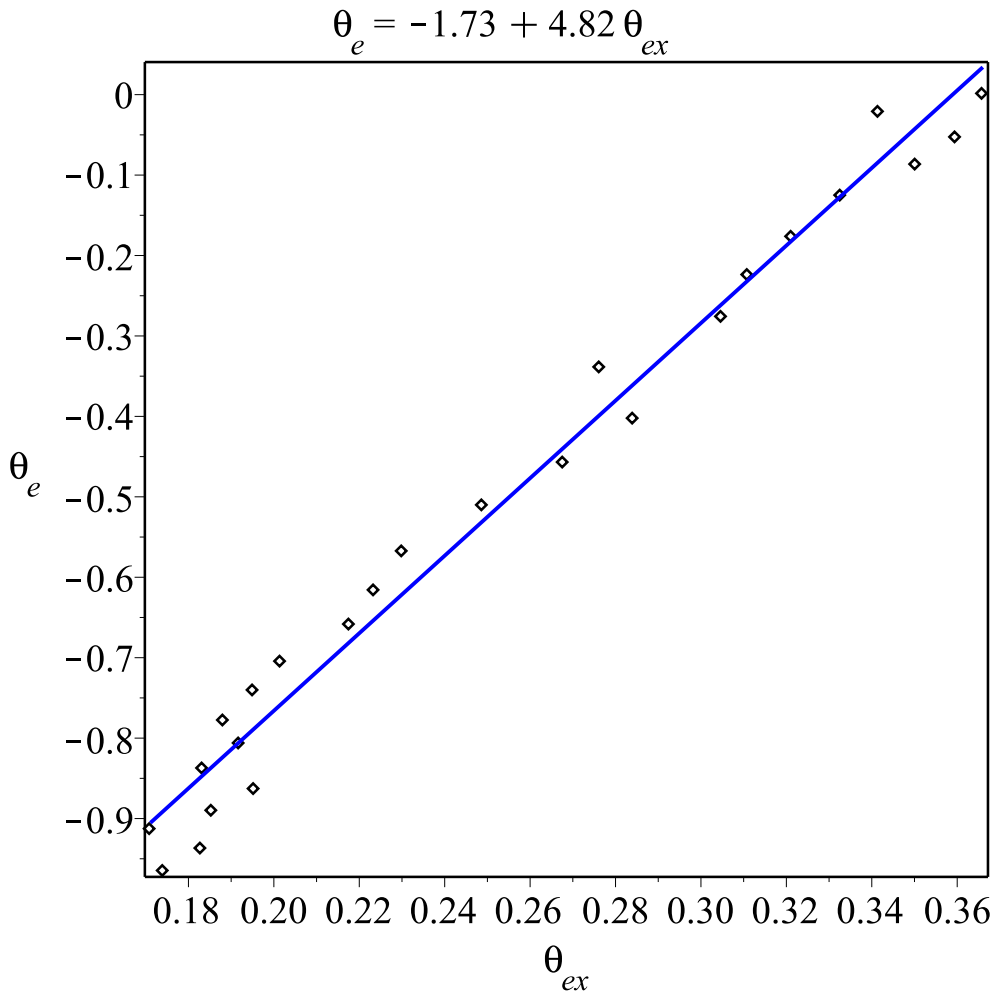

Figure 3.61: Pt(100) cathodic θ_e vs θ_{ex} Plot with uncorrected CV with fitted line for first cycle with sweep rate 20 mV/s. Data from EC file Pt100_07 and X-ray file Pt100_03 at the CH5918 beamtime at ID31 at the ESRF in July 2021.

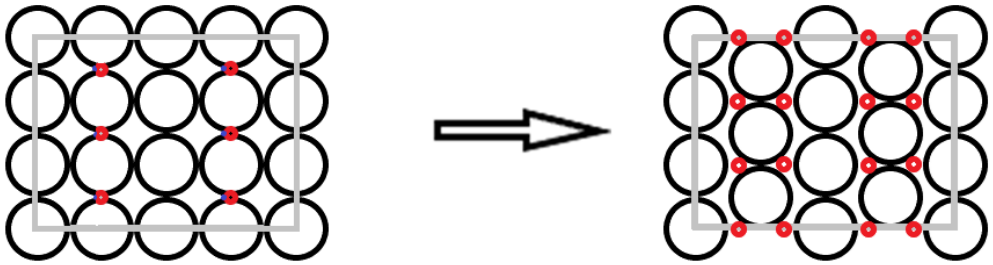

Figure 3.62: Pt(100) oxidation reaction from 12-Pt-atom unit cell with 6 OH_{ads} to 6 extracted Pt in two chains.

effect from previous surface oxidation. The segmented baseline corrected θ_e is 1.24 ML from CV, and 1.16 ML from θ_e vs θ_{ex}. Similar as Section 3.2.2, they are a little different because the potential range of the first one starts from 0.9 V, the start point of oxide peak; but the potential range of the later one starts from ∼1.0 V, the first point before θ_{ex} rises up. θ_{ex} is 0.39 ML for first cycle, and slope of θ_e vs θ_{ex} is 3, so the reaction happens as below, for each 10 surface Pt atoms:

$$1 \times (\mathrm{OH(ads)} \rightarrow \mathrm{O(ads)} + \mathrm{H^+} + \mathrm{e^-}) \tag{3.16}$$

$$4 \times (\mathrm{Pt} + \mathrm{OH(ads)} + \mathrm{H_2O} \rightarrow \mathrm{PtO_2(ex)} + \mathrm{Pt} + 3\mathrm{H^+} + 3\mathrm{e^-}) \tag{3.17}$$

Similar as Fig. 3.48, Pt extraction forms as long PtO_2 chains [70], but with higher coverage PtO_2 chains, lower coverage of O_{ads}, and addition of both is 1/2 ML. The extracted Pt forms as long chains in Fig. 3.62.

If we use this to compare with early research as run 664 of IHCH925 in 2015 from previous section 3.2.2, for the cyclic voltammogram as in Fig. 3.63, the first cycle this time has lower H/OH mixed peak before 0.7 V, and higher Pt oxide peak and

flat part after it, but the oxide peak has nearly the same current as the early research without the top part. And for the charge density vs potential as in Fig. 3.64, the H/OH peak this time is 25 μC cm^{-2} (0.12 ML) lower than early research, and the oxide peak this time is 257 μC cm^{-2} (1.24 ML), 61 μC cm^{-2} (0.29 ML) higher than early research, 197 μC cm^{-2} (0.95 ML). The slope of θ_e vs θ_{ex} in early research is 3.7, a little higher than 3 for first cycle this time, some other reactions except platinum extraction like formation of O_{ads} group are happening to make the slope larger than 3.

As right half part baseline in Fig. 3.51 with slope is still not sure, if only horizontal baseline as left half part is used, than charge density vs potential is shown as Fig.3.65, the oxide peak this time is 324 μC cm^{-2} (1.56 ML), 67 μC cm^{-2} (0.32 ML) higher than segmented baseline corrected one, 257 μC cm^{-2} (1.24 ML).

If the CV of first cycle isn't baseline corrected, θ_e is 1.73 ML from CV, and 1.59 ML from θ_e vs θ_{ex}. The difference is 0.15 ML. They are very different as was found in Section 3.2.2. The coverage of the reduction peak is 1.24 ML, much lower than θ_e as was found in Section 3.2.2. θ_{ex} is 0.39 ML, the reaction happens same as Section 3.2.2, but with higher coverage of Pt extraction, lower coverage of O_{ads}, and addition of O_{ads} and extracted Pt atoms are 0.5 ML, like Table 3.3 shows. So similar as Eq. 3.13 but with different coverage, the reaction happens as below, for each 10 surface Pt atoms:

$$1 \times (\mathrm{OH(ads)} \rightarrow \mathrm{O(ads)} + \mathrm{H^+} + \mathrm{e^-}) \tag{3.18}$$

$$1 \times (4\mathrm{Pt} + 4\mathrm{OH(ads)} + 6\mathrm{H_2O} \rightarrow \mathrm{Pt_4O_{10}(ex)} + 16\mathrm{H^+} + 16\mathrm{e^-}) \tag{3.19}$$

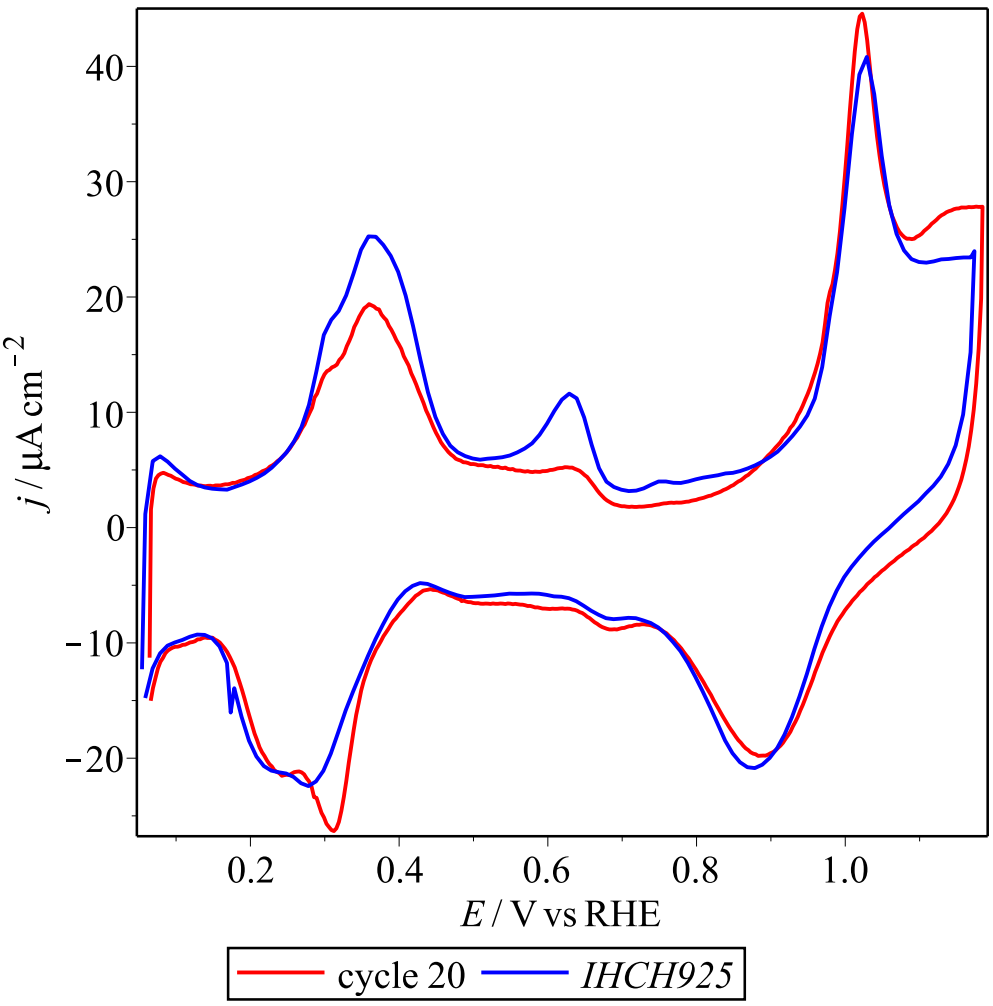

Figure 3.63: Pt(100) cyclic voltammetry spectra comparison between first cycle from Pt100_07 at the CH5918 (in red) and IHCH925 (in blue). Data from EC file Pt100_07 at the CH5918 beamtime at ID31 at the ESRF in July 2021, and run 664 at IHCH925 beamtime in February 2015.

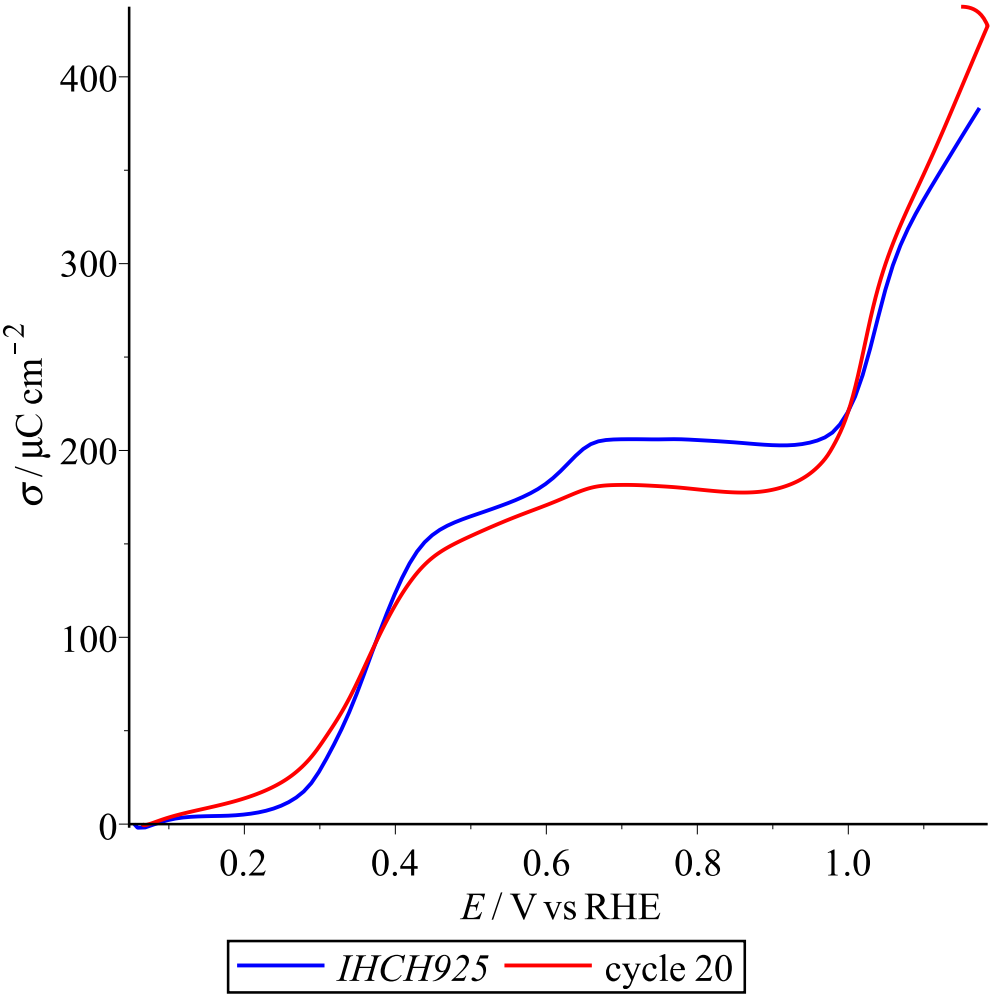

Figure 3.64: Pt(100) charge density spectra comparison between first cycle from Pt100_07 at the CH5918 (in red) and IHCH925 (in blue). Data from EC file Pt100_07 at the CH5918 beamtime at ID31 at the ESRF in July 2021, and run 664 at IHCH925 beamtime in February 2015.

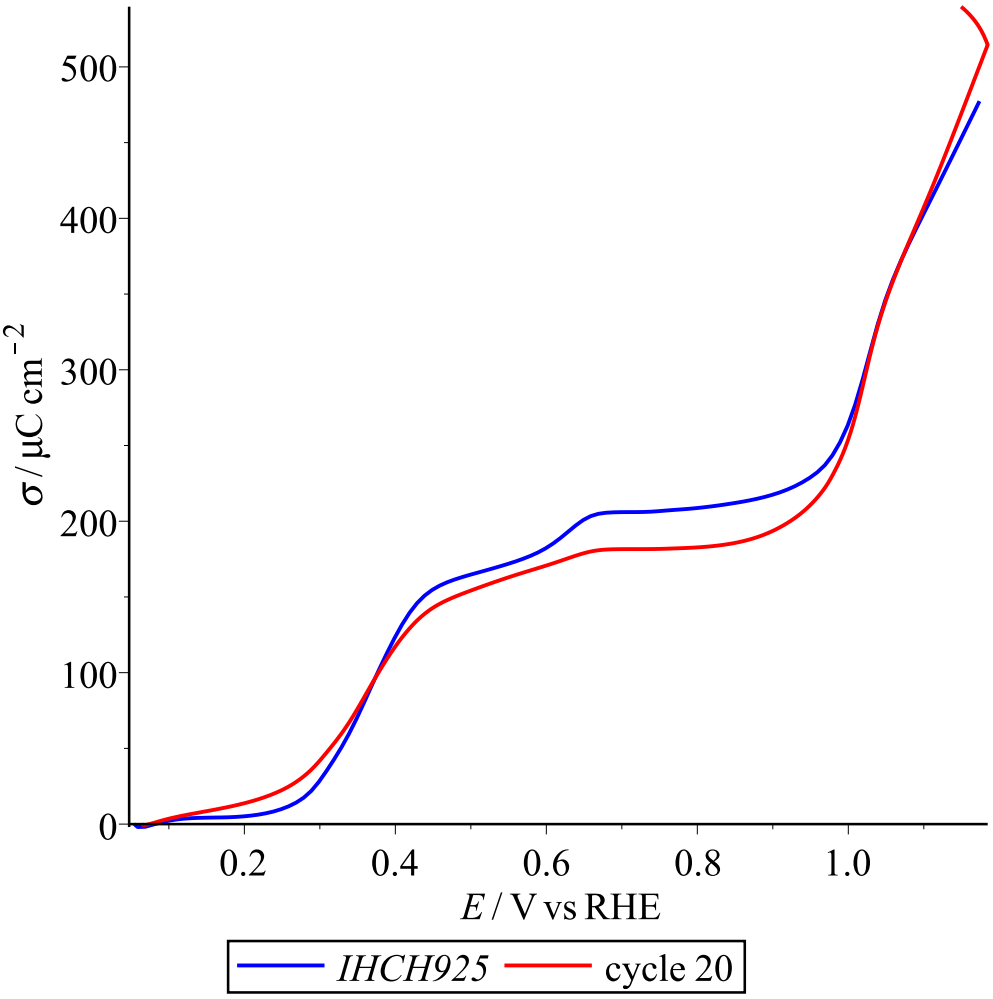

Figure 3.65: Pt(100) charge density spectra comparison with horizontal baseline between first cycle from Pt100_07 at the CH5918 (in red) and IHCH925 (in blue). Data from EC file Pt100_07 at the CH5918 beamtime at ID31 at the ESRF in July 2021, and run 664 at IHCH925 beamtime in February 2015.

Here the extracted Pt forms a short extracted Pt chain with 4 Pt_{ex} atoms, like shown in Fig. 3.49.a. Another possibility is that extracted Pt oxides can form short extracted Pt chain with 3 Pt_{ex} atoms, and independent extracted PtO_2, like shown in Fig. 3.49.b as:

$$4Pt + 4OH(ads) + 6H_2O \rightarrow Pt_3O_8(ex) + PtO_2(ex) + 16H^+ + 16e^- \quad (3.20)$$

Name	uncorrected θ_e	θ_{ex}	O_{ads}	Pt_{ex}
IHCH925	1.24 ML	0.25 ML	0.25 ML	0.25 ML
CH5918	1.59 ML	0.39 ML	0.11 ML	0.39 ML

Table 3.3: Comparison of coverages for Pt(100) voltammograms

3.2.4 Pt(100) Potential Steps

In this subsection, the data of oxidation potential steps for Pt(100) is treated to find the slope of θ_e vs θ_{ex}, and the direct logarithmic relation between θ_e and log time as the last place exchange part of Section 2.2.4 introduced.

Oxidation Potential Steps for Pt(100) from the Double Layer

The oxidation portion of potential steps from the double layer between 0.87 and 1.22 V is from EC file 57 at the CH4977 beamtime at ID31 at the ESRF in July 2017. In all, it runs as EC plot in Fig. 3.66 and X-ray plot in Fig. 3.67. For each step, the potential is held at 0.42 V for 10 s, then goes up to a number, e.g. 1.22 V, inside 1 data point and is held for 60 s, and then returns to 0.42 V. This is then repeated

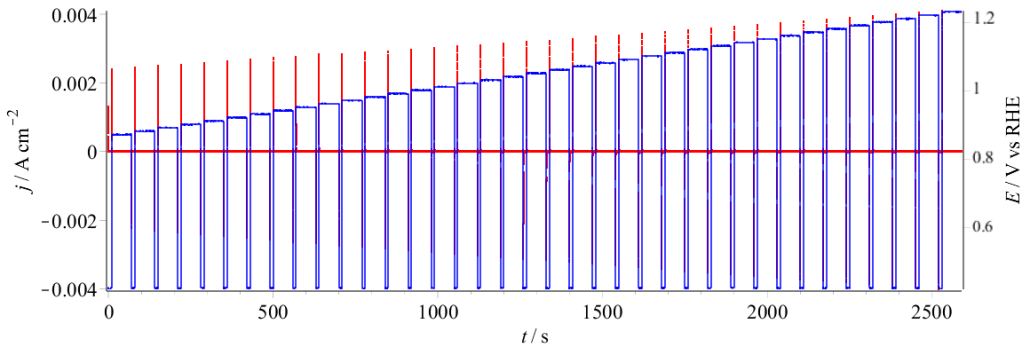

Figure 3.66: Potential(blue) and current density(red) plots of Pt(100) Potential steps in 0.1 M $HClO_4$ from the double layer. Data from EC file 57 at the CH4799 beamtime at ID31 at the ESRF in July 2017.

but stepping to a higher potential, as shown in Fig. 3.69 and 3.70. The initial and final potentials for steps are shown in Fig. 3.68. The current density goes up to 0.004 A·cm^{-2} inside 0.0008 s and goes down to close to zero inside 2 s and keeps running for a total of 60 s. It is an example to show how the potential steps work, and potential steps from the double layer at other potentials work in the similar way. For the X-ray intensity, when it drops between 1000 s to 1500 s in Fig. 3.67, the intensity stays at a high level between steps at 0.42 V, and suddenly drops to a low intensity that is maintained during the steps, e.g. at 1.10 V, then it rises back to a high intensity but a little lower than before, and then stays steady for 10 s as Fig. 3.71 shows.

Coverages θ_e and θ_{ex} vs time from Potential Steps

For the data treatment before θ_e is calculated, the time from data is corrected to begin from 0 s for each step. The current density is corrected by subtracting the average current density of the last 10000 points, or ∼50 s, which is the flat part with

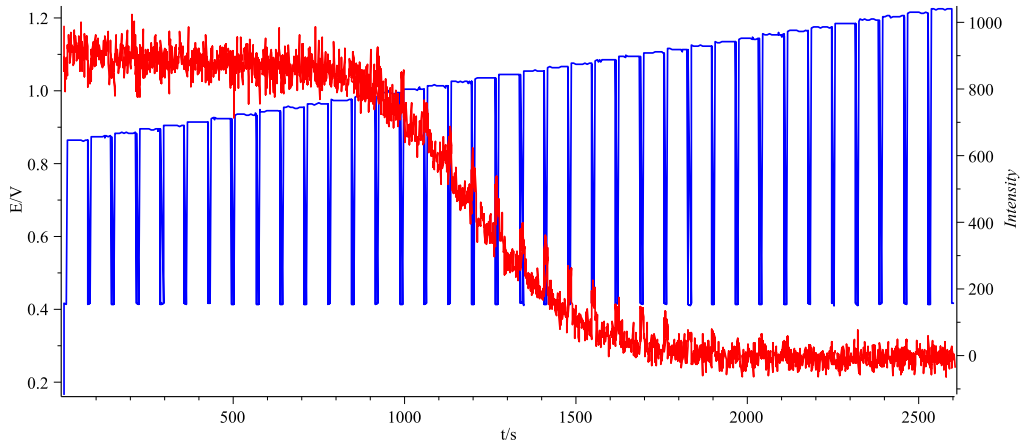

Figure 3.67: Potential(blue) and X-ray(red) plots of Pt(100) Potential steps in 0.1 M $HClO_4$ from the double layer. Data from EC file 57 at the CH4799 beamtime at ID31 at the ESRF in July 2017.

current density very close to 0 after ∼2s caused by beam damage as Fig. 3.72 shows, and the blue line is the baseline before subtraction.

Then the θ_e of the potential step is obtained from the running integral of time and baseline-corrected current density. Fig. 3.73 shows the θ_e vs time for the potential step to 1.22 V with data from Fig. 3.70 as an example, and it works in a similar way for potential steps at other potentials.

$\Delta\theta_e$ shown in Fig. 3.74 means the final θ_e minus the initial θ_e in each step. θ_e does not change too much in the flat part after 10 s (1 for log(time)).

For the X-ray intensity, θ_{ex} is transferred from intensity as $\theta_{ex} = 0.5007(1 - \sqrt{\frac{I}{I_{0.9V}}})$ from Section 2.3.4, the standard of all steps is the intensity of the first point of the step to 0.90 V vs RHE. The changes in θ_{ex} for each step are shown as Fig. 3.75. The largest θ_{ex} of each step goes up from 0 to 0.5 ML step by step between 1.0 and 1.1 V.

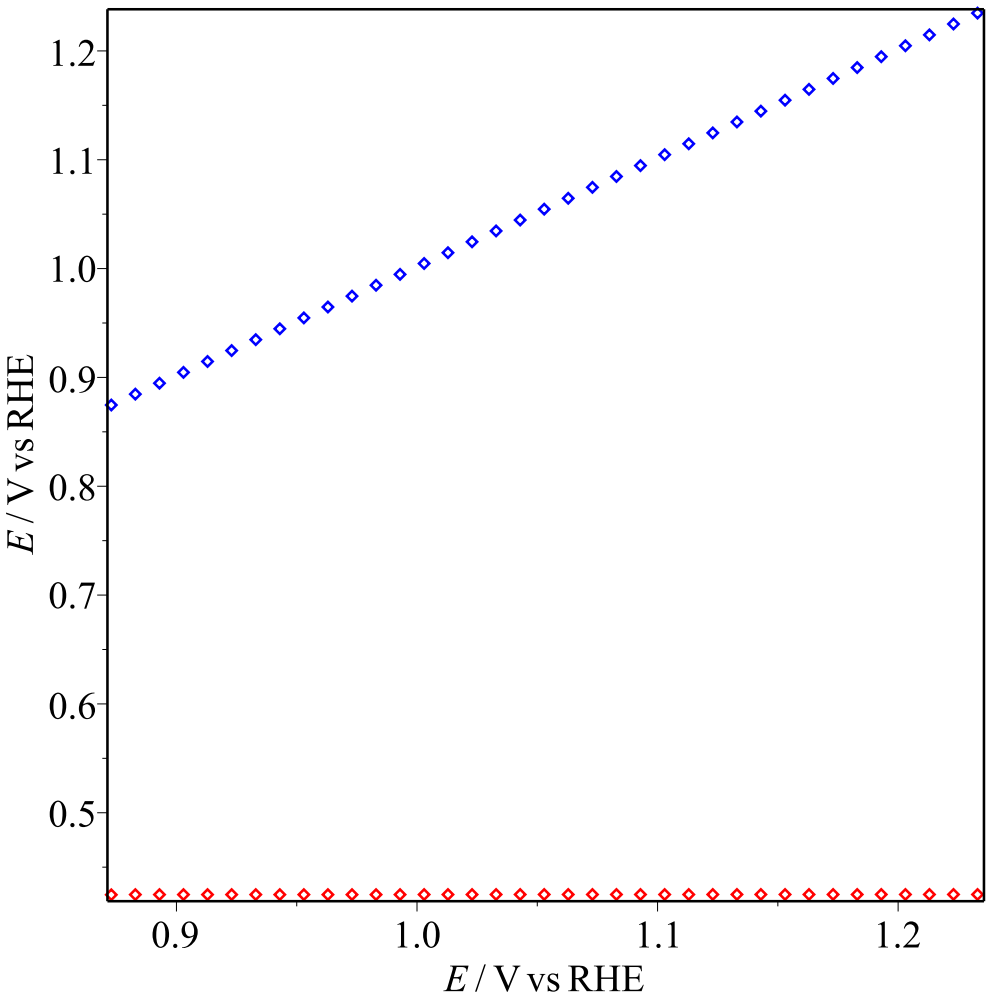

Figure 3.68: The initial and final potentials for oxidation potential steps from 0.87 V to 1.22 V on Pt(100) in 0.1 M $HClO_4$ from the double layer. The left curve is initial potentials and the right curve is final potentials. Data from EC file 57 at the CH4977 beamtime at ID31 at the ESRF in July 2017.

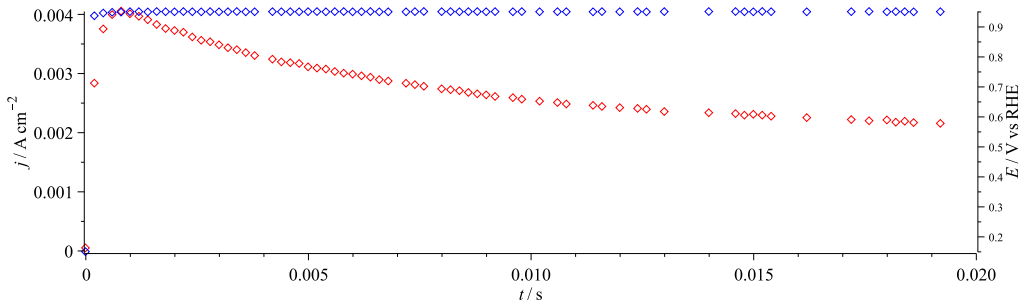

Figure 3.69: First 0.020 s of The oxidation portion of potential step to 1.22 V on Pt(100) in 0.1 M $HClO_4$ from the double layer. The red curve is current density and the blue curve is potential. Data from EC file 57 at the CH4977 beamtime at ID31 at the ESRF in July 2017.

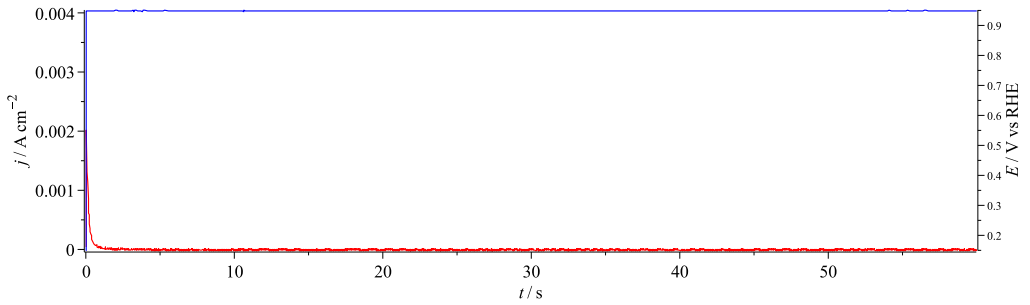

Figure 3.70: The oxidation portion of potential step to 1.22 V on Pt(100) in 0.1 M $HClO_4$ from the double layer. The red curve is current density and the blue curve is potential. Data from EC file 57 at the CH4977 beamtime at ID31 at the ESRF in July 2017.

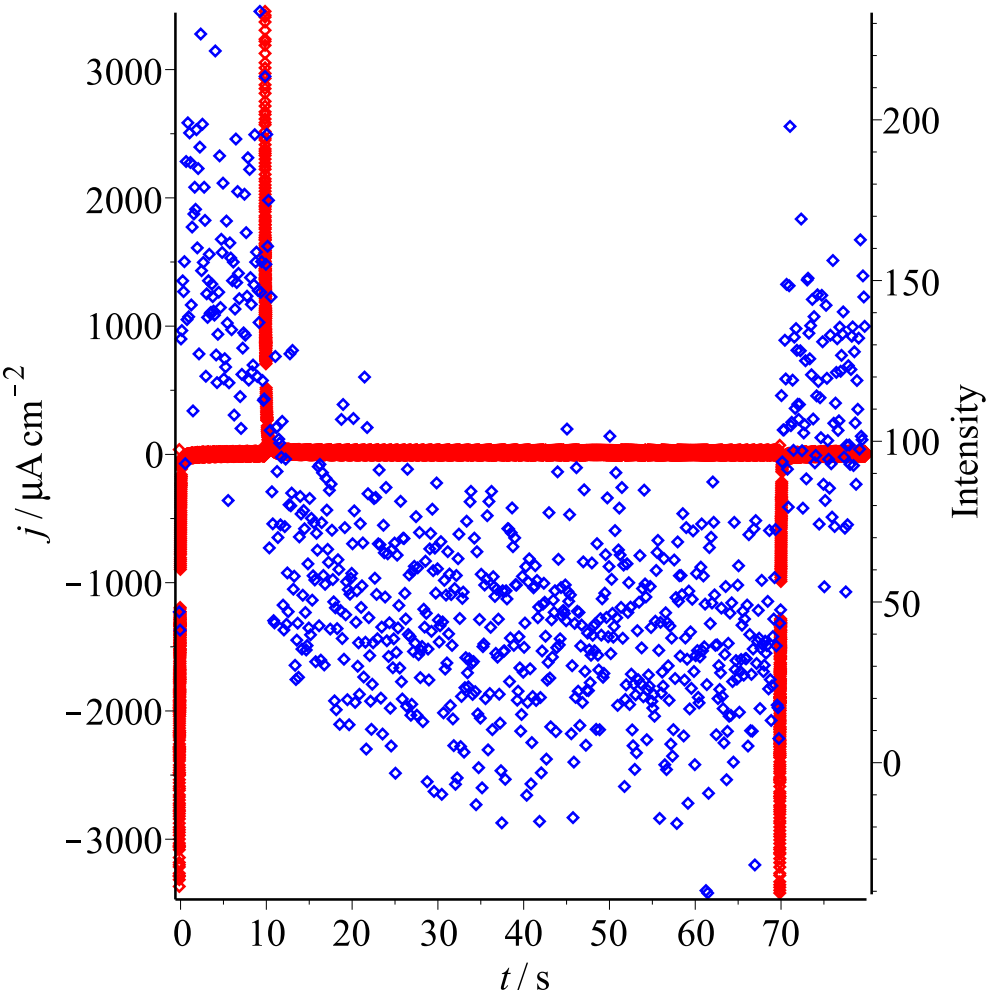

Figure 3.71: The Current density(red) and X-ray(blue) plots for the oxidation portion of potential step to 1.10 V on Pt(100) in 0.1 M $HClO_4$ from the double layer. Data from EC file 57 at the CH4977 beamtime at ID31 at the ESRF in July 2017.

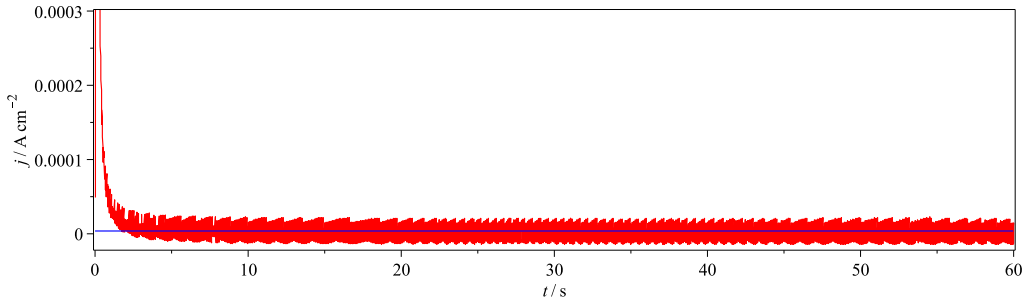

Figure 3.72: The oxidation portion of potential step to 1.22 V on Pt(100) in 0.1 M $HClO_4$ from the double layer. The red curve is current density and the blue line is the baseline for correction. Data from EC file 57 at the CH4977 beamtime at ID31 at the ESRF in July 2017.

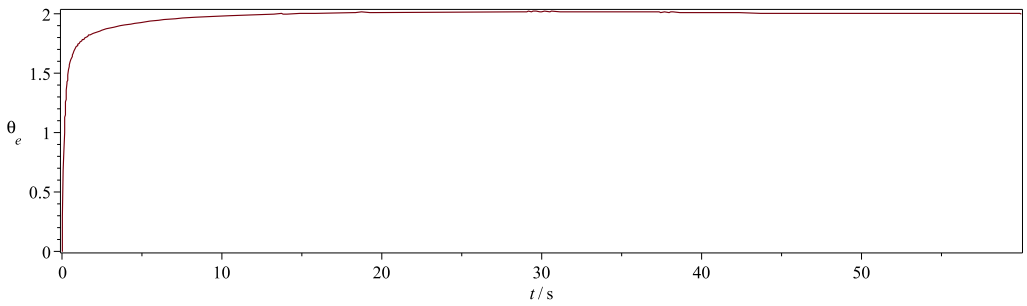

Figure 3.73: θ_e vs time for oxidation portion of potential step to 1.22 V on Pt(100) in 0.1 M $HClO_4$ from the double layer. Data from EC file 57 at the CH4977 beamtime at ID31 at the ESRF in July 2017.

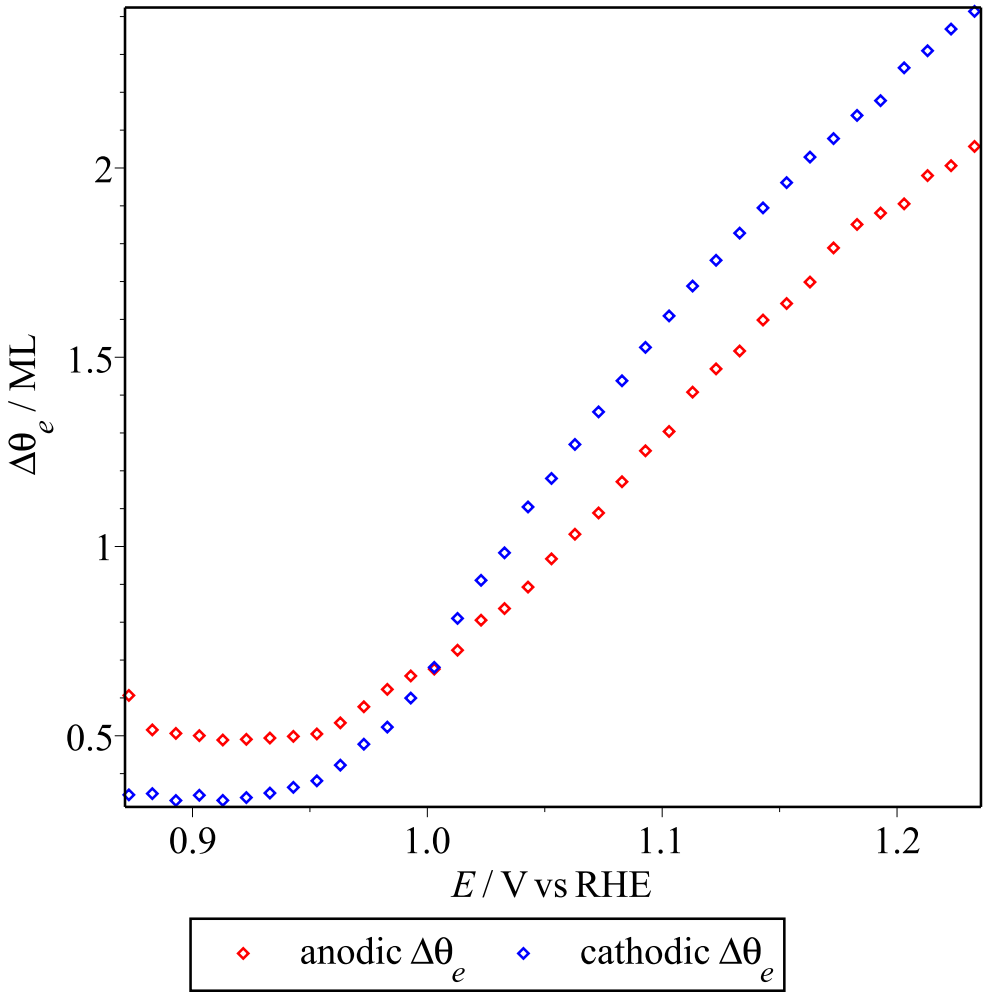

Figure 3.74: Change in θ_e for oxidation portion of potential steps on Pt(100) from 0.87 to 1.22 V. Data from EC file 57 at the CH4977 beamtime at ID31 at the ESRF in July 2017.

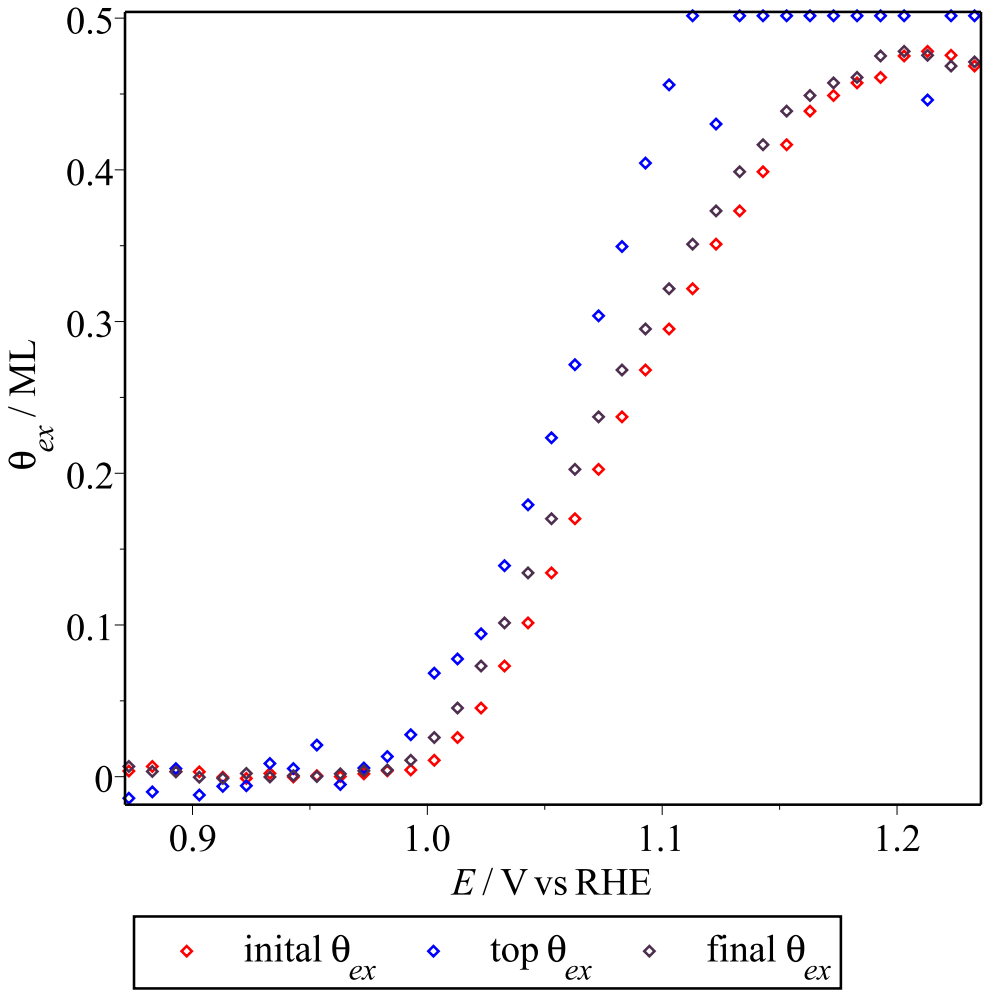

Figure 3.75: θ_{ex} for oxidation portion of potential steps on Pt(100) from 0.87 to 1.22 V. The red points are initial θ_{ex} of each step, the blue points are maximum θ_{ex} of each step, and the purple points are final θ_{ex} of each step. Data from EC file 57 at the CH4977 beamtime at ID31 at the ESRF in July 2017.

Similar to $\Delta\theta_e$, $\Delta\theta_{ex}$ is plotted in Fig 3.76, to show the final θ_{ex} minus the initial θ_{ex}. $\Delta\theta_{ex}$ plot is a peak centred at 1.1 V, very different from $\Delta\theta_e$ plot in Fig 3.74, which is more close to θ_e plot in Fig 3.75.

After $\Delta\theta_e$ and $\Delta\theta_{ex}$ are calculated from EC and X-ray data, they are compared via potential in Fig 3.77. $\frac{\Delta\theta_e}{\Delta\theta_{ex}}$ is heavily noisy before 1.0 V when θ_{ex} is steady at 0 ML in Fig 3.75; then $\frac{\Delta\theta_e}{\Delta\theta_{ex}}$ keeps flat between 1.0 and 1.11 V with average as 11.10 when θ_{ex} increases from 0 to 0.5 ML; last $\frac{\Delta\theta_e}{\Delta\theta_{ex}}$ linearly increases after 1.1 V when θ_{ex} is steady at 0.5 ML.

Coverage θ_e and θ_{ex} vs $\log_{10}$time and fitted line

After we get the θ_e vs time as the Fig. 3.73 shows, θ_e vs $\log_{10}t$ is plotted by the θ_e data from previous data treatment and the $\log_{10}t$ from the log of corrected time omitting the first point at zero time log(0) is minus infinity. The diagrams of θ_e vs $\log_{10}t$ and their derivative for steps to 0.87 V, 1.07 V and 1.22 V, which are the lowest, middle, and highest potential limit in data from EC file 57 at the CH4799 beamtime at ID31 at the ESRF in July 2017, are shown as Fig. 3.80, Fig. 3.79, and Fig. 3.78. The curves of θ_e vs $\log_{10}t$ go up slowly first before around $\log_{10}(t/\mathrm{s})$ = -2 for all three cases. Then there are large slopes for all three figures that are approximately straight lines, which we need to fit. Lastly, after the sharp part around $\log_{10}(t/\mathrm{s})$ = -0.5, the curves come back to very flat almost horizontal lines for all three spectra, Fig. 3.80, Fig. 3.79, and Fig. 3.78.

Because the region to fit is only part of the curve, an objective way to determine the range to fit was sought. The middle of the range was defined as the inflection point, and was found from where the derivative is maximum. To find when the slope departs too much from its value at the middle of the range, it was arbitrarily decided

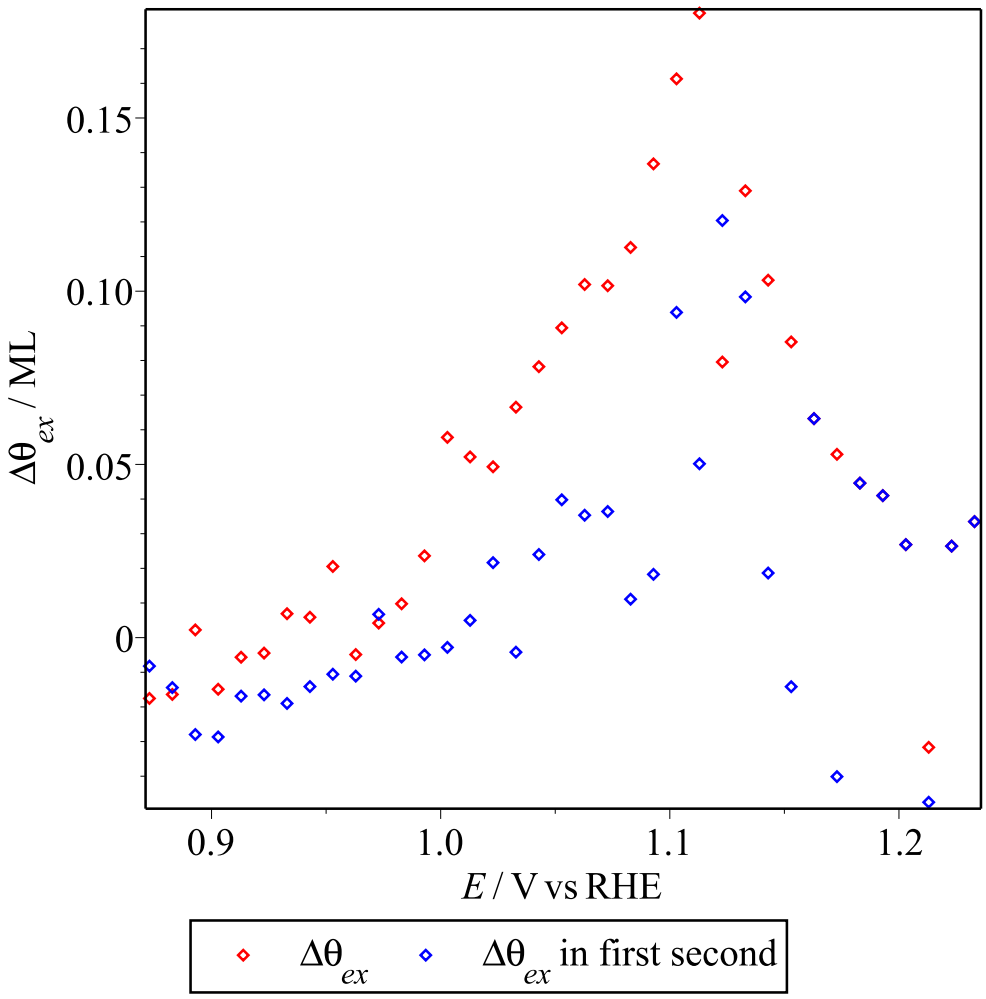

Figure 3.76: Change in θ_{ex} for oxidation portion of potential steps on Pt(100) from 0.85 to 1.20 V. The red points are changes in θ_{ex} for the the whole step, the blue points are changes in θ_{ex} for first second of the step. Data from EC file 57 at the CH4977 beamtime at ID31 at the ESRF in July 2017.

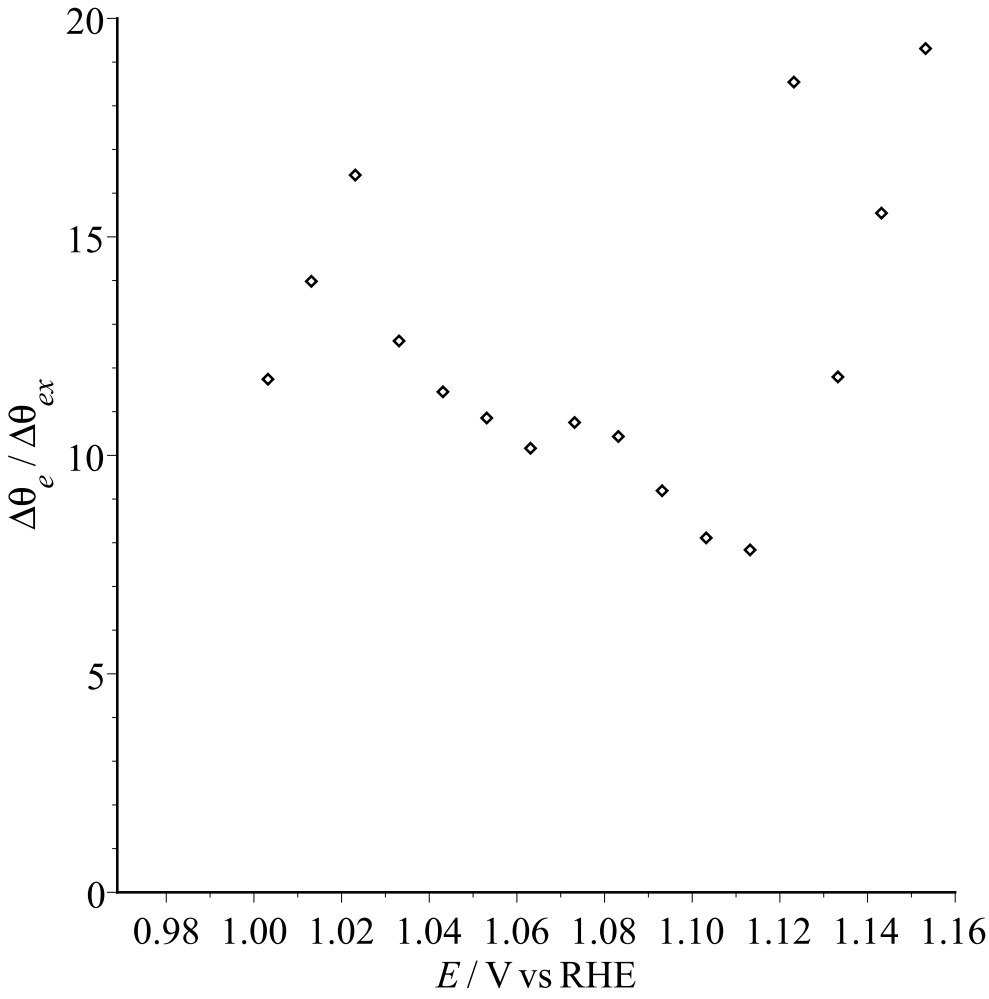

Figure 3.77: $\frac{\Delta\theta_e}{\Delta\theta_{ex}}$ plot for oxidation portion of potential steps on Pt(100) with flat part from 1.0 to 1.11 V. Data from EC file 57 at the CH4977 beamtime at ID31 at the ESRF in July 2017.

that a slope of half the maximum value would define the ends of the range. Here as middle panels in Fig. 3.78, Fig. 3.79, and Fig. 3.80 show, all parts with derivatives higher than half of maximum are included in the middle part in which θ_e increases very fast. Also large derivatives after 1 s are removed as meaningless because they come from noise in current data. The functions of fitted lines of θ_e vs $\log_{10}t$ are shown on the top of each figure, also the slopes and intercepts for functions under all potential steps from 0.87 to 1.22 V are shown in Fig. 3.81.

Also, θ_{ex} vs log$t$ plots are treated in the same way, but these curves increase directly with large noise close the largest time, with curves of steps to 0.87 V, 1.07 V and 1.22 V as examples in Fig. 3.82, and the slopes vs potential are shown in Fig. 3.83. The slope is steady at 0 ML before 0.95 V, then has a sharp peak from 1 to 1.2 V centred at 1.1 V with top as 0.045 ML, and then returns back to around 0 ML after 1.2 V.

Discussion on Potential Steps of Pt(100)

The θ_e from potential steps are shown as Fig. 3.78, 3.79, and 3.80, and summarized in Fig. 3.74 and 3.81. Different from the literature, the charge vs log$t$ plots only linearly increase in a limited time range when log$t$ is around -2 to 0, or just for the first second of each step, and keeps flat before and after the range, but it linearly increases over a very large range in the reference shown in Section 2.2.6 [103, 104]. The fitted lines of these limited ranges show how fast the electrons transfer when the potential changes from one value to another. The slope is steady at 0.3 ML before 0.95 V, then linearly increases from 0.31 ML to 1.1 ML, when potential increases from 0.95 V to 1.22 V, later than 0.9 V from Conway's research, of which the Pt surfaces were reacted in 0.5 M H_2SO_4, and its oxide peak starts from 0.8 V as a flat

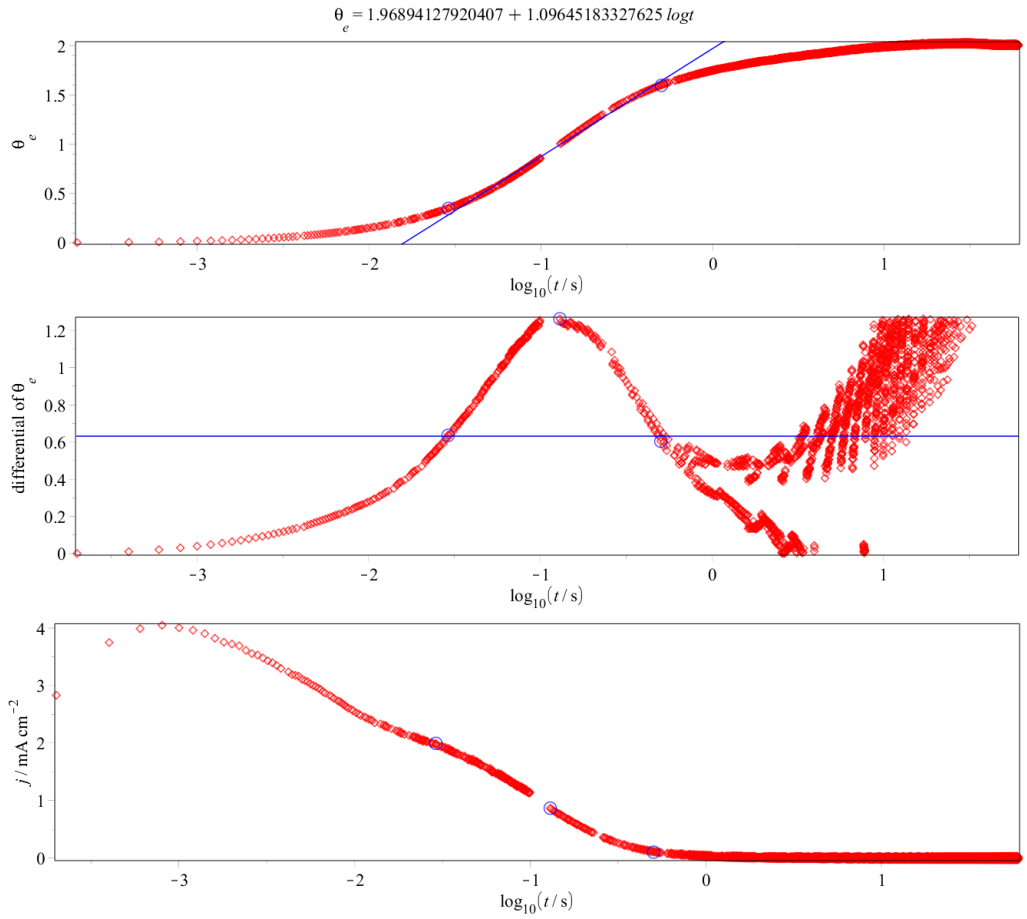

Figure 3.78: θ_e vs $\log_{10}$time (upper), derivative (middle) and current density (bottom) for the oxidation portion of potential step to 1.22 V on Pt(100) in 0.1 M $HClO_4$ from the double layer. The two circles in both diagrams are left and right end point for the range of data to fit the line. The line in upper diagram is the fitted line and its function. The horizontal line in the differentive diagram is half the maximum of the differentive peak. Data from EC file 57 at the CH4977 beamtime at ID31 at the ESRF in July 2017.

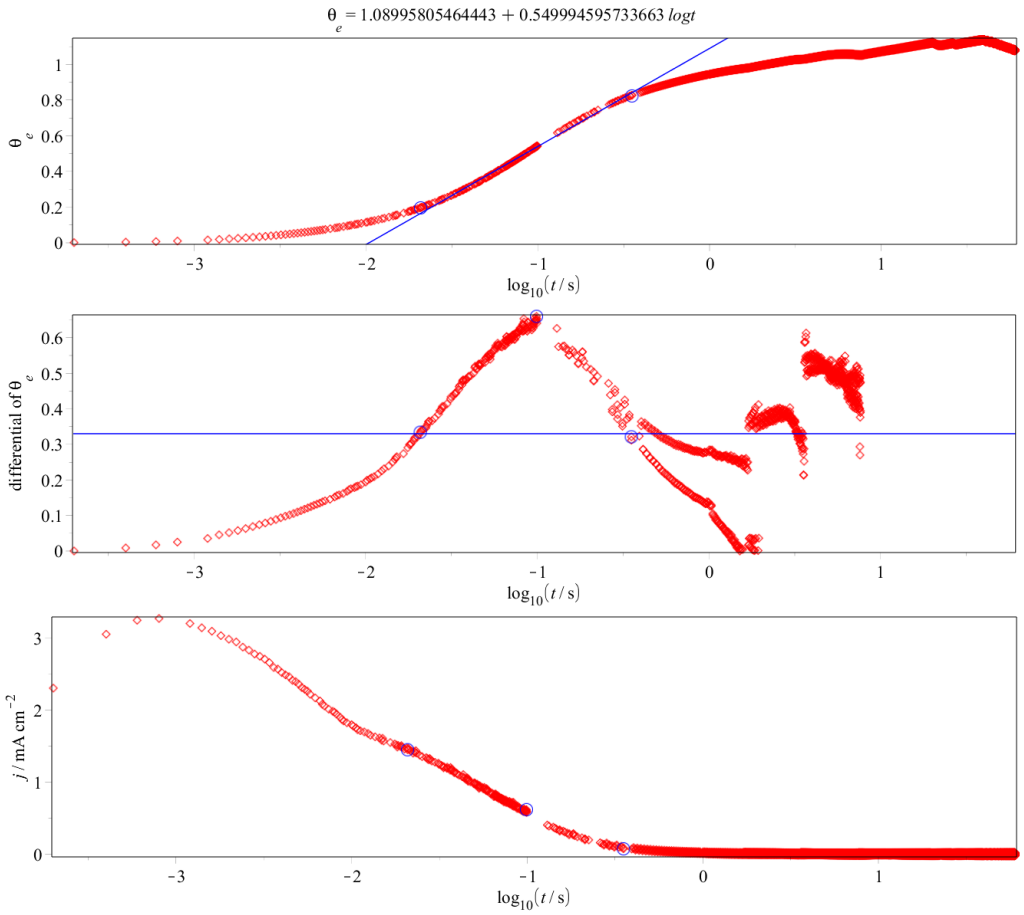

Figure 3.79: θ_e vs $\log_{10}$time (upper), derivative (middle) and current density (bottom) for the oxidation portion of potential step to 1.07 V on Pt(100) in 0.1 M $HClO_4$ from the double layer. The line in upper diagram is the fitted line and its function. The horizontal line in the differentive diagram is half the maximum of the differentive peak. Data from EC file 57 at the CH4977 beamtime at ID31 at the ESRF in July 2017.

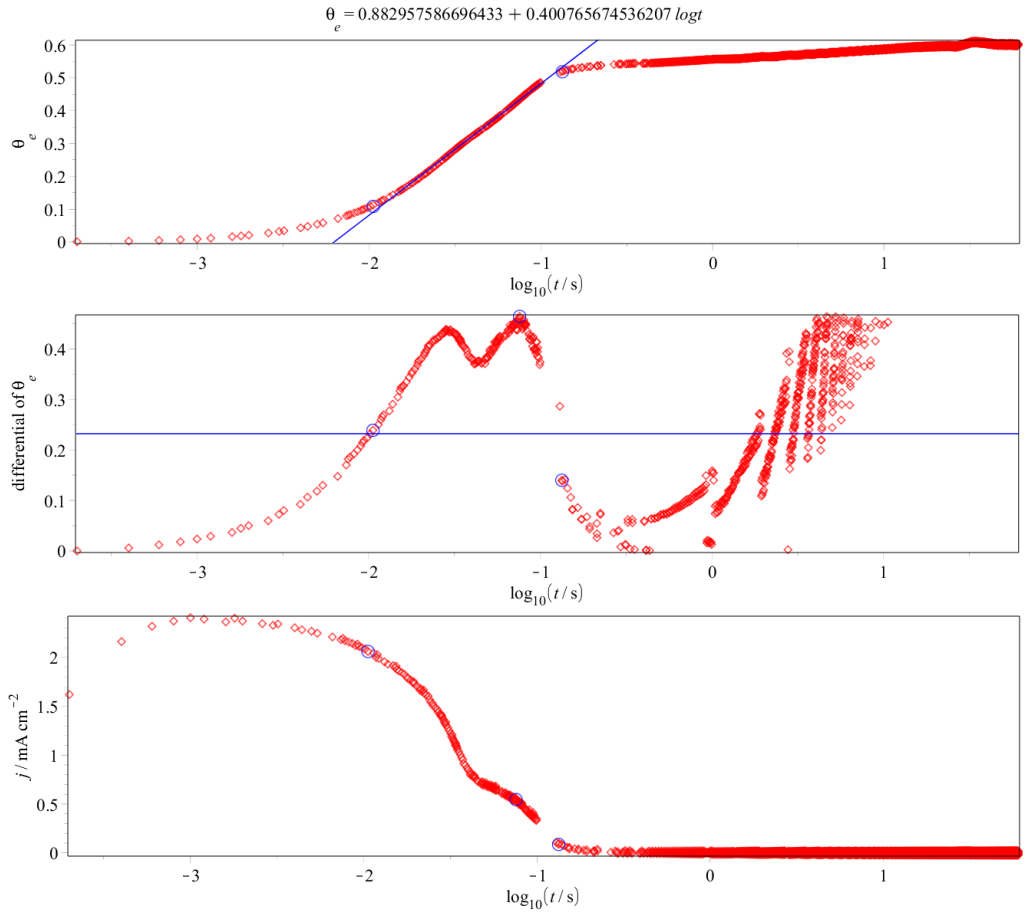

Figure 3.80: θ_e vs $\log_{10}$time (upper), derivative (middle) and current density (bottom) for the oxidation portion of potential step to 0.87 V on Pt(100) in 0.1 M $HClO_4$ from the double layer. The line in upper diagram is the fitted line and its function. The horizontal line in the differentive diagram is half the maximum of the differentive peak. Data from EC file 57 at the CH4977 beamtime at ID31 at the ESRF in July 2017.

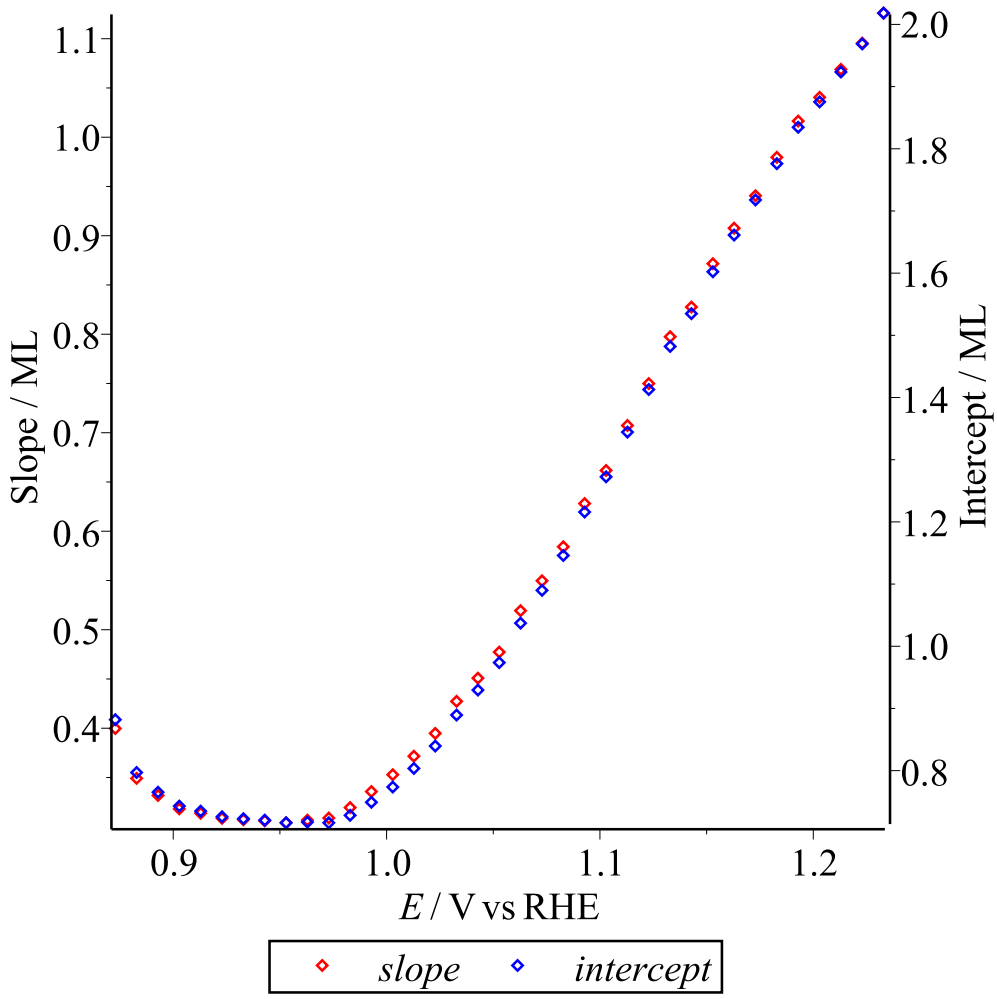

Figure 3.81: The slopes and intercepts of fitted lines for θ_e vs $\log_{10}$time spectra of oxidation potential steps from 0.87 V to 1.22 V on Pt(100) in 0.1 M $HClO_4$ from the double layer. Data from EC file 57 at the CH4977 beamtime at ID31 at the ESRF in July 2017.

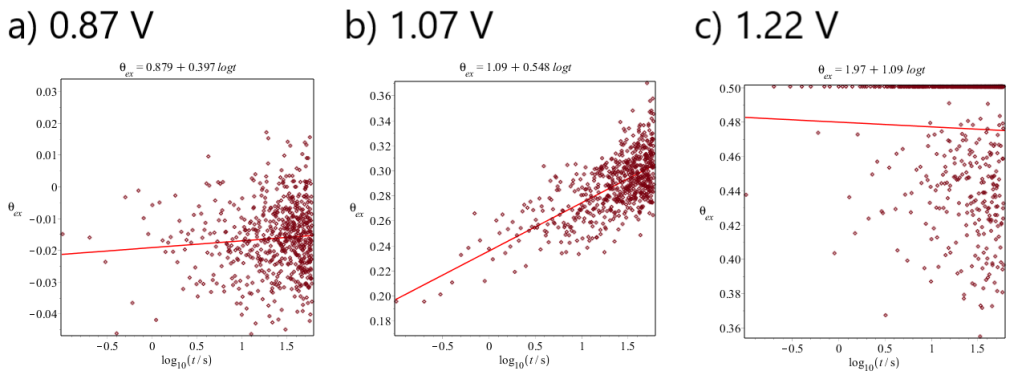

Figure 3.82: θ_{ex} vs $\log_{10}$time plots and fitted lines for oxidation portion of potential step to (a) 0.87 V, (b) 1.07 v and (c) 1.22 V on Pt(100) in 0.1 M $HClO_4$. Data from EC file 57 at the CH4977 beamtime at ID31 at the ESRF in July 2017.

high stage [104]. The slopes of the linearly increasing part are also linearly related to the potential, but they are much higher than 30 μC cm^{-2} (0.14 ML) to 60 μC cm^{-2} (0.29 ML) in Conway's research [104], mostly because the double layer charges are not removed, and different oxidation reactions may occur as the electrolyte here is 0.1 M $HClO_4$ but it was 0.5 M H_2SO_4 in reference [104].

For θ_{ex} vs log$t$ plots, all of the curves increase linearly with large noise near the largest time, but its slope vs potential doesn't increase linearly, it has a sharp peak from 1.0 V to 1.2 V centred at 1.1 V, because the Pt extraction only happens in this potential range, and the peak-shaped curve fits the normal distribution.

For $\Delta\theta_e$ vs $\Delta\theta_{ex}$, θ_{ex} mainly increases between 1.0 and 1.1 V in Fig. 3.75, $\frac{\Delta\theta_e}{\Delta\theta_{ex}}$ stays around 11.10 in this range in Fig. 3.77, so e$^-$ transfer from EC and Pt extraction from X-ray is linearly related during oxide peak from 1.0 to 1.1 V, other reactions with e$^-$ transfer are happening at the same time of Pt extraction, and this fact supports the straight θ_e vs θ_{ex} line from CV data in Section 3.2.2 and 3.2.3. But the ratio 11.10 is much higher than 3 to 4 e$^-$s transferred per extracted Pt from CV

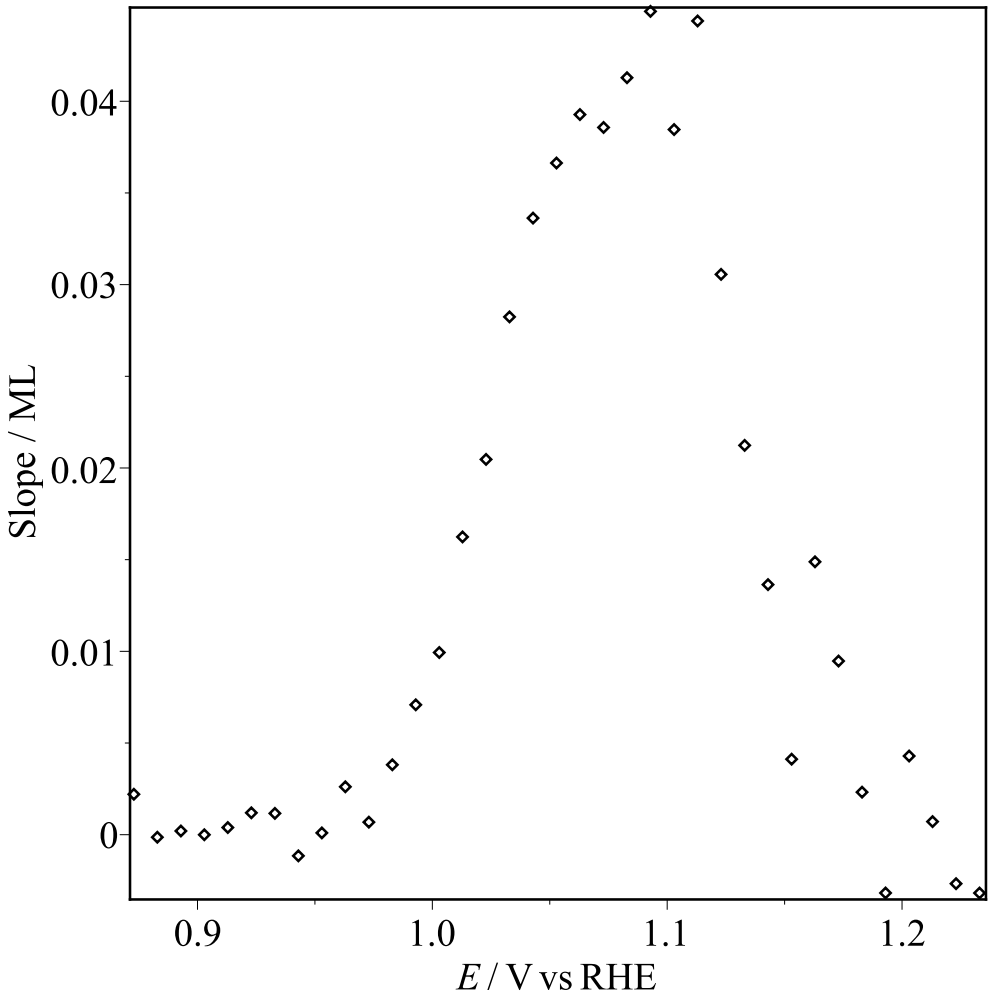

Figure 3.83: The slopes of fitted lines for θ_{ex} vs log$t$ plots of oxidation potential steps from 0.87 V to 1.22 V on Pt(100) in 0.1 M $HClO_4$ from the double layer. Data from EC file 57 at the CH4977 beamtime at ID31 at the ESRF in July 2017.

data, because the double layer charges are not removed, also during the potential step experiment, the potential goes back to the original potential 0.42 V and causes reduction reactions to happen after each step, so the Pt surface is extracted and restructured after each step, and this makes the reaction different because the Pt surface isn't flat and smooth any more for the steps after the first step with Pt extraction.

3.2.5 Pt(100) Potential Steps with New Dataset

In this subsection, a second data set of oxidation potential steps for Pt(100) is treated to find the direct logarithmic relation between θ_e, θ_{ex} and log time with the way to treat EC data in Section 3.2.4 and the way to treat X-ray data in Section 3.2.2. The initial potential for the steps is slightly different from before.

Oxidation Potential Steps for Pt(100) from the Double Layer

The oxidation portion of potential steps from the double layer between 0.574 and 1.574 V vs RHE is from EC file Pt100_18 and corresponding X-ray file Pt100_12 at the CH5918 beamtime at ID31 at the ESRF in July 2021. The potential and current of the whole potential steps experiment is shown as Fig. 3.84, and the potential and X-ray intensity of the whole potential steps experiment is shown as Fig. 3.85. For each step, the potential is held at E_0 as 0.2 V vs 3.4 M Ag/AgCl (0.474 V vs RHE) for 5 s, then sharply goes up inside 1 data point to a potential, E_{step} like 0.3 V vs 3.4 M Ag/AgCl (0.574 V vs RHE) for 1st step, and is held at it for 20 s, then returns to E_0 sharply inside 1 data point to a potential. The E_0 and E_{step} vs RHE of different steps is shown in Fig. 3.86. Inside the 20 s of a step, the current sharply increases to

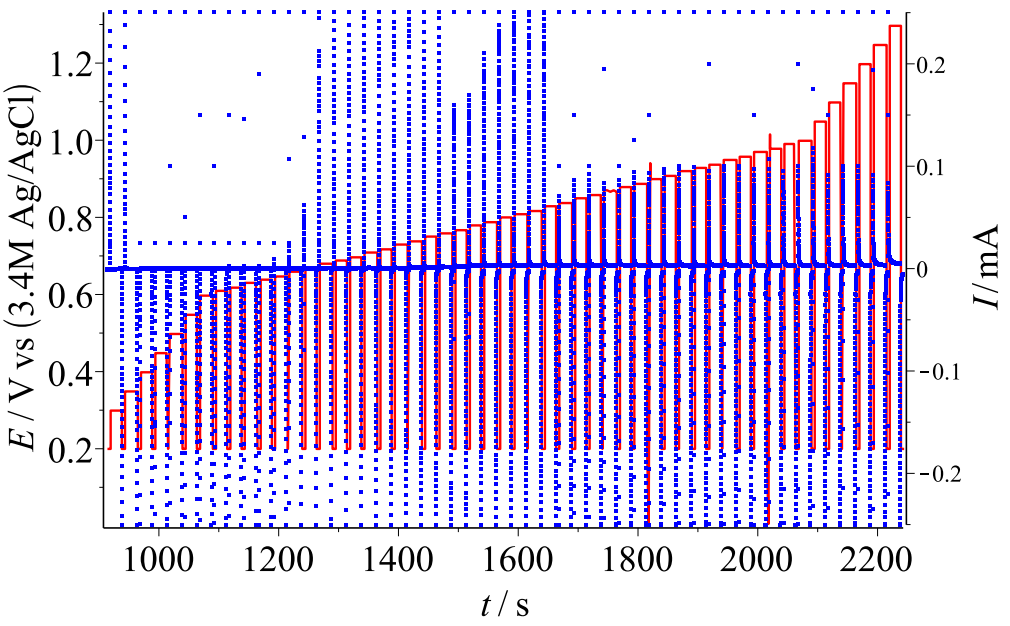

Figure 3.84: Potential and Current plots of Pt(100) Potential steps in 0.1 M $HClO_4$ from the double layer. The red curve is potential vs 3.4 M Ag/AgCl electrode and the blue curve is current. Data from EC file Pt100_18 at the CH5918 beamtime at ID31 at the ESRF in July 2021.

a high point, then back to 10 μA inside 1 s. For the X-ray, the intensity shows only noise as usual if it's out of potential range of extraction; if the step is in the potential range of extraction, also 500 to 800 s in Fig. 3.85, the intensity sharply decreases at the first data point, then slowly decreases for ∼18 s, last sharply goes up till nearly intensity of first data point, just like the Fig. 3.87 as a step to 1.074 V vs RHE.

Coverages θ_e and θ_{ex} from Potential Steps

Similar as Section 3.2.4, the 10 μA current from beam damage is removed by dividing average current of last 100 points of total 220 to 250 points, as later half part of total 20 s. Then, θ_e is translated from the charge density from the integration of

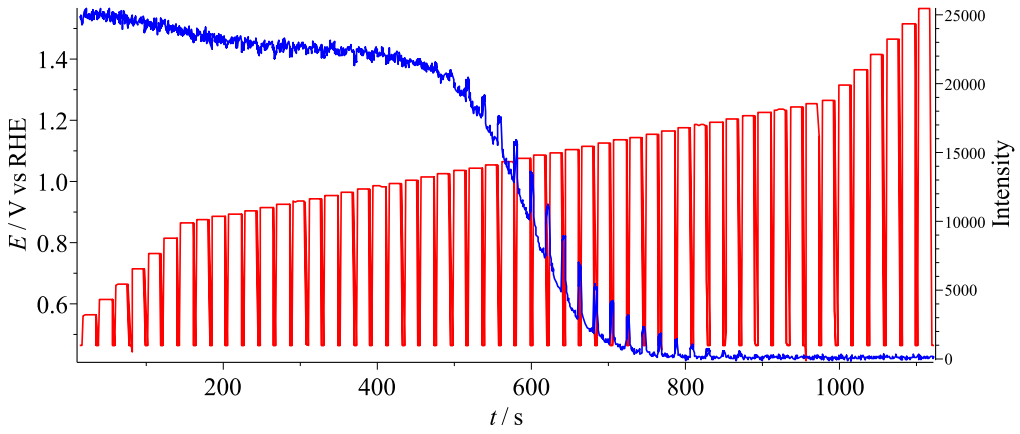

Figure 3.85: [Potential and X-ray intensity plots of Pt(100) Potential steps in 0.1 M $HClO_4$ from the double layer. The red curve is potential vs 3.4 M Ag/AgCl electrode and the blue curve is X-ray intensity. Data from X-ray file Pt100_12 at the CH5918 beamtime at ID31 at the ESRF in July 2021.

current density and time. Also, θ_{ex} is normalized from X-ray intensity with function $0.5007\times(1-\sqrt{\frac{I}{I_{0.9V}}})$ from Section 2.3.4, and here intensity of first data point of step to 0.63 V vs 3.4 M Ag/AgCl (0.904 V vs RHE) is used as standard of normalization. $\Delta\theta_e$ and $\Delta\theta_{ex}$ between last number and first number of each step is shown in Fig. 3.88. $\Delta\theta_e$ keeps at ~0.08 ML till 0.95 V, then increases to ~0.8 ML until 1.25 V and stays there, lastly sharply increases after 1.4 V until 1.8 ML of last data point at 1.574 V. $\Delta\theta_{ex}$ keeps around 0 until 1.0 V, then has a sharp peak with height 0.12 ML centred at 1.1 V from 1.0 V to 1.2 V, finally back to 0 until the end.

Similar as Section 3.2.2, $\Delta\theta_e$ and $\Delta\theta_{ex}$ are compared to get a ratio in Fig. 3.89. Here, $\frac{\Delta\theta_e}{\Delta\theta_{ex}}$ is heavily noisy before 1.04 V, then stays flat between 1.04 and 1.18 V with average as 5.79, and then increases after 1.18 V. The Pt extraction, or flat part in Fig. 3.89 has wider potential range 1.04 to 1.18 V than 1.0 to 1.11 V from Section 3.2.2, but its average $\frac{\Delta\theta_e}{\Delta\theta_{ex}}$ is only half of 11.10 from Section 3.2.2.

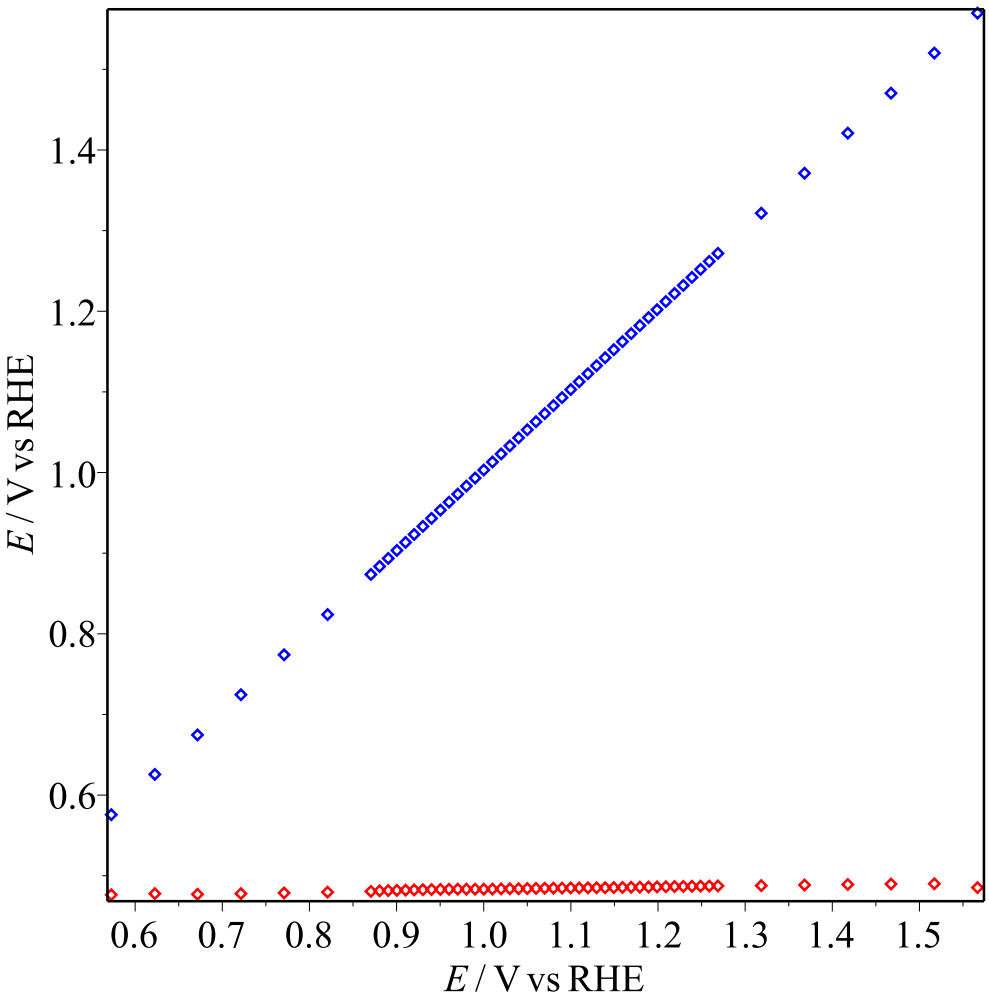

Figure 3.86: [The initial and final potentials of Pt(100) Potential steps in 0.1 M $HClO_4$ from the double layer. The red points are initial potential, E_0. The blue points are final points, E_{step}. Data from EC file Pt100_18 at the CH5918 beamtime at ID31 at the ESRF in July 2021.

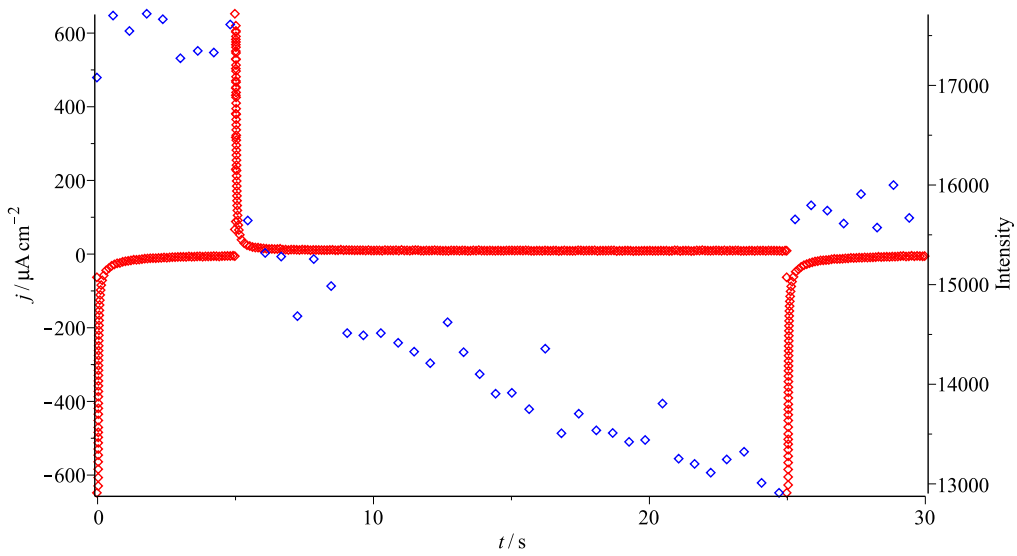

Figure 3.87: The oxidation portion of potential step to 1.074 V on Pt(100) in 0.1 M $HClO_4$ from the double layer. The red curve is current and the blue curve is X-ray intensity. Data from EC file Pt100_18 and corresponding X-ray file Pt100_12 at the CH5918 beamtime at ID31 at the ESRF in July 2021.

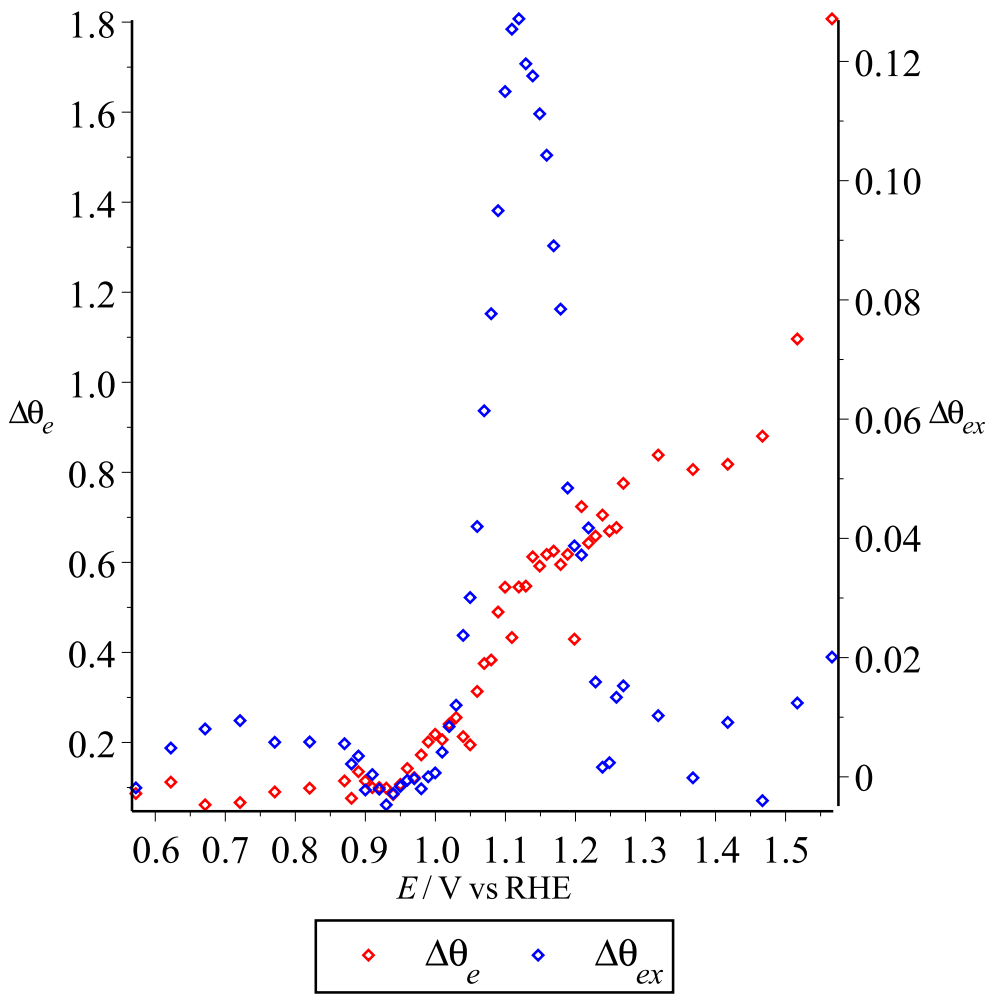

Figure 3.88: $\Delta\theta_e$ and $\Delta\theta_{ex}$ of Pt(100) Potential steps in 0.1 M $HClO_4$ from the double layer. The red points are $\Delta\theta_e$ and the blue points are $\Delta\theta_{ex}$. Data from EC file Pt100_18 and corresponding X-ray file Pt100_12 at the CH5918 beamtime at ID31 at the ESRF in July 2021.

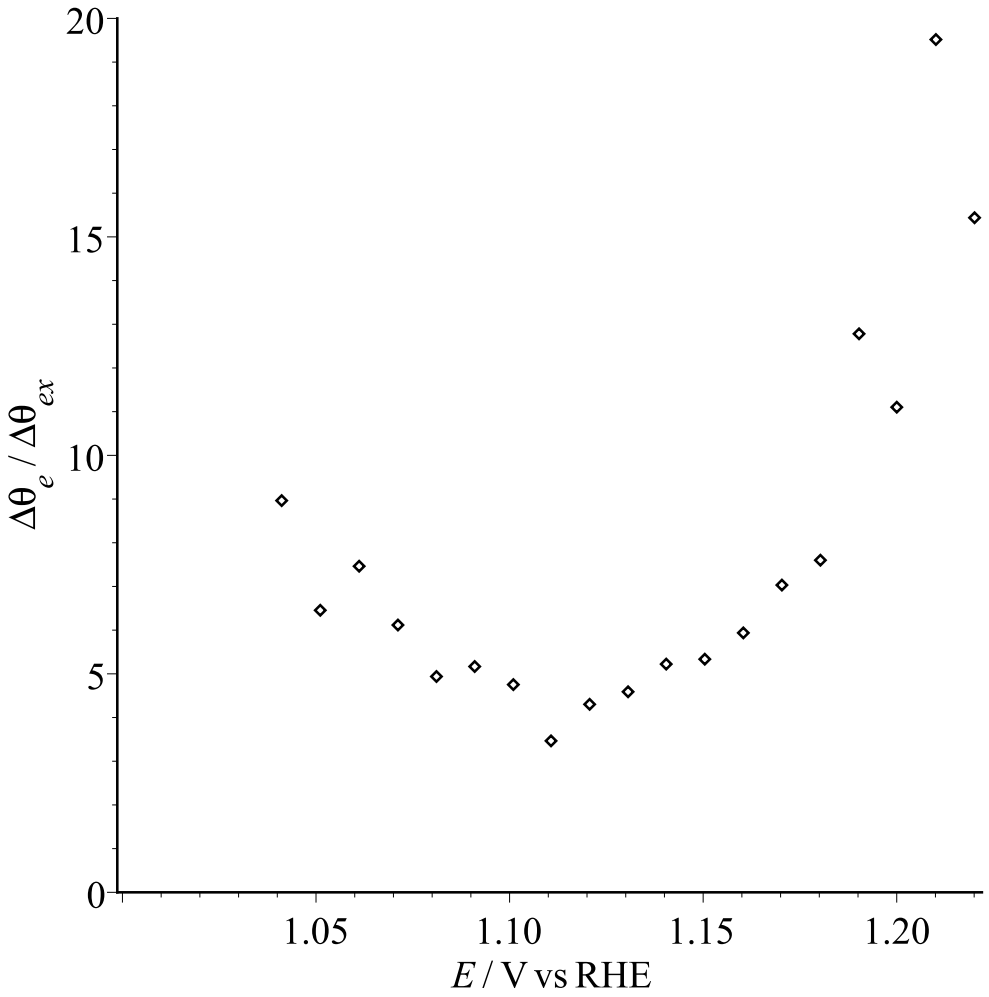

Figure 3.89: $\frac{\Delta\theta_e}{\Delta\theta_{ex}}$ plot of Pt(100) Potential steps in 0.1 M $HClO_4$ from the double layer with flat part from 1.04 to 1.18 V. Data from EC file Pt100_18 and corresponding X-ray file Pt100_12 at the CH5918 beamtime at ID31 at the ESRF in July 2021.

Coverage θ_e and θ_e vs $\log_{10}$time from Potential Steps

Similar as Section 3.2.4, θ_e and θ_{ex} in previous step is compared with $\log_{10}$time to learn the charging speed in potential steps. They are treated in same way, with half of maximum of derivative for θ_e vs $\log_{10}$time as two endpoints for the range of fast increasing part of θ_e, but the double layer charges haven't been removed. The slopes and intercepts of different steps is shown as Fig. 3.90. Different from Fig. 3.81 in Section 3.2.4, the slope here slowly increases from 0 to 0.3 as potential from 0.574 to 1.574 V, and the intercept here keeps around 0 until 1.0 V, then linearly increases to 0.6 ML from 1.0 to 1.3 V, then stays there after 1.3 V.

For θ_{ex} vs log$t$, same as Section 3.2.4, the θ_{ex} vs log$t$ increases linearly with large noise near largest time, so they are fitted to get the slopes. The slope vs potential is shown in Fig. 3.91, same as Section 3.2.4, the slope is steady at 0 ML before 1.0 V and after 1.2 V, and has a sharp peak between 1.0 V and 1.2 V centred around 1.1 V with top as 0.045 ML.

Discussion on Potential Steps of Pt(100)

θ_e of oxide peak from EC data of potential steps is 0.8 - 0.08 = 0.72 ML, nearly half of 1.5 ML from potential step at CH4977 in Section 3.2.4, and this is because current data at first 0.1 s of some steps are lost as Fig. 3.92 shows for step to 1.114 V. The ratio $\frac{\Delta\theta_e}{\Delta\theta_{ex}}$ during extraction is 5.79, much lower than 11.10 from Section 3.2.4, mainly for the lower charges caused by this current data missing, but it is still steady from 1.04 to 1.18 V, which provide the linear relation between charges and Pt extraction.

For the θ_e vs $\log_{10}$time plots, similar to Section 3.2.4, it only increases in a limited time range before 1 s, which is different from infinite increase of reference [103, 104].

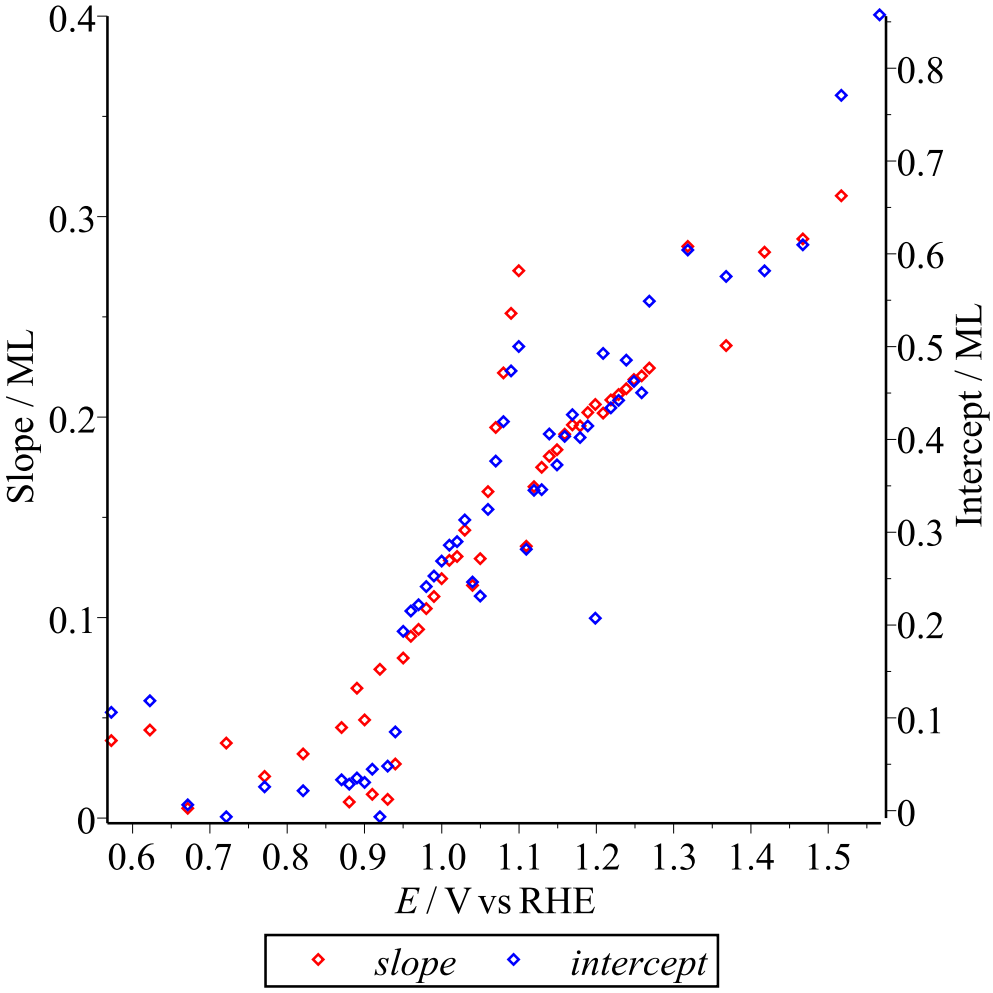

Figure 3.90: Slope and intercept for fitted lines for θ_e vs log$t$ spectra of Pt(100) Potential steps in 0.1 M $HClO_4$ from the double layer. The red points are slope and the blue points are intercept. Data from EC file Pt100_18 at the CH5918 beamtime at ID31 at the ESRF in July 2021.

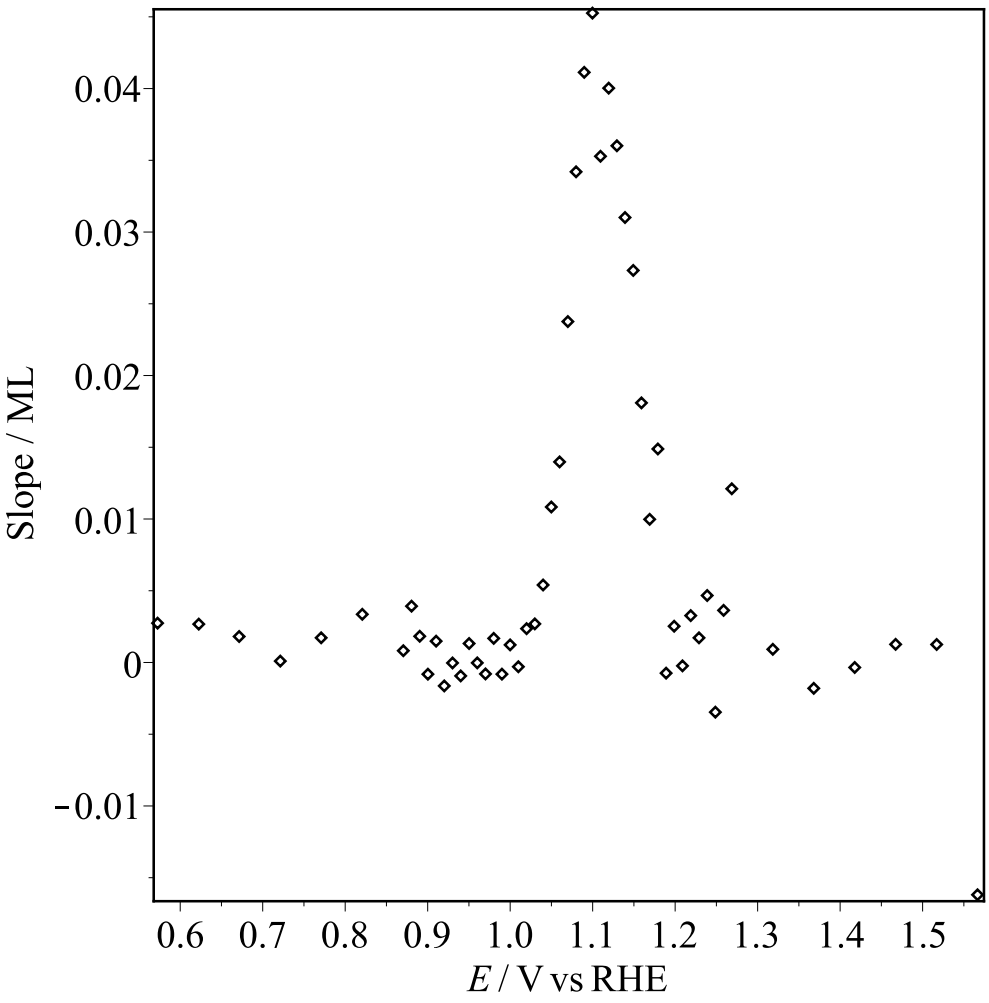

Figure 3.91: Slope and intercept for fitted lines for θ_{ex} vs log$t$ plots of Pt(100) Potential steps in 0.1 M $HClO_4$. The red points are slope and the blue points are intercept. Data from X-ray file Pt100_12 at the CH5918 beamtime at ID31 at the ESRF in July 2021.

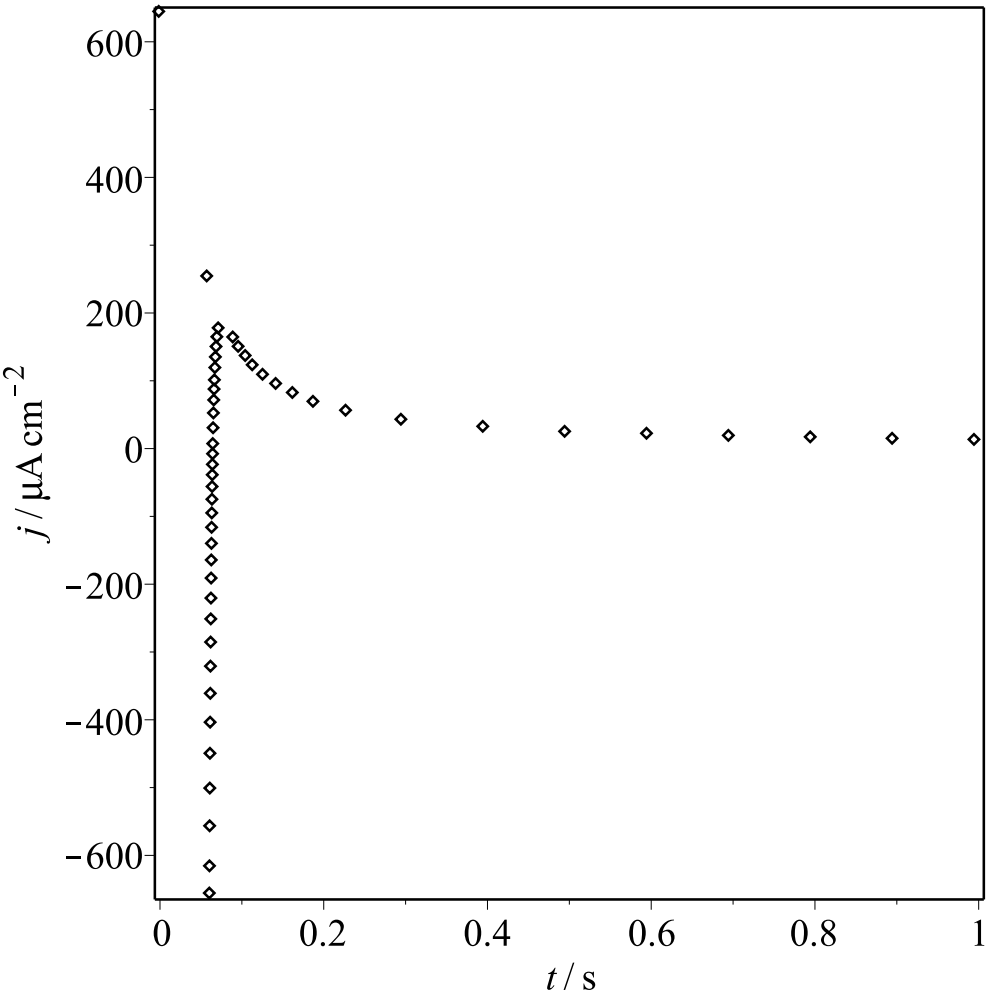

Figure 3.92: The current density for the oxidation portion of potential step to 1.114 V on Pt(100) in 0.1 M $HClO_4$ from the double layer. Data from EC file Pt100_18 at the CH5918 beamtime at ID31 at the ESRF in July 2021.

For the increasing rate, the slope is steady at 0.03 ML before 0.9 V, then linearly increases after 0.9 V. The slope increases from 0 to 0.2 ML when potential is from 0.9 V to 1.2 V, and to 0.31 ML when potential is to 1.5 V, similar shape with reference [104], much lower than Section 3.2.4, but more closer to Conway's research, as 30 μC cm^{-2} (0.14 ML) at 0.9 V, 60 μC cm^{-2} (0.29 ML) at 1.2 V, and 80 μC cm^{-2} (0.38 ML) at 1.5 V [104]. The slopes are a little lower than reference, because too much current points are missed at first 1 s for each steps as Fig. 3.92 shows, most double layer currents and a little part of charges for reactions are included in the missing current points, which makes θ_e lower than expected.

For the θ_{ex} vs log$t$ plots, same as Section 3.2.4, the curves increases linearly with large noise near the largest time, and the slope vs potential plot is nearly as same as Fig. 3.83, also steady at 0 ML before 1.0 v and after 1.2 V, same has a peak from 1.0 to 1.2 V centred as 1.1 V, and the peak height is also same as 0.045 ML. This means the Pt extraction happens in the same way as another Pt(100) surface sample in Section 3.2.4, also the reactions on two surfaces should be same, and this also means their difference on θ_e must be caught by some error, like the loss of 0.1 s current data as shown in Fig. 3.92.

3.2.6 Pt(100) Sweep Holds

In this subsection, the data of sweep holds for Pt(100), in which potential sweeps similar to cyclic voltammetry but with potential holds before reversing. It is treated to find the direct logarithmic relation between current density and structure factor vs log time with a method similar to that in Section 3.2.2.

Sweep Hold experiments for Pt(100)

Sweep hold experiments with maximum potential (E_{hold}) from 0.892 to 1.282 V are from EC file Pt100_19 and corresponding X-ray file Pt100_13 at the CH5918 beamtime at ID31 at the ESRF in July 2021. In each cycle of sweep holds, the potential is held at 0.154 V vs RHE (-0.12 V vs 3.4 M Ag/AgCl) for 5 s, then sweep to E_{hold} as 0.892 to 1.282 V for different cycles with sweep rate as 20 mV/s similar as cyclic voltammetry, then is held at at the maximum potential for 20 s, next sweeps down to minimum potential at 0.096 V vs RHE, and lastly goes up back to the start point 0.154 V for the next cycle. Fig. 3.93 as an example shows the X-ray voltammogram for cycle 25 of the sweep holds with E_{max} as 1.112 V vs RHE.

The voltammogram of all cycles of sweep holds is shown as Fig. 3.94. The pair of H/OH mixed peaks at ∼0.32 V increases in size with cycle numbers when $E_{hold} <$ 1.0 V, and decreases but with an extra pair of peaks at ∼0.25 V increasing with cycle numbers when $E_{hold} > 1.0$ V. Also, the Pt oxide peak after 0.95 V and corresponding reduction peak at 0.8 V increases when E_{hold} increases cycle by cycle.

Charge Density of Sweep Holds for Pt(100)

Similar as previous sections, the charge density (σ) was found by integration of time and current density, and the charge densities of the anodic and cathodic processes are shown in Fig. 3.95. The difference between anodic and cathodic charge density becomes higher and higher when Pt oxidation continues as E_{max} increases.

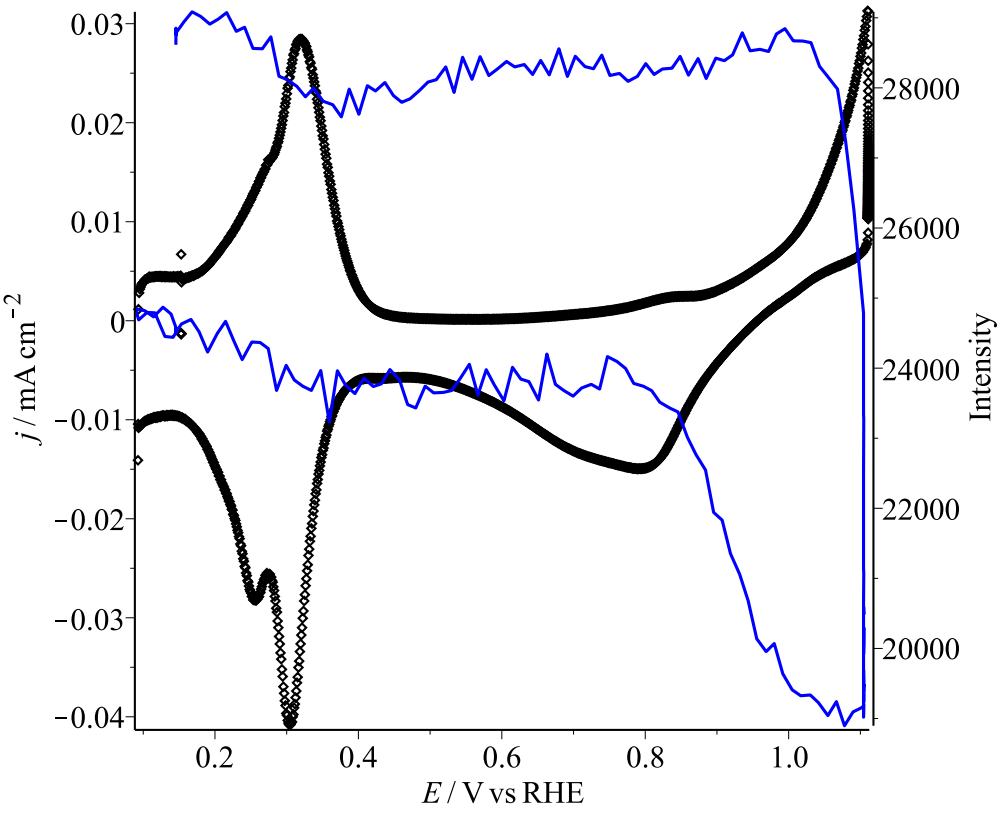

Figure 3.93: X-ray voltammogram of sweep hold cycle 25 with E_{max} as 1.112 V on Pt(100) in 0.1 M $HClO_4$. The black curve is current and the blue curve is X-ray intensity. Data from EC file Pt100_19 and corresponding X-ray file Pt100_13 at the CH5918 beamtime at ID31 at the ESRF in July 2021.

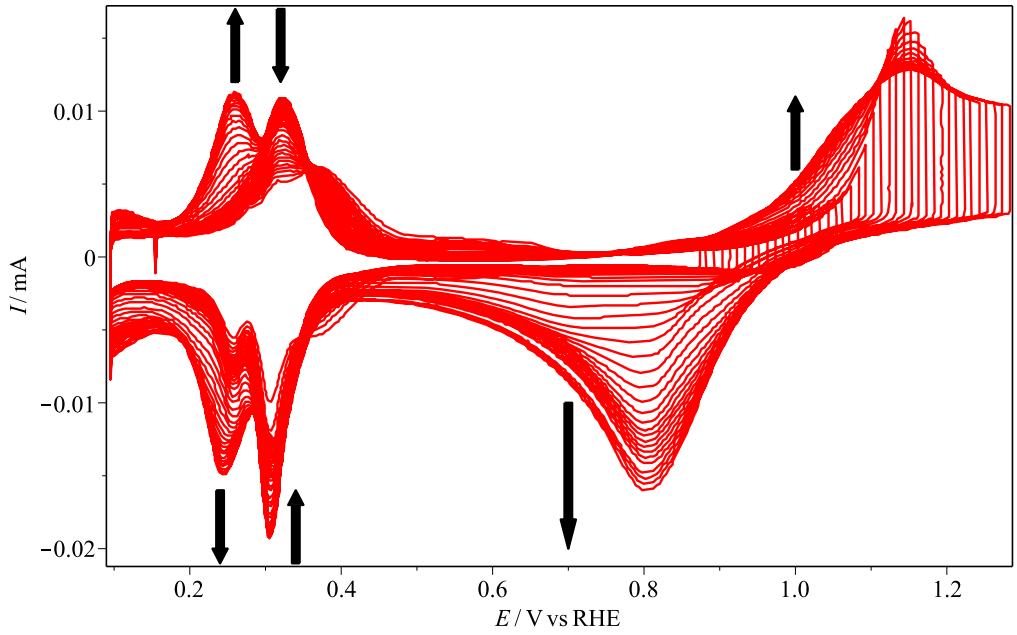

Figure 3.94: Sweep hold voltammogram of Pt(100) in 0.1 M $HClO_4$ from the double layer. Data from EC file Pt100_19 at the CH5918 beamtime at ID31 at the ESRF in July 2021.

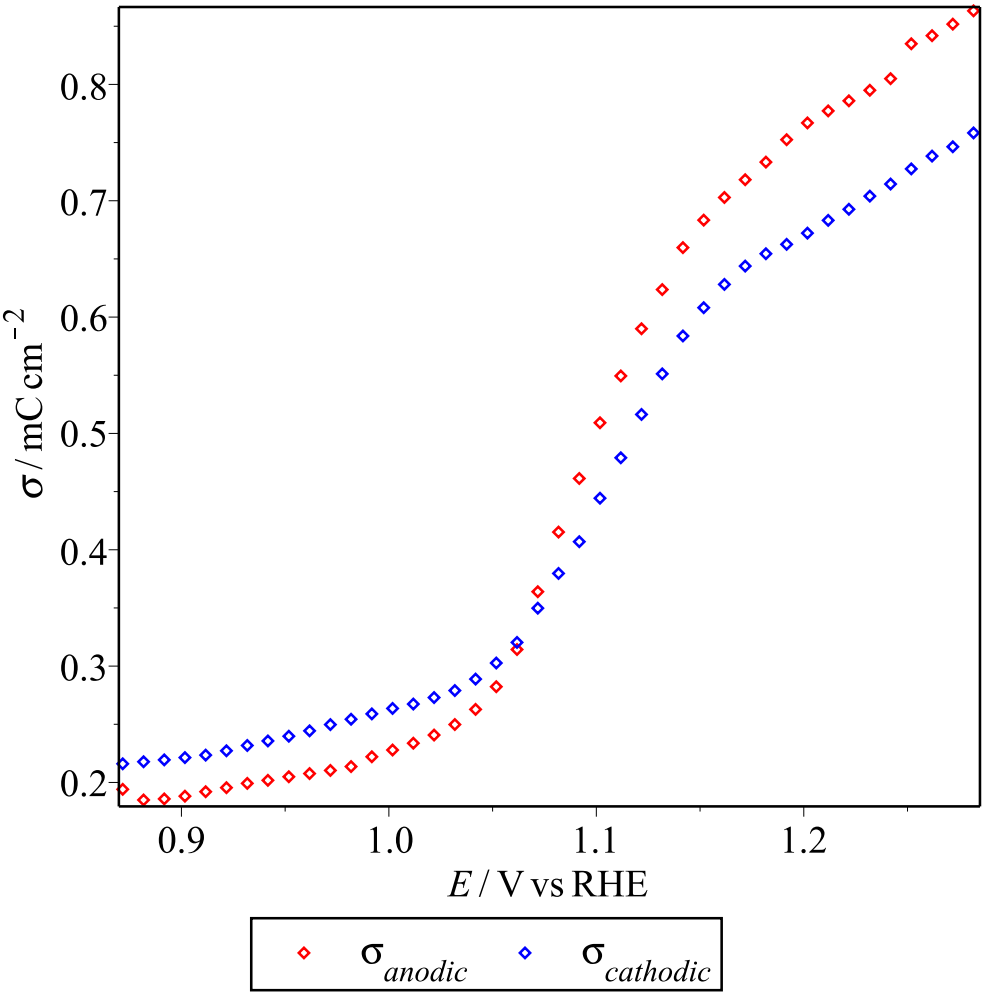

Figure 3.95: The anodic and cathodic charge densities of Pt(100) sweep holds in 0.1 M $HClO_4$ from the double layer. The red points are charge densities of whole anodic process for each cycle, and the blue points are charge densities of whole cathodic process for each cycle. Data from EC file Pt100_19 at the CH5918 beamtime at ID31 at the ESRF in July 2021.

θ_e and θ_{ex} vs $\log_{10}$time

To determine the rate law of the Pt oxide peak, θ_e from EC data and θ_{ex} from X-ray data were plotted vs $\log_{10}$time during the 20 s hold at E_{hold} and compared with each other.

The magnitude of the structure factor was obtained from X-ray data as in Section 2.3.4 by the function $\theta_{ex} = 0.5007 \times (1 - \sqrt{I/I_{0.9V}})$, with $I_{0.9V}$ as the first point at 0.9 V in 5th cycle for all curves. Then compare both θ_e and θ_{ex} to $\log_{10}$time and linear fit the 20 s hold period at E_{hold} of both curves. For example, cycle 25 of sweep holds with E_{hold} as 1.112 V is shown in Fig. 3.96 for θ_e vs $\log_{10}$time and Fig. 3.97 for θ_{ex} vs $\log_{10}$time.

The slopes of θ_e and θ_{ex} vs $\log_{10}$time are shown as Fig. 3.98 with E_{hold} as horizontal coordinate. The slope of θ_e vs $\log_{10}$time sharply increases from 1.05 V to 1.15 V, and the slope of θ_{ex} vs $\log_{10}$time has a sharp peak at the same potential range centred at 1.1 V.

For the slope of θ_e vs θ_{ex} during the 20 s held at E_{max}, it shows as Fig. 3.99. The slope is steady at zero before 1.0 V, then sharply increases to 80 with large noise from 1.0 to 1.15 V, and then is steady at $\sim$10 with more noise after 1.15 V.

Discussion on Sweep holds of Pt(100)

In Fig. 3.95, the difference between anodic and cathodic charge densities stays unchanged before 1.05 V and after 1.15 V, but the anodic charge sharply increases and is much more than cathodic charge from 1.05 V to 1.15 V, which means there are a large part of reaction in Pt oxide peak is irreversible, e.g. a part of Pt extraction.

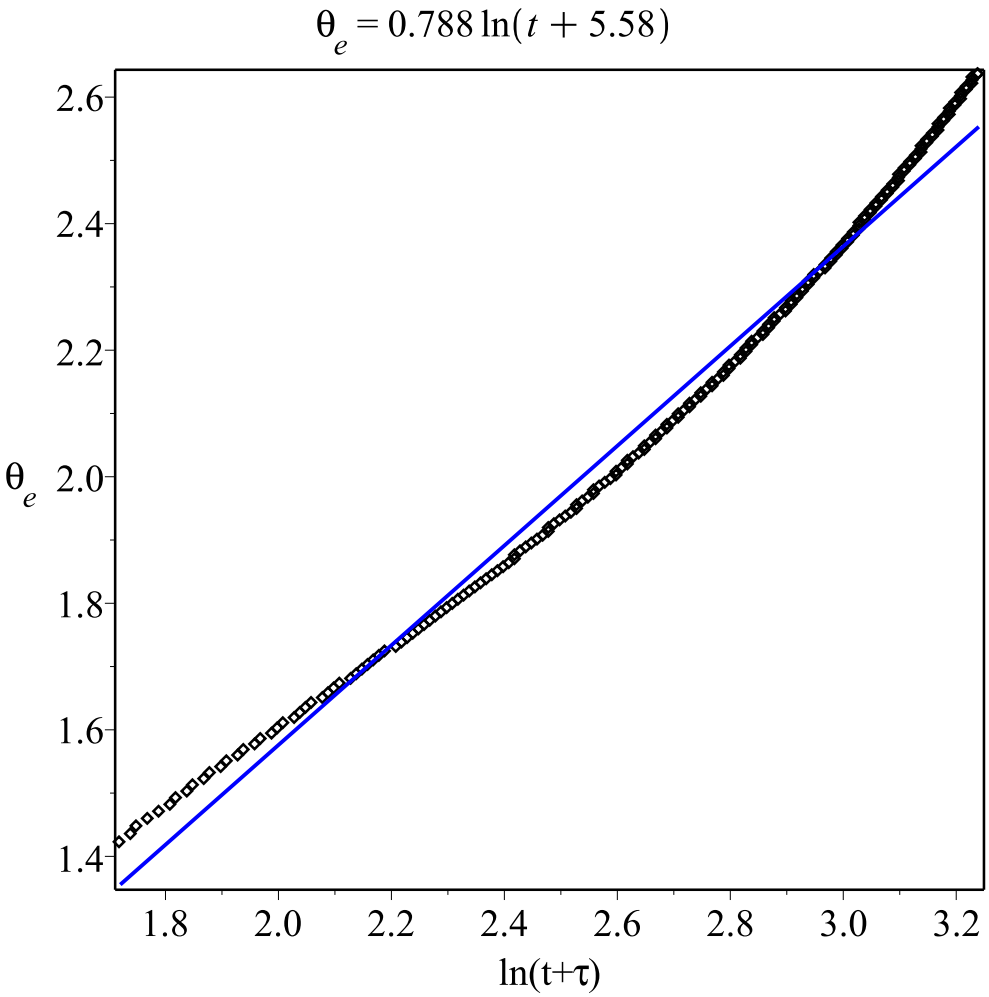

Figure 3.96: θ_e vs $\log_{10}$time of sweep hold cycle 25 with E_{max} as 1.112 V on Pt(100) in 0.1 M $HClO_4$. Data from EC file Pt100_19 at the CH5918 beamtime at ID31 at the ESRF in July 2021.

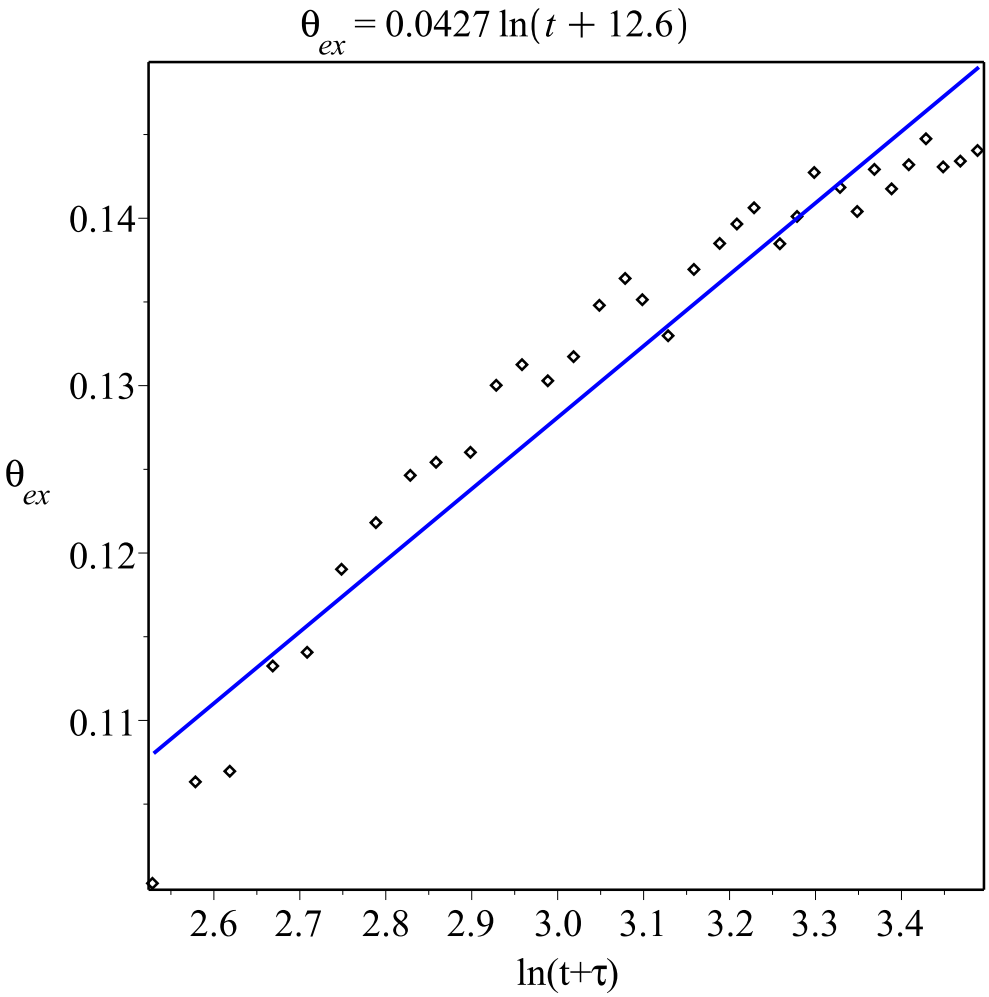

Figure 3.97: θ_{ex} vs $\log_{10}$time of sweep hold cycle 25 with E_{max} as 1.112 V on Pt(100) in 0.1 M $HClO_4$. Data from X-ray file Pt100_13 at the CH5918 beamtime at ID31 at the ESRF in July 2021.

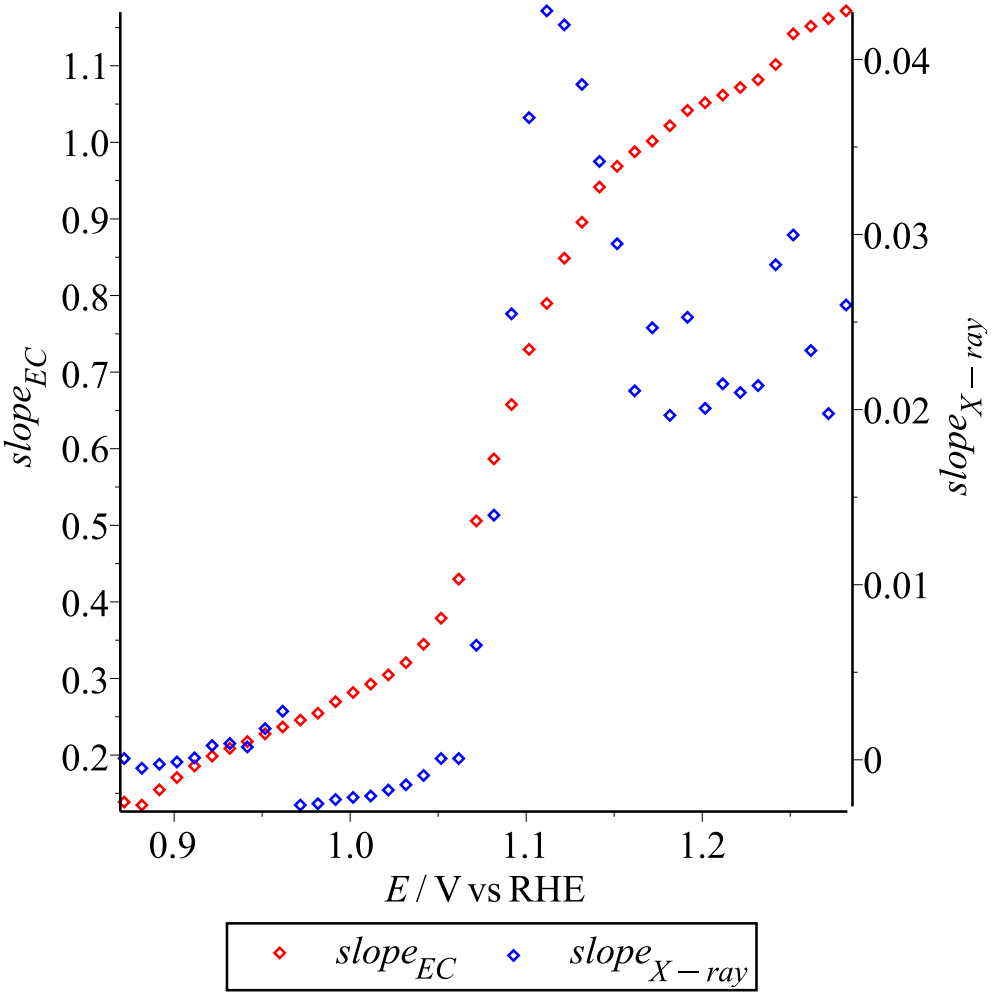

Figure 3.98: The slopes of 20 s on E_{hold} for θ_e and θ_{ex} vs $\log_{10}$(time) of Pt(100) sweep holds in 0.1 M $HClO_4$ from the double layer. The red points are slopes from θ_e vs $\log_{10}$(time), and the blue points are slopes from θ_{ex} vs $\log_{10}$(time). Data from EC file Pt100_19 and corresponding X-ray file Pt100_13 at the CH5918 beamtime at ID31 at the ESRF in July 2021.

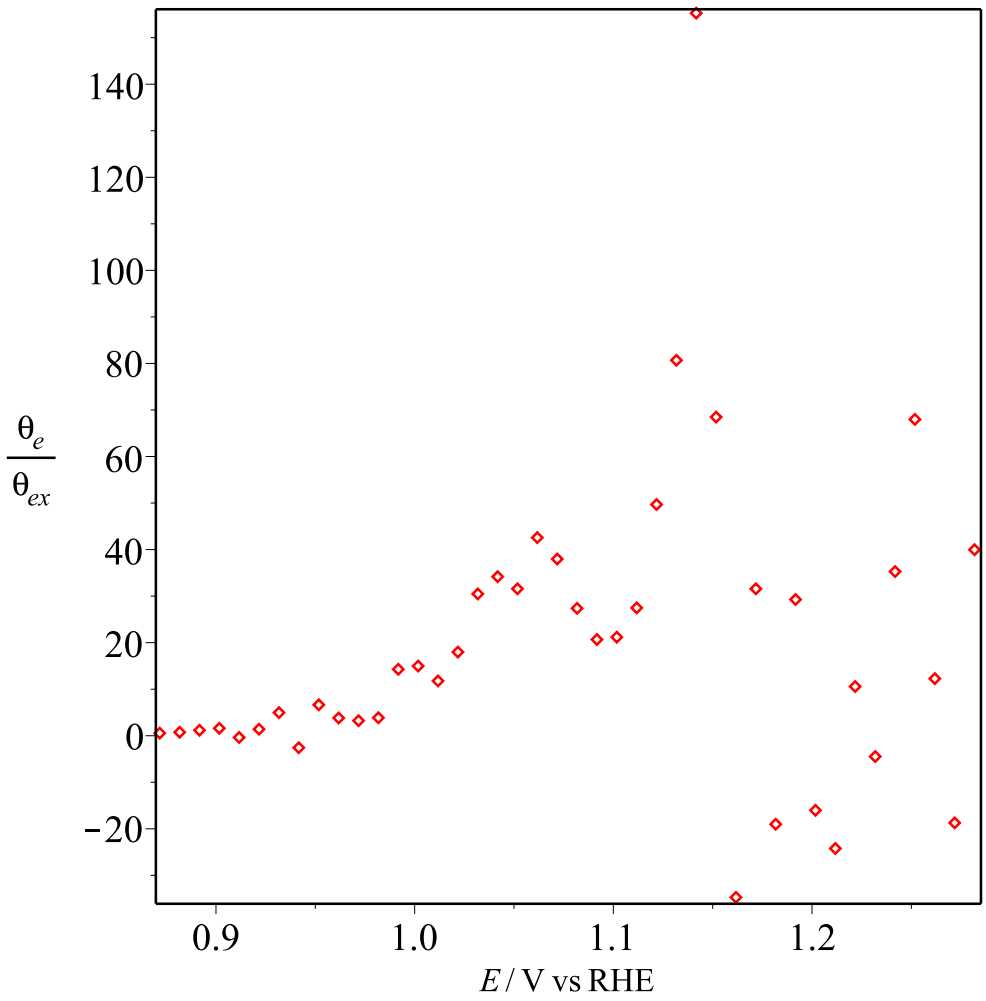

Figure 3.99: The ratio between slopes of 20 sec on E_{max} for θ_e and θ_{ex} vs $\log_{10}$(time) of Pt(100) sweep holds in 0.1 M $HClO_4$ from the double layer. Data from EC file Pt100_19 and corresponding X-ray file Pt100_13 at the CH5918 beamtime at ID31 at the ESRF in July 2021.

For the θ_e vs ln$t$ plot from EC data and θ_{ex} vs ln$t$ plot from X-ray data, they both don't linearly increase vs ln$t$ in Fig. 3.96 and 3.97, and the slopes don't linearly relate to hold potential as shown in Fig. 3.99, which is different from the potential step tests in Section 3.2.4 and 3.2.5, and references [103, 104]. Both slopes stay flat before 1.05 V and after 1.15 V, sharply increase from 1.05 to 1.1 V, and decrease from 1.1 to 1.15 V. They both sharply change from 1.05 and 1.15 V, so the Pt extraction shown by X-ray data happens at the same time with other reactions in the oxide peak like O_{ads} formation shown by EC data, and both reactions grow to fastest reacting speed at ∼1.1 V. However, after 1.15 V, the slope of θ_e is still very high, but the slope of θ_{ex} is steady at a lower number ∼0.02 ML, so there are still some reactions with e^- transfer happening but not too much Pt extraction any more.

Chapter 4

Conclusions

This thesis has investigated the nature of the reactions that occur as Pt(111) and Pt(100) single-crystal surfaces are electrochemically oxidised. In these reactions, Pt atoms are extracted from their lattice sites, which remodels the Pt surfaces. Eventually, after many oxidation and reduction cycles, the Pt surface is degraded, and in Pt fuel cell catalysts this limits the lifetime of the catalysts. The oxidation was studied by combined electrochemical and surface X-ray diffraction experiments carried out at ESRF, Grenoble, France and DESY, Hamburg, Germany. Several types of electrochemical experiments were carried out, including cyclic voltammetry, potential steps, and potential sweep-hold experiments.

This first stage of the data analysis was to estimate the double layer charges of CV data. Different baselines were used to subtract off these charges, which do not contribute to the electrochemical reactions. The remaining charges are due to the oxidation and reduction reactions, and were integrated to get the number of electrons transferred, expressed as coverages of electrons, θ_e, which are the number of electrons per surface atom.

The number and locations of the oxidized Pt atoms were determined by surface X-ray diffraction experiments that were analysed by our collaborators. After the structures with the coordinates of the Pt atoms were determined from surface crystallography through analysis of crystal truncation rods, the calibration relationship between X-ray intensity and the number of extracted atoms was determined. This calibration curve could then be used to calculate the coverage of extracted atoms, θ_{ex}, from the X-ray intensity during a CV or other electrochemical experiment. The two coverages θ_e and θ_{ex} were then compared to decide what the possible reactions were, including their stoichiometry and the oxidation states of the Pt atoms. Potential step experiments and potential sweep-hold experiments were also analyzed to find these coverages, and their time dependence was used to determine the kinetics. A logarithmic growth law has been suggested in the literature for similar experiments on polycrystalline or cycled single-crystal surfaces, and this possibility was investigated here for the initial stages of oxidation on these single-crystal surfaces.

In all, the surface degradation of Pt(100) surface is much faster than Pt(111), so for the real nanoparticle Pt catalyst in fuel cells, it's better to have more Pt(111) surfaces and fewer Pt(100) for longer lifetime with fewer degradation, and Pt(111) surfaces in Pt catalyst because Pt(100) surfaces are fast degraded after several times of use, and Pt(111) surfaces are left for research of long term lifetime research of thousands or even millions times of turning on and off of fuel cell.

For the Pt(111) extraction, from CV data with segmented baseline correction, 6 to 7.5 e^-s are transferred per extracted Pt but θ_{ex} is very low, and the possible product is 0.5 ML adsorbed oxygen and a few extracted PtO. If CV isn't baseline corrected, more than 10 e^-s are transferred per extracted Pt, and the extraction process products 0.5 ML O_{ads} and a few extracted PtO_2. However, its corresponding

cathodic charge for the reduction process is much lower than the anodic charge if there is no baseline correction.

For the extraction of Pt(100) with CV segmented baseline correction, there are 3 to 4 e^-s transferred per extracted Pt, and it produces O_{ads} and extracted PtO_2 units in long chains, with the addition of both groups as 0.5 ML, and extracted PtO_2 units as θ_{ex} (0.25 ML to 0.39 ML). If there is no baseline correction on CV data, there are 4 to 5.2 e^-s transferred per extracted Pt, which matches the reaction to form 0.5 ML O_{ads} and $\frac{\theta_{ex}}{4}$ short extracted Pt_4O_{10} chains or short extracted Pt_3O_8 chains with an equal number of independent extracted PtO_2, of which the coverage is $\frac{\theta_{ex}}{4}$. Similar to Pt(111), the cathodic charge without baseline correction is much lower than the corresponding anodic one.

For Pt(100) potential steps, θ_e only fits the logarithmic growth law in the first second of each step, and then is unchanged after ∼1 s (the limit time is different via steps). The slope of θ_e vs log t was linearly related to potential, but with different values from reference [104]. This difference is probably caused by the errors on charge data. Then θ_{ex} vs log t shows the Pt extraction only happens at 1.0 to 1.2 V, and the reactions happened in two datasets are nearly same. The θ_e vs θ_{ex} ratio is larger than for the CV data. This is because the double layer charges and surface restructuring from Pt extraction-reduction cycles occur for each step after ∼1 V, which makes the Pt surface different for different steps, with different reactions.

For the Pt(100) sweep holds, θ_e and θ_{ex} vs log$t$ show an increasing relationship that is not very linear. Also, their slopes are not linearly related to potential. Both the slopes sharply change during the potential range of Pt extraction from 1.05 to 1.15 V, and are steady out of this range.

In terms of future work, the immediate next steps would be more tests on Pt(111)

after fast scans, because there needs to be an reference X-ray intensity measurement at 0.9 V on the flat and smooth surface before the fast scans begin, in order to determine the absolute values of θ_{ex}. Then, the mechanism of changes on Pt(111) surface after fast scans need to be learnt, because both Pt(111) surfaces are pre-treated by fast scans in Section 3.1.3 and Section 3.1.4, but the Pt surface performances on X-ray are absolute different. Also, we need more work on potential step tests on Pt(100) surface, because double layer charges of first experiment need to be removed, and the first 0.1 s current data of second experiment are missing.

In the longer term, other catalyst materials could be studied. Pt catalysts are too expensive and too rare if the fuel cell is really mass produced. Therefore, Pt extraction or other similar reactions on cheaper materials need to be researched. For example, platinum metal alloy catalysts such as Pt-Co, Pt-Cr are said to be very stable in lifetime tests compared with other platinum metal alloys [116].

References

[1] V. Climent, J. M. Feliu, Thirty years of platinum single crystal electrochemistry, Journal of Solid State Electrochemistry 15 (2011) 1297.

[2] J. Greeley, N. M. Markovic, The road from animal electricity to green energy: combining experiment and theory in electrocatalysis, Energy & Environmental Science 5 (2012) 9246–9256.

[3] V. R. Stamenkovic, D. Strmcnik, P. P. Lopes, N. M. Markovic, Energy and fuels from electrochemical interfaces, Nature materials 16 (2017) 57–69.

[4] A. M. Gómez-Marín, R. Rizo, J. M. Feliu, Oxygen reduction reaction at Pt single crystals: a critical overview, Catalysis Science & Technology 4 (2014) 1685–1698.

[5] A. Chen, P. Holt-Hindle, Platinum-based nanostructured materials: synthesis, properties, and applications, Chemical reviews 110 (2010) 3767–3804.

[6] J. P. Owejan, J. E. Owejan, W. Gu, Impact of platinum loading and catalyst layer structure on PEMFC performance, Journal of The Electrochemical Society 160 (2013) F824.

[7] M. T. Koper, Structure sensitivity and nanoscale effects in electrocatalysis, Nanoscale 3 (2011) 2054–2073.

[8] M. Akhairi, S. Kamarudin, Catalysts in direct ethanol fuel cell (DEFC): An overview, International journal of hydrogen energy 41 (2016) 4214–4228.

[9] I. Katsounaros, S. Cherevko, A. R. Zeradjanin, K. J. Mayrhofer, Oxygen electrochemistry as a cornerstone for sustainable energy conversion, Angewandte Chemie International Edition 53 (2014) 102–121.

[10] A. F. Ghenciu, Review of fuel processing catalysts for hydrogen production in PEM fuel cell systems, Current opinion in solid state and materials science 6 (2002) 389–399.

[11] X. Cheng, Z. Shi, N. Glass, L. Zhang, J. Zhang, D. Song, Z.-S. Liu, H. Wang, J. Shen, A review of PEM hydrogen fuel cell contamination: Impacts, mechanisms, and mitigation, Journal of Power Sources 165 (2007) 739–756.

[12] R.-A. Felseghi, E. Carcadea, M. S. Raboaca, C. N. Trufin, C. Filote, Hydrogen fuel cell technology for the sustainable future of stationary applications, Energies 12 (2019) 4593.

[13] B. Tanç, H. T. Arat, E. Baltacıoğlu, K. Aydın, Overview of the next quarter century vision of hydrogen fuel cell electric vehicles, International Journal of Hydrogen Energy 44 (2019) 10120–10128.

[14] L. Wood, Hydrogen fuel cells global market report 2021: Market is expected to reach $16.50 billion in 2025 at a cagr of 43.8% with long-term forecast to 2030 - researchandmarkets.com, https://www.businesswire.com/news/home/20211207005952/en/

Hydrogen-Fuel-Cells-Global-Market-Report-2021-Market-is-Expected-to-Reach-16.50-Billion-in-2025-at-a-CAGR-of-43.8-with-Long-term-Forecast-to-2030---Research com, 2021 (accessed June 13, 2022).

[15] E. Huang, Fuel-cell vehicles are set for big gains in china's commercial truck market, jpmorgan says, https://www.cnbc.com/2021/08/25/jpmorgan-fuel-cell-vehicles-set-for-gains-in-china-truck-market.html, 2022 (accessed June 13, 2022).

[16] E. Staff, More than 800 hydrogen buses at the beijing winter olympics: A gold medal result, https://www.sustainable-bus.com/fuel-cell-bus/more-than-800-hydrogen-buses-at-the-beijing-winter-olympics/, 2022 (accessed June 13, 2022).

[17] A. Frangoul, Hydrogen-powered train a step closer to passenger service in germany, https://www.cnbc.com/2022/03/16/hydrogen-powered-train-a-step-closer-to-passenger-service-in-germany.html, 2022 (accessed June 13, 2022).

[18] S. A. Vilekar, R. Datta, The effect of hydrogen crossover on open-circuit voltage in polymer electrolyte membrane fuel cells, Journal of Power Sources 195 (2010) 2241–2247.

[19] J. Zhang, Y. Tang, C. Song, J. Zhang, H. Wang, Pem fuel cell open circuit voltage (ocv) in the temperature range of 23 c to 120 c, Journal of power sources 163 (2006) 532–537.

[20] F. Barbir, T. Gomez, Efficiency and economics of proton exchange membrane (pem) fuel cells, international journal of hydrogen energy 22 (1997) 1027–1037.

[21] V. A. Kovtunenko, L. Karpenko-Jereb, Lifetime of catalyst under voltage cycling in polymer electrolyte fuel cell due to platinum oxidation and dissolution, Technologies 9 (2021) 80.

[22] A. Björling, J. M. Feliu, Electrochemical surface reordering of Pt (1 1 1): A quantification of the place-exchange process, Journal of electroanalytical chemistry 662 (2011) 17–24.

[23] J. Drnec, D. A. Harrington, O. M. Magnussen, Electrooxidation of Pt (111) in acid solution, Current Opinion in Electrochemistry 4 (2017) 69–75.

[24] G. Jerkiewicz, G. Vatankhah, J. Lessard, M. P. Soriaga, Y.-S. Park, Surface-oxide growth at platinum electrodes in aqueous h2so4: Reexamination of its mechanism through combined cyclic-voltammetry, electrochemical quartz-crystal nanobalance, and auger electron spectroscopy measurements, Electrochimica Acta 49 (2004) 1451–1459.

[25] D. V. Heyd, D. A. Harrington, Platinum oxide growth kinetics for cyclic voltammetry, Journal of Electroanalytical Chemistry 335 (1992) 19–31.

[26] M. Ackermann, T. Pedersen, B. Hendriksen, O. Robach, S. Bobaru, I. Popa, C. Quiros, H. Kim, B. Hammer, S. Ferrer, et al., Structure and reactivity of surface oxides on Pt (110) during catalytic CO oxidation, Physical review letters 95 (2005) 255505.

[27] Y. Liu, A. Barbour, V. Komanicky, H. You, X-ray crystal truncation rod studies of surface oxidation and reduction on Pt (111), The Journal of Physical Chemistry C 120 (2016) 16174–16178.

[28] T. Shirasawa, T. Masuda, W. Voegeli, E. Arakawa, C. Kamezawa, T. Takahashi, K. Uosaki, T. Matsushita, Fast structure determination of electrode surfaces for investigating electrochemical dynamics using wavelength-dispersive x-ray crystal truncation rod measurements, The Journal of Physical Chemistry C 121 (2017) 24726–24732.

[29] Z. Nagy, Electrochemistry at synchrotrons, Journal of Solid State Electrochemistry 15 (2011) 1679–1695.

[30] Y. Takagi, H. Wang, Y. Uemura, E. Ikenaga, O. Sekizawa, T. Uruga, H. Ohashi, Y. Senba, H. Yumoto, H. Yamazaki, et al., In situ study of an oxidation reaction on a Pt/C electrode by ambient pressure hard X-ray photoelectron spectroscopy, Applied Physics Letters 105 (2014) 131602.

[31] D. W. Rankin, Crc handbook of chemistry and physics, edited by david r. lide, 2009.

[32] B. B. Damaskin, O. A. Petrii, Historical development of theories of the electrochemical double layer, Journal of solid state electrochemistry 15 (2011) 1317–1334.

[33] A. Boronat-González, E. Herrero, J. M. Feliu, Determination of the potential of zero charge of Pt/CO electrodes using an impinging jet system, Journal of Solid State Electrochemistry 24 (2020) 2871–2881.

[34] K. Holub, Relaxation of electrode processes with simultaneous consideration of double-layer charging and faradaic current. Part I, Journal of Electroanalytical Chemistry and Interfacial Electrochemistry 17 (1968) 277–287.

[35] R. Parsons, The contribution to the capacity of an electrode from a species adsorbed with partial charge transfer, Canadian Journal of Chemistry 59 (1981) 1898–1902.

[36] N. Garcia-Araez, V. Climent, E. Herrero, J. M. Feliu, J. Lipkowski, Thermodynamic approach to the double layer capacity of a Pt (1 1 1) electrode in perchloric acid solutions, Electrochimica acta 51 (2006) 3787–3793.

[37] U. Hamm, D. Kramer, R. Zhai, D. Kolb, The pzc of Au (111) and Pt (111) in a perchloric acid solution: an ex situ approach to the immersion technique, Journal of electroanalytical Chemistry 414 (1996) 85–89.

[38] T. Pajkossy, D. Kolb, Double layer capacitance of Pt (111) single crystal electrodes, Electrochimica acta 46 (2001) 3063–3071.

[39] Z. Kerner, T. Pajkossy, L. A. Kibler, D. M. Kolb, The double layer capacity of Pt (1 0 0) in aqueous perchlorate solutions, Electrochemistry communications 4 (2002) 787–789.

[40] V. Prabhu, L. Zarapkar, R. Dhaneshwar, Electrochemical studies of hydrogen peroxide at a platinum disc electrode, Electrochimica Acta 26 (1981) 725–729.

[41] M. J. Van Der Niet, N. Garcia-Araez, J. Hernández, J. M. Feliu, M. T. Koper, Water dissociation on well-defined platinum surfaces: The electrochemical perspective, Catalysis today 202 (2013) 105–113.

[42] M. Martins, C. Zinola, G. Andreasen, R. Salvarezza, A. Arvia, The possible existence of subsurface H-atom adsorbates and H2 electrochemical evolution reaction intermediates on platinum in acid solutions, Journal of Electroanalytical Chemistry 445 (1998) 135–154.

[43] B. Podlovchenko, A. Pshenichnikov, A. Skundin, Metallic and metal-modified electrocatalysts, Russian electrochemistry 29 (1993) 534–546.

[44] H. Tanaka, S. Sugawara, K. Shinohara, T. Ueno, S. Suzuki, N. Hoshi, M. Nakamura, Infrared reflection absorption spectroscopy of OH adsorption on the low index planes of Pt, Electrocatalysis 6 (2015) 295–299.

[45] A. Berná, V. Climent, J. M. Feliu, New understanding of the nature of OH adsorption on Pt (1 1 1) electrodes, Electrochemistry Communications 9 (2007) 2789–2794.

[46] V. Climent, R. Gómez, J. M. Orts, J. M. Feliu, Thermodynamic analysis of the temperature dependence of OH adsorption on Pt (111) and Pt (100) electrodes in acidic media in the absence of specific anion adsorption, The Journal of Physical Chemistry B 110 (2006) 11344–11351.

[47] H. A. Baroody, G. Jerkiewicz, M. H. Eikerling, Modelling oxide formation and growth on platinum, The Journal of Chemical Physics 146 (2017) 144102.

[48] F. Bizzotto, H. Ouhbi, Y. Fu, G. K. Wiberg, U. Aschauer, M. Arenz, Examining the structure sensitivity of the oxygen evolution reaction on Pt single-crystal electrodes: A combined experimental and theoretical study, ChemPhysChem 20 (2019) 3154–3162.

[49] T. Kondo, T. Masuda, N. Aoki, K. Uosaki, Potential-Dependent Structures and Potential-Induced Structure Changes at Pt(111) Single-Crystal Electrode/Sulfuric and Perchloric Acid Interfaces in the Potential Region between Hydrogen Underpotential Deposition and Surface Oxide Formation by In Situ

Surface X-ray Scattering, The Journal of Physical Chemistry C 120 (2016) 16118–16131.

[50] M. T. Koper, Blank voltammetry of hexagonal surfaces of Pt-group metal electrodes: Comparison to density functional theory calculations and ultra-high vacuum experiments on water dissociation, Electrochimica Acta 56 (2011) 10645–10651.

[51] J. Drnec, M. Ruge, F. Reikowski, B. Rahn, F. Carla, R. Felici, J. Stettner, O. M. Magnussen, D. A. Harrington, Initial stages of Pt (111) electrooxidation: dynamic and structural studies by surface x-ray diffraction, Electrochimica Acta 224 (2017) 220–227.

[52] A. M. Gómez-Marín, J. M. Feliu, Oxide growth dynamics at Pt(111) in absence of specific adsorption: A mechanistic study, Electrochimica Acta 104 (2013) 367–377.

[53] A. M. Gómez-Marín, J. Clavilier, J. M. Feliu, Sequential Pt(111) oxide formation in perchloric acid: An electrochemical study of surface species interconversion, Journal of Electroanalytical Chemistry 688 (2013) 360–370.

[54] D. Strmcnik, D. Tripkovic, D. Van der Vliet, V. Stamenkovic, N. Marković, Adsorption of hydrogen on Pt (1 1 1) and Pt (1 0 0) surfaces and its role in the HOR, Electrochemistry communications 10 (2008) 1602–1605.

[55] E. Skúlason, G. S. Karlberg, J. Rossmeisl, T. Bligaard, J. Greeley, H. Jónsson, J. K. Nørskov, Density functional theory calculations for the hydrogen evolution reaction in an electrochemical double layer on the Pt (111) electrode, Physical Chemistry Chemical Physics 9 (2007) 3241–3250.

[56] G. Jerkiewicz, Hydrogen sorption ATIN electrodes, Progress in Surface Science 57 (1998) 137–186.

[57] G. W. Watson, R. P. Wells, D. J. Willock, G. J. Hutchings, A comparison of the adsorption and diffusion of hydrogen on the {111} surfaces of Ni, Pd, and Pt from density functional theory calculations, The Journal of Physical Chemistry B 105 (2001) 4889–4894.

[58] E. Protopopoff, P. Marcus, Effects of chemisorbed sulphur on the hydrogen adsorption and evolution on metal single crystal surfaces, Journal de chimie physique 88 (1991) 1423–1452.

[59] N. Marković, P. Ross, Electrocatalysts by design: from the tailored surface to a commercial catalyst, Electrochimica Acta 45 (2000) 4101–4115.

[60] H. A. Gasteiger, N. M. Marković, P. N. Ross, Bromide adsorption on Pt (111): Adsorption isotherm and electrosorption valency deduced from RRDPt (111) E measurements, Langmuir 12 (1996) 1414–1418.

[61] J. Mostany, E. Herrero, J. M. Feliu, J. Lipkowski, Determination of the gibbs excess of H and OH adsorbed at a Pt (1 1 1) electrode surface using a thermodynamic method, Journal of Electroanalytical Chemistry 558 (2003) 19–24.

[62] A. Michaelides, P. Hu, A density functional theory study of hydroxyl and the intermediate in the water formation reaction on Pt, The Journal of Chemical Physics 114 (2001) 513–519.

[63] A. M. Gómez-Marín, J. M. Feliu, Pt (1 1 1) surface disorder kinetics in perchloric acid solutions and the influence of specific anion adsorption, Electrochimica acta 82 (2012) 558–569.

[64] V. Tripković, E. Skúlason, S. Siahrostami, J. K. Nørskov, J. Rossmeisl, The oxygen reduction reaction mechanism on Pt (1 1 1) from density functional theory calculations, Electrochimica Acta 55 (2010) 7975–7981.

[65] E. M. Karp, C. T. Campbell, F. Studt, F. Abild-Pedersen, J. K. Nørskov, Energetics of oxygen adatoms, hydroxyl species and water dissociation on Pt (111), The Journal of Physical Chemistry C 116 (2012) 25772–25776.

[66] H. Ogasawara, B. Brena, D. Nordlund, M. Nyberg, A. Pelmenschikov, L. Pettersson, A. Nilsson, Structure and bonding of water on Pt (111), Physical review letters 89 (2002) 276102.

[67] G. Karlberg, G. Wahnström, An interaction model for OH+ H_2O-mixed and pure h 2 o overlayers adsorbed on Pt (111), The Journal of chemical physics 122 (2005) 194705.

[68] D. Fantauzzi, J. Bandlow, L. Sabo, J. E. Mueller, A. C. van Duin, T. Jacob, Development of a reaxff potential for Pt–O systems describing the energetics and dynamics of Pt-oxide formation, Physical Chemistry Chemical Physics 16 (2014) 23118–23133.

[69] V. Viswanathan, H. A. Hansen, J. Rossmeisl, T. F. Jaramillo, H. Pitsch, J. K. Nørskov, Simulating linear sweep voltammetry from first-principles: application to electrochemical oxidation of water on Pt (111) and $Pt_3Ni(111)$, The Journal of Physical Chemistry C 116 (2012) 4698–4704.

[70] T. Fuchs, J. Drnec, F. Calle-Vallejo, N. Stubb, D. J. S. Sandbeck, M. Ruge, S. Cherevko, D. A. Harrington, O. M. Magnussen, Structure dependency of the

atomic-scale mechanisms of platinum electro-oxidation and dissolution, Nature Catalysis 3 (2020) 754–761.

[71] J. M. Hawkins, J. F. Weaver, A. Asthagiri, Density functional theory study of the initial oxidation of the Pt (111) surface, Physical Review B 79 (2009) 125434.

[72] M. J. Eslamibidgoli, M. H. Eikerling, Atomistic mechanism of Pt extraction at oxidized surfaces: insights from DFT, Electrocatalysis 7 (2016) 345–354.

[73] Y.-H. Fang, Z.-P. Liu, Toward anticorrosion electrodes: site-selectivity and self-acceleration in the electrochemical corrosion of Platinum, The Journal of Physical Chemistry C 114 (2010) 4057–4062.

[74] Z. Gu, P. B. Balbuena, Absorption of atomic oxygen into subsurfaces of Pt (100) and Pt (111): Density functional theory study, The Journal of Physical Chemistry C 111 (2007) 9877–9883.

[75] W. Lew, M. C. Crowe, E. Karp, O. Lytken, J. A. Farmer, L. Árnadóttir, C. Schoenbaum, C. T. Campbell, The energy of adsorbed hydroxyl on Pt (111) by microcalorimetry, The Journal of Physical Chemistry C 115 (2011) 11586–11594.

[76] K. Domke, E. Herrero, A. Rodes, J. M. Feliu, Determination of the potentials of zero total charge of Pt(100) stepped surfaces in the [] zone. effect of the step density and anion adsorption, Journal of Electroanalytical Chemistry 552 (2003) 115–128.

[77] R. Gómez, J. M. Orts, B. Álvarez-Ruiz, J. M. Feliu, Effect of temperature on

hydrogen adsorption on Pt (111), Pt (110), and Pt (100) electrodes in 0.1 m $HClO_4$, The Journal of Physical Chemistry B 108 (2004) 228–238.

[78] J. A. Santana, J. J. Saavedra-Arias, Y. Ishikawa, Electrochemical hydrogen oxidation on Pt (100): a combined direct molecular dynamics/density functional theory study, Electrocatalysis 6 (2015) 534–543.

[79] M. J. van der Niet, A. den Dunnen, L. B. Juurlink, M. T. Koper, The influence of step geometry on the desorption characteristics of O_2, D_2, and H_2O from stepped Pt surfaces, The Journal of chemical physics 132 (2010) 174705.

[80] B. Han, V. Viswanathan, H. Pitsch, First-principles based analysis of the electrocatalytic activity of the unreconstructed Pt (100) surface for oxygen reduction reaction, The Journal of Physical Chemistry C 116 (2012) 6174–6183.

[81] P. Moussounda, M. Haroun, P. Légaré, Adsorption of methanol and atomic oxygen on the Pt (100) surface: a first-principles periodic density functional theory study, Physica Scripta 81 (2010) 045603.

[82] Q. Ge, P. Hu, D. King, M.-H. Lee, J. White, M. Payne, Site symmetry dependence of repulsive interactions between chemisorbed oxygen atoms on Pt {100}-(1× 1), The Journal of chemical physics 106 (1997) 1210–1215.

[83] D.-J. Liu, J. W. Evans, Interactions between oxygen atoms on Pt (100): implications for ordering during chemisorption and catalysis, ChemPhysChem 11 (2010) 2174–2181.

[84] A. Zolfaghari, G. Jerkiewicz, New findings on hydrogen and anion adsorption

at a Pt (111) electrode in aqueous H_2SO_4 solution generated by temperature variation, Journal of Electroanalytical Chemistry 422 (1997) 1–6.

[85] R. Jinnouchi, T. Hatanaka, Y. Morimoto, M. Osawa, First principles study of sulfuric acid anion adsorption on a Pt (111) electrode, Physical Chemistry Chemical Physics 14 (2012) 3208–3218.

[86] K. Itaya, S. Sugawara, K. Sashikata, N. Furuya, I nsitu scanning tunneling microscopy of platinum (111) surface with the observation of monatomic steps, Journal of Vacuum Science & Technology A: Vacuum, Surfaces, and Films 8 (1990) 515–519.

[87] X. Deng, F. Galli, M. T. Koper, In situ electrochemical AFM imaging of a Pt electrode in sulfuric acid under potential cycling conditions, Journal of the American Chemical Society 140 (2018) 13285–13291.

[88] M. A. Van Spronsen, J. W. Frenken, I. Groot, Observing the oxidation of platinum, Nature communications 8 (2017) 1–7.

[89] R. M. Arán-Ais, Y. Yu, R. Hovden, J. Solla-Gullón, E. Herrero, J. M. Feliu, H. D. Abruña, Identical location transmission electron microscopy imaging of site-selective Pt nanocatalysts: electrochemical activation and surface disordering, Journal of the American Chemical Society 137 (2015) 14992–14998.

[90] H. You, Z. Nagy, Oxidation-reduction-induced roughening of platinum (1 1 1) surface, Physica B: Condensed Matter 198 (1994) 187–194.

[91] T. Fuchs, J. Drnec, F. Calle-Vallejo, N. Stubb, D. Sandbeck, M. Ruge, S. Cherevko, D. Harrington, O. M. Magnussen, In situ studies of the oxide

structure and oxide growth on single crystal platinum surfaces, in: ECS Meeting Abstracts, 49, IOP Publishing, p. 1464.

[92] P. P. Lopes, D. Strmcnik, D. Tripkovic, J. G. Connell, V. Stamenkovic, N. M. Markovic, Relationships between atomic level surface structure and stability/activity of platinum surface atoms in aqueous environments, Acs Catalysis 6 (2016) 2536–2544.

[93] D. Miller, H. Öberg, S. Kaya, H. S. Casalongue, D. Friebel, T. Anniyev, H. Ogasawara, H. Bluhm, L. G. Pettersson, A. Nilsson, Oxidation of Pt (111) under near-ambient conditions, Physical review letters 107 (2011) 195502.

[94] N. Seriani, Z. Jin, W. Pompe, L. C. Ciacchi, Density functional theory study of platinum oxides: From infinite crystals to nanoscopic particles, physical review B 76 (2007) 155421.

[95] M. Ruge, J. Drnec, B. Rahn, F. Reikowski, D. A. Harrington, F. Carlà, R. Felici, J. Stettner, O. M. Magnussen, Electrochemical oxidation of smooth and nanoscale rough Pt (111): An in situ surface X-ray scattering study, Journal of The Electrochemical Society 164 (2017) H608.

[96] E. F. Holby, J. Greeley, D. Morgan, Thermodynamics and hysteresis of oxide formation and removal on platinum (111) surfaces, The Journal of Physical Chemistry C 116 (2012) 9942–9946.

[97] L. Jacobse, V. Vonk, I. T. McCrum, C. Seitz, M. T. Koper, M. J. Rost, A. Stierle, Electrochemical oxidation of Pt (111) beyond the place-exchange model, Electrochimica Acta (2022) 139881.

[98] D. J. Sandbeck, O. Brummel, K. J. Mayrhofer, J. Libuda, I. Katsounaros, S. Cherevko, Dissolution of platinum single crystals in acidic medium, ChemPhysChem 20 (2019) 2997–3003.

[99] V. Dam, F. De Bruijn, The stability of PEMFC electrodes: platinum dissolution vs potential and temperature investigated by quartz crystal microbalance, Journal of The Electrochemical Society 154 (2007) B494.

[100] R. M. Darling, J. P. Meyers, Kinetic model of platinum dissolution in pemfcs, Journal of the Electrochemical Society 150 (2003) A1523.

[101] P. P. Lopes, D. Tripkovic, P. F. Martins, D. Strmcnik, E. A. Ticianelli, V. R. Stamenkovic, N. M. Markovic, Dynamics of electrochemical Pt dissolution at atomic and molecular levels, Journal of Electroanalytical Chemistry 819 (2018) 123–129.

[102] V. Komanicky, K. Chang, A. Menzel, N. Markovic, H. You, X. Wang, D. Myers, Stability and dissolution of platinum surfaces in perchloric acid, Journal of the Electrochemical Society 153 (2006) B446.

[103] B. Conway, B. Barnett, H. Angerstein-Kozlowska, B. Tilak, A surface-electrochemical basis for the direct logarithmic growth law for initial stages of extension of anodic oxide films formed at noble metals, The Journal of chemical physics 93 (1990) 8361–8373.

[104] B. E. Conway, G. Jerkiewicz, Surface orientation dependence of oxide film growth at platinum single crystals, Journal of Electroanalytical Chemistry 339 (1992) 123–146.

[105] D. Gilroy, Oxide growth at platinum electrodes in h2so4 at potentials below 1.7 v, Journal of Electroanalytical Chemistry and Interfacial Electrochemistry 71 (1976) 257–277.

[106] M. Alsabet, M. Grden, G. Jerkiewicz, Comprehensive study of the growth of thin oxide layers on Pt electrodes under well-defined temperature, potential, and time conditions, Journal of Electroanalytical Chemistry 589 (2006) 120–127.

[107] Y. Furuya, T. Mashio, A. Ohma, N. Dale, K. Oshihara, G. Jerkiewicz, Surface oxide growth on platinum electrode in aqueous trifluoromethanesulfonic acid, The Journal of chemical physics 141 (2014) 164705.

[108] A. Minguzzi, L. Montagna, A. Falqui, A. Vertova, S. Rondinini, P. Ghigna, Dynamics of oxide growth on Pt nanoparticles electrodes in the presence of competing halides by operando energy dispersive X-ray absorption spectroscopy, Electrochimica Acta 270 (2018) 378–386.

[109] S. G. Rinaldo, W. Lee, J. Stumper, M. Eikerling, Mechanistic principles of platinum oxide formation and reduction, Electrocatalysis 5 (2014) 262–272.

[110] Z. Nagy, H. You, Applications of surface X-ray scattering to electrochemistry problems, Electrochimica Acta 47 (2002) 3037–3055.

[111] Y. Gründer, C. A. Lucas, Surface X-ray diffraction studies of single crystal electrocatalysts, Nano Energy 29 (2016) 378–393.

[112] M. Nakamura, New insights on structural dynamics of electrochemical interface by time-resolved surface X-ray diffraction, Current Opinion in Electrochemistry 14 (2019) 200–205.

[113] M. Bogar, I. Khalakhan, A. Gambitta, Y. Yakovlev, H. Amenitsch, In situ electrochemical grazing incidence small angle x-ray scattering: From the design of an electrochemical cell to an exemplary study of fuel cell catalyst degradation, Journal of power sources 477 (2020) 229030.

[114] J. Gustafson, M. Shipilin, C. Zhang, A. Stierle, U. Hejral, U. Ruett, O. Gutowski, P.-A. Carlsson, M. Skoglundh, E. Lundgren, High-energy surface x-ray diffraction for fast surface structure determination, Science 343 (2014) 758–761.

[115] I. Tidswell, N. Marković, P. Ross, Potential dependent surface relaxation of the Pt (001)/electrolyte interface, Physical review letters 71 (1993) 1601.

[116] E. Antolini, J. R. Salgado, E. R. Gonzalez, The stability of Pt–M (M= first row transition metal) alloy catalysts and its effect on the activity in low temperature fuel cells: a literature review and tests on a Pt–Co catalyst, Journal of Power Sources 160 (2006) 957–968.